DISS. ETH NO. 27018

LEAD-FREE LOW-DIMENSIONAL MAIN GROUP METAL HALIDES: NEW SELF-TRAPPED EXCITONIC EMITTERS AND THEIR APPLICATIONS

A thesis submitted to attain the degree of

DOCTOR OF SCIENCES of ETH ZURICH

(Dr. sc. ETH Zurich)

presented by

Bogdan Markovich Benin

Master of Science

Kent State University

Born on 05.04.1993

citizen of the United States of America

Accepted on the recommendation of

Prof. Dr. Maksym V. Kovalenko, examiner

Prof. Dr. Markus Niederberger, co-examiner

2020

Declaration

I hereby confirm that I am the sole author of the written work herein enclosed and that I have compiled it in my own words. Parts excepted are corrections of form and content by the supervisor.

Title of work:

Lead-Free Low-Dimensional Main Group Metal Halides: New Self-Trapped Excitonic Emitters and Their Applications

With my signature I confirm:

− I have committed none of the forms of plagiarism.

− I have documented all methods, data, and processes truthfully.

− I have not manipulated any data.

− I have mentioned all persons who were significant contributors to this work, as described below.

− I obtained copyright permissions from the journal for reproducing the text and Figures in this thesis, where needed.

− I am aware that the work may be screened electronically for plagiarism.

Place, date — Signature(s)

Winterthur 20.07.20

Dr. S. Yakunin (ETH Zürich) performed numerous optical experiments including both RT and temperature dependent PL, PLE, and TRPL as well as quantum yield determination for *Chapters* 2-5. He also did much of the data processing and analysis for thermal imaging as well as the thermometric precision experiments in *Chapter 3*.

Dr. K.M. McCall (ETH Zürich) assisted with much of the crystallography in *Chapter 4 and 5.* He also performed the Raman measurements and some of the temperature dependence measurements in *Chapter 4.*

Dr. M. Wörle (ETH Zürich) assisted and checked all the crystallography throughout this dissertation. He also performed the single crystal measurements in *Chapter 2*.

Dr. D.N. Dirin (ETH Zürich) assisted in the characterization and description of the materials in *Chapter 2*.

Dr. S. Cattaneo and Dr. C. Hofer (CSEM) developed the ToF-FLI imager used in *Chapter 3.*

Dr. Y. Shynkarenko (ETH Zürich) played a significant role in the data treatment and analysis for thermal imaging in *Chapter* 3. He also performed several optical experiments including quantum yield and absorption coefficient determination (*Chapter 4 and 5*).

Dr. G. Raino (ETH Zürich) performed he temperature dependent PL measurements in *Chapter 2*.

Dr. O. Nazarenko (ETH Zürich) assisted with the solid-state growth of materials in *Chapter 2*. She additionally prepared one of the materials utilized in *Chapter 3.*

Dr. M.I. Bodnarchuk (ETH Zürich) prepared one of the materials utilized in *Chapter 3*.

M. Aebli (ETH Zürich) performed the ssNMR experiments and processed all the relevant data in *Chapter 4*.

Dr. F. Krumeich (ETH Zürich) took SEM images and performed EDS measurements in *Chapter 2.*

V. Morad (ETH Zürich) performed the DFT calculations in *Chapter 2 and 4.*

K. Sakhatskyi (ETH Zürich) performed electrical characterization as well as photoconductivity and X-ray photoconductivity measurements of the materials presented in *Chapters 4 and 5.*

M. Fischer (ETH Zürich) prepared some of the polycrystalline powders of materials presented in *Chapter 2.*

D. Borgeaud dit Advocat (ETH Zürich) prepared some of the single crystals of materials presented in *Chapter 5.*

Acknowledgements

There is an African proverb, “it takes a village to raise a child.” Well, it takes a research group to raise a researcher.

First, I want to thank the head of that research group, Prof. Dr. Maksym V. Kovalenko for the opportunity to come to his group, to find my niche, for supporting my work, and offering his guidance.

I want to thank Prof. Dr. Markus Niederberger for accepting to evaluate my dissertation and act as a co-referee for the final examination.

This dissertation would not have been possible without the numerous contributions, support, and mentorship of Dr. Sergii Yakunin, Dr. Michael Wörle, Dr. Dmitry N. Dirin, and Dr. Kyle M. McCall. At the same time, I want to thank Dr. Yevhen Shynkarenko, Viktoriia Morad, and Marcel Aebli for providing optical measurements, calculations, and NMR measurements.

Furthermore, the entire Kovalenko group has been an amazing team of researchers and colleagues to work with, and I look forward to seeing what each person achieves in the coming years.

Additionally, I will always fondly remember the open and creative environment (and the never-ending supply of sweets) fostered by Kyle and Martin in H111.

I want to specially thank Marcel, Dominic, Matthias, Matyas, Dylan, Nick, Laura, Marco, Kyle, Sergii, Federico, Michael, Darius, Matt, Ryan and a few others for, at one point or another, sharing a bite or a drink and stirring-up new ideas or just lightening the mood.

Finally, I thank my parents, Mark & Galina Benin, and Aylin Crugnale, for their inexhaustible support and love.

Table of Contents

Declaration ... **ii**
Acknowledgements ... **iv**
Table of Contents ... **v**
List of Abbreviations ... **viii**
Abstract ... **x**
Zusammenfassung ... **xii**
Chapter 1. Metal-halides and their dimensional diversity ... **1**
1.1. A brief history of luminescent materials ... 1
1.2. Lead-halide perovskites ... 3
1.3. Lead-free alternatives ... 5
1.3.1. AMX_3 alternatives ... 6
1.3.2. Double perovskites — In^+, Sb^{3+}, and Bi^{3+} ... 6
1.4. Lowering dimensionality ... 8
1.4.1. General trends ... 8
1.4.2. Self-trapped excitons ... 9
1.4.2.1. Excitons ... 9
1.4.2.2. Wannier-Mott and Frenkel excitons ... 10
1.4.2.3. The Importance of phonons and polarons ... 11
1.4.2.4. Self-trapped excitons ... 11
1.4.3. Two-dimensional metal-halides ... 12
1.4.4. One-dimensional materials ... 14
1.4.5. Zero-dimensional materials ... 16
1.4.5.1. Overview ... 16
1.4.5.2. Applications for 0D metal-halides ... 20
1.5. Thesis outline ... 22
Chapter 2. Highly Emissive Self-Trapped Excitons in Fully Inorganic Zero-Dimensional Tin Halides ... **25**
2.1. Abstract ... 25
2.2. Introduction ... 27
2.3. Experimental details ... 27
2.4. Results and Discussion ... 28
2.5. Conclusion ... 36
Chapter 3. High-resolution remote thermometry and thermography using luminescent low-dimensional tin-halide perovskites ... **37**
3.1. Abstract ... 37
3.2. Introduction ... 38
3.3. Experimental details ... 40
3.4. Results and Discussion ... 40
3.5. Conclusion ... 52
Chapter 4. The $Rb_7Bi_{3-3x}Sb_{3x}Cl_{16}$ family: A Fully Inorganic Solid Solution with Room-Temperature Luminescent Members ... **53**
4.1. Abstract ... 53

4.2. Introduction 54
4.3. Experimental details 55
4.4. Results and Discussion 55
4.5. Conclusion 81
Chapter 5. Intervalent and mixed-valent zero-dimensional metal-halides of the $Rb_{23}Sb^{III}_{7-x}Bi^{III}_{x}Sb^{V}_{2}Cl_{54}$ family ($x \leq 3.5$) 82
5.1. Abstract 82
5.2. Introduction 83
5.3. Experimental Methods 85
5.4. Results and Discussion 85
5.5. Conclusion 96
Chapter 6. Summary and Outlook 98
6.1. Summary 98
6.2. Outlook 98
6.2.1. Luminescent solar concentrators 100
6.2.2. Fluorescent-lifetime encoded security tags 101
6.2.3. "STED" microscopy and FLIM-nanoscopy 101
Chapter 7. Materials and Methods 104
7.1. Materials 104
7.2. Synthetic procedures 104
7.2.1. Cs_4SnBr_6 synthesis 104
7.2.2. $Cs_{4-x}A_xSn(Br_{1-y}I_y)_6$ (A = Rb, K; $x \leq 1$, $y \leq 1$) synthesis 105
7.2.3. $Rb_7Sb_3Cl_{16}$ synthesis 105
7.2.4. $K_7Sb_3Cl_{16}$ synthesis 105
7.2.5. $Rb_7Bi_3Cl_{16}$ synthesis 105
7.2.6. $Rb_7Bi_{3-3x}Sb_{3x}Cl_{16}$ synthesis 106
7.2.7. $Rb_{23}Bi^{III}_{7-x}Sb^{III}_{x}Sb^{V}_{2}Cl_{54}$ synthesis 106
7.3. Structural Characterization 107
7.3.1. Powder X-ray Diffraction 107
7.3.2. Single-Crystal X-ray Diffraction 107
7.3.3. Scanning Electron Microscopy and Energy-Dispersive X-ray Spectroscopy 107
7.3.4. ^{87}Rb NMR 107
7.4. Optical characterization 108
7.4.1. UV-Vis Diffuse Reflectance Measurements 108
7.4.2. RT PL and PLE Measurements 108
7.4.3. Absolute PLQY measurements 108
7.4.4. RT TRPL 108
7.4.5. Absorption Coefficient determination 108
7.4.6. dT-PL, dT-PLE, dT-TRPL, TRES, dW-PL Measurements 109
7.4.6.1. $Cs_{4-x}A_xSn(Br_{1-y}I_y)_6$ (A = Rb, K; $x \leq 1$, $y \leq 1$) 109
7.4.6.2. $Rb_7Bi_{3-3x}Sb_{3x}Cl_{16}$ and $K_7Sb_3Cl_{16}$ 109
7.4.7. Raman 109
7.4.8. DFT calculations 110

7.4.8.1. $Cs_{4-x}A_xSn(Br_{1-y}I_y)_6$ (A = Rb, K; $x \leq 1$, $y \leq 1$) 110
7.4.8.2. $Rb_7Bi_{3-3x}Sb_{3x}Cl_{16}$ and $K_7Sb_3Cl_{16}$.....110
7.4.9. Conductivity and X-ray photoconductivity measurements..... 111
Chapter 8. Appendix..... 112
8.1. Appendix to Chapter 2..... 112
8.2. Appendix to Chapter 3..... 133
8.3. Appendix to Chapter 4..... 143
8.4. Appendix to Chapter 5..... 183
References..... 198
Curriculum Vitae..... 223

List of Abbreviations

CB	Conduction Band
CC	Configurational Coordinate
CRI	Color Rendering Index
DFT	Density Functional Theory
DOS	Density of States
dT-PL	Temperature dependent Photoluminescence
dT-PLE	Temperature dependent Photoluminescence Excitation
dT-TRPL	Temperature dependent Time-Resolved Photoluminescence
dW-PL	Power dependent Photoluminescence
EDS	Energy Dispersive X-ray Spectroscopy
FA	Formamidinium
FLI	Fluorescence Lifetime Imaging
FLIM	Fluorescence Lifetime Imaging Microscopy
FOM	Figure-Of-Merit
FWHM	Full-Width-at-Half-Maximum
HOMO	Highest Occupied Molecular Orbital
ICP-MS	Inductively Coupled Plasma Mass Spectrometry
IR	Infrared
KM	Kubelka-Munk
LED	Light Emitting Diode
LSC	Luminescent Solar Concentrator
LUMO	Lowest Unoccupied Molecular Orbital
MA	Methylammonium
MQMAS	Multi-Quantum-Magic-Angle Spinning
NC	Nanocrystal
PCE	Power Conversion Efficiency
PL	Photoluminescence Spectroscopy
PLE	Photoluminescence Excitation Spectroscopy
PXRD	Powder X-Ray Diffraction
QY/PLQY	Photoluminescence Quantum Yield
ROT	Remote-Optical Thermography
RT	Room-temperature
SCXRD	Single Crystal X-ray Diffraction
SEM	Scanning Electron Microscopy
SHG	Second Harmonic Generation
SSL	Solid-State Lighting
ssNMR	Solid-State Nuclear Magnetic Resonance

STCTE	Self-Trapped Charge-Transfer Exciton
STE	Self-Trapped Exciton
STED	Stimulated Emission Depletion
TCSPC	Time-Correlated Single Photon Counting
ToF	Time-of-Flight
TRES	Time-Resolved Emission Spectroscopy
TRPL	Time-Resolved Photoluminescence
UV-Vis	Ultraviolet-Visible
VB	Valence Band
XRD	X-Ray Diffraction
μτ	Mobility-Lifetime Product
0D	Zero-Dimensional
1D	One-Dimensional
2D	Two-Dimensional
3D	Three-Dimensional

Abstract

LEAD-FREE LOW-DIMENSIONAL MAIN GROUP METAL HALIDES: NEW SELF-TRAPPED EXCITONIC EMITTERS AND THEIR APPLICATIONS

Bogdan Markovich Benin

Metal-halide based semiconductors have been in the limelight for the past few years as a result of the outstanding performance of devices in a variety of optoelectronic applications utilizing lead-halide perovskites. Lead-free materials based on Sb, Sn, or Bi with a three-dimensional (3D) framework, on the other hand, have yet to provide a true alternative.

This thesis instead explores the field of low-dimensional, specifically zero-dimensional (0D), lead-free metal-halides as luminescent materials. These 0D materials contain disconnected metal-halide octahedra, which drastically alters their optoelectronic properties compared to fully connected 3D structures and, prior to 2017, the library of such 0D metal-halides was exceedingly small.

This work began with the study of the optical properties of one known yet uninvestigated incongruently melting phase — Cs_4SnBr_6. This material was found to exhibit broad yet efficient room temperature photoluminescence (RT PL), which occurs as a result of the recombination of self-trapped excitons (STEs). The STE emission in this phase was then found to be compositionally tunable within the $Cs_{4-x}A_xSn(Br_{1-y}I_y)_6$ (A=Rb,K; x,y≤1) family. The discovery of this and other phases by the community prompted a closer look at the optical properties of various additional Sn-based 0D and 1D materials such as $(C_4H_{14}N_2I)_4SnI_6$ and $[C(CH_2)_3]_2SnBr_4$. In doing so, it became evident that their PL lifetimes were extremely temperature dependent (~ 20 ns/K). This opened the door to using 0D metal-halides as remote-optical thermometric and thermographic luminophores *i.e.* materials which can be used to optically determine temperature. In addition to this thermal sensitivity, this emission process was found to be intrinsic and incredibly robust with no changes to the PL lifetime observed between synthetic batches or after partial degradation or partial oxidation. These two factors together allowed for a thermometric precision of ±13 mK.

Although this was quite impressive, the fact of the matter remained that these are still tin-based materials and they will, inevitably, fully oxidize. This inspired the dimensional reduction of the pnictogen halides to discover new, oxidatively stable 0D materials for remote-optical thermometry. This resulted in the $Rb_7Bi_{3-3x}Sb_{3x}Cl_{16}$ (x≤1) family of materials, which also exhibit STE PL with a similar thermal sensitivity as the tin-based materials. Furthermore, these structures contain edge-shared octahedral dimers, which were determined to be the source of RT PL and the luminescent properties of structures containing them have not been previously investigated.

This work also led to the discovery of a new set of mixed-valent materials with the composition $Rb_{23}M^{III}_7Sb^{V}_2Cl_{54}$ (M^{III} = Bi, Sb). These 0D structures contain octahedra of with

various oxidation states (3+ and 5+) and exhibit intense colors as a result of intervalent/mixed-valent charge transfer. While non-luminescent even at 12 K, these materials do exhibit relatively high mobility-lifetime products under X-ray illumination, suggesting that the site-to-site tunneling through this structure may provide a potentially useful tool for new X-ray and hard-radiation detector materials.

In summary, the work presented here has resulted in several, substantial contributions to the low-dimensional metal-halide community, which include the synthesis and characterization of several new materials as well as the identification and successful demonstration of remote-optical thermometry/thermography as a new application for this class of materials. This dissertation serves as an effective foundation for further research in the field by giving other researchers an overview of the field as well as insights into potentially interesting avenues for investigation, both for materials as well as possible applications.

Zusammenfassung

LEAD-FREE LOW-DIMENSIONAL MAIN GROUP METAL HALIDES: NEW SELF-TRAPPED EXCITONIC EMITTERS AND THEIR APPLICATIONS

Bogdan Markovich Benin

Metallhalogenid basierende Halbleiter standen in den letzten Jahren durch die herausragende Leistung von Elementen für optoelektronische Anwendungen, unter Verwendung von Bleihalogenid Perowskiten, im Rampenlicht. Im Gegensatz dazu müssen sich bleifreie Materialien, welche sich auf einem dreidimensionalen (3D) Netzwerk mit Sb, Sn oder Bi basieren, erst noch als nützliche Alternative beweisen.

Diese Doktorarbeit erkundet das Feld der niedrigdimensionalen, insbesondere die nulldimensional (0D), bleifreien Metallhalogeniden als lumineszente Materialien. Diese 0D Materialien bestehen aus abgetrennten Metallhalogenid-Oktaeder, was die optoelektronischen Eigenschaften drastisch verändert im Vergleich zu den vollkommen verknüpften 3D Strukturen. Vor dem Jahr 2017 war die Sammlung solcher 0D Metallhalogeniden äusserst klein.

Diese Arbeit begann mit der Studie der optischen Eigenschaften einer bereits bekannten, aber noch nicht untersuchten inkongruent schmelzender Phase – Cs_4SnBr_6. Dieses Material zeigt eine breite, aber effiziente Photolumineszenz bei Raumtemperatur (RT PL), welche durch die Rekombination von selbstfangende Exzitonen (STEs) hervorgerufen wird. Die STE-Emission in dieser Phase kann durch Veränderung der Komposition innerhalb der $Cs_{4-x}A_xSn(Br_{1-y}I_y)_6$ (A=Rb,K; x,y≤1) Familie eingestellt werden. Die Entdeckung dieser und anderer Phasen von der Gemeinschaft regte zur Untersuchung der optischen Eigenschaften von zahlreichen Sn-basierenden 0D und 1D Materialien wie $(C_4H_{14}N_2I)_4SnI_6$ und $[C(CH_2)_3]_2SnBr_4$ an. Dabei wurde ersichtlich, dass deren PL Lebensdauer extrem temperaturabhängig sind (~ 20 ns/K). Dies öffnete die Tür um 0D Metallhalogenide als fern-optisch thermometrisch und thermographische Luminophore zu verwenden. Zusätzlich zu dieser Temperaturempfindlichkeit ist die Emission intrinsisch und unglaublich robust. Kein Unterschied in der PL Lebensdauer kann im Vergleich von mehreren Synthesen, teilweiser Zersetzung oder Oxidation beobachtet werden. Diese zwei Faktoren zusammen erlauben eine thermometrische Präzision von ±13 mK.

Dies ist zwar sehr beeindruckend, jedoch bleibt die Tatsache bestehen, dass diese Zinn basierende Materialien unvermeidlich komplett oxidieren.

Daher stammte die Inspiration zur Entwicklung neuer niedrigdimensionaler Pnictogenhalogeniden. Diese nulldimensionalen Strukturen sind stabil gegenüber Oxidation und geeignet für fern-optische Thermometrie. Die $Rb_7Bi_{3-3x}Sb_{3x}Cl_{16}$ (x≤1) Familie, welche ebenfalls STE PL mit einer vergleichbaren thermischen Empfindlichkeit wie die Zinn basierten Materialien zeigen, waren das Resultat dieser Untersuchung. Des Weiteren beinhalten diese Strukturen

kantenverknüpfte Oktaeder Dimere, welche als Quelle der RT PL ermittelt wurden. Die lumineszenten Eigenschaften von Strukturen mit diesem Merkmal wurden bisher noch nicht untersucht.

Diese Arbeit führte auch zur Entdeckung von einem neuen Set aus Materialien der Komposition $Rb_{23}M^{III}_{7}Sb^{V}_{2}Cl_{54}$ (M^{III} = Bi, Sb), welche gemischte Oxidationszustände gleichzeitig beinhalten. Diese 0D Strukturen bestehen aus Oktaedern mit den nominellen Oxidationszuständen 3+ und 5+ und zeigen eine intensive Färbung auf Grund des Ladungstransfers zwischen den verschiedenen Zuständen. Obwohl sie selbst bei 12 K keine Lumineszenz zeigen, besitzen sie dennoch hohe Mobilitäts-Lebenszeiten Produkte unter Röntgenstrahlung, was auf einen Tunnelvorgang von einer Stelle zu einer anderen hindeutet. Dies macht diese Verbindungen zu möglichen Detektormaterialien für Röntgen- und weiterer Hochenergiestrahlung.

Zusammenfassend zeigt die hier präsentierte Arbeit zahlreiche, wesentliche Beiträge für die niedrigdimensionierten Metallhalogenid-Gemeinschaft, welche die Synthese und die Charakterisierung von mehreren neuen Materialen, sowie die Identifikation und erfolgreichen Demonstration von fern-optischer Thermometrie/Thermographie als neue Anwendung für diese Klasse an Materialien beinhaltet. Diese Doktorarbeit dient als effektives Fundament für weitere Forschung in diesem Feld, indem es eine breite Übersicht, sowie genauere Einblicke in die Untersuchung und Entwicklung von Materialien und möglichen Anwendungen gewährt.

Chapter 1. Metal-halides and their dimensional diversity

1.1. A brief history of luminescent materials

The tendency for some materials to "glow-in-the-dark" or phosphoresce, or for other materials to exhibit colors only under certain conditions (fluorescence) has been observed, although not understood, since at least the renaissance.[1] At this time, several doctors and scholars took note of various wood-bark samples, which were collected from the then "new world" of Mexico, that would result in a blue aqueous solution after soaking the wood. These same bark samples would later be studied by 17th century scientists in an effort to understand the origin of this color.[2-5]

Figure 1.1. An image of an alkaline aqueous solution containing *Eysenhardtia polystachia* under daylight illumination. Reprinted (adapted) with permission from *J. Chem. Educ.* 2011, 88, 6, 731-738. Copyright 2011 American Chemical Society.

Newton even describes such a solution in his treatise on optics.[6] In the end, he concluded that the blue color is a sort of reflection rather than the emission that we understand today.

By the 19th century, several additional luminescent solutions and materials were identified such as "Bolognian phosphor" or a doped barium sulfide;[5] fluorospar — now referred to as fluorite or CaF_2;[7-8] an alcoholic infusion of leaves (chlorophyll);[9] and quinine (a bitter antimalarial molecule that was made more palatable with the invention of tonic water).[5, 10-12]

It was not until 1852, however, that the term fluorescence, utilized eponymously after fluorite, was attributed to the ability of certain materials to "… cause the sensation of light" by Sir George Stokes.[13-14] The experiment that Stokes used to identify this property as something other than reflection was by splitting sunlight into its components with a prism and then passing a quinine solution through each component until he observed that the colorless area after violet (ultraviolet) resulted in the test tube to glow blue. Around the same time, a French scientist,

Edmond Becquerel, performed a similar experiment on calcium sulfide and discovered what he would later term phosphorescence.[5, 15-16] Later in 1888, the general term luminescence was introduced as an umbrella term for the emission of light from a material.[17] Since then this phenomenon has been observed in a wide variety of materials such as organic molecules and dyes, proteins, inorganic salts, transition metal and rare-earth doped materials, diamonds, and semiconductors. In fact, the luminescent fluorite that Stokes and others studied has since been identified as Eu^{2+}-doped CaF_2.[18]

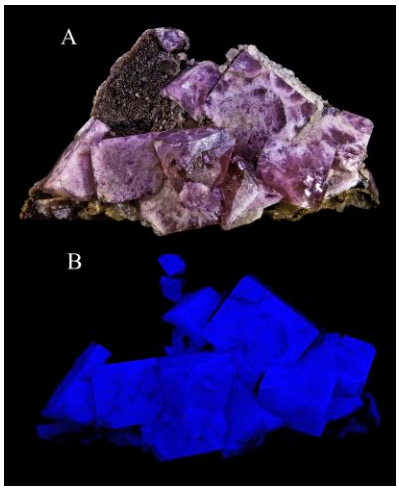

Figure 1.2. A sample of blue-luminescent fluorite from the U.K. Photo by Didier Descouens - Own work, CC BY-SA 4.0; https://commons.wikimedia.org/w/index.php?curid=7528654)

While these have all found use in some application, some of the most versatile and important materials are semiconductors, which have been used in a plethora of applications in the modern age: scintillation, computer displays, lasers, communication, high-speed internet — all thanks to the ability of these solid-state materials to emit light.[19] Some of the best-known examples of luminescent semiconductors today include $Ga_{1-x}Al_xN$, GaAs, InP, CdSe, CdTe, PbS, and HgTe; between these materials the entire range from ultraviolet (UV) to infrared (IR) light up to nearly 4 μm is covered.[20-21] The utility of these materials also stems from their ability to be compositionally tuned and made into thin-films and nanocrystals (NCs). For instance, blue light emitting diodes (LEDs) are made with thin films of GaN, and their emission can be redshifted through In-doping. The global adoption of this technology led to the 2014 Nobel prize in physics being awarded to Akasaki, Amano, and Nakamura for *"the invention of efficient blue light-emitting diodes which has enabled bright and energy-saving white light sources*."[22] Furthermore, materials such as InP, CdSe, CdTe, and PbS have also been demonstrated to be excellent emitters when prepared as quantum dots, and InP quantum dots have even been commercialized by Samsung in their QLED™ televisions as green and red phosphors.[23] As impressive as these materials are as visible phosphors, they all continue to face considerable synthetic and regulatory barriers.

There has been a growing need for materials discovery in the solid-state and materials

chemistry communities to discover brighter and more efficient light sources. One recent success story, which have also inspired our own efforts, are the lead-halide perovskites.

1.2. Lead-halide perovskites

Although the perovskite classification has been known since 1839 with the discovery of $CaTiO_3$, these cubic structures would not enter the limelight until 2012 with the use of $MAPbI_3$ ($MA = CH_3NH_3^+$) as an absorptive layer in a solar cell.[24-27]

The general formula for these metal-halide materials is ABX_3, in which A is a large, monovalent cation such as Cs^+, MA, or $CH(NH_2)_2^+$ (FA) that sits in the cuboctahedral voids of an anionic framework composed of corer-sharing BX_6 octahedra. B is a divalent main group metal such as Pb^{2+} or Sn^{2+}, and X is Cl^-, Br^-, or I^- (Figure 1.3).

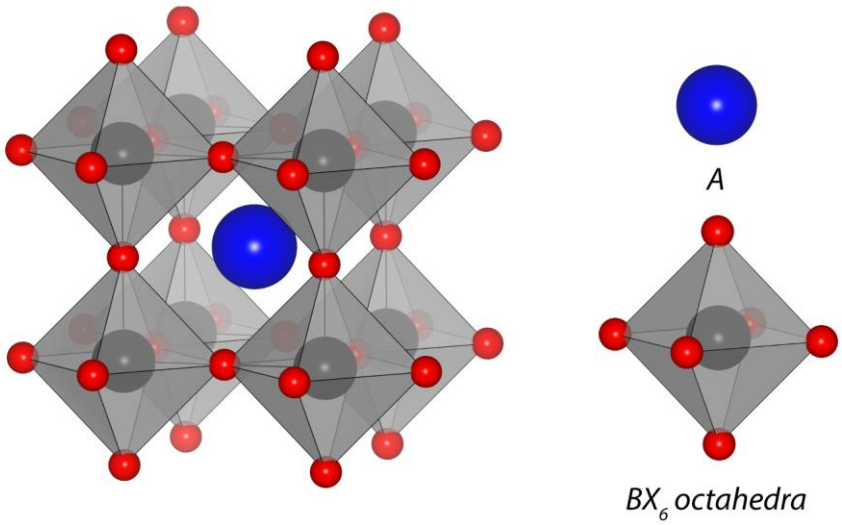

Figure 1.3. Ideal cubic ABX_3 perovskite. The large, central A-site cation is a blue sphere, which is typically Cs, MA, or FA in the case of halide perovskites; the surrounding anionic framework is shown as corner-sharing BX_6 octahedra (grey and red), which are typically composed of Pb or Sn as the B cation and Cl, Br, or I as the X halide. Structure generated using $CaTiO_3$ as a template (ICSD# 16925).

The stability of this cubic structure is dictated by a geometric restraint known as the Goldschmidt tolerance factor:[28]

$$t = \frac{(r_a + r_x)}{\sqrt{2}(r_b + r_x)} \quad (1)$$

in which r_a is the radius of the A-site cation, r_b is the radius of the B-site cation, and r_x is the radius of the halide. An ideal cubic structure is therefore stable when $0.8 \leq t \leq 1.0$. As this value decreases

below 0.8 the structure distorts to a lower symmetry and adopts a structure with edge shared polyhedra similar to those present in NH_4CdCl_3.[29] This is observed in $RbPbI_3$ and $CsPbI_3$ (although the Cs-analogue is able to also adopt distorted tetragonal structures as well). Values of $t \geq 1$ tend to result in structures containing face-shared octahedra with hexagonal symmetry (Figure 1.4).

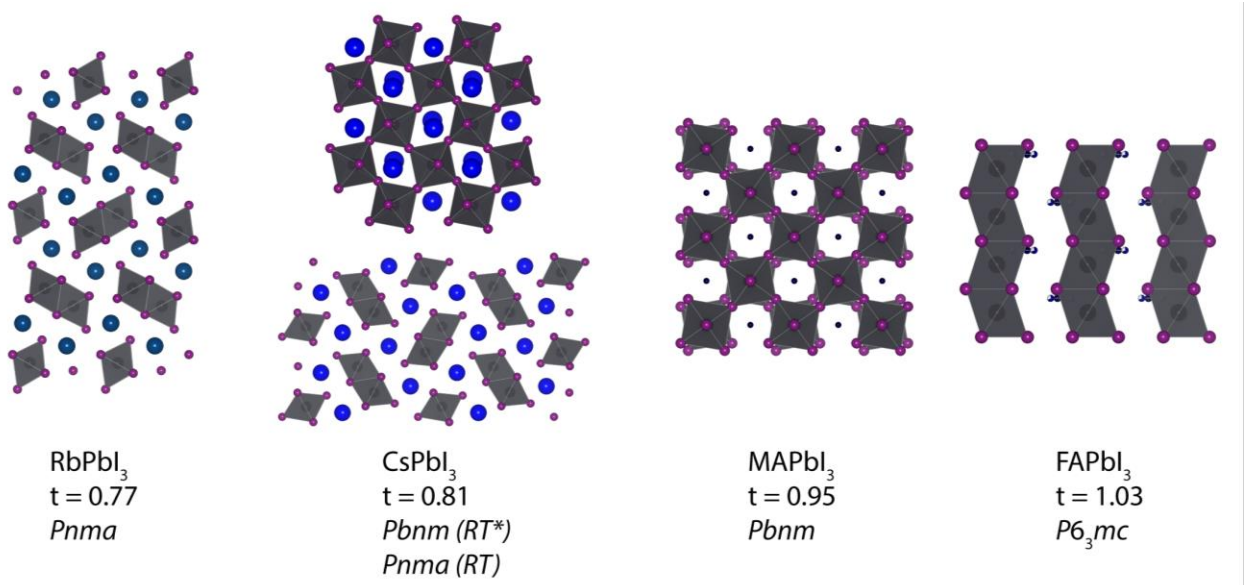

Figure 1.4. The influence of cation size on the perovskite structure. These structures were generated in Vesta using CCDC-1819569 (FA), ICSD-97851 (Cs, *Pbnm*), ICSD-161480 (Cs, *Pnma*), ICSD-194995 (MA), ICSD-6067 (Rb).[29-32]

While solar cell research has been revolutionized by the utilization of lead-iodide perovskites, lead-bromide and lead-iodide based perovskites have also launched a renaissance in numerous other optoelectronic fields such as LEDs, lasers, scintillation, full-color imaging, photodetection, and X-ray and hard-radiation detection.[33-40]

The miraculous improvements that these materials bring about to these other fields is attributable to three special characteristics of the metal-halide perovskite structure: softness/ease-of-production, tunability, and defect-tolerance. These materials have been often referred to as "soft" given their ionic nature and low melting points ($CsPbBr_3$ melts at 567 °C).[41] This has opened numerous possibilities for the growth of these materials as single crystals from solution,[42-45] the mechanochemical synthesis of NCs,[46] or as inclusions in other templates[47] or matrices.[48-49]

Among the most optoelectronically relevant semiconductors (*e.g.* CdSe, PbS, InP), the optical properties cannot be as easily or rapidly altered as in lead-halide perovskites.[50] This is related again to the soft lattice as well as a low defect density and high ionic mobility within these materials.[45, 51] As halide vacancies migrate through the structure, new anions from a surrounding growth solution are easily incorporated, leading to fast anion exchange.[50] Most importantly, the alteration of the halide composition directly affects the band gap and the photoluminescence (PL)

of these materials as the valence band (VB) comprises Pb 6*s* and X n*p* orbitals whereas the conduction band (CB) is composed of predominantly Pb 6*p* orbitals (Figure 1.5).[52-54]

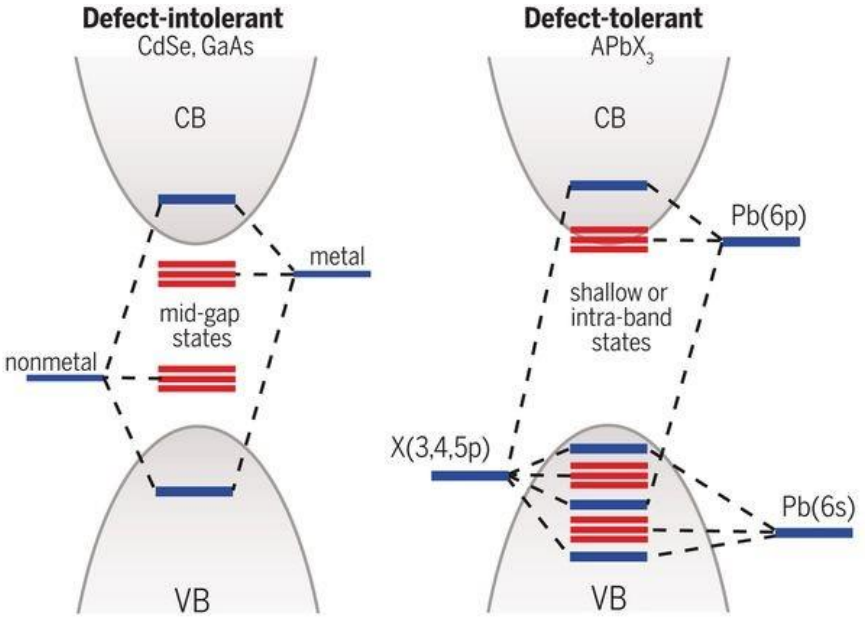

Figure 1.5. A comparison of the band-edge states in defect-tolerant lead-halide perovskites and traditional defect-intolerant materials such as CdSe or GaAs. From *Science*, 358 (6364), 745-750. Reprinted with permission from AAAS. Reprinted (adapted) with permission from *Chem. Mater.* 2017, 29, 11, 4667–4674. Copyright 2017 American Chemical Society.

This not only results in the facile bandgap variation that has been observed in such materials, but also in the apparent defect-tolerance that these materials possess.[47, 49, 53-57] Contrary to traditional semiconductors such as CdSe where the transition from VB to CB occurs between predominantly bonding and antibonding orbitals, the transition in perovskites occurs between predominantly antibonding states. Therefore, trap states generally find themselves within or near the bands. This is supported by calculations that suggest that the most energetically feasible defects will only form shallow traps and that potentially deep trap states have conversely very high formation energies.[57]

As promising as these materials are, they are hindered by the apparent toxicity of the lead. The amount of heavy metals such as Pb that can be incorporated into a device is now regulated by the European union.[58] While these quantities may be attainable in some applications, the discovery of suitable lead-free alternatives is preferable from the both the standpoint of public health and safety as well as regulatory restrictions.

1.3. Lead-free alternatives

The selection of potential replacements to lead are rather limited. This is especially true if

the number of beneficial properties for light emission exhibited by perovskites are to be maximized. Central to these is the ns^2 lone pair of the Pb^{2+} cation, which forms the valence band along with the halide n*p* orbital and has been implicated in its role in contributing to the effective defect-tolerance.[54, 57, 59] Therefore, the selection of main-group metals that retain this lone pair and lie close to Pb in the periodic table are In^+, Tl^+, Sn^{2+}, Ge^{2+}, Sb^{3+}, and Bi^{3+}. Of course, we will not consider Tl^+ containing materials any further as a result of its acute toxicity. The remaining five elements have all been investigated as replacements for Pb^{2+} in a three-dimensional (3D) structure.

1.3.1. AMX_3 alternatives

The only ns^2-containing elements that can satisfy the $APbX_3$ stoichiometry of the lead-halide perovskites, and themselves form true-perovskite phases, are the divalent Sn^{2+} and Ge^{2+}.[60-61] Although the Sn^{2+} analogue demonstrates some of the properties expected from the metal-halide perovskite phase such as narrow PL, both elements fail to be suitable replacements as they are intrinsically unstable in the 2+ oxidation state as a result of the weaker inert pair effect in lighter elements.[62] This tendency to oxidize rapidly degrades the optoelectronic performance of these materials as a result of the increased carrier concentration due to self-doping from the increasing M(IV) concentration.

1.3.2. Double perovskites — In^+, Sb^{3+}, and Bi^{3+}

In order to achieve a three-dimensional structure, while still sticking to the other parameters such as the presence of the ns^2 lone pair, the 2+ charge of the Pb can be effectively replaced by a monovalent and a trivalent cation, together:

$$AM^{II}X_3 \rightarrow A_2M^{IV}X_6 \rightarrow A_2M^{I}M^{III}X_6$$

These structures are known as “double-perovskites” due to the fact that they maintain a cubic structure with alternating M^I and M^{III} corner-sharing octahedra as well as the doubling of the original AMX_3 stoichiometry. These materials were initially investigated as potential replacements in solar cells with $Cs_2AgBiCl_6$ and $Cs_2AgBiBr_6$ (Figure 1.6).[63-64] However, these have materials tend to have indirect bandgaps and are non-emissive at RT. Further work has since been carried out experimenting with various combinations of M(I) and M(III) cations to better emulate the properties of the 3D perovskites with several direct band gap materials being discovered: $Cs_2AgInCl_6$, $Cs_2AgTlBr_6$, and $(MA)_2TlBiBr_6$.[65-68]

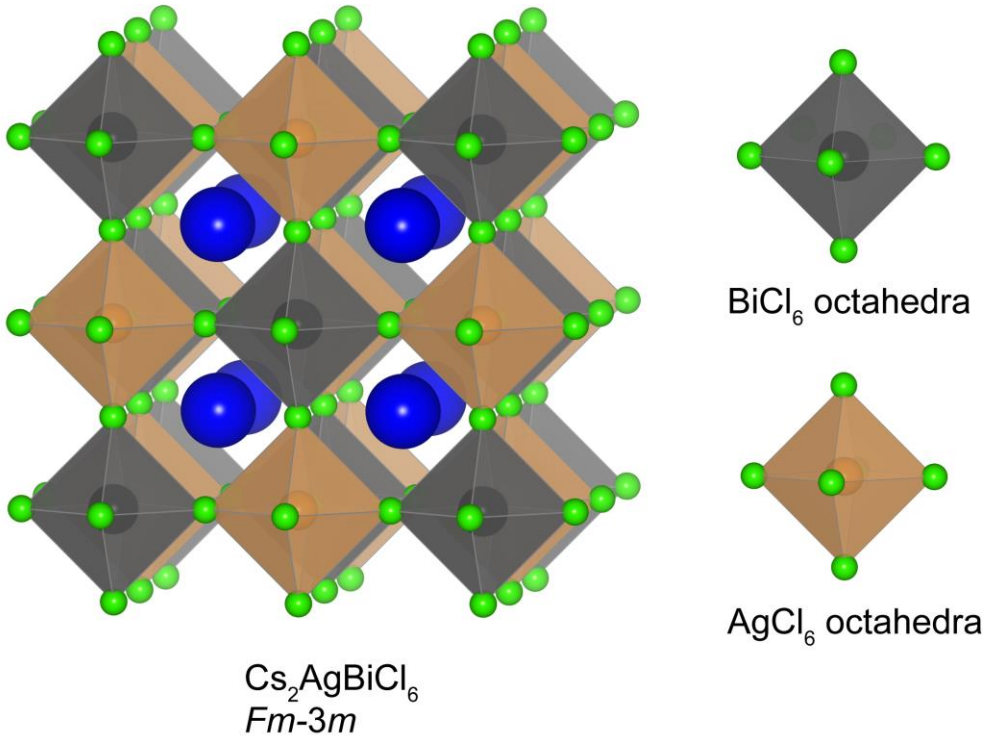

Figure 1.6. $A_2M^IM^{III}Cl_6$ Elpasolite (double perovskites) $Cs_2AgBiCl_6$

Additionally, since the report of weak, broadband orange PL from $Cs_2AgInCl_6$, various studies have expanded on the potential for double perovskites to be either themselves emissive or to be the host lattice for emissive dopants.[68] As far as pure and undoped bulk materials go, the only other double perovskite to have reported emission is $Cs_2AgBiBr_6$ with broad PL centered around 2 eV.[64, 69] While unimpressive, this opened the door to studies on the use of these materials as host-lattices for doping with luminescent transition metal cations (Mn, Cr)[70-72] and main group ns^2 ions (Sn, Bi, or Sb).[73-76] These most recent additions that utilize dopant quantities of Bi or Sb have been found to demonstrate room temperature PL quantum yields (RT PLQYs) of 86% for $Cs_2(Ag_{0.6}Na_{0.4})InCl_6$:Bi and 93% for $Cs_2KIn_{0.95}Cl_6$:$Sb_{0.05}$.[74, 76] While impressive, these materials are still broad emitters with wide bandgaps and require careful control over doping and substitution as a result of concentration quenching effects.

Aside from the above-mentioned combinations of Ag, Tl, Sb, In, and Bi, one recent report studied the combination of In^+ and In^{3+}.[77] Interestingly this combination does form a cubic double perovskite at elevated temperatures, but distorts into a "twisted" tetragonal structure upon cooling and is non-emissive at RT.

However promising the recent advances in the field of double perovskites, the search for true, viable, lead-free replacements for $APbX_3$ perovskites has thus far only cemented the importance of lead-halide perovskites for optoelectronic applications that require excellent charge transport or bright, narrow emission. Rather than focus on attempting to find such 3D alternatives,

we have chosen to focus on lower structural dimensionalities, which are comparatively less investigated.

1.4. Lowering dimensionality

1.4.1. General trends

In chemistry and physics, dimensionality can have two meanings. It can be related to the morphology of a material (*i.e.* quantum dots/wells, nanorods/wires, thin films), but it can also refer to the connectivity of the structure.[78-79] In this context, 3D structures contain connected polyhedra that result in an infinite framework that extends along all crystallographic directions. 2D structures are therefore achieved by effectively breaking some of these connections to create layers of polyhedra. These layers can be of varying thickness (n) up to the 3D case where n = ∞ (Figure 1.7).

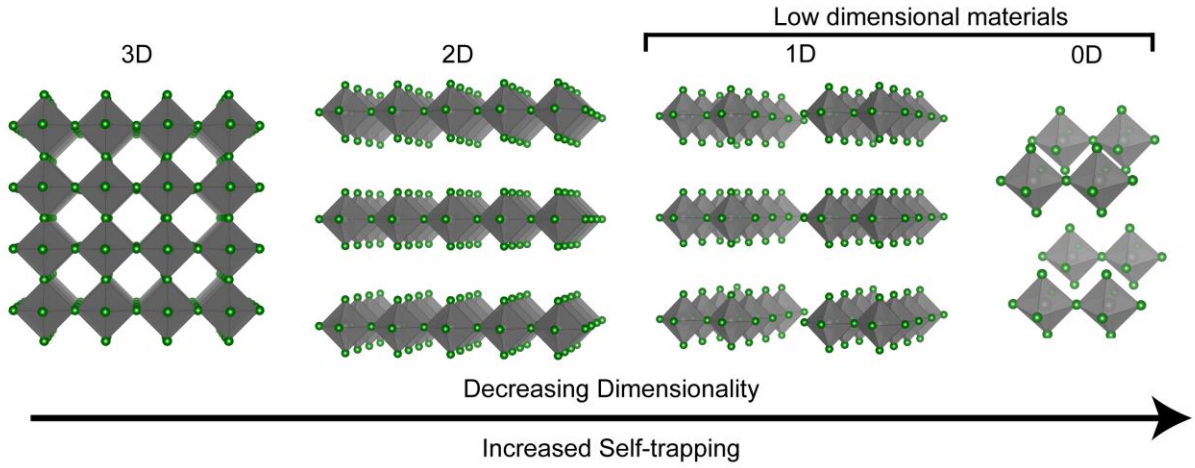

Figure 1.7. Structural dimensionality. As polyhedra such as the octahedra shown become increasingly disconnected, the dimensionality of the structure decreases.

Further disconnection results in the formation of so-called low-dimensional structures in which the polyhedra are formed into one-dimensional (1D) chains or 0D isolated units. Although 2D, 1D, and 0D crystal structures can all be considered as low-dimensional, 2D structures tend to share more in common with 3D structures than 1D and 0D structures. We will therefore consider 1D and 0D as truly low-dimensional. Furthermore, the decreased dimensionality brings about new properties and opens the door to niche applications where 2D and 3D materials are less suitable.

One well known way in which dimensionality will affect the optical properties of semiconductors in in the appearance of their absorption spectra (Figure 1.8).[79] The increasing

confinement with decreased dimensionality gradually reduces the optical transitions and increases their energy.

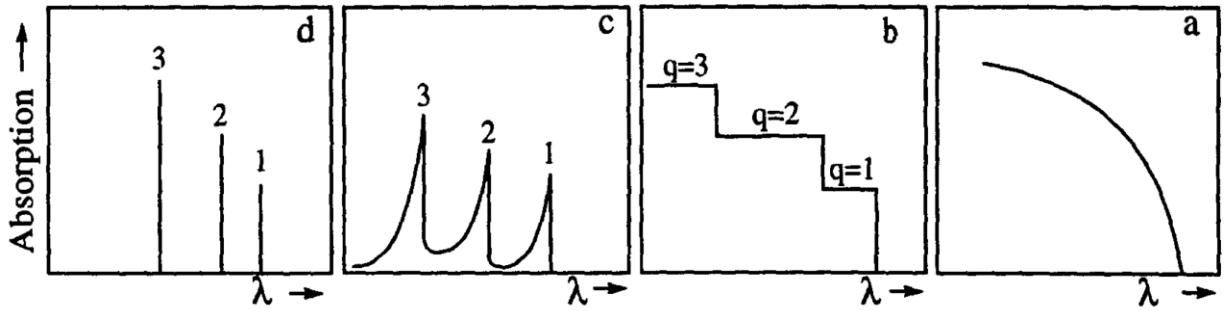

Figure 1.8. The effect of dimensionality on semiconductor absorption spectra for a) 3D, b) 2D, c) 1D, and d) 0D crystal lattices. Reproduced from Three- and low-dimensional inorganic semiconductors, 25(3), Papavassilou, G.C.; Prog. Sol. State Chem., 125-270, © 1997, with permission from Elsevier.

Of course, the schematic representations of the various dimensionalities in Figure 1.7 are simplified (any cations acting as spacers have been omitted) and idealized. There are numerous transitional cases that span the 3D-to-0D range.[79] For example, 2D structures may be very thick and planar (as mentioned above) or they may be thin with a high degree of corrugation, or zig-zagging, resulting in significantly decreased conductivity and blue shifted absorption spectra akin to that observed in 1D chain-like structure.[80-82]

1.4.2. Self-trapped excitons

1.4.2.1. Excitons

Excitons are neutral quasiparticles that exist as an electron-hole pair. These appear after photoexcitation in a semiconductor, and these are made energetically more stable than free carriers by the coulombic attraction between oppositely charged particles. The degree to which these oppositely charged particles are attracted to one-another is termed the exciton binding energy, E_b. The magnitude of this exciton stabilization is a key parameter in understanding why some semiconductors are emissive at RT and why others may not be.

The key for excitonic PL is the recombination of the electron and hole to generate light. The probability of this occurrence increases when the two charge-carriers stay bound to one another as an exciton, and this occurs when $E_b > k_BT$.[83] For example, traditional III-V and II-VI semiconductors such as InP and CdSe only exhibit sharp, narrow excitonic PL at cryogenic temperatures,[84] and they have very small E_b values of <20 meV.[85-88] This tendency for excitons to dissociate increases the probability that charge carriers become localized around defects, which may form deep, mid-gap trap states. This defect trapping is often associated with decreased QY

and may result in broadened PL, if any at all. This mechanism is particularly important in many luminescent 3D semiconductors such as CdSe or InP but is less important in halide perovskites (defect tolerance) and low-dimensional systems (high E_B; increased exciton localization).

1.4.2.2. Wannier-Mott and Frenkel excitons

Two primary classes of excitons exist, and their classification is dependent on the degree of exciton-lattice coupling or, in other words, the extent to which the exciton can delocalize.[89] In the Section 1.4.1, the excitons found in traditional semiconductors (IV, II-VI, and III-V) were mentioned, and these are typically referred to as Wannier-Mott excitons. Such excitons are delocalized over many unit cells, and they tend to have lower binding energies.[89] These are the predominant class of exciton in 3D crystal lattices. The optical processes in semiconductors with these excitons can be considered as a transition from the valence band to the conduction band across the band gap (absorption/excitation) followed by emission from the top of the conduction band back to the valence band (emission) with a small Stokes shift and a emission lifetime that is inversely proportional to the band gap for a given lattice (Figure 1.9).[90]

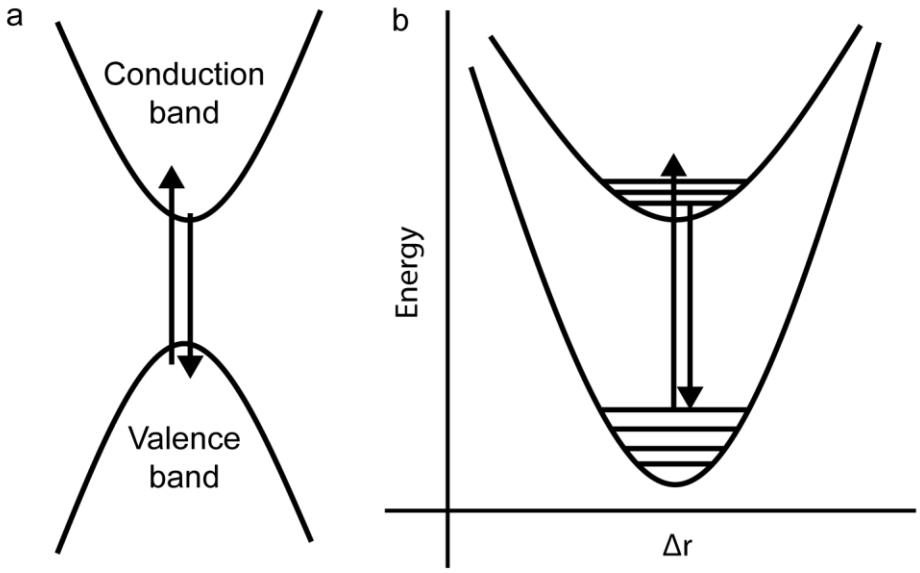

Figure 1.9. Wannier-Mott excitons. a) absorption and emission between the conduction and valence bands. b) A 1D configurational coordinate diagram depicting the same process.

This same process that occurs from one dispersive band to another can also be considered in a 1D configurational coordinate diagram (CC; Figure 1.9b). Here the wells no longer represent the infinite states of the electronic bands of the semiconductor but rather the local bonding environment of the highest occupied molecular orbital (HOMO; bottom) and lowest unoccupied

molecular orbital (LUMO; top) in the lattice. The x-axis represents the change in atomic position that occurs during after an electronic transition as a result of different orbital occupancies. The horizontal lines represent vibrational energy levels. Therefore, unlike in Figure 1.9a where the solid arrows refer primarily to changes in electronic state, the arrows in Figure 1.9b indicate vibronic transitions. In the case of Wannier-Mott excitons and the emission that is typically observed from $APbX_3$ perovskites, the top and bottom wells would be only very slightly displaced from one another illustrating the very small change in bonding that occurs and the concomitantly small Stokes shift between absorption and emission; furthermore, the emission is expected to be very narrow.[90]

In materials such as organic molecular crystals or ionic crystals, the exciton can be so strongly confined that it may only exist in the space of a single unit cell or an even smaller volume such as an atom or a molecule. Such localized excitons are known as Frenkel excitons.[91-92]. The effect of this localization is that the electron and hole become strongly bound resulting a high exciton binding energy, and the exciton and the lattice strongly interact.

1.4.2.3. The Importance of phonons and polarons

Although the image of the exciton as a delocalized quasiparticle in a static lattice may be suitable at times, it is too simplistic when attempting to rationalize the origin of various optical features in semiconductors. In reality, the crystal lattice is like a living, breathing entity which is always dynamic with its constituent atoms vibrating about an equilibrium position.[90] However, just like molecules, the lattice of crystal is also subject to collective motions or vibrations known as phonons. These not only transmit thermal energy through the lattice, but they are also able to interact with excitons. Importantly, phonons can impart momentum and assist in forbidden or indirect optical processes.

When these phonons couple to charge carriers or excitons, they form a quasiparticle known as a polaron. Polarons are, in other words, excitons dressed in phonons that deform the surrounding lattice. These screen carriers from one another and, in doing so, increase their effective mass. This increased effective mass decreases their mobility and can even immobilize the exciton.[89, 93] The extent to which a polaron is spread out over the structure, or the extent to which a polaron deforms the lattice, determines whether it is considered a large (Frohlich) or small polaron.

1.4.2.4. Self-trapped excitons

When a lattice supports the formation of localized Frenkel excitons, the resulting exciton-phonon coupling or polaron can severely deform the lattice and immobilize the exciton in the newly generated potential well. This is conceptually different from an exciton becoming trapped in the potential well of a permanent defect (Figure 1.10a), wherein the potential well of the deformation is always present and can be investigated using steady-state methods. In the case of a

self-trapped exciton, the ground-state lattice is the same as that of the perfect, ideal crystal lattice, and the deformation occurs only upon excitation and exciton creation (Figure 1.10b).

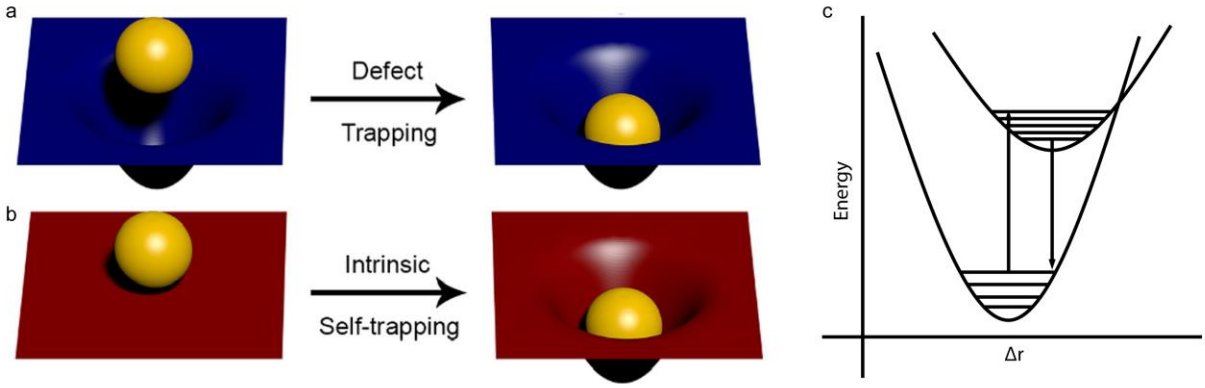

Figure 1.10. Self-trapped excitons. a) The trapping of an exciton by a permanent defect; b) an exciton deforming the surrounding lattice to form a self-trapped exciton; c) a CC diagram depicting the absorption and emission from a self-trapped exciton. Reprinted (adapted) with permission from *Acc. Chem. Res.* 2018, 51, 3, 619–627. Copyright 2018 American Chemical Society.

In 3D semiconductors such as IV, II-VI, or III-V materials, no self-trapped state exists. Broad emission is therefore from defects or of an extrinsic origin *i.e.* dopants or impurities. In some 3D lattices such as thallous halides or silver halides, these two states can coexist depending on composition and temperature.[89] In other 3D systems, such as alkali halides and doped alkali halides where self-trapped phenomena were first studied and related to the formation of color (F) centers and halide (H) center, the self-trapped exciton is the primary mechanism for PL.[89 94-95]

The tendency for a self-trapped exciton to form in a material depends on two factors: lattice rigidity/deformability and dimensionality.[89, 96] These together determine if there is a potential barrier to trapping, how large it might be, and the energy that the lattice may expend when relaxing to the new excited state minimum (top well in Figure 1.10c). The dimensionality of the structure is therefore a critical aspect that can be controlled to influence the electronic properties, the bandgap as well as band-dispersion, the type of exciton that may form, and the luminescence (intrinsically narrow or broad) from the structure.

1.4.3. Two-dimensional metal-halides

2D systems span the entire range of properties based on their thickness and connectivity.[97-98] Systems with thick layers tend to be more planar and behave like their 3D counterparts; as a result, they are more likely to exhibit lower resistivities and possibly the presence of narrow, excitonic emission. This has been demonstrated in several lead-based materials and the $Cs_2AgBiBr_6$ double perovskite, most notably in long-chain alkylamines and alkyldiamines.[99,100]

As mentioned before, systems with very thin layers (*e.g.* n = 1 or 2) will have larger band gaps (as a result of increased quantum confinement); this was demonstrated by the same group of

authors who also explain the broad emission at low temperatures.[96-97, 101] The decreased temperature favors the STE state as there is no longer enough thermal energy to cross the potential barrier that separates FE and STE states.

The connectivity or the construction of these thin layers begins to play a significant role in the height of the thermal barrier and the observed luminescence. 2D systems begin to favor the formation of STEs at higher temperatures through thin-layers and corrugation.[97] Corrugation is a structural feature in which the layers are no longer flat planes like those found in the (001) perovskites. Instead, the layers exhibit regular kinks or turns that effectively decrease band dispersion even further and this effectively impedes the transport of charges through the layer and restricts exciton delocalization. These are effectively quasi-2D systems that begin to exhibit STEs at RT and have been demonstrated to emit white light with a PLQY of up to 9%[102] or in one case even 17%.[103]

Although the majority of earlier works on luminescent 2D metal-halides has been conducted on lead-halides,[102, 104-111] an increasing body of work has also emerged regarding tin-halides.[80-81, 112] Interestingly, these lead-free materials can in some cases have more efficient STE emission as evidenced by their PLQY reaching values over 80%.[113-114]

The field of quasi-2D and lower dimensional materials is not restricted, as previously mentioned, to materials or elements that can form and stabilize slices or portions of a cubic perovskite framework. These relaxed parameters allow for the exploration of other combinations, and a strict adherence to a divalent or an average divalent B-cation is no longer required although the utilization of ns^2 cations is still preferred. Therefore, by utilizing only an M(III) cation (*i.e.* Sb^{3+} or Bi^{3+}) on the B-site, a series of related 2D "3-2-9" structures can be obtained.

Although a structural departure from the perovskite family, these can still be considered in the broader framework of vacancy ordered perovskites in which a 1-1-3 stoichiometry can still be attained. This stems from the fact that the vacancies correspond to one-third of the trivalent metal sites thereby resulting in an overall 3-3-9 ratio of A, B, and X sites.[115-116] A greater amount of the corresponding alkali cation must be introduced to charge balance the trivalent cation, and the material adopts a (111) oriented 2D structure (Figure 1.11).[117-118]

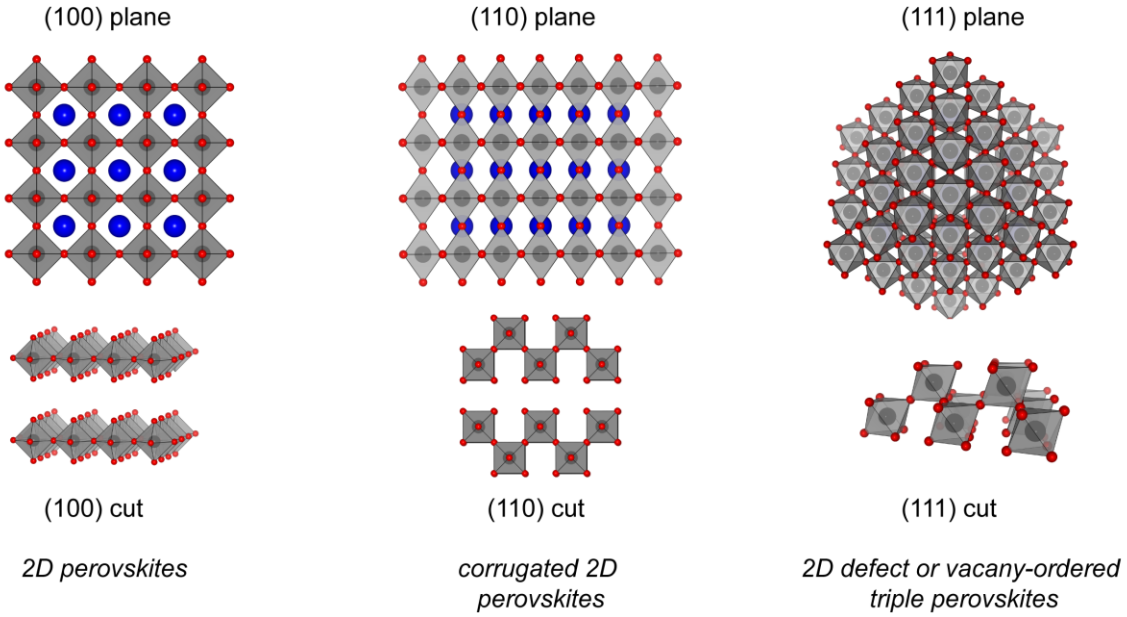

Figure 1.11. The generation of 2D perovskites by removing (100), (110), or (111) planes to generate the corresponding structure. These structures were generated by cutting the respective plane from an ideal structure (based on $CaTiO_3$).

These (111) type structures are found for the majority of $A_3B_2X_9$ (A = Rb, Cs; B = Sb, Bi; X = Br, I) structures (N.B. $Cs_3B_2I_9$ forms a 0D structure). The quasi-2D nature of these materials has been demonstrated in $Rb_3Sb_2I_9$ by its weak, strongly Stokes shifted, broadband RT PL which increases in intensity with cooling and a total lack of narrow excitonic emission.[118] Similar observations have been made for the isostructural $Cs_3B_2Cl_9$ (B = Sb, Bi).[119]

1.4.4. One-dimensional materials

Further dimensional reduction from the varying types of 2D sheets results in the formation of 1D chains. Here again, the connectivity and chain thickness play a role in dictating the optical properties; however, the number of known structures is lower, and their corresponding optical properties have been investigated to a much lesser degree.[120-121] Again, as in the case of 2D metal-halides, 1D Pb-X materials have been studied far more intensively in the past 20 years than their lead-free counterparts.[121] As of 2020, at least 21 unique 1D Pb-halides have been discovered and investigated; the structural motifs most commonly include corner-, edge-, and face-shared octahedra.[121-136] Although not all have been extensively characterized in terms of their optical properties, several structures have been demonstrated to exhibit broad-STE emission with relatively high QYs at RT.[125] This is possible due to the lack of a thermal barrier separating

delocalized Wannier-Mott excitons and localized Frenkel excitons in these systems; as a result, all excitons become trapped and distort the lattice.[89]

Given these promising results, the investigation into lead-free 1D systems has slowly increased although at the time of writing this dissertation only four luminescent 1D systems have been described in the literature: $C_4N_2H_{14}SnBr_4$ (Figure 1.12a),[137] $[C(NH_2)_3]_2SnBr_4$ (Figure 1.12b),[138] $(CH_3)_3SSnI_3$,[139] and $(C_6H_{14}N_2)_2[Sb_2Cl_{10}]\cdot H_2O$.[140]

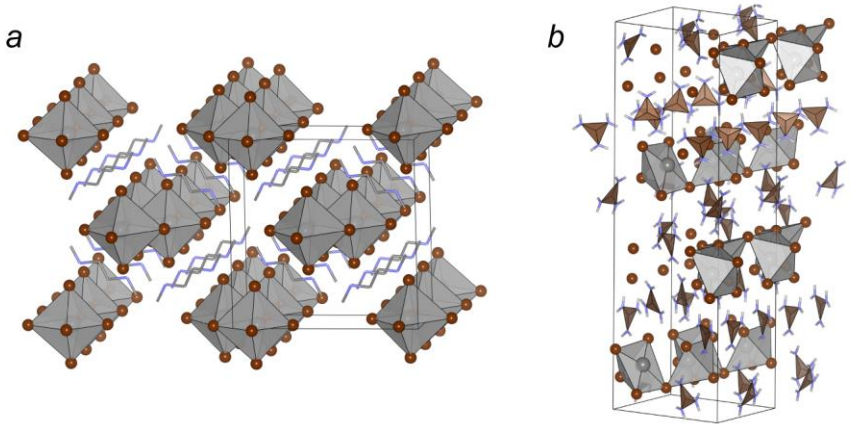

Figure 1.12. Luminescent 1D tin-halides: a) $C_4N_2H_{14}SnBr_4$[137, 141] and b) $[C(NH_2)_3]_2SnBr_4$[138]. Tin-bromide polyhedra are grey with the red-brown spheres representing bromine atoms. The blue and grey lines in **a** represent the ethylenediammonium cation whereas the brown triangle in **b** represents the guanidinium cation. In both cases hydrogen atoms have been omitted for clarity.

The former (Figure 1.12a) is composed of chains of edge shared $SnBr_6$ octahedra and is non-emissive at standard temperature and pressure. This material does begin to exhibit broad STE emission once the pressure is increased to 2.06 GPa.[125, 141] The underlying mechanism, as explained by the authors, involves a phase transition in which the individual octahedra distort with off-centering of the Sn atom.[141] This off centering and octahedral distortion alters the Br-Sn-Br angle further from 180°. This may potentially reduce the orbital overlap between adjacent octahedra and decrease dispersion throughout the chain, effectively dimensionally reducing the 1D chain and enhancing the PLQY. The latter example has intrinsically poor dispersion, which was supported by DFT calculations; this 1D structure may therefore be closer to a pseudo-1D structure. This is furthermore supported by the fact that it exhibits broad yellow emission with a PLQY of 2% at RT, which increases to 75% at 77 K.[138]

In both cases, these materials have shown the ability to exhibit efficient, broad STE emission when cooled or pressed. This is unlikely to be coincidence, and it is rather symptomatic of a general trend among lead-free metal-halides: dimensional reduction, however it may occur, increases PL.

1.4.5. Zero-dimensional materials

1.4.5.1. Overview

The 0D case represents the limit to this structural disconnection or dimensional reduction. At this point all the metal-halide building blocks are spatially separated or isolated from one another, and these polyhedra are generally restricted to trimers, dimers, and single isolated polyhedra.

Historically, these phases have received little-to-no widespread attention in the broader scientific community even though the various phases in the ternary metal-halide compositional space have been studied since at least the late 19th century.[142-143] Later reports in the mid-20th century observed that the Cs_4PbX_6 materials, which could form alongside the 3D ABX_3 perovskites, exhibited vastly different optical characteristics from their 3D counterparts.[144-147] The optoelectronic properties of such 0D phases were not actively investigated further until the latter half of the 20th century with studies on the absorption and conductivity of Sn^{2+} materials (Cs_4SnBr_6),[148-149] as well as the first studies on the luminescence of 0D Te^{4+} materials (Cs_2TeX_6).[150] These initial articles focusing on Sn^{2+} described the both the wide-bandgap and high resistivity that can be expected from these disconnected, 0D structures. The work on Te^{4+}, on the other hand, provided the first look at such materials as phosphors, which exhibit broadband, strongly Stokes-shifted PL at cryogenic temperatures. These initial observations of PL inspired several groups to look deeper at the structures and optical properties of 0D materials with Te(IV), Sb(III), and Bi(III) given their common ns^2 electronic configuration. These studies sought to link the ground state crystallographic structure, and the extent to which metal-halide octahedra are disordered, to the PL width and Stokes shift.[151-153] Interestingly, they found that these systems are intrinsically broad emitters with varying Stokes shifts and features in the PL spectra based on the strength of exciton-phonon coupling and the degree to which the excited state could distort. Briefly, more strongly coupled systems would be expected to have more Stokes shifted emission with weaker intensity and less features.[154] In general, these studies laid the framework upon which we continue to build and discuss such 0D materials.

Aside from these initial advances, very little has been done prior to 2017 in luminescent materials discovery with only two antimony-chloride based 0D materials effectively characterized.[155-156] In fact, the relatively small library of investigated and characterized materials speaks to the young state of this field.[157] With the perovskite-era, these 0D curiosities have since undergone renewed interest as their light emission has become an attractive lure. Looking at their structures, several motifs can be identified in most $5s^2$ and $6s^2$ metal-halides (Figure 1.13).

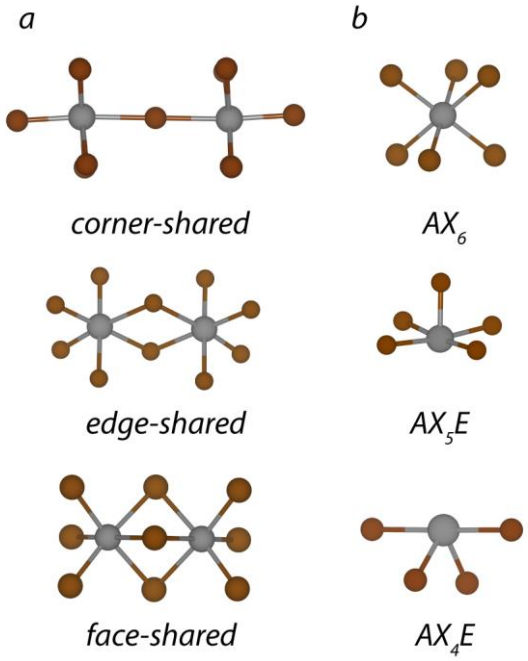

Figure 1.13. Structural motifs found in 0D metal-halides: a) polynuclear units, b) mononuclear polyhedra.

The preferred motif for a specific material may affect its tendency to be emissive at RT and is dependent on several factors: metal center, organic vs. inorganic "A" cations, stoichiometry, and lone pair stereoactivity. The metal-center and more specifically its group (*i.e.* tetrel, pnictogen, chalcogen) has a significant effect on the coordination geometries that it can adopt, mostly as a result of the charge required to maintain the ns^2 electronic configuration. These trends are evident in the $5s^2$ metals *viz.* Te(IV), Sb(III), Sn(II). The high charge of Te(IV) requires a greater number of ligands to create a stable ternary metal-halide. As a result, the known catalogue of 0D Te(IV) materials is, for the most part, restricted to octahedra (AX_6). Sb(III), on the other hand, is able to also adopt geometries containing fewer ligands such as square pyramids (AX_5E). Finally, Sn(II), having the lowest charge, adopts these geometries as well as disphenoids or "see-saws" (AX_4E). The adoption of these various geometries in different structures appears to be strongly influenced by the size and structure-directing ability of the "A" cation. Although no general rules or strategies currently exist for the design of structures, it can be observed that coordinatively unsaturated metals are only available *via* one of two approaches: the selection of large, bulky organic cations or the use of halide anions with very different sizes (*e.g.* Cl^- and I^-).[157-158] Furthermore, the extent to which these various polyhedra are distorted is associated with a phenomenon known as the lone-pair effect.

This is related to the stereoactivity or the physical presence of the lone pair in a structure. In coordinatively unsaturated systems such as disphenoids or square pyramids, the lone pair is expressed. In octahedral cases, the expression of this lone pair appears to be correlated with the

underlying symmetry and density of the structure. In high symmetry, fully inorganic systems such as Cs_4SnBr_6 (or even the 3D $CsSnBr_3$) the octahedra may appear undistorted, masking the lone pair.[159] This may be attributed to crystal lattice effects related to site symmetry or the reported interaction of the ns^2 pair in this structure with the d-orbitals of the Br^-.[160] At the opposite end of this spectrum lie the $[SnX_6]^{4-}$ octahedra of $(C_4N_2H_{14})_4SnX_6$, which appear very distorted with bond lengths ranging from 3.17 Å to 3.27 Å.[161]

As these various factors determine the structural motif adopted by the metal-center, they also determine the appearance or absence of PL at RT and its PLQY. While no general trends exist that can be used to predict the resulting properties of a structure, empirical observations can be drawn from examples in the literature to predict which materials and elements may be the most likely to result in efficient RT emitters. Interestingly, most, if not all, of these motifs have luminescent examples as of 2020. The factors that appear to most often quench PL in these systems are the use of $6s^2$ cations such as Pb^{2+} or Bi^{2+} and heavier halides such as Br^- or I^-, depending on the system. An excellent set of examples for this comes, in part, from our discoveries in Chapter 2 and Chapter 3 of this dissertation. From these chapters, several A_4SnX_6 materials can be compared along with their fully inorganic $6s^2$ counterpart — Cs_4PbBr_6 (Figure 1.14).

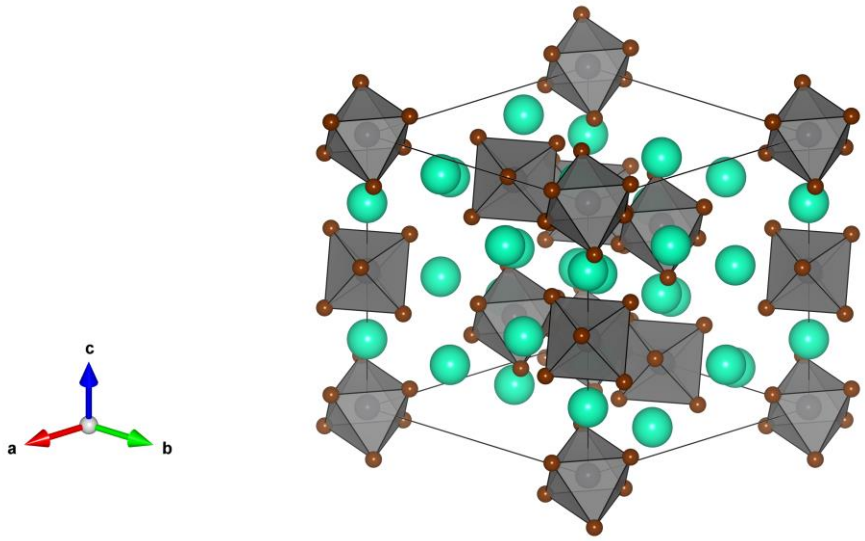

Figure 1.14. The unit cell of Cs_4PbBr_6.

This material, known since the early 20th century,[143, 147] has an aristotypical 0D structure with disconnected $[PbBr_6]^{4-}$ octahedra separated by Cs^+ cations. The 0D nature of this structure is reflected in its optical and electronic properties, with initial reports describing the material as white (wide bandgap) and very resistive with cryogenic PL in the UV.[149, 162-167] This is clearly at odds with recent articles that have erroneously identified this phase as having narrow, green emission, which could be expected from free-exciton recombination but seems highly unlikely for the self-trapped excitonic recombination that should take place in a 0D material.[168] More recent reports

have found that this narrow emission originates from nanocrystalline impurities of $CsPbBr_3$, whereas the Cs_4PbBr_6 phase is non-emissive at RT and may possess UV-blue emission at cryogenic temperatures.[49, 169-171] This is in stark contrast to the isostructural Cs_4SnBr_6, which exhibits broadband RT PL centered at 540 nm with a QY of 15±5% (presented in Chapter 2).

This remarkable difference in optical activity, as well as recent articles on Sb(III) and Bi(III) based metal-halides, demonstrates that $5s^2$ metal ions tend to be red-shifted and more emissive than their heavier $6s^2$ counterparts, given the same cation and coordination.[118, 172] This is the first of two empirical generalizations on 0D metal-halides which we can currently make.

The second so far only applies to octahedrally coordinated metal centers, as it stems from the comparison of Cs_4SnBr_6 to $(C_4N_2H_{14})_4SnBr_6$. Between these it can be seen that the fully inorganic structures tend to feature symmetric octahedra with reduced lone pair stereoactivity, whereas the hybrid organic-inorganic counterparts have increased distortion and increased lone pair expression. This observation is paired with the fact that hybrid organic-inorganic materials are routinely more emissive (15% compared to >80%, respectively).

While the optical performance of hybrid materials is many cases superior to those of their fully inorganic counterparts, the search for new, fully inorganic 0D metal-halides is a necessary step towards understanding these materials and finding ways to utilize them. One instance in which fully inorganic materials may provide a distinct advantage, is in the synthesis of NCs. Several articles on Cs_4PbX_6 NCs and other fully inorganic 0D systems have already been published,[169, 173-177] and only one year after our report on the RT PL of Cs_4SnBr_6 (Chapter 2), two publications reported the successful preparation of these NCs.[178-179] To date no hybrid organic-inorganic 0D materials have been successfully prepared.

Another unexplored area within the realm of 0D metal-halides, which we sought to investigate was the optical properties and potential uses of polynuclear 0D metal-halide clusters. At the time of starting this work, the most prominent example of such a system came from the $Cs_3M_2I_9$ ($M = Sb^{3+}$, Bi^{3+}; Figure 1.15).[118, 180-181]

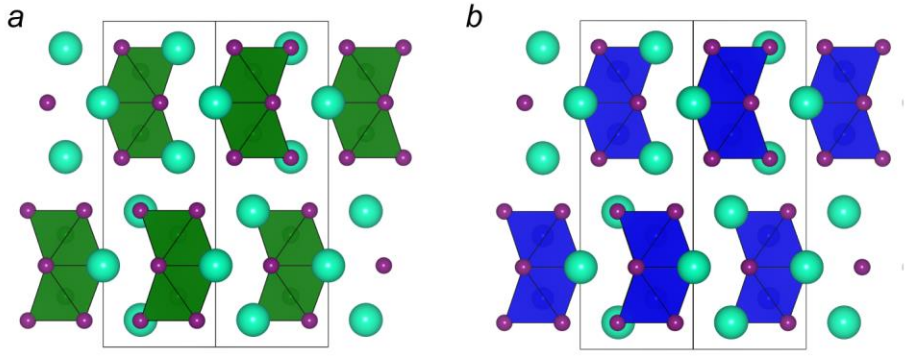

Figure 1.15. The crystal structures of a) $Cs_3Sb_2I_9$ and b) $Cs_3Bi_2I_9$.

These materials have been demonstrated to exhibit very weak RT PL, which has been difficult to

observe in fully inorganic systems containing heavy halides such as Br^- or I^-. Furthermore, in the past two years, examples of luminescent hybrid organic-inorganic materials with bi-nuclear or tri-nuclear lead-halide clusters have emerged and drawn increasing attention.[182-186] Our own contribution to this growing body of work can be found in Chapter 4.

1.4.5.2. Applications for 0D metal-halides

The properties of 0D metal-halides that have been described so far include broadband emission, long PL lifetimes, temperature dependent PLQY, and generally sub-400 nm excitation bands. These properties are ill suited for most, popular optoelectronic applications such as solar cells, and light emitting diodes for both consumer electronics (displays) and solid-state lighting (SSL). Even more recent and niche applications such as solar concentrators that benefit from their large Stokes shift also appear to be a poor match (Table 1.1).

Table 1.1. Properties and applications for 0D metal-halides.

Application	*Broad PL*	*Large Stokes Shift*	*Long RT PL lifetime*	*Temp. dep. PLQY*	*λ_{exc} <400 nm*
Displays	–	+	–	–	–
Photovoltaics	–	~	+	–	–
SSL	+	+	~	–	–

Displays are clearly a poor choice for these materials. Their broad emission, long lifetime, thermal quenching, and UV emission are incongruent with the requirements for the next generation of displays. It should come as no surprise that these materials have therefore not been considered in the literature for this use. More surprising is the potential use of 0D metal halides as solar cell materials.[116] For example, Cs_2SnI_6 has a vacancy-ordered double perovskite structure; a cubic 0D structure with alternating octahedra and voids common to ternary tetravalent metal-halides; and has been used in solar cells.[187] With the 0D Cs_2SnI_6 as a hole-blocking layer in a dye-sensitized solar cell, a power conversion efficiency (PCE) of between 4% and 8% could be achieved.[188-190] The use of this material will likely be restricted to hole blocking or electron blocking layers, as the low carrier mobilities (given the 0D crystal structure) would make it an inefficient absorbing layer. This has in fact been shown with Cs_2TiBr_6, Cs_2PdBr_6, and the $A_3M_2I_9$ materials which all possess 0D crystal structures (cubic vacancy ordered double perovskites for Ti^{4+} and Pd^{4+}; face sharing dimers for $A_3M_2I_9$). Solar cells constructed utilizing Cs_2TiBr_6 as an absorptive layer exhibit PCE <4%,[187] and those utilizing $A_3M_2I_9$ (A=Rb, Cs, MA; M=Sb,Bi) exhibit PCE < 1.5%.[116, 191-195] The

poor performance of these materials is most likely due to their low electronic dimensionality which results in increased effective carrier masses. For this reason, Cs_2PdBr_6 is not expected to achieve high PCE values and has not been utilized in a solar cell.[196]

Many articles in the 0D metal-halide field rather focus on their use as potential SSL phosphors.[156, 161, 197-199] The ultimate goal for SSL is to achieve bright, low-cost, white light that effectively matches the solar spectrum. Daylight is composed of a continuous spectrum of wavelengths that peak in the visible range around 500-600 nm. As a result, the colors that we see are effectively rendered by subtractive color mixing. Pigments in the world around us absorb swathes of the visible spectrum and appear as a mixture of the reflected or unabsorbed light. Any gaps or deviations from the solar spectrum in this incident light spectrum alters the color we can perceive. For this reason, not all light sources are created equally. For example, lasers which are effectively line sources (emitting monochromatic light) could be made to additively emit white light through the combination of a red, green, and blue laser. This would qualify as a white-light LED, but it would have an abysmal color rendering index (CRI).

The CRI is one of the figure-of-merit (FOM) for SSL.[200] It effectively communicates how well a given light source can reproduce the colors of an object. The tricolor Laser approach mentioned above, would only generate roughly 8 colors by various combinations of reflected red, green, and/or blue light. In spaces where colors are critical, such as museums, galleries, stores, *etc.*, a much higher CRI is required.

Another often cited FOM for SSL is color temperature.[200] For a given white color, the hue is related to the equivalent temperature of a blackbody emitter. Therefore, white light sources with a blueish appearance have high temperatures whereas more red tones have lower temperatures.

To achieve high CRIs with pleasant color temperatures broadband emitters are required. Several approaches to achieve this have been described in the literature: tricolor LEDs, UV LEDs with RGB phosphors, and partial conversion. The tricolor LED approach is effectively the same as the RGB laser approach except that each color should be broad with its center in the appropriate spectral range *i.e.* broad red, broad green, and broad blue.[201-202] The benefit of this approach would be the ability to tune the color temperature during operation, as well as the higher efficiency of directly converting current to light without down conversion losses. However, the majority of materials that could be suited for electroluminescence are relatively narrow emitters. This makes this approach highly sought after in the display industry, but it would result in low CRI values in lighting (*ca.*70-80).[201] Rather than rely on electroluminescence the next two approaches utilize down conversion or PL. The approach that would naturally lend itself to higher CRI values would be the combination of UV or "purple" (405 nm) LEDs with RGB phosphors. While this may be technologically feasible, it is far from perfect and it may be economically unsatisfactory for several reasons. First, the industry standard has been and still is blue excitation.[203] Second, materials that emit in the blue and green may suffer from reabsorption by the red phosphor. Third, the effect of phosphor heating during operation may not affect all phosphors equally, and this may result in a slow change in the color temperature over time. These numerous engineering obstacles stand in

the way of this method. The final and most common approach for SSL is known as partial conversion. This approach typically utilizes a blue LED to excite a yellow phosphor (*e.g.* $Y_{3-x}Ce_xAl_5O_{12}$) while still allowing some of the blue light to pass through; the combination of the broad blue and yellow produce white.[200-201] These LEDs typically produce colder colors as a result of the weaker red emission. Today, some groups have found that this approach can result in high CRIs with warm temperatures through the addition of red phosphors such as $Sr_2Si_5N_8:Eu^{2+}$ or $Sr(LiAl_3N_4):Eu^{2+}$.[200-201, 204] However, higher QY phosphors with high absorption coefficients, which are potentially free of rare-earth elements altogether, are still necessary to further improve device efficiencies.[205-206]

While many of the known, lead-free 0D metal-halides (particularly organic-inorganic hybrids) exhibit broad PL with high PLQYs at RT, these materials would nonetheless be ill suited as SSL phosphors for two primary reasons: UV peak excitation and thermal sensitivity. The first of these is apparent from the absorption and PL excitation (PLE) spectra of the majority of studied, luminescent 0D metal-halides. Typically, these materials have molecular-like excitation spectra that peak below 400 nm and absorption spectra that cut-off near or below this same value. This severely reduces the potential light output from any device even with the use of 405 nm purple LEDs. This effectively disqualifies the vast majority of emissive 0D metal-halides, though a few remain which exhibit RT emission. These, however, face the issue of phosphor heating. In Chapter 3, we discuss the extreme thermal sensitivity that the PLQY and lifetime of these materials share, which further dampens the potential performance of these materials.[207-208]

1.5. Thesis outline

In summary, the goal of this Ph.D. was to expand the emerging field of emissive, lead-free 0D metal-halides. To do so, we first set about re-discovering known 0D lead-free metal-halides by investigating their ability to emit light. We then sought to broaden our knowledge of their properties and attempt to apply these materials in new ways. Finally, we investigated the properties and use of polynuclear 0D metal-halide clusters and the potential influence of intervalent and metal-metal charge transfer on excitation.

Although metal-halide perovskites have been in vogue since 2014 after their introduction as absorptive layers in solar cells and 2D metal-halides have been intensively studied since the early 1990's, little-to-no results or studies had been published focusing on the light-emissive properties of 0D metal-halides until 2017. Then in 2018, the first results in the field of lead-free 0D metal-halides were published concurrently with the Cs_4SnBr_6 material presented in **Chapter 2.** Here we demonstrated Cs_4SnBr_6 to be an efficient source of PL at RT. Furthermore, we attributed the broad-PL that this material exhibits to the formation and subsequent radiative recombination of self-trapped excitons as discussed in Section 1.4. We then explored the optical tunability of this phase and the structural changes that this tuning brings about through the combination of XRD and optical studies to fully describe the $Cs_{4-x}A_xSn(Br_{1-y}I_y)_6$ (A=Rb,K; x,y≤1)

family. Finally, we were able to rationalize our experimental observations through the use of DFT calculations and found that STE emission can be influenced through anisotropic unit cell compression. This family of materials offered a first glance at the broader field of luminescent 0D lead-free-metal-halides in our group that became the focus of this dissertation.

In **Chapter 3**, we expanded our work on the Cs_4SnBr_6 material to investigate the influence of temperature on PL lifetime and discovered a niche application for low-dimensional metal-halides altogether. We had previously observed drastic variations in the average lifetime that appeared to shift from day-to-day, and in carefully investigating this behavior discovered that the lifetime indeed exhibits a strong dependence on temperature. In fact, the steepness of the PL lifetime variation around RT was one of the steepest (~ 20 ns/K) at the time of this publication in 2019. From this point we realized that this trend may indeed be a general feature found amongst other STE-emitting low-dimensional metal-halides, and we found this to be true in $(C_4N_2H_{14}I)_4SnI_4$ (0D) and $[C(NH_2)_3]_2SnBr_4$ (1D). Finally, we collaborated with the Swiss Center for Electronics and Microtechnology (CSEM) to demonstrate successful remote-optical thermography or thermal imaging using Cs_4SnBr_6 as a thermally sensitive phosphor. However, we were aware of the oxidative instability of our Sn-based phosphors and so we began to search for oxidatively stable 0D alternatives based on similar ns^2 lone-pair containing metals.

This lead to the work presented in **Chapter 4**, in which we discovered the $Rb_7Bi_{3-3x}Sb_{3x}Cl_{16}$ ($x \leq 1$) family of materials. These all exhibit unusual 0D structures comprised of isolated octahedra and edge-shared octahedra in the form of dimers. Again through the use of a combination of structural analysis, spectroscopy, and DFT calculations we demonstrate that these materials have the potential to be excellent thermometric/thermographic agents and that the unusual edge-shared dimers may be the key to unlocking RT PL for 0D, inorganic pnictogen-halides.

At this point, we saw that one of the consistent drawbacks of these 0D metal-halides is their lack of absorption of blue light. In fact, these materials tend to be excitable only with UV light, and any effort to narrow the bandgap of these materials through the alloying of heavier halides such as Br^- or I^- tends to effectively quench their PL.

The results of the previous chapters demonstrated that 0D metal-halides exhibit unique properties, promising for optoelectronic applications such as thermometry and thermography. While previous publications have also demonstrated the utility of such materials in high-energy excitation applications such as X-ray scintillation, the vast majority of optoelectronic applications use blue excitation sources. However, most 0D metal-halides have sub-400 nm excitation maxima with only weak 450-460 nm absorption. Therefore, finding suitable strategies to narrow the band gap of these materials are required. One obvious possibility is of course to substitute with heavier halides such as Br^- or I^-. This strategy, while easy to implement, is hindered by decreased quenching temperatures and concomitantly lower PLQY values.

One potential solution that we sought to investigate in **Chapter 5** was through the use of 0D mixed-valent materials. These tend to have broad absorption bands that extend into the visible range, giving many of these materials red or even black colors. Given this strong visible absorption,

we were determined to see if any such materials may be luminescent at any temperature as no reports existed on the topic. Furthermore, we identified a yet-to-be-answered question within the literature regarding the existence and structure of the "$Rb_4Sb^{III}Sb^{V}Cl_{12}$" and "$Rb_{2.55}SbCl_6$" phases.

Therefore, we synthesized this phase and found the stoichiometry to be $Rb_{23}Sb^{III}_7Sb^{V}_2Cl_{54}$, with an orthorhombic structure (*Cmcm*) and red color. No low temperature PL was observed; however, we were able to discover a series of new materials once the Sb^{III} was partially or even fully substituted with Bi^{III}. These instead crystallize in a trigonal crystal system with a *R*32 space group. Incidentally, this belongs to one of the piezoelectric space groups and suggests that these phases may exhibit piezoelectricity or second harmonic generation. To confirm this space group, we performed SHG measurements and found strong evidence of its existence. Regarding optical properties, the charge transfer bands for these materials blue shift as the amount of Bi^{III} increases compared to the Sb-only phases, but still no PL was observed at any temperature down to 12 K.

The dissertation concludes with a brief summary as well as outlook on the field of 0D lead-free metal-halides as emissive materials and their niche applications.

Chapter 2. Highly Emissive Self-Trapped Excitons in Fully Inorganic Zero-Dimensional Tin Halides

Figures and excerpts reprinted with permission from Benin, B.M.; Dirin, D.N.; Morad, V.; Wörle, M.; Yakunin, S.; Rainò, G.; Nazarenko, O.; Fischer, M.; Infante, I.; Kovalenko, M.V. "Highly Emissive Self-Trapped Excitons in Fully Inorganic Zero-Dimensional Tin Halides", *Angew. Chem. Int. Ed.,* **2018**, *57* (35), 11329-11333; *Angew. Chem.,* **2018**, 130 (35), 11499-11503. Copyright 2018 Wiley-VCH Verlag GmbH & Co. KGaA.

2.1. Abstract

In this chapter, we made our first foray into low-dimensional, and specifically 0D materials. Through the use of solid-state methods, we were able to grow phase-pure powders of the incongruently melting Cs_4SnBr_6 phase. We were the first to discover that this phase exhibits efficient RT PL (RT QY = 15% ± 5%), and we sought to investigate both the origins and the tunability of this luminescence.

To our initial surprise, the PL was observed to be very broad with a full-width-at-half-maximum (FWHM) of 0.51 eV (120 nm) and highly Stokes shifted (1.2 eV). In agreement with the structure-property relationships observed in other metal-halides, the excitation and emission could be shifted *via* anion substitution; however, the substitution was limited to iodide only, expanding the formula to $Cs_4Sn(Br_{1-y}I_y)_6$ ($y \leq 1$). Furthermore, iodide substation past $Cs_4SnBr_3I_3$ could be measured crystallographically, but no longer resulted in RT luminescent phases.

We then discovered that the emission and Stokes shift could be tuned through the partial substitution of Cs^+ with smaller cations such as Rb^+ and K^+ to yield the final formula, $Cs_{4-x}A_xSn(Br_{1-y}I_y)_6$ (A=Rb,K; $x,y \leq 1$). Briefly, smaller cations blueshift the PL and decrease the Stokes shift. This is contrary to what has been observed for higher-dimensional metal-halides such as the 3D $APbX_3$ perovskites, in which the A-site cation indirectly influences both the bandgap and the emission wavelength by altering the Pb-X-Pb angle and decreasing the band width as the structure deviates from an ideal cubic one.[29] However, in both cases the large, monovalent cations do not contribute to the density-of-states (DOS) at the bandgap.

To determine the structural origin of this effect in the 0D $Cs_{4-x}A_xSn(Br_{1-y}I_y)_6$, density functional theory (DFT) calculations were utilized. First, the STE state was modelled and determined to occur as a Jan-Teller like distortion of a $[SnX_6]^{4-}$ octahedron. With partial substitution of some of the Cs atoms for Rb and K, the unusual PL trend was also investigated. By

relaxing the structure in the excited state, the PL energy could be determined from the energy difference between the STE state and the ground state. The results fit very well with what was observed experimentally, and they described a situation in which the smaller unit cell effectively restricts the space into which the $[SnX_6]^{4-}$ octahedra can distort. The spatial restriction decreases the energy that can be lost towards octahedral distortion, effectively blue shifting PL and decreasing the Stokes shift.

2.2. Introduction

Interest in low-dimensional metal-halide semiconductors,[80, 101, 105, 109-112, 209-216] and ultimately their 0D counterparts,[168, 170, 217] has been spurred by the increasing interest in 3D lead halide perovskites.[53, 170, 218-219] In recent years, lead-halide perovskites have risen to prominence in the field of optoelectronics with their use in full-color imaging,[34] photodetection,[36, 220] X-ray imaging,[221] hard-radiation detection,[33, 41] solar cells,[25-26] and light-emitting diodes,[38] owing to their defect-tolerant photophysics and charge transport.[59, 222-223]

As the dimensionality decreases, the metal halide octahedra become progressively less connected and the optical and electrical properties shift away from those of a delocalized, 3D network towards 0D, molecular-like, isolated octahedra. In such structures, self-trapped excitons (STEs) form due to the local deformation of the crystal lattice upon photoexcitation. This strong spatial localization, and the absence of electronic trapping processes that are inherent in electronically extended (higher dimensionality) solids, favors radiative recombination. Previously, the spatial confinement of carriers in 3D perovskites has been attained through crystal size control at the nanoscale (*i.e.* top-down and bottom-up synthesis of NCs).[46-47, 52, 224-226] In the case of 0D materials, such elaborate crystal size engineering is not required as the optical properties are instead governed by their structural dimensionality. Highly localized Frenkel-like excitons are formed instead of Wannier-Mott type excitons.

The library of 0D metal halides with octahedral building units includes both lead-based and lead-free compounds: Ti(IV),[187] Hf(IV),[227-228] Zr(IV),[229] Pd(IV),[196] Pb(II),[230] Sn(IV),[188, 190] Te(IV),[150-151, 231-232] Sb(III),[155, 233-234] and Bi(III).[235] However, only several of these examples exhibit PL at RT; and this emission is seldom characterized by a high PLQY. The first examples with high QYs in excess of 50% were demonstrated only recently: $(C_4N_2H_{14}Br)_4SnBr_6$ (QY = 95%±5%) and $(C_4N_2H_{14}Br)_4SnI_6$ (QY = 75%±4%).[161, 197] Both structures are constructed from disconnected $[SnX_6]^{4-}$ octahedra, separated by large organic cations with a distance of >1 nm between Sn^{2+} centers.

Given the high PL QY of these hybrid materials and their novel approach towards exciton localization, we chose, herein, to pursue fully inorganic analogues such as Cs_4SnBr_6. While several studies have reported on the structure and basic properties of Cs_4SnBr_6, none have observed PL at RT.[149, 236] Recently, calculations have shown that the Cs_4SnBr_6 phase should have a bandgap of 3.37 eV.[237] We prepared $Cs_{4-x}A_xSn(Br_{1-y}I_y)_6$ (A = Rb, K) materials using a simple solid-state "heat-and-beat" approach, characterized them structurally and found them to be luminescent at RT.

2.3. Experimental details

For detailed experimental details regarding materials, synthetic procedures, and characterization techniques, see chapter 7. Materials and Methods.

Further details on the crystal structure investigation(s) may be obtained from the

Fachinformationszentrum Karlsruhe, 76344 Eggenstein-Leopoldshafen, Germany (fax: (+49)7247-808-666; e-mail: crysdata@fiz-karlsruhe.de), on quoting the depository number CSD-434641, 434642, 434643, 434644, 434645, 434646, and 434647.

2.4. Results and Discussion

According to the CsBr-$SnBr_2$ pseudo-binary phase diagram (Figure 2.1Figure 2.1a), Cs_4SnBr_6 melts incongruently and competes with the decomposition into the black $CsSnBr_3$ and CsBr. Therefore, phase pure Cs_4SnBr_6 cannot be obtained by cooling from a melt of this composition. Instead, solid pellets of a mixture of CsBr (4.5 eq.) and $SnBr_2$ (1 eq.) were repeatedly heated to 350 °C for 60 hours and reground in a glovebox between heating cycles. The highlighted green region in Figure 2.1a represents the experimental conditions that were found to yield the purest materials, *i.e.* at temperatures below the decomposition point of Cs_4SnBr_6 (Figure 8.1,Figure 8.2; Table 8.1. Refinement of Cs4SnBr6.,8.2). Single crystals of Cs_4SnBr_6 were obtained by tempering a solid pellet at 350 °C. Cs_4SnBr_6 crystallizes in a trigonal crystal system (R-3c space group, Figure 2.1b, Table 8.3-8.9), wherein $[SnBr_6]^{4-}$ octahedra are separated by Cs^+ cations. The Cs^+ cations occupy two distinct crystallographic positions (Figure 8.3).

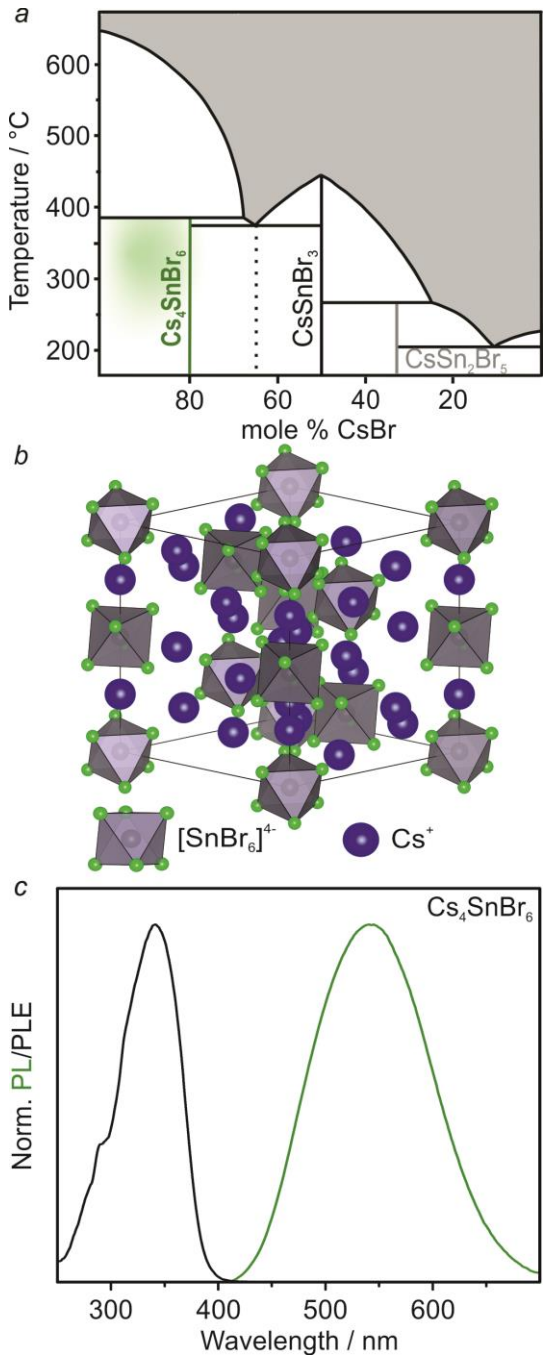

Figure 2.1. (a) The pseudo-binary CsBr-$SnBr_2$ phase diagram.[149] The highlighted green region represents the experimental conditions found to yield the purest Cs_4SnBr_6 material. (b) The crystal structure of Cs_4SnBr_6 viewed along the (111) axis with $[SnBr_6]^{4-}$ octahedra (grey with green bromine atoms) separated by Cs^+ cations (blue). (c) PL and PLE spectra for Cs_4SnBr_6 (at RT).

Unlike the isostructural Cs_4PbBr_6, which shows narrow excitonic PL only at low temperatures and at wavelengths <400 nm,[164] Cs_4SnBr_6 exhibits broad-band green-yellow PL at

RT from STEs (peak maximum at 540 nm, Figure 2.1c). Upon measuring the PL excitation (PLE) it was found that Cs_4SnBr_6 resembled a molecular material with a sharp excitation peak at 340 nm yielding a large Stokes shift of *ca.* 1.2 eV. These results are, however, at odds with the off-white visual appearance of our Cs_4SnBr_6 powders. To investigate this inconsistency, absorption spectra were measured in diffuse reflectance to determine the effective band-edge of this Cs_4SnBr_6 material as well as any impurities that may be present (Figure 2.2).

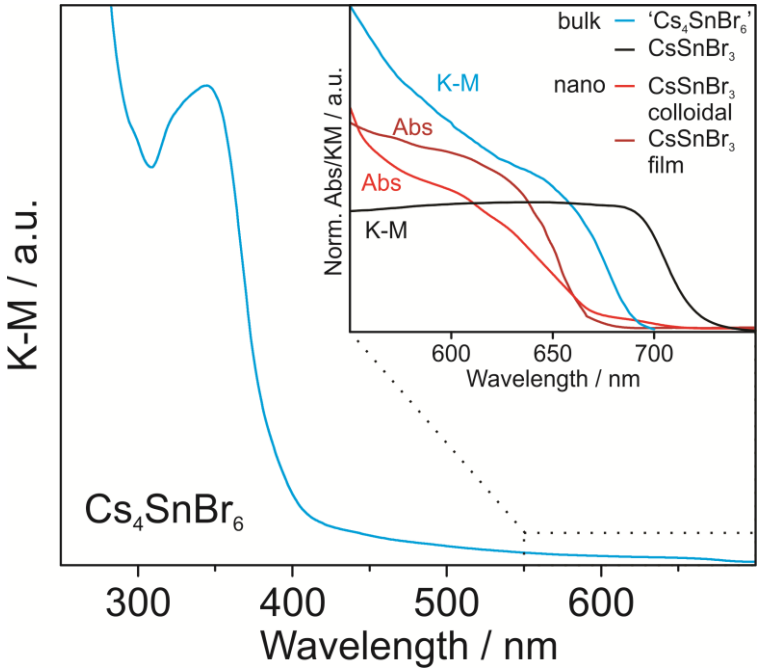

Figure 2.2. Absorption (Kubelka-Munk, or K-M in the Figure) spectra of Cs_4SnBr_6 with a comparison to other $CsSnBr_3$ absorption spectra (inset).

In agreement with the measured PLE, the absorption spectrum demonstrates an absorption edge that ends at roughly 400 nm. It was also observed that a tail extends towards longer wavelengths and may be the culprit behind the visually off-white appearance. This shoulder is expanded in the inset to Figure 2.2 and a shoulder at 670 nm is observed. This shoulder likely results from an impurity of $CsSnBr_3$ that, although too small (in amount and in size) to be measurable by XRD, slightly discolors the otherwise white powder giving it an off-white appearance. This is plotted in comparison to bulk and nanocrystalline $CsSnBr_3$ in the inset. The colloidal NCs of $CsSnBr_3$, plotted in red, are reported as being 10.7 nm ± 6.4 nm in diameter and these exhibit the most blue absorption edge in agreement with their size (data taken from Ref.[238]) Furthermore, films prepared from $CsSnBr_3$ nanocubes also have absorption edges that are blue shifted from that of bulk $CsSnBr_3$ and near to that of colloidal $CsSnBr_3$ NCs (data taken from Ref.[239]). Given this optical data, the tail and shoulder observed in the absorption spectrum of Cs_4SnBr_6 are ascribed to $CsSnBr_3$. Even with this minute impurity, a PLQY of 15±5% was measured at RT.

The PLE and PL spectra were found to be tunable through the partial substitution of both A-site cations (Cs with Rb, K) and the halide anions (Br with I). Na was not observed to substitute Cs; instead, a mixture of NaBr, Cs_4SnBr_6, and $CsSnBr_3$ are produced (Figure 2.3).

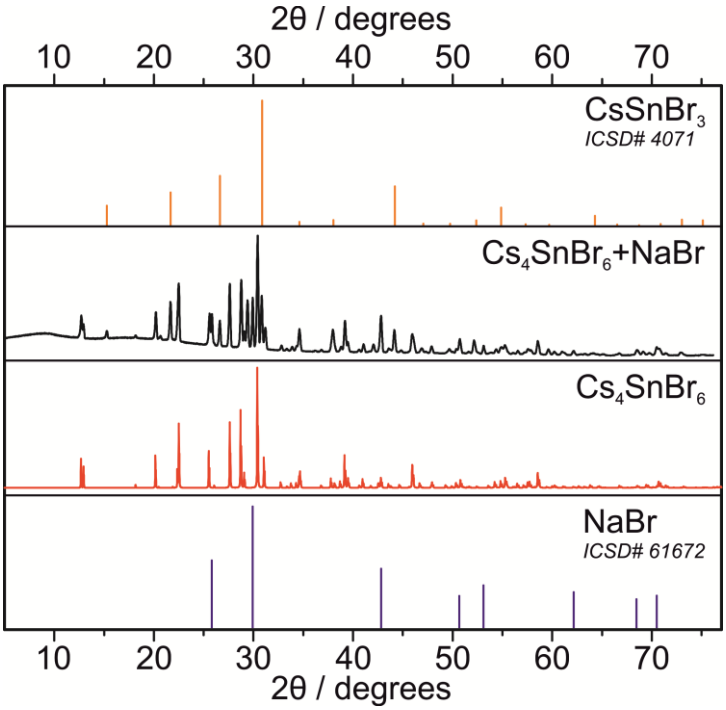

Figure 2.3. Substitution with Na. Cations smaller than K^+ do not substitute Cs^+ in Cs_4SnBr_6. The addition of Na resulted in a mixture of Cs_4SnBr_6, $CsSnBr_3$ (ICSD# 4071), CsBr (not shown), and NaBr (ICSD# 61672).

In $(C_4N_2H_{14}Br)_4SnX_6$ (X = Br/I),[161, 197] the addition of iodide red-shifts both the excitation and STE emission spectra. Similarly, the PL of Cs_4SnX_6 shifts to 620 nm (orange emission) at a Br:I ratio of *ca.* 1:1 (Figure 2.4a). In agreement with Vegard's law, a linear change in both the *a* and *c* lattice parameters was observed over the range of compositions from Cs_4SnBr_6 to Cs_4SnI_6 (Figure 8.4, Figure 8.5; Table 8.10,Table 8.11). Samples with greater than 50% substitution by iodide, however, did not exhibit PL at RT and were not investigated further.

While bromide and iodide occupy the same general position within the structure of Cs_4SnBr_6, Rb^+ and K^+ could potentially substitute two distinct crystallographic positions of Cs^+ (Figure 8.3). Substitution by Rb^+ or K^+ occurred only on the smaller Cs(2) site (1/4 of all Cs, six-fold coordination, Figure 2.4b, Figure 8.6; Table 8.12, Table 8.13). This preferential substitution explains the experimentally observed 25%-limit for substitution (Figure 8.7). Furthermore, much higher loadings tend to yield samples with greater amounts of impurities such as the darkly colored $CsSnBr_3$.

Plotting the lattice constants against the molar fractions of K^+ or Rb^+ ions, estimated from

the Rietveld refinement and energy-dispersive X-ray spectroscopy (EDS), yields a seemingly linear trend for the *c* parameter, in agreement with Vegard's law, whereas the *a* parameter increases only slightly (Figure 2.4c, Figure 8.7-Figure 8.9). The larger error bars for the samples with Rb-substitution in Figure 8.9 come as a result of the smaller differences in electron density between Cs and Rb than between Cs and K.

The site affected by substitution is part of an infinite chain of $[SnBr_6]^{4-}$ octahedra separated by Cs/Rb/K ions. Since the chain is oriented parallel to the *c*-axis, substitution by Rb or K will cause the largest effect along this axis resulting in a decrease in the *c* parameter.

The substitution of Cs^+ by Rb^+ or K^+ results in a blueshift of the PL maximum. This shift is dependent on both the degree of substitution and on the identity of the substituting cation. For 25% substitution, Rb^+ shifts the PL peak to 519 nm, whereas K^+ yields a PL peak at 500 nm (Figure 2.4d). Strikingly, the PLE remains unaffected. The same scenario was observed for the other examined Br:I ratios (*ca.* 5:1, 2:1, 1:1, Figure 2.4e, Figure 8.10; Table 8.14,Table 8.15).

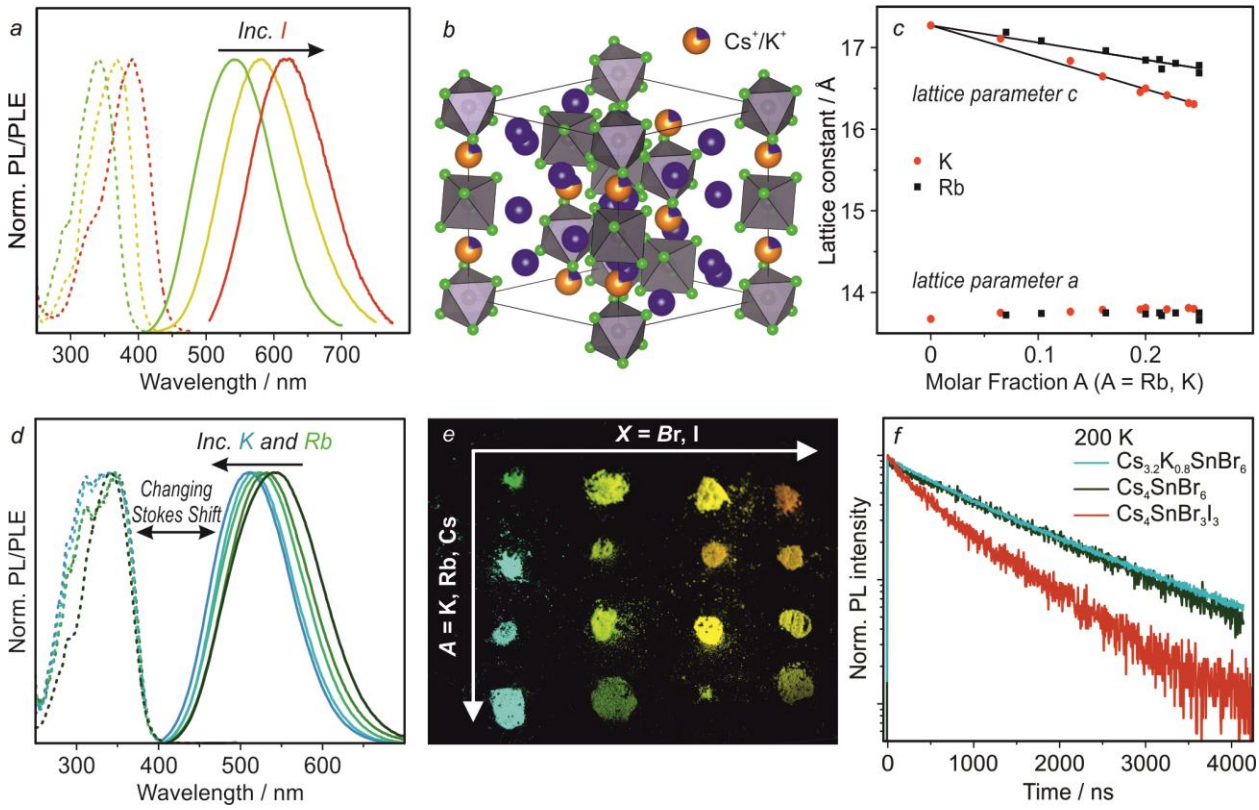

Figure 2.4. Structural and optical characterization of $Cs_{4-x}A_xSn(Br,I)_6$ compounds (A=K, Rb). (a) PL and PLE spectra of $Cs_4Sn(Br,I)_6$. (b) Crystal structure of $Cs_{3.2}K_{0.8}SnBr_6$ determined by Rietveld refinement. (c) The change in the *a* and *c* lattice parameters upon Cs^+ substitution by Rb^+ and K^+. (d) PL and PLE spectra for Rb^+ or K^+ substituted compounds. (e) Image of $Cs_{4-x}A_xSn(Br,I)_6$ powders under 365 nm UV light. (f) TRPL of Cs_4SnBr_6, $Cs_{3.2}K_{0.8}SnBr_6$, and $Cs_4SnBr_3I_3$ at 200 K.

Temperature-dependent PL spectra were measured down to 6 K (Figure 8.11, Figure 8.12). It was found that the PL intensity increased with decreasing temperature and, in the case of Cs4SnBr6, the emission intensity reached a maximum at ca. 200 K. Given a RT QY of 15±5%, the QY of Cs4SnBr6 is estimated to be near unity at 200 K (Figure 8.13a). No higher-energy emission, i.e. from free excitons, could be observed in Cs4SnBr6 or Cs4SnBr3I3 at any temperature (Figure 8.12). However, the integrated PL vs. temperature plot indicates that there are two regions present: region 1 and region 2. Region 1 involves a PL increase, and is related to an increasing QY since any decrease in absorption in Region 1 is still met with an increase in the PL intensity. Region 2, however, demonstrates a loss of PL with decreasing temperature, which is also observed in Figure 8.12a,b. This loss is explained by Figure 8.13b with PLE measured at 78 K. As the temperature decreases, it is observed that the excitation peak narrows and that the peak position slightly blue shifts. These two effects inhibit the material from being efficiently excited with a 355 nm laser. The slight blue shift in the PLE can be explained by the lattice contraction observed in Table 8.3. Furthermore, the average Sn-Br distance decreases from 2.9939 (7) Å to 2.9854 (6) Å when cooled from 273 K to 100 K.

The time-resolved PL (TRPL) of Cs4SnBr6 at RT exhibits a monoexponential decay with an average lifetime of 540 ns (Figure 2.5). TRPL decays were then recorded at 200 K (the temperature that corresponds to highest QY, Figure 2.4f,Figure 8.13), and it was observed that the lifetime increased to 1381 ns (1424 ns for K-substitution), while remaining monoexponential (Figure 2.4f).

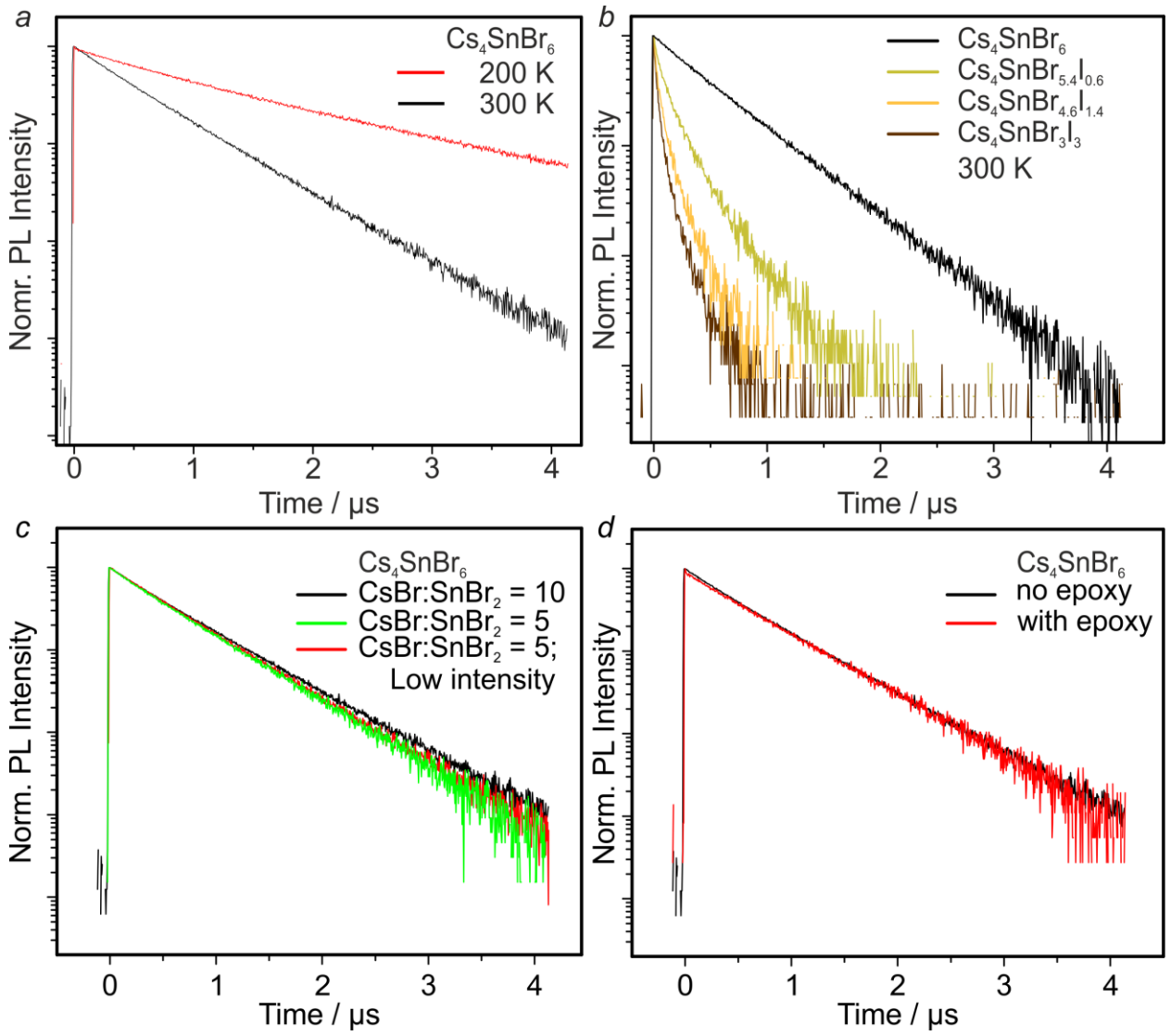

Figure 2.5. Time-resolved PL spectra. (a) Changing temperature results in a lengthening of the PL lifetime. (b) The addition of iodide shortens the average PL lifetime. (c) Preparing Cs_4SnBr_6 with different $CsBr:SnBr_2$ ratios yields materials with equivalent average lifetimes. Furthermore, the PL lifetime is intensity- independent. (d) Encapsulation with a UV-curable epoxy also does not affect the measured PL lifetime.

Substitution with iodide accelerated the average lifetime (600 ns at 200 K for $Cs_4SnBr_3I_3$, Figure 2.4f; see Figure 2.5b for RT comparison). It should be noted that this acceleration in PL decay occurs concomitantly with an apparent reduction in the PL intensity at the same temperature. This may indicate that substitution with heavier anions increase the non-radiative relaxation rate. The radiative lifetime was also found to be insensitive towards dilution with CsBr, excitation intensity, crystallinity and encapsulation within a UV curable epoxy (Figure 2.5c,d) indicating a lack of surface effects on PL properties in these 0D materials.

Broad-band, strongly Stokes shifted emission with relatively long radiative lifetimes

indicates the formation of STEs (Figure 2.6a). As in molecular complexes and similarly small entities, structural changes occur between the ground state and the excited state. Emission from STEs is then somewhat similar to an indirect-gap optical transition since coupling to phonons is required.[240] Besides 0D-tin halides,[161] emission from STEs has also been observed in 1D- and 2D-layered materials.[102, 125, 241]

To rationalize the effect of A-site substitution observed in these materials, calculations of the partial density of states (DOS) by density functional theory (DFT) were utilized (Figure 2.6b, Figure 8.14; Table 8.16).

A 1x1x1 unit cell (66 atoms) was used as a model system for Cs_4SnBr_6, $Cs_3RbSnBr_6$, and Cs_3KSnBr_6 materials. The electronic states were found to be highly localized in all three compositions and the band gap was found to consist of Sn 5*s*, Br 5*p* (conduction band/LUMO) and Sn 5*p*, Br 5*p* orbitals (valence band/HOMO). A-cation orbitals do not significantly contribute to HOMO and LUMO states (Figure 8.14). This is corroborated by the experiment given that A-site substitution did not substantially affect the PLE spectra.

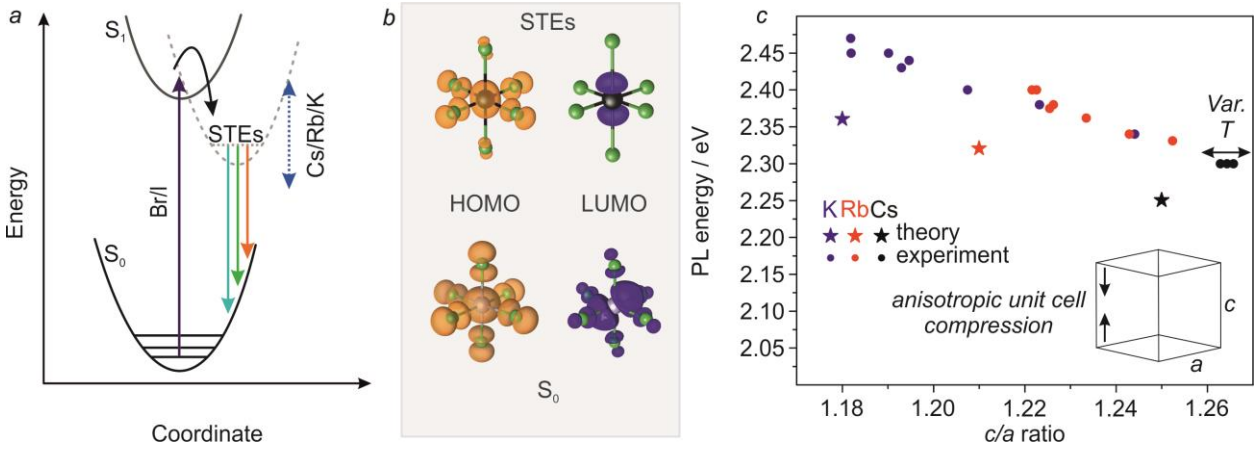

Figure 2.6. (a) Generic CC diagram depicting formation illustrating the origin of STE PL in $Cs_{4-x}A_xSn(Br_{1-y}I_y)_6$. (b) Ground state and excited state (STE) HOMOs and LUMOs. (c) Experimental and theoretical results demonstrating that PL energy varies linearly with the ratio of c-axis to a-axis length. Variable temperature measurements (three data points; black circles) are plotted for Cs_4SnBr_6 at 100 K, 200 K, and 273 K

It was previously shown that both tin- and lead-halide octahedra distort significantly upon photoexcitation in low dimensional materials.[242-243] By modeling the excited state and ground state geometries, we find that the extent of distortion was the principle reason for the Stokes shift (Figure 2.6b). A pseudo-Jahn-Teller distortion was observed with elongation of up to 17% in the axial Sn-Br bonds, and a contraction of up to 7% in the equatorial bonds. This distortion was found to be greatest in Cs_4SnBr_6 and decreased from Cs^+ to Rb^+ to K^+ (Table 8.17). In other words, the energy required for distortion correlates well with the measured Stokes shift. Larger distortion is allowed

by greater distance between the octahedra; primarily along the c-axis. The ratio between the lengths of the *c*- and *a*-axes was found to correlate most strongly with PL energy, experimentally and in calculations (Figure 2.6c). On the other hand, isotropic changes to the unit cell (i.e. contraction during cooling) do not affect the PL (Table 8.18).

2.5. Conclusion

In summary, several new 0D Sn-halides with the general formula $Cs_{4-x}A_xSn(Br_{1-y}I_y)_6$ have been found to exhibit broad-band RT PL that is tunable from 500 nm to 620 nm. The PL peak position and Stokes shifts can be concomitantly adjusted by the substitution of Cs^+ with either Rb^+ or K^+ as well as Br^- by I^-. PL properties were rationalized by the DFT analysis of STEs. Future studies might concern applications of such materials in luminescent solar concentrators and light emitting devices, harnessing their structural tunability and fully inorganic compositions.

Chapter 3. High-resolution remote thermometry and thermography using luminescent low-dimensional tin-halide perovskites

Figures and excerpts reprinted with permission from Yakunin, S.; Benin, B.M.; Shynkarenko, Y.; Nazarenko, O.; Bodnarchuk, M.I.; Dirin, D.N.; Hofer, C.; Cattaneo, S.; Kovalenko, M.V. "High-resolution remote thermometry and thermography using luminescent low-dimensional tin-halide perovskites", *Nat. Mater.*, **2019**, *18*, 846-852; Copyright 2019 Nature Publishing Group.

3.1. Abstract

During our investigation of the luminescent properties of the $Cs_{4-x}A_xSn(Br_{1-y}I_y)_6$ (A=Rb,K; x,y≤1) family of materials (Chapter 2), we noticed that the PL lifetime of these phases exhibited a very strong thermal dependence. We set about investigating this further and discovered that these phases exhibit extremely temperature sensitive PL lifetimes and PLQYs. Furthermore, this trend appeared to be general for other known low-dimensional tin-halides such as $[C(NH_2)_3]_2SnBr_4$ and $(C_4N_2H_{14}I)_4SnI_6$.

While the thermal dependence of the PLQY in these materials was initially viewed as a disadvantage, we later understood that the PL lifetime could be a route towards utilizing these materials as optical thermometers. The PL lifetime, unlike PL intensity, was found to be consistent regardless of external surrounding, oxidation, impurities, etc. This effectively gave us an intrinsic probe of the material's thermal environment. To our surprise, these low-dimensional materials exhibit thermal sensitivities on par with the best remote-optical thermometric materials to date (~ 20 ns K^{-1}).

This finding opened the door for a new class of remote-optical thermoluminophores as this field has predominantly made use of rare-earth or transition metal dopants in oxide host lattices, in which the PL intensity varies with temperature. While the sensitivity of such materials can be high, they require very precise control over dopant concentration and their PL lifetimes can be too long for easy measurement. To characterize the thermometric performance and precision of these materials, we measured a series of lifetime traces while maintaining a fixed sample temperature. In doing so, we were able to estimate a thermometric precision of ±13 mK over 51 traces.

To further improve upon this discovery, we collaborated with CSEM who had developed a prototype time-of-flight (TOF) fluorescent lifetime imager (FLI). With this we were able to demonstrate the first example of remote-optical thermography with full-motion video utilizing our low-dimensional tin-halides.

3.2. Introduction

Remote thermal imaging or thermography, lends itself to numerous applications ranging from medicine[244] and defense, to biological research[245], or the diagnosis of technical failures[246]. In all these applications, remote thermal detection falls into two main categories: IR or visible.

IR-based detectors exploit the long-wave IR emission (LWIR, *e.g.* thermal emission) of a studied object using the fact that the integral radiation intensity emitted from the blackbody scales with its temperature (T) as $\sim T^4$. This emission can be recorded with rather costly photodetector arrays composed of narrow bandgap semiconductors (InSb, $In_{1-x}Ga_xAs$ and $Hg_{1-x}Cd_xTe$)[247-248], and this method is predominantly used for scientific and military purposes. Alternative and less expensive bolometric detectors, owing to advancements in MEMS-technologies (Micro-Electro-Mechanical Systems) [249-250], have already entered the consumer electronics market, and are able to record thermal images with both high speed and high resolution. However, their thermographic performance, based on measurements of IR radiation intensity, is inherently limited by the transparency and emissivity/reflectivity of an observed object and, more importantly, by any material and medium (window, coating, matrix, solvent *etc*.) situated within the path between the detector and an object (Figure 3.1). As one of the major consequences, IR thermography cannot be easily combined with conventional optical microscopy or other enclosed optical systems such as cryostats or microfluidic cells.

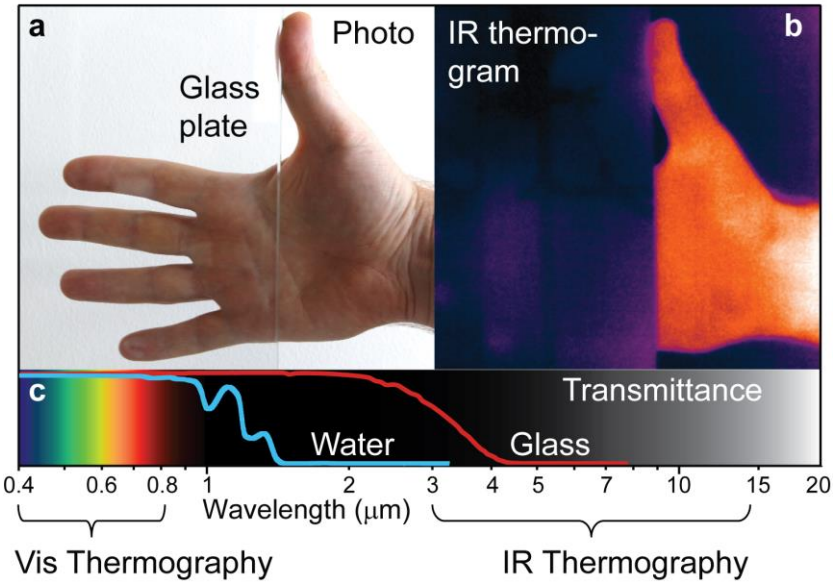

Figure 3.1. Visible-light and IR thermography comparison. Differences in transmittance for visible and IR light are demonstrated in (a) photograph, and in (b) IR thermogram captured using a commercial LWIR bolometry camera. (c) The transparency ranges of two ubiquitous optical media.

An alternative method for remote thermography, which is unhindered by enclosures or IR-absorptive media, utilizes temperature sensitive luminophores (i.e. fluorophores or phosphors) with PL in the visible spectral range (Figure 3.1c) that are deposited onto, or incorporated into, the object of interest as temperature probes[251-259]. To probe an object's temperature, the luminophore is then excited by an ultraviolet or visible (UV-Vis) pulsed source (*e.g.* laser or light-emitting diode) and the temperature-dependent PL lifetime decay is then analyzed by time-resolving detectors. This PL-lifetime approach exhibits several benefits: the excitation power and, consequently the PL intensity, can be adjusted to a value appropriate for the dynamic range of the detector. Additionally, the use of UV-Vis light, rather than mid- to long-wavelength IR radiation, allows for the direct integration of this method with conventional optical spectroscopy and microscopy applied in biological studies and materials research. Furthermore, higher spatial resolutions can be obtained with visible light (400-700 nm) as the diffraction-limit is ca. 20-times sharper than for LWIR (7-14 μm); this potentially extends the utility of remote thermography to intracellular, *in vitro*, and *in vivo* studies[260].

To promote the advancement and widespread use of remote thermography, a much broader portfolio of luminescent, thermally sensitive, and temperature-range tunable materials is required. These emitters must exhibit a fully reproducible radiative lifetime *vs.* temperature dependence and demonstrate an invariant behavior towards excitation-light intensity. While emitters satisfying these conditions do exist, the precision of thermometry utilizing them was so far reported to be only in the 0.1-1 °C range[252, 258, 261]. This level of thermometric precision (the reproducibility with which a single point's temperature can be measured) can be again attributed to two factors: the often moderate thermal sensitivity of available luminophores[261], and the PL lifetime measurement techniques that have been traditionally applied in industry. On the other hand, thermographic precision is related to the reproducibility of temperatures across an entire image, which adds spatial resolution as an additional parameter, as well as different detection hardware (suitable for recording images). As a result, progress in the development of PL-lifetime thermography has suffered from the exclusive use of expensive, bulky techniques that are in fact single-point measurements, which prohibit fast image acquisition. To address these shortcomings, we present (i) a family of low-dimensional tin-halide luminophores well-suited for remote thermography due to their strongly temperature-dependent, compound-specific PL lifetimes, (ii) thermometric precision down to 0.013 °C with operation in a broad temperature range from -100 to 110 ºC, and (iii) a thermographic method utilizing ToF cameras[262-263] for cost-effective, high-resolution, fast thermal imaging.

3.3. Experimental details

For detailed experimental details regarding materials, synthetic procedures, and characterization techniques, see chapter 7. Materials and Methods.

3.4. Results and Discussion

Low-dimensional tin-halide perovskite-derived luminophores. In the search for suitable thermographic luminophores, we analyzed the potential of lead- or tin halides with perovskite or lower-dimensional perovskite-like crystal structures. These compounds are formed by metal-halide polyhedral anions, typically MX_6^{4-} octahedra (M = Pb, Sn), which are either fully isolated and surrounded by positively-charged counterions (so-called 0D-compounds) or connected into extended one-, two- or three-dimensional (1D-3D) frameworks through corner-, edge- or face-sharing[131, 264]. In particular, 3D lead-halide perovskites, have recently emerged as prominent optoelectronic materials for photovoltaics and photodetectors[25, 34, 265-267], hard-radiation detection[33, 221, 268], as well as bright light emitters[40, 269-271]. Although bright luminescence has been reported at all dimensionalities for metal-halides, we have found that only 0D- and 1D-compounds exhibit a suitable set of optical characteristics for remote thermography.

In low-dimensional, and specifically 0D metal-halides, the electronic structure evolves from disperse electronic bands in 2D-3D materials to more localized states (molecule-like) in 0D-1D compounds[131]. Stemming from this, the mechanism of luminescence is also drastically different, and ranges from rather large, delocalized Wannier-type excitons in 3D materials to ultra-small Frenkel-like self-trapped excitons (STEs) in the 0D-compounds[125, 137, 217, 272]. We have tested a range of highly-luminescent, fully-inorganic and hybrid organic-inorganic 0D and 1D tin-halide compounds for their suitability for thermography in the range of -40 to 120 °C. Based on temperature-dependent PL and PL-lifetime measurements, three suitable candidates have been shortlisted: $[C(NH_2)_3]_2SnBr_4$ [$C(NH_2)_3$ = guanidinium][138], Cs_4SnBr_6[273] and $(C_4N_2H_{14}I)_4SnI_6$[161] (Figure 3.2;

Table 3.1). All of these compounds exhibit temperature-dependent PL lifetimes in the range of 1 ns – 1µs, and thus ideally match the optimal modulation range for most commercial ToF sensors (e.g. from tens of kHz to tens of MHz). This is in sharp contrast to the thermographic luminophores based on rare-earth-doped oxides[252, 256, 259, 274-275], which are characterized by much slower emission that is typically in the ms-range. Furthermore, the absorption coefficients of tin-halides for the UV-A range (315–400 nm, convenient for optical excitation) are high, and they are comparable to the bandgap absorption values (Figure 3.2) as each octahedron within the structure can act as an absorber/emitter. In contrast, the UV-A range absorption of rare-earth-doped oxide luminophores is weak due to a limited concentration of dopants (activator) or absorbing centers[252].

Both solid-state and solution-based methods were used to prepare the three types of luminophores utilized within this work. The fully-inorganic, 0D Cs_4SnBr_6 was synthesized

through a solid-state approach in which a mixture of CsBr and $SnBr_2$ were repeatedly pressed and heated at sub-melting temperatures as described in our recent report[273]. Cs_4SnBr_6 (*R-3c* space group) is composed of $[SnBr_6]^{4-}$ octahedra separated by Cs^+ cations (Figure 3.2a)[149]. A 1D hybrid organic-inorganic compound, guanidinium tin-bromide, $[C(NH_2)_3]_2SnBr_4$ ($Pna2_1$ space group), was crystallized from a solution of the respective ions in concentrated HBr. Its tin-halide backbone consists of corner-sharing $[SnBr_5]_\infty^{2-}$ square pyramids (Figure 3.2b). Another 0D hybrid compound, $(C_4N_2H_{14}I)_4SnI_6$, was prepared by co-precipitation from a dimethylformamide solution according to Ref.[161] $(C_4N_2H_{14}I)_4SnI_6$ comprises isolated $[SnI_6]^{4-}$ octahedra surrounded by large, organic cations (Figure 3.2c). Powder X-ray diffraction patterns of all three materials indicate high phase-purity (Figure 8.15-Figure 8.17).

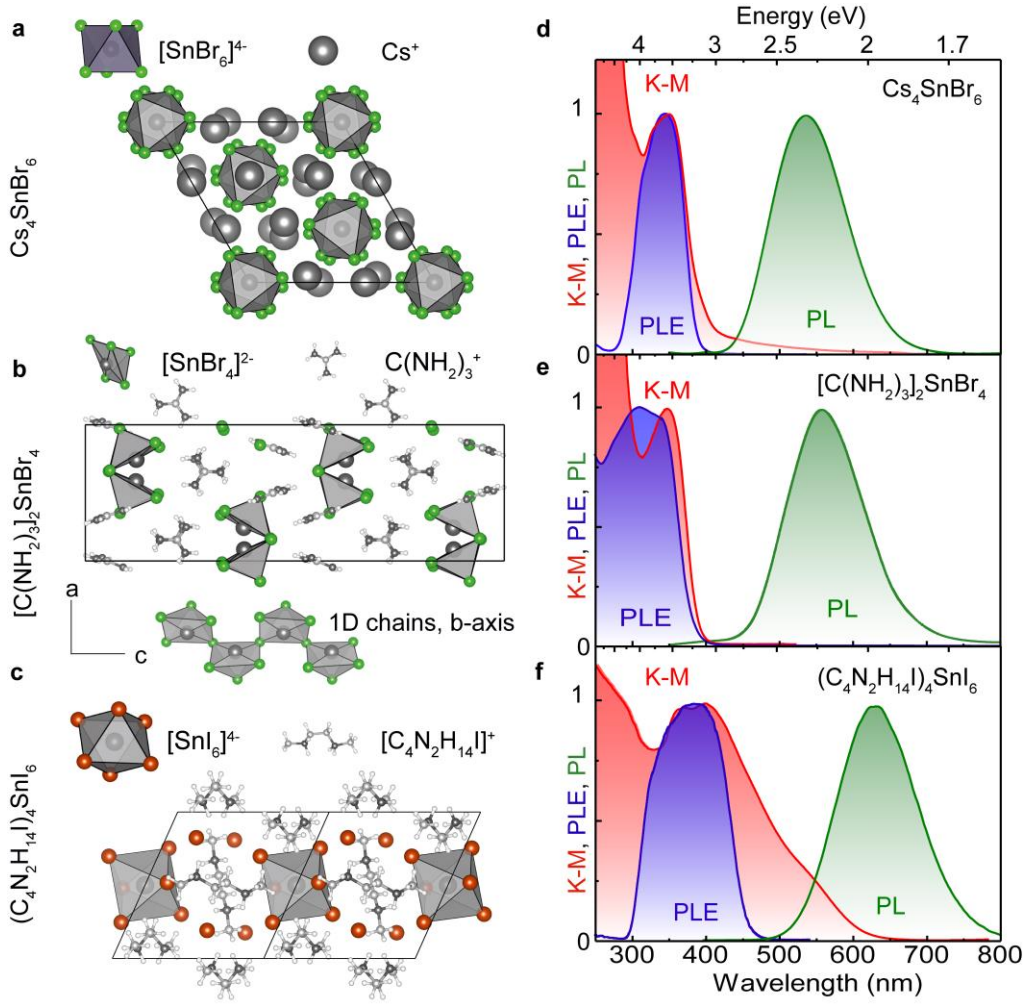

Figure 3.2. Crystallographic structures and basic optical properties of select thermographic luminophores. Crystal structure of (a) Cs_4SnBr_6, (b) $[C(NH_2)_3]_2SnBr_4$ and (c) $(C_4N_2H_{14}I)_4SnI_6$ and their corresponding absorption (Kubelka-Munk transformed spectrum), PL, and PLE spectra.

Optical properties of low-dimensional tin-halides. Although diverse in their compositions, structures and syntheses, all present materials are qualitatively unified by their broadband and highly Stokes-shifted PL. Their optical absorption behavior was determined through the measurement of both PL excitation (PLE) and absorption via the application of the Kubelka-Munk (K-M) transformation to diffuse reflectance spectra (Figure 3.2d-f). The absorption of 0D tin-halides, Cs_4SnBr_6 and $(C_4N_2H_{14}I)_4SnI_6$, appears as molecular-like bands that coincide with the PLE spectra. Additionally, both materials exhibit absorption features at shorter wavelengths that do not contribute to emission (Figure 3.2d,f). This differs from the 1D compound, $[C(NH_2)_3]_2SnBr_4$, which instead exhibits a continuous PLE spectrum (Figure 3.2e). Such behavior can be associated with the partial band dispersion that occurs along the polyhedral chain in 1D metal-halides[125].

These molecular-like characteristics of the absorption spectra of low-dimensional compounds are reflected in their emission. Unlike $CsSnBr_3$ (a 3D perovskite semiconductor) that exhibits weakly Stokes shifted and narrow PL (as a result of excitonic-recombination) with very low PLQY[238, 276], Cs_4SnBr_6 shows RT, green broadband PL centered at 535 nm, with a FWHM of 120 nm, and a QY of about 20% (Figure 3.2b,

Table 3.1). Such broadband and highly Stokes shifted emission has been observed for other low-dimensional metal-halide compounds such as $[C(NH_2)_3]_2SnBr_4$, $(C_4N_2H_{14}Br)_4SnBr_6$, and $(C_4N_2H_{14}I)_4SnI_6$, and is commonly associated with STE recombination (Figure 3.2b,d,f and Figure 8.18)[125, 137, 217, 272]. Recent studies [125, 161, 217] have considered low-dimensional tin-halides as promising down-conversion phosphors for solid-state-lighting. Herein, we focus rather on the existence and practical utility of thermally activated and sensitive non-radiative relaxation pathways in these materials. Furthermore, we see that the temperature ranges, at which these pathways appear, are material specific. These two findings will assist other researchers striving to optimize these materials for lighting-based applications.

Table 3.1. Structural and optical characteristics of tin-halide thermographic luminophores.

Composition	*Space group*	Structure	Abs. max		**Em. Max**		Em. FWHM		**Stokes shift**	QY (RT)	Temp. range
			nm	**eV**	nm	**eV**	nm	**eV**	**eV**	%	°C
$[C(NH_2)_3]_2SnBr_4$	*Pna*2_1	1D	350	**3.55**	555	**2.24**	125	**0.5**	**1.31**	2	[-100, -30]
Cs_4SnBr_6	*R*-3*c*	0D	345	**3.6**	535	**2.32**	120	**0.51**	**1.28**	20	[-30, 40]
$(C_4N_2H_{14}I)_4SnI_6$	*P*-1(#2)	0D	400	**3.11**	630	**2.0**	125	**0.4**	**1.14**	75	[40, 110]
$(C_4N_2H_{14}I)_4SnBr_6$	*P*-1(#2)	0D	335	**3.71**	575	**2.18**	107	**0.4**	**1.54**	~100	N/A

The materials typically used in remote thermometry are either rare-earth-doped or transition-metal-doped phosphors exhibiting intracenter dopant emission[252, 256, 258] or transition metal oxides with STE based emission[277]. As a result of thermal de-trapping, the emission from

thermographic luminophores is generally mono-exponential and strongly dependent on the material's temperature; the typical relaxation time for this process is in the range of µs to ms. With the low-dimensional tin-halides, presented here, we have also found the emission lifetime strongly temperature-sensitive, and we associate this with STE de-trapping. The corresponding energy diagram in Figure 3.3a depicts this process: upon photon absorption (1), an electron is promoted to an excited state and, after its thermalization (2), is trapped (3) in a long-lived STE state. This trapping is then followed by a radiative recombination with broadband emission (4). A thermally assisted de-trapping pathway (5), followed by fast non-radiative recombination, is also present and plays a key role in the temperature-dependence of the PL characteristics. During de-trapping, a distorted lattice around a STE can be returned back to its original state through exciton-phonon coupling. Thus higher temperatures facilitate de-trapping and assist relaxation via a fast non-radiative channel. In agreement with this mechanism, a strong thermally-driven acceleration of the PL lifetime is observed (measured with time-resolved PL, TRPL, Figure 3.3b-d). Furthermore, the PL intensity scales with the change in PL lifetime (Figure 8.19), and its change is fully reversible with temperature (Figure 8.20).

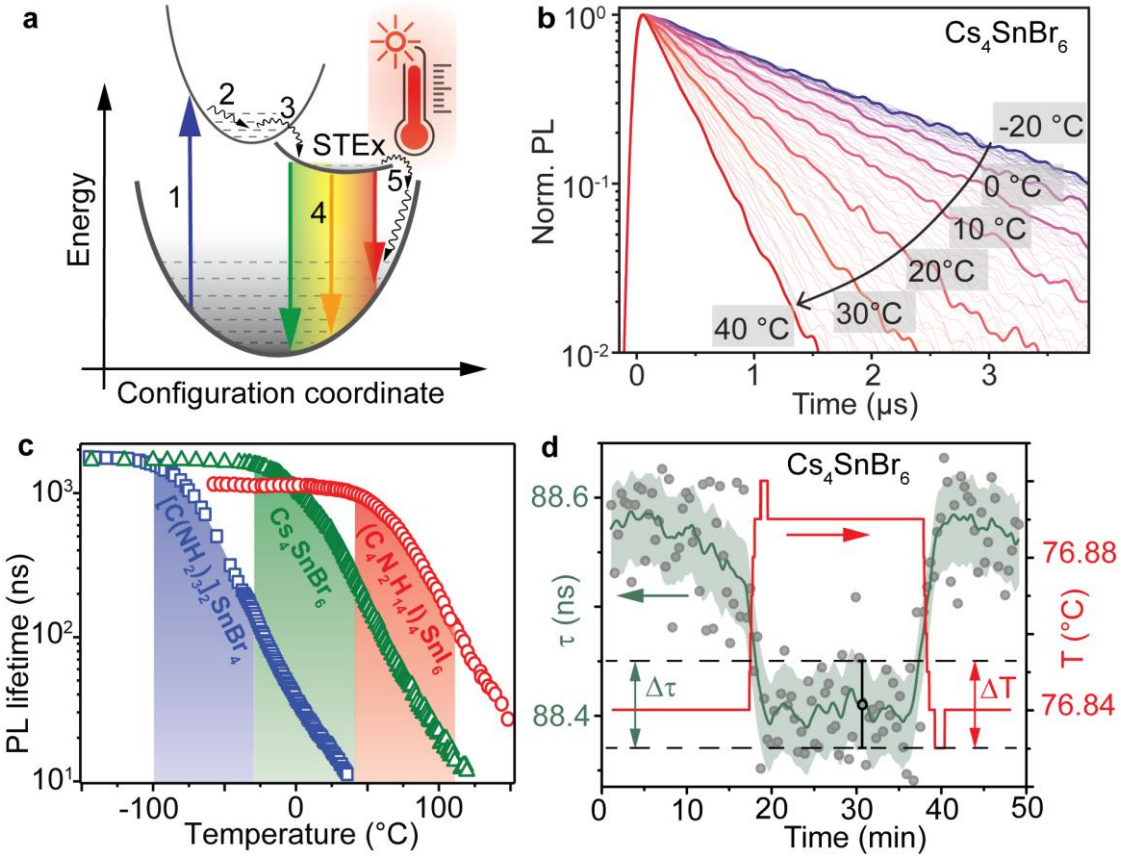

Figure 3.3. Thermal effects on PL lifetime variation of self-trapped excitonic (STE) emission in low-dimensional tin-halides. (a) Energy diagram depicting the STE processes: 1 - photon absorption, 2 -

thermalization, 3 - trapping, 4 - radiative recombination, 5 -thermally-assisted de-trapping followed by non-radiative recombination. (b) Temperature evolution of TRPL traces for Cs_4SnBr_6 excited at 355 nm. (c) PL lifetime temperature dependence for $[C(NH_2)_3]_2SnBr_4$ (blue curve), Cs_4SnBr_6 (green curve), $(C_4N_2H_{14}I)_4SnI_6$ (red curve). (d) The response of PL lifetime to a controlled temperature step of 0.05 °C. Repeated measurements yield a PL lifetime and temperature standard deviation of ±0.04 ns and ±0.013 °C, respectively.

The absolute PL QYs within the thermal sensitivity range vary between *ca*. 100 % at temperatures below -40 °C to less than 1% at temperatures above 100 °C. Aside from the high sensitivity of such STE-based emitters, other aspects also prove useful for thermometric or thermographic applications. These include the independence of PL lifetime from excitation intensity (Figure 3.4) and the fact that the PL lifetime is the same throughout the whole emission band (Figure 3.5).

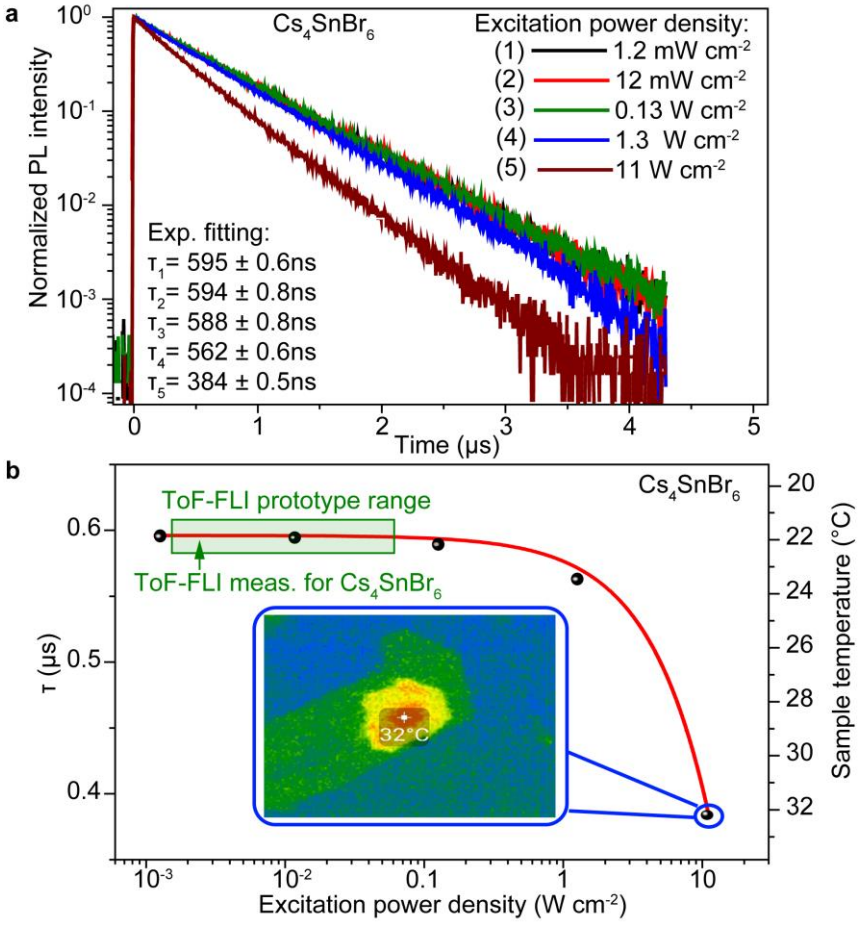

Figure 3.4. Excitation induced heating effects (a) Time-resolved PL traces for Cs_4SnBr_6 at different excitation power densities. (b) Corresponding lifetime values. Inset shows a thermogram captured with a bolometric camera depicting the excitation-induced heating effect for a sample under 11 W cm^{-2} laser excitation. The green arrow depicts the level of excitation power density used in the measurements shown in Figure 3.3d, Figure 3.11, and Supplementary Videos 1,2; the green rectangle shows the intensity range for the ToF-FLI setup.

The independence of the lifetime on excitation power (up to nearly 0.1 W cm^{-1} power density) demonstrates that these materials may be potentially applicable as thermographic luminophores with a wide assortment of measurement instrumentation. Furthermore, the lifetime deviation at higher excitation densities can be traced back to sample heating (Figure 3.4b). This indeed agrees with previous reports that such materials emit through transient STE states rather than permanent defects.[118, 273]

The independence of the PL lifetime on emission wavelength is not only a useful feature in an application as it could provide flexibility in the measurement itself, but it also suggests that the previous report[273] was correct in proposing one STE state responsible for the observed broadband emission (Figure 3.5). It should be noted that the observed variation in lifetime is most likely the result of thermal fluctuations.

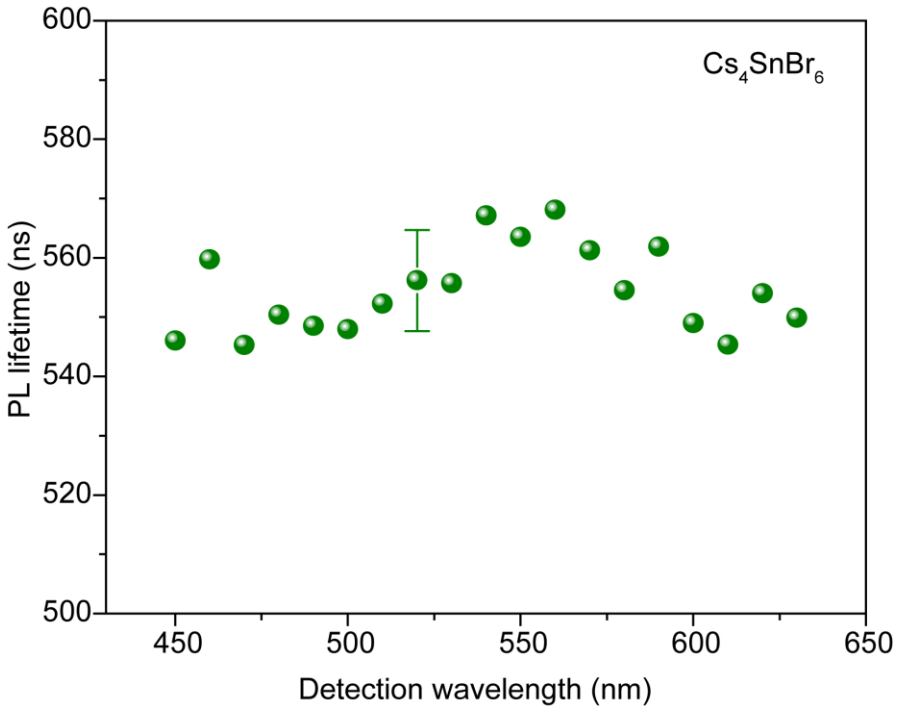

Figure 3.5. Spectrally resolved PL emission lifetimes for Cs_4SnBr_6.

In addition, the PL lifetime is also independent of the material's environment (freestanding or immersed within a polymer matrix, Figure 8.21), and it is highly reproducible from batch-to-batch (Figure 8.22) despite differences in the degree of crystallinity and purity. Even more impressively, the lifetime remains unchanged after partial oxidation (Figure 3.6). This suggests that the origin of the temperature-dependence is not related to the freezing-out of defect or trap states, but rather a phonon-assisted de-trapping process that is followed by fast non-radiative relaxation. This set of PL characteristics is clearly advantageous over semiconductive metal-

halides with delocalized electronic structures (2D, 3D-compounds), wherein the PL decay is a complex function of the density, types, and depths of defect states, as well as the electronic doping level, the state of the surface, and size-quantization. As a result, there is often high batch-to-batch variability, even within similar synthetic methods.

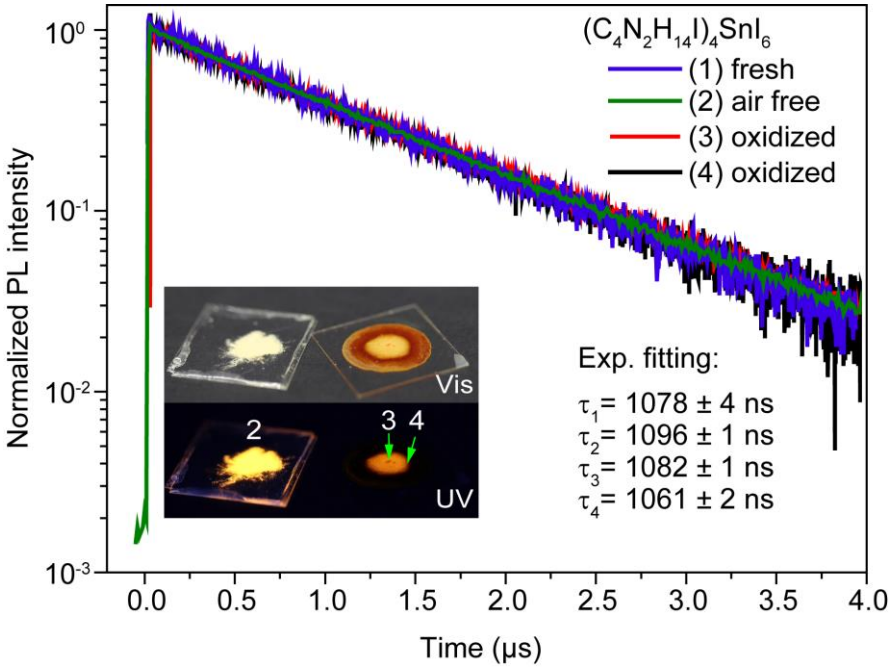

Figure 3.6. Invariance of PL lifetime of $(C_4N_2H_{14}I)_4SnI_6$ on oxidation and long-term (about 1-year) storage. Inset shows the corresponding non-oxidized (2) and oxidized (various levels of oxidation with point 3 having less and point 4 having more) samples under ambient and UV illumination. Trace 1 depicts the PL lifetime from the as-synthesized $(C_4N_2H_{14}I)_4SnI_6$ sample. Measured lifetimes vary mostly as a result of RT fluctuation.

Such behavior of the STE emission, in terms of PL lifetime and PL QY, is not unique to Cs_4SnBr_6, but is also shared by the other tested 0D and 1D metal-halides (Figure 3.3c). Due to the phonon-assisted thermal effect, the temperature range for thermal sensing can be compositionally and/or structurally engineered to either higher or lower temperatures than in the case of Cs_4SnBr_6. In the temperature range from -200 °C to 110 °C, $[C(NH_2)_3]_2SnBr_4$ begins to exhibit PL lifetime acceleration at the lowest temperatures, with a sensitivity range of -100 to -30 °C; Cs_4SnBr_6 has a sensitivity range from -30 °C to 40 °C, whereas $(C_4N_2H_{14}I)_4SnI_6$ exhibits sensitivity from 40 °C up to 110 °C (these ranges are shown as colored areas in Figure 3.3c). While $(C_4N_2H_{14}Br)_4SnBr_6$ also exhibits broadband STE emission, our measurement setup was not able to reach the thermally sensitive range. This suggests that this range lies at much higher temperatures (Figure 8.23), and the use of this material as a thermographic luminophore would be rather limited by its thermal stability.

Highly reproducible variation of the PL lifetime, by several orders of magnitude (*e.g.* 2 orders over a 100 °C range for Cs_4SnBr_6), makes these metal-halides potent luminophores with high thermometric precision. To assess the practically achievable resolution for thermographic applications, we tested the variation of the PL lifetime of a single encapsulated sample of Cs_4SnBr_6 in response to a temperature step of 0.05 °C (Figure 3.3d), and we could clearly observe this temperature change and determine the thermometric precision of our method from the measured PL lifetime. Within the constant temperature range (at T = 76.84 °C), the PL lifetime was found to have a standard deviation of 0.04 ns over 51 measurements, and was confirmed by repeating the whole experiment 2 times; this yields a high thermometric precision of 0.013 °C, which is several times better than previous estimates for fluorescent lifetime thermography[261].

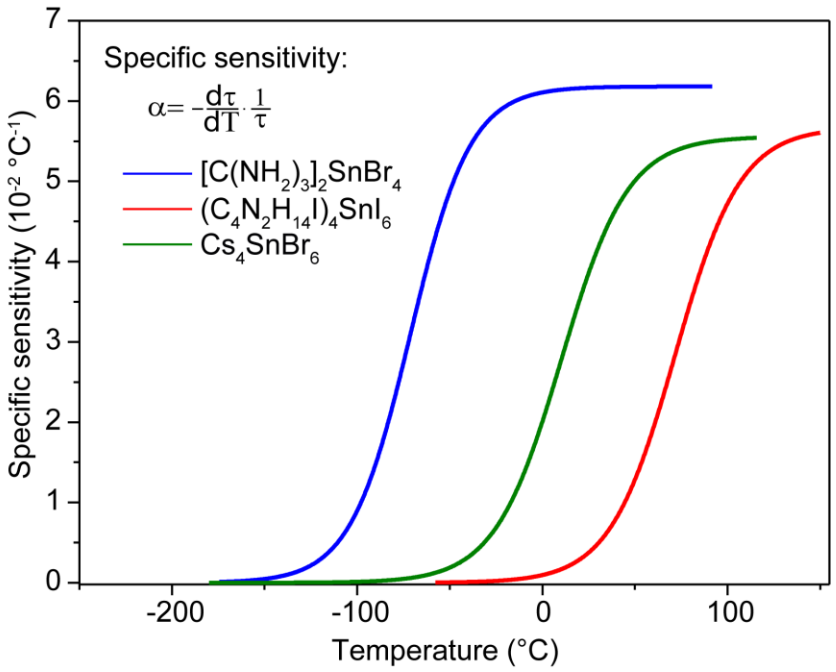

Figure 3.7. Specific sensitivity. The dependence of specific sensitivity on temperature for $[C(NH_2)_3]_2SnBr_4$ (blue), Cs_4SnBr_6 (green), $(C_4N_2H_{14}I)_4SnI_6$ (red).

Furthermore, an additional FOM for thermographic luminophores is the specific sensitivity, $\alpha = \frac{1}{\tau}\frac{d\tau}{dT}$, which in the case of low-dimensional tin-halides reaches values of 0.06 $°C^{-1}$ (**Figure 3.7**). This is among the highest reported values for thermographic luminophores[278]. Higher resolutions have been demonstrated, but only for a specific case where operation was limited to a narrow temperature range around a phase transition. Further work is needed to shed light into the physics of the STE emission of these metal-halide luminophores. Herein, we have applied several models to fit the experimental temperature-dependencies of PL lifetime (Figure 8.24-Figure 8.26; Table 8.19-Table 8.21). Although they all provide a satisfactory fit, each has difficulties providing

physically meaningful fitting parameters. For instance, the Mott model, commonly used for thermal luminophores[251], results in rather unphysical values for the activation temperature/energy, whereas the exciton-phonon scattering model[279] suggests the participation of up to 13 phonons per single de-trapping event.

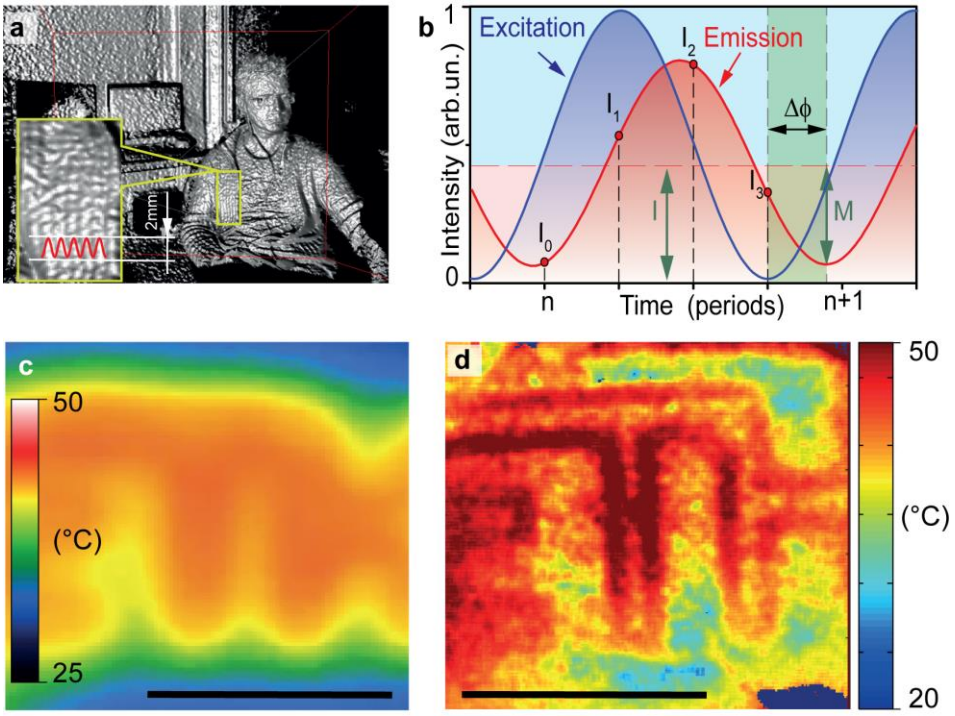

Figure 3.8. Demonstration of the principles for remote thermography based on ToF sensors. (a) 3D depth image acquired with a commercial ToF camera showing a depth resolution of 2 mm in the inset. This is equivalent to a precision of about 10 ps in the time-domain. (b) Recalculation of phase-locked intensities to a phase-shift in the frequency domain. (c) Thermographic image of a sample that consists of encapsulated Cs_4SnBr_6 powder placed between patterned ITO and a glass coverslip, and then acquired with a commercial LWIR bolometry camera equipped with a ZnSe lensed macro-objective. The image was taken as a current passed through the ITO resulting in resistive heating. (d) ToF-FLI thermogram of the same sample under the same heating conditions from (c). Scale bars in (c) and (d) are 3 mm.

Time-of-flight thermography using low-dimensional tin-halides. Although several time-resolved measurement techniques like PL decay trace-measurements, TCSPC (Figure 3.3b-d) or phase fluorometry (frequency domain time-resolved fluorescence) could be used to precisely measure the PL-lifetime of these materials, all of these have traditionally been limited by the fact that they only use a single channel detector[280]. Consequently, lengthy acquisition through point-by-point scanning is required, and this severely limits the thermographic image capture rate.

As a solution to this problem, we adopted the use of ToF-FLI[262-263] – a frequency domain time-resolved technique that can be used to acquire a 2D map of PL-lifetimes[281] – and combined

it with thermally sensitive luminophores. ToF-FLI is thus used for thermographic imaging. This approach offers both the rapid acquisition speed and the excellent depth precision of ToF detectors such as those found in consumer electronics (*e.g.* the Kinect 2.0), which we confirmed to be several mm at a distance of about 2 m (inset to Figure 3.8a; Figure 8.27)[282].

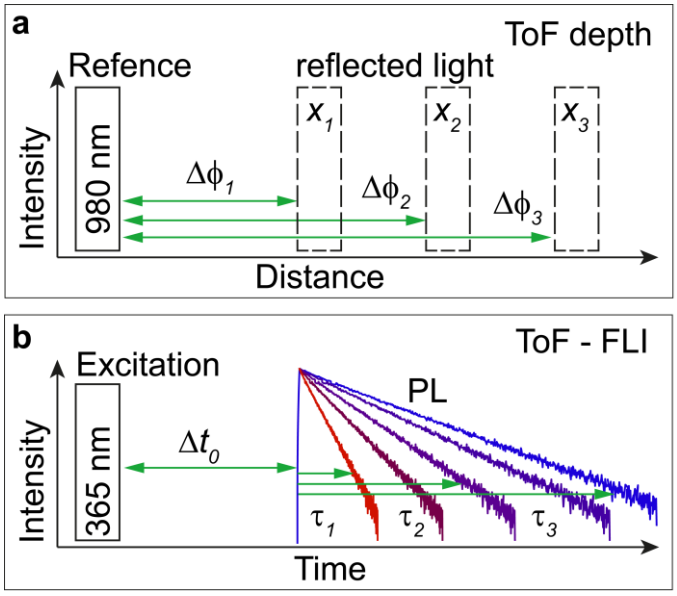

Figure 3.9. Scheme describing optical ToF measurements. (a) The estimation of distance *x* by the measured phase shift *Δϕ*. (b) Similar ToF hardware principles apply to the estimation of PL decay.

By converting this depth variation into an equivalent delay time (Figure 3.9), we find that such a technique could have a precision in the range of tens-to-hundreds of picoseconds, and this suggested that lifetime precisions approaching those of conventional TCSPC methods were possible. Furthermore, this level of precision is achieved in real-time with video recording. Briefly, the working principle for such a ToF-FLI image sensor is based on the acquisition of four, phase-locked images at 0°, 90°, 180° and 270° phase differences with respect to the excitation signal (I_0, I_1, I_2 and I_3 on Figure 3.8b) followed by the recalculation of the average intensity I, modulation depth M and phase delay, $\Delta\phi$.

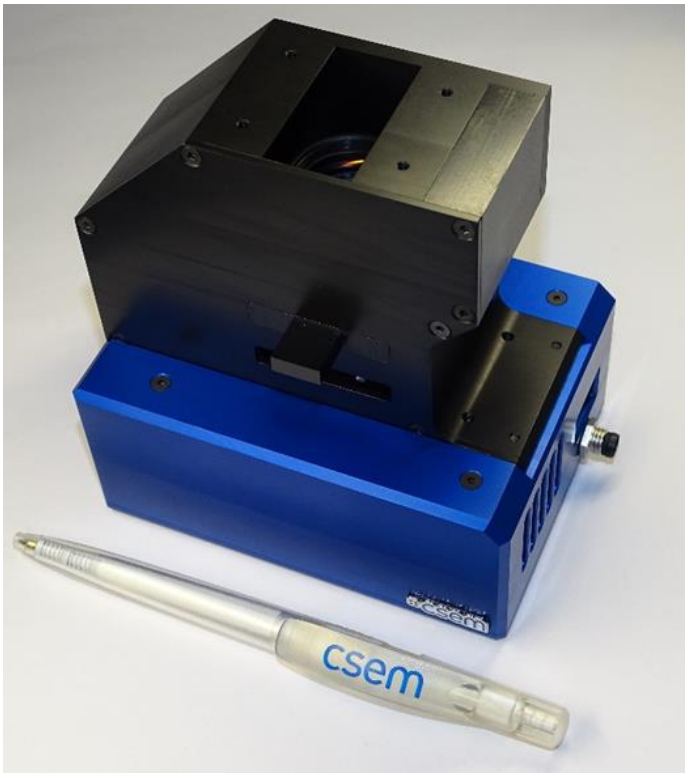

Figure 3.10. Compact stand-alone ToF-FLI prototype developed by CSEM (Switzerland) for real-time, wide-field fluorescence lifetime imaging in the nano- to micro-second range. Detailed description of image sensor architecture can be found in Ref. [283]

To demonstrate the concept of affordable ToF-FLI thermography with low-dimensional tin-halides, we used a compact, stand-alone prototype developed by some of the co-authors from CSEM (Switzerland), in which all the necessary hardware components for wide-field frequency-domain FLI were incorporated (Figure 3.10, Note 8.1). As a test of the thermographic performance of our system, we deposited a Cs_4SnBr_6 powder over a resistively heated pattern and enclosed the material with a glass coverslip, and then measured the resulting lifetime image of the heated pattern. Compared to a conventional bolometric thermogram (Figure 3.8c,d), the ToF-FLI method showed a much higher lateral thermographic resolution. The blurring observed in the bolometric thermogram of the sample is mostly due to absorption by the coverslip in the mid- to far-IR range (compare Figure 3.8c with the bolometric thermogram of the uncovered ITO pattern during heating in Figure 8.28). These absorption effects highlight a major obstacle, *i.e*. absorption of thermal emission by glass and similar media, which prevent the combination of bolometric thermography with conventional optical systems that utilize glass or quartz elements.

While a still image demonstrates the ability of this system to precisely measure a 2D map of PL-lifetime, observing dynamic processes requires the ability to record video and to measure at sufficiently high rates. To demonstrate the potential of our ToF-FLI prototype – whose sensor can

record with a rate of up to 100 frames per second – for thermographic video acquisition, we recorded a video of the thermal response of a $(C_4N_2H_{14}I)_4SnI_6$ powder through 1 mm of a glass substrate to the brief contact of a soldering pin (temperature at the apex was approx. 120 °C; ToF-FLI specifications in Note 8.1; Supplementary Video 1 available from Ref. [284]). Indeed, it was possible to observe the dynamic temperature changes that occurred as well as the heat transfer through and along the substrate - a challenge for pixel-by-pixel scanning technologies. To furthermore benchmark our approach, we analyzed the pixel-to-pixel variation in a single frame taken from Supplementary Video 2 (available from Ref. [284]), where a homogenous temperature source (32.5 °C) was applied over the entire area of a single encapsulated sample of Cs_4SnBr_6 sample (Figure 3.11).

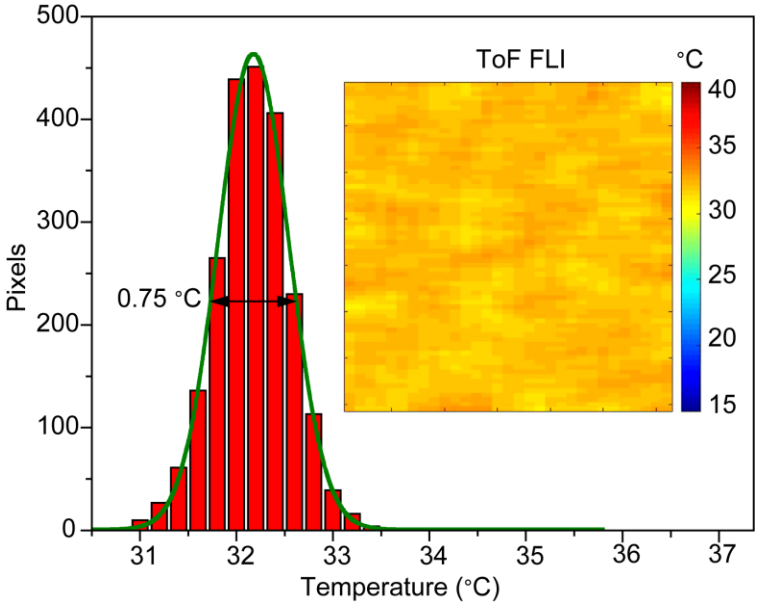

Figure 3.11. Histogram of pixel-to-pixel temperature variation in a still image (shown in the inset) taken from a ToF-FLI thermographic video recorded for a homogenously heated sample of Cs_4SnBr_6. The evaluated image area contains roughly 2200 pixels.

From the pixel vs. temperature histogram, a FWHM of 0.75 °C was obtained from an area of over 2000 pixels.

3.5. Conclusion

In summary, we discovered that the de-trapping process of STEs in low-dimensional tin-halides exhibits extreme thermal sensitivity over a compositionally tunable range of temperatures. In particular, such emission is characterized by monoexponential decays with a steep dependence of PL lifetime on temperature (up to 20 ns $°C^{-1}$). We then applied these features to high-precision thermometric measurements over a wide temperature range (-100 °C to 110 °C), and furthermore demonstrated an approach to remote optical thermography by combining these low-dimensional tin-halide luminophores with ToF-FLI. By doing so, we have succeeded in achieving low-cost, precise, and high-speed PL-lifetime thermographic imaging which approaches that of commercial IR bolometric cameras operating at RT.

Chapter 4. The $Rb_7Bi_{3-3x}Sb_{3x}Cl_{16}$ family: A Fully Inorganic Solid Solution with Room-Temperature Luminescent Members

Figures and excerpts reprinted with permission from Bogdan M. Benin, Kyle M. McCall, Michael Wörle, Viktoriia Morad, Marcel Aebli, Sergii Yakunin, Yevhen Shynkarenko, and Maksym V. Kovalenko "The $Rb_7Bi_{3-3x}Sb_{3x}Cl_{16}$ family: A Fully Inorganic Solid Solution with Room-Temperature Luminescent Members", *Angew. Chem. Int. Ed.*, **2020**, *59*, 2-10; *Angew. Chem.*, **2020**, 132, 2-10. Copyright 2020 Wiley-VCH Verlag GmbH & Co. KGaA.

4.1. Abstract

Low-dimensional ns^2-metal halide compounds have recently received immense attention for applications in solid-state lighting, optical thermometry and thermography, and scintillation. However, these are based primarily on the combination of organic cations with toxic Pb^{2+} or unstable Sn^{2+}, and a stable inorganic luminescent material has yet to be found. Herein we present the 0D $Rb_7Sb_3Cl_{16}$ phase, which is comprised of isolated $[SbCl_6]^{3-}$ octahedra and edge-sharing $[Sb_2Cl_{10}]^{4-}$ dimers and demonstrates RT PL centered at 560 nm with a PLQY of 3.8±0.2% at 296 K (99.4% at 77 K). The temperature dependent PL lifetime of this material rivals that of previous low-dimensional materials with a specific temperature sensitivity above $0.06\ K^{-1}$ at RT, showcasing it as an excellent thermometric material. Utilizing both density-functional theory (DFT) and chemical substitution with Bi^{3+} in the $Rb_7Bi_{3-3x}Sb_{3x}Cl_{16}$ ($x \leq 1$) family, we present the edge-shared $[Sb_2Cl_{10}]^{4-}$ dimer as a design principle for antimony-based luminescent materials discovery.

4.2. Introduction

Low-dimensional metal-halide semiconductors, especially their 0D counterparts,[168, 170, 217] exhibit vastly different properties as compared to the 3D metal-halide perovskites.[53, 218-219] While 3D metal-halide perovskites have advanced the field of optoelectronics with significant improvements in full-color imaging,[34] photodetection,[36, 220] X-ray imaging,[221] hard-radiation detection,[33, 41] solar cells,[25-26] and light-emitting diodes,[38] in part due to their defect-tolerant photophysics and charge transport properties,[59, 222-223] their low-dimensional counterparts have found their niche in complementary fields such as solid-state lighting,[161, 285] scintillation,[172] and remote optical thermometry (ROT) and thermography.[284] ROT and thermography are critical methods in several fields ranging from the diagnosis of technical failures to medical diagnostics in which thermal fluctuations or temperature deviations must be precisely identified.[244, 246]

Many previous examples of luminescent 0D materials have focused on tetrel group metals (*i.e.* Pb^{2+}, Sn^{2+}, and Ge^{2+}).[124, 161, 172, 273] Of these, materials containing Sn^{2+} octahedra and disphenoids have been demonstrated to have RT PLQYs of up to 20% in fully inorganic cases[273] and above 80% in hybrid organic-inorganic ones.[172, 286] Regardless of their performance, these materials are still hindered by their oxidative instability, which necessitates post-processing to shield them from the environment. This challenge is exacerbated for finely dispersed forms of these materials; for example, Cs_4SnBr_6 NCs are stable for only several hours before significant degradation is observed.[178]

Further progress in the field of 0D optoelectronics requires the discovery of oxidatively stable and thermally robust phosphors that exhibit either of the two most useful features of their tetrel counterparts: high RT PL from the relaxation of self-trapped excitons (STEs) for solid-state lighting, or temperature-dependent lifetimes for ROT. The closest ns^2-analogue to the tetrel-STE emitters are the trivalent pnictogens (*e.g.* Sb^{3+} and Bi^{3+}).[287] While several hybrid organic-inorganic low-dimensional pnictogen-halide phases are known,[234] their fully inorganic counterparts, such as the $A_3B_2X_9$ (A = Rb, Cs; X = Cl, Br, I) family of compounds and the $A_2B^IB^{III}X_6$ (A = Rb, Cs; B^I = Na, Ag; B^{III} = Sb, Bi; X = Cl) double perovskites exhibit either no, or very inefficient, RT PL.[69, 118-119, 177, 288]

It was found that Sb^{3+}-doped and Bi^{3+}-doped structures are photoluminescent at RT, and that these are efficient STE emitters.[74, 289-290] This is true despite the higher structural dimensionality of many of these materials, as the doping provides isolated environments for the Sb^{3+} and Bi^{3+} centers, effectively reducing the electronic dimensionality to 0D.[291] We posited that 0D structures with isolated ns^2 centers, as observed in the hybrid organic-inorganic perovskites based on Sb^{3+},[234] would be the most effective fully inorganic solid-state emitters. We thus sought to replicate such a 0D environment through dimensional reduction of the pnictogen halide family through the exploration of alkali-halide-rich structures.

Herein we present the synthesis, structural tunability, and characterization of several new low-dimensional pnictogen chlorides of the $Rb_7Bi_{3x}Sb_{3-3x}Cl_{16}$ family that exhibit RT PL. These

compounds were first prepared by Wells as early as 1897,[292-293] but their structures and optical properties remained undetermined until a recent report on $Rb_7Bi_3Cl_{16}$ NCs.[174] This article suggested that these Bi-based NCs should exhibit blue PL; however, we find compelling evidence that this maybe incorrect and that these are red emissive at cryogenic temperatures and that the Sb-analogue is a oxidatively stable, yellow emissive material at RT (Figure 4.1).

4.3. Experimental details

For detailed experimental details regarding materials, synthetic procedures, and characterization techniques, see chapter 7. Materials and Methods.

Further details on the crystal structure investigation(s) may be obtained from the Fachinformationszentrum Karlsruhe, 76344 Eggenstein-Leopoldshafen, Germany (fax: (+49)7247-808-666; e-mail: crysdata@fiz-karlsruhe.de), on quoting the depository number CSD-1990675, 1990676, 1990672, 1990673, 1990674, 1990680, and 1990681.

4.4. Results and Discussion

The antimony based $Rb_7Sb_3Cl_{16}$ was synthesized solvothermally from Sb_2O_3 and RbCl in concentrated HCl at 160 °C. After holding this temperature for 24 hours, the reaction was slowly cooled to RT at a rate of 5 °C/hr. The contents of the reaction were separated by vacuum filtration to yield clear, colorless hexagonal platelets as the only product.

Single crystal X-ray diffraction at RT reveals that $Rb_7Sb_3Cl_{16}$ crystallizes in the hexagonal space group *P*-62*m*, with lattice parameters $a = b = 12.9802(4)$ Å, $c = 34.2522(11)$ Å (Figure 4.1a; Table 8.22Table 8.31), with powder X-ray diffraction confirming that the product is phase pure and structurally stable over months (Figure 8.29,Figure 8.30). This quasi-0D structure is comprised of alternating layers of isolated $[Sb_2Cl_{10}]^{4-}$ edge-shared dimers and $[SbCl_6]^{3-}$ octahedra; these layers are stacked along the *c*-axis. Intriguingly, the $[Sb_2Cl_{10}]^{4-}$ edge-sharing dimer unit is distorted with a slight bend towards one side, which might be a consequence of the lone pair of the central Sb(III) cations, as suggested by Ruck *et al.* for the similar compound, $Tl_7Bi_3I_{16}$.[294]

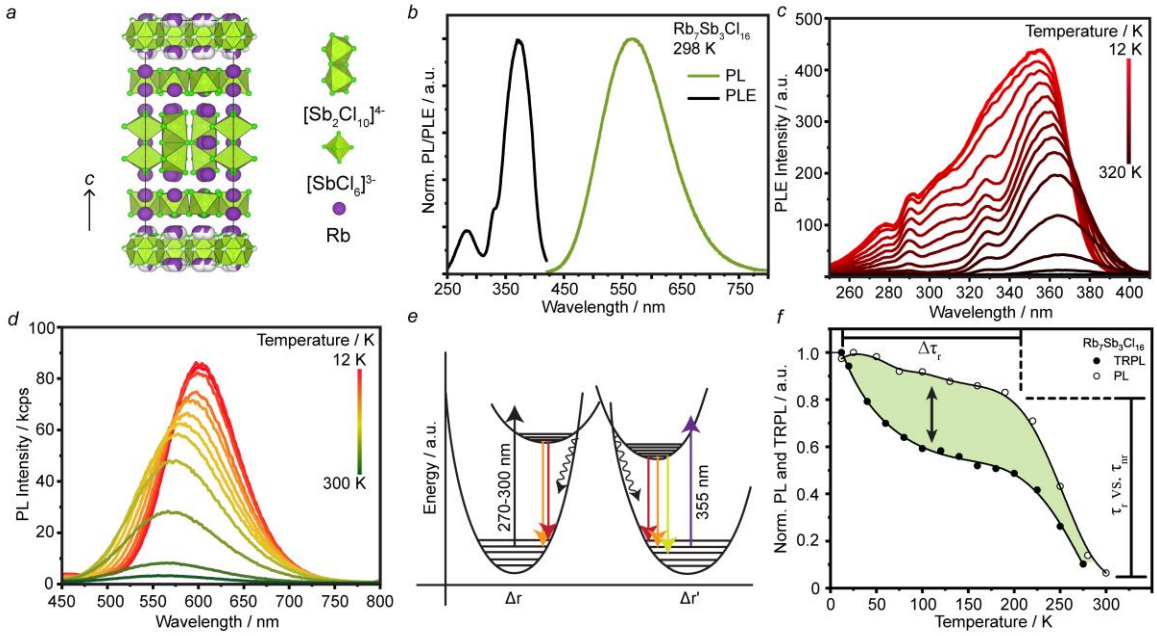

Figure 4.1. (a) The crystal structure of $Rb_7Sb_3Cl_{16}$ as viewed along the [100] axis contains $[Sb_2Cl_{10}]^{4-}$ dimers and $[SbCl_6]^{3-}$ octahedra (green with green chlorine atoms) separated by Rb^+ cations (purple). (b) RT PL and PLE spectra for $Rb_7Sb_3Cl_{16}$. (c) dT-PLE spectra of $Rb_7Sb_3Cl_{16}$ measured at the PL max for each temperature. (d) dT-PL spectra for $Rb_7Sb_3Cl_{16}$ measured at the PLE-max at each temperature. (e) The proposed CC diagram for $Rb_7Sb_3Cl_{16}$. (f) A comparison of the integrated PL intensity from subpanel (d) and the average, intensity weighted, lifetime for $Rb_7Sb_3Cl_{16}$.

Every other dimer layer exhibits 3-fold rotational disorder in the *a*-*b* plane, with equal one-third occupancy for each possible rotation providing the best structural refinement (Figure 4.2; Figure 8.31). The dimers are ordered by orienting along one of three possible orientations as demonstrated by the yellow dimer in Figure 4.2c.

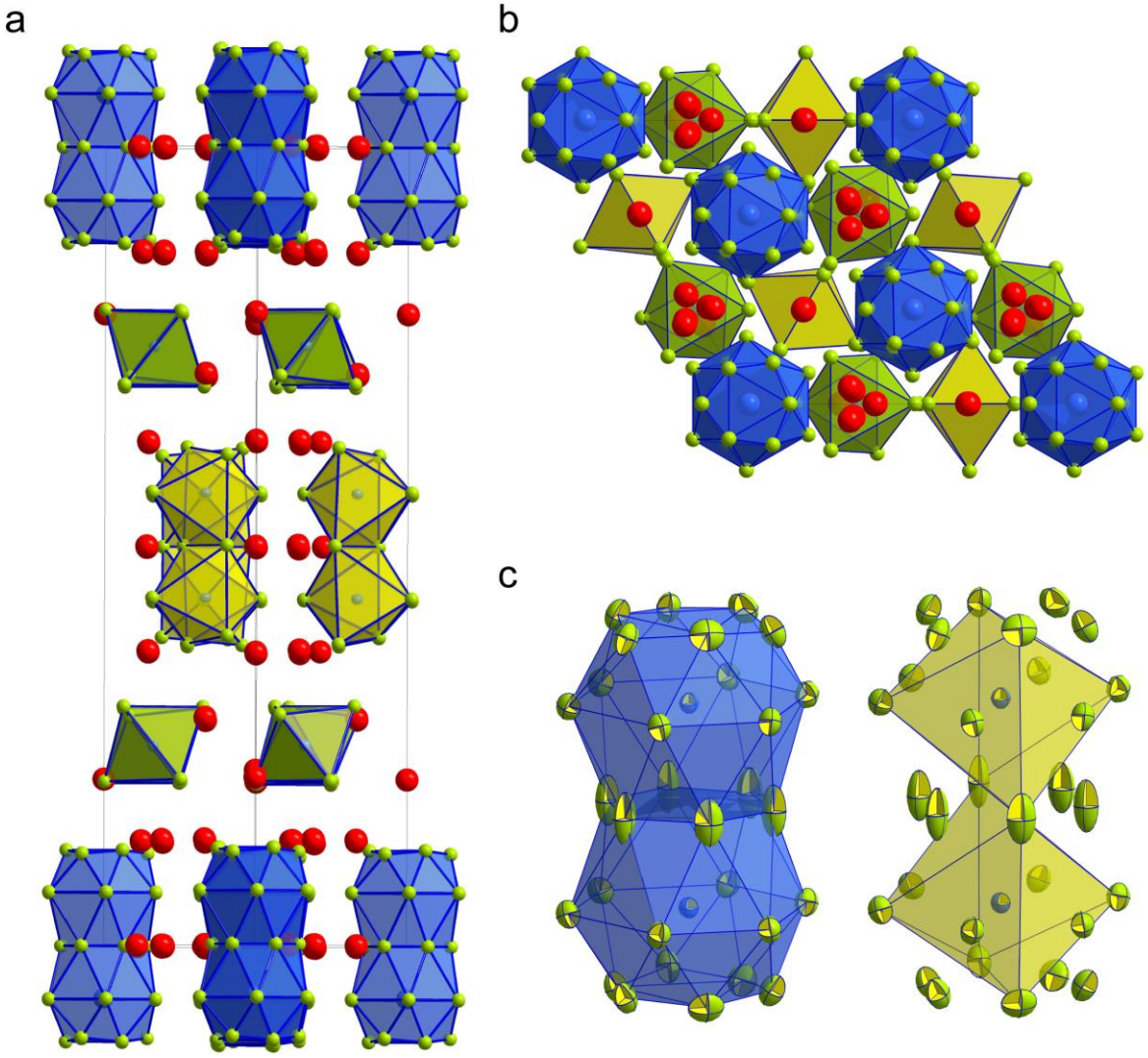

Figure 4.2. Disorder in the $Rb_7Sb_3Cl_{16}$ structure. a) The $Rb_7Sb_3Cl_{16}$ structure with color-coded ordered (yellow) and disordered (blue) units. Rubidium atoms are colored red. b) A view of the same structure down the *c*-axis depicting the three possible positions for the Rb (1/3 occupancy). c) A side-by-side comparison of the ordered and disordered $[Sb_2Cl_{10}]^{4-}$ dimers (ellipsoids indicate 50% probability).

This asymmetry in the dimer layers also affects the adjacent $[SbCl_6]^{3-}$ octahedral layers, as the thermal parameters of the neighboring Cl atoms are significantly higher than those on faces neighboring the ordered dimer layer (Figure 4.3).

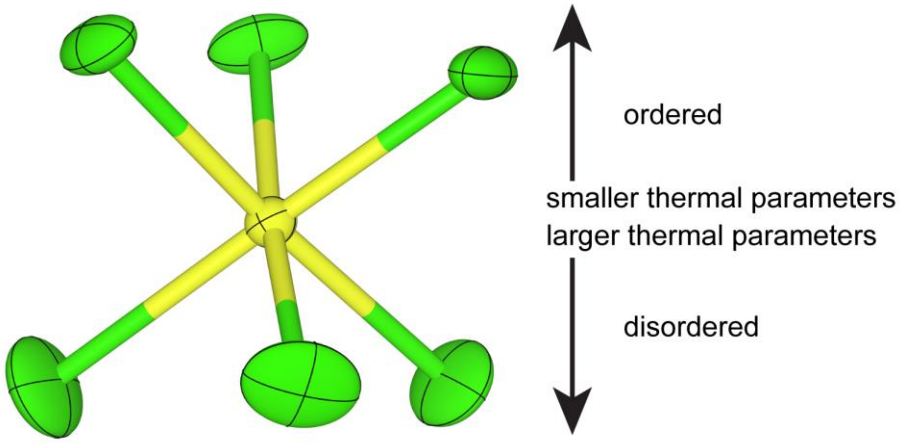

Figure 4.3. Thermal parameters of Cl atoms in the $[SbCl_6]^{3-}$ octahedra in the layer next to the disordered layer. Ellipsoids indicate 50% probability.

Interestingly, this disorder appears to be intrinsic to this compound, as cooling to 230 K or 100 K yields isostructural refinements with decreasing lattice parameters and no changes to either the rotational disorder or the unit cell ordering (Figure 8.32; Table 8.22-Table 8.31).

By obtaining single crystals of $Rb_7Sb_3Cl_{16}$, we were also able to measure an absorption coefficient of ~150 cm^{-1} for these materials (Figure 4.4; Figure 8.33). Additionally, $Rb_7Sb_3Cl_{16}$ is most likely a direct bandgap material and the bandgap was determined to be 3.27 eV (inset to Figure 4.4). We found this surprising, given the fact that the measured absorption coefficient for $Rb_7Sb_3Cl_{16}$ is only 3x higher than that of Mn(II) coordinated by iodide (~50 cm^{-1}; forbidden transition),[295] and it is several orders of magnitude smaller between 350 nm and 400 nm than that of other direct-gap semiconductors such as CdSe, InP, PbS, or $CsPbBr_3$, which range from 10^4 cm^{-1} to 10^5 cm^{-1}, respectively.[296-302] We were, however, able to reconcile these two, initially contradictory pieces of evidence by again considering the structural dimensionality of $Rb_7Sb_3Cl_{16}$. The effective structural disconnection that occurs with dimensional reduction is expected to effectively increase the dielectric constant and may result in a decreased absorption coefficient even though the material retains a direct band gap (similar to the size-dependent absorption coefficient observed in quantum dots).[300, 303-305] It is also worth noting that there have been no other reports on the absorption coefficient of such low-dimensional metal-halides even though it is critical for numerous optoelectronic applications.

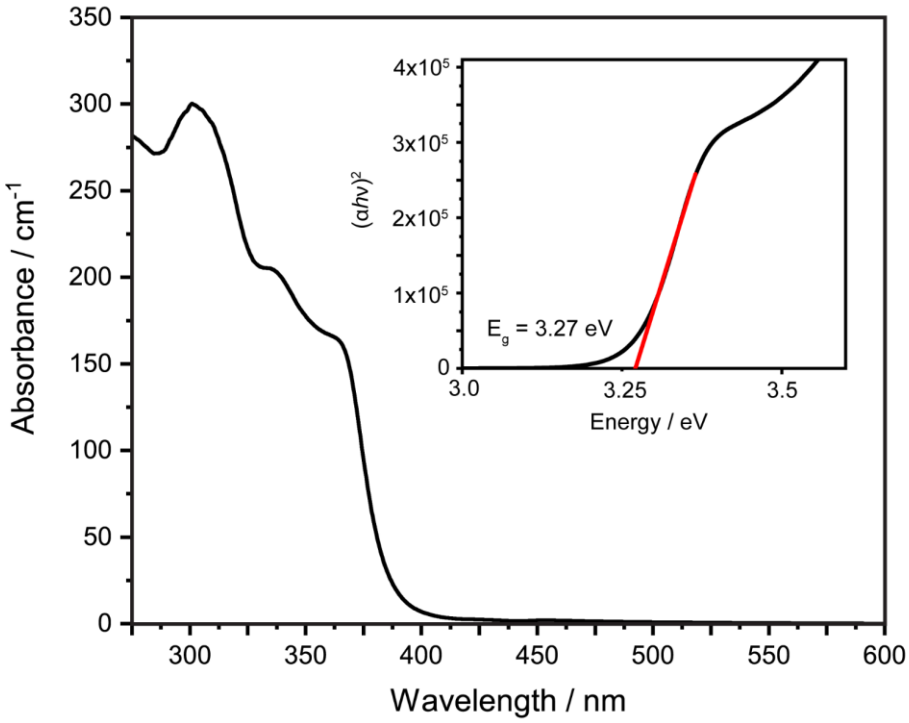

Figure 4.4. Absorption spectrum for $Rb_7Sb_3Cl_{16}$. Inset: Tauc plot for direct-gap semiconductor.

Exposing $Rb_7Sb_3Cl_{16}$ crystals to ultraviolet (UV) light at RT results in yellow PL centered at 560 nm with a FWHM of 0.53 eV, and a RT (*viz.* 296 K) PLQY of 3.8±0.2% (Figure 4.1b) and a PLQY of 99.4±0.5% at 77 K (Figure 4.5). The drastic increase in PLQY with cooling has been observed to be a general feature of such 0D materials.[284] Furthermore, the PLQY remains stable over a course of 2 months after storage under ambient conditions.

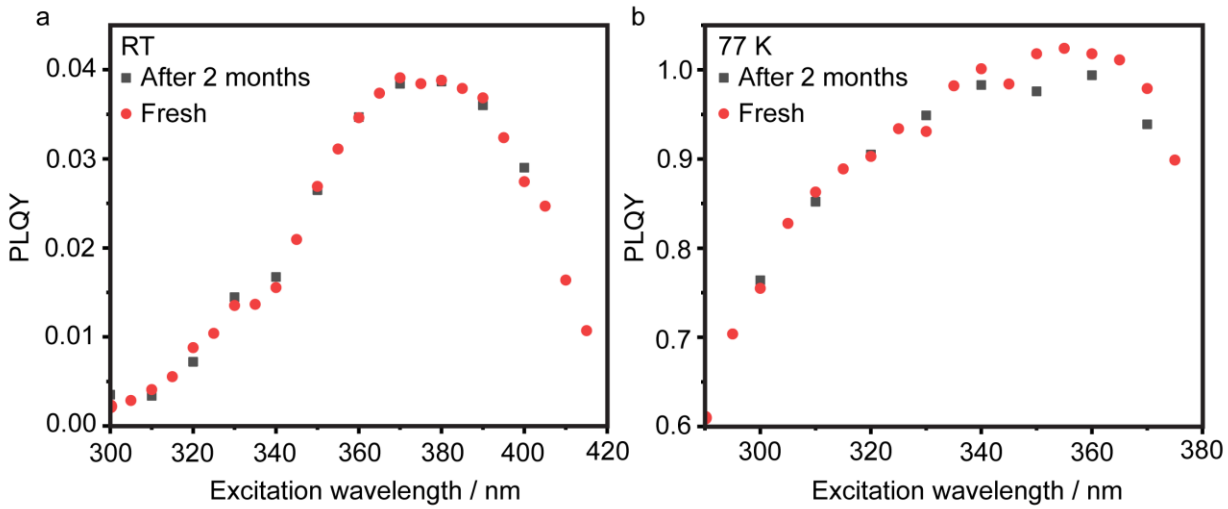

Figure 4.5. PLQY comparison at a) RT and b) 77 K.

The PLQY at both RT and 77 K follows the PL excitation (PLE) spectrum, with a molecular-like peak in the UV, which is typical for 0D STE phosphors. This UV peak in the PLE results in a large Stokes shift of 1.16 eV, which is again symptomatic of STE emission in 0D metal-halides.

To further characterize these properties and gain insight into the source of emission in $Rb_7Sb_3Cl_{16}$, we first conducted a series of steady-state spectroscopic experiments: excitation-power dependent PL (dW-PL) at RT (Figure 4.6), temperature dependent PLE (dT-PLE) and PL (dT-PL) experiments from RT down to 12 K (Figure 4.1c,d; Figure 8.34).

The RT PL and PLE shown in Fig. 1b are typical for STE-emissive 0D materials. Further evidence for this mechanism was obtained by performing power-dependent PL measurements from an average excitation power of 2 µW to 2 mW (Figure 4.6).

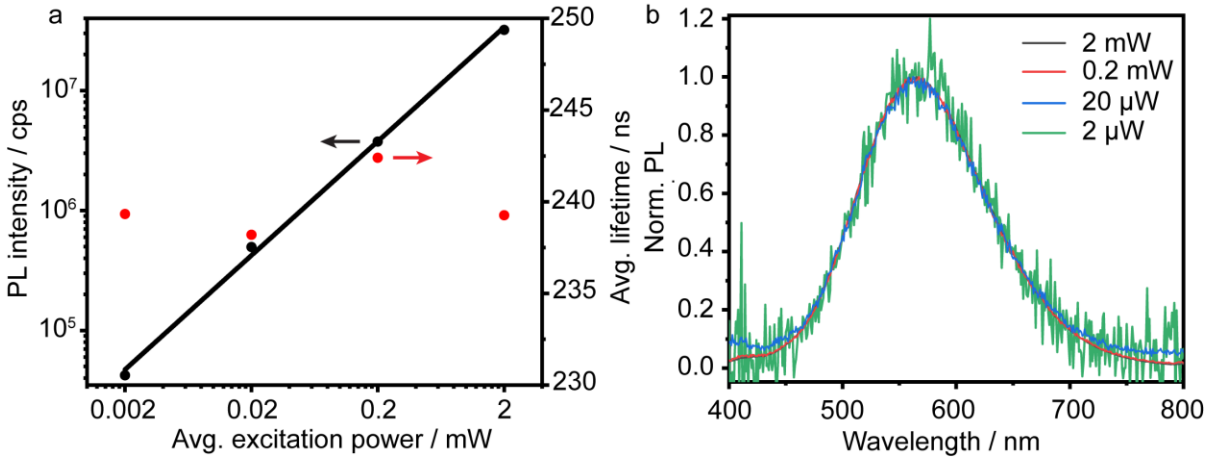

Figure 4.6. dW-PL of $Rb_7Sb_3Cl_{16}$: a) Log intensity vs. Log power, b) dW-PL spectra. The fitted line in (a) has a slope of m = 0.95 and R^2 = 0.998.

The clearly linear behavior (slope = 0.95, R^2 = 0.998) supports the STE hypothesis, as permanent defects may be saturated at sufficiently high excitation intensities.[118] This also provides a base reference for later thermometric experiments, as the excitation intensities utilized are insufficient to increase non-radiative thermal quenching and do not cause any spectral shifting. It is important to note that the deviation in PL lifetime away from a flat, horizontal line is the result of thermal fluctuations at RT.

A clear blueshift in the main excitation peak is observed in the PLE as temperature decreases, along with the appearance of several additional bands (Figure 4.1c). These additional peaks appear strongly overlapped and convoluted, but can be approximately placed at 270 nm, 290 nm, 305 nm, and 330 nm. As the temperature increases, these either disappear due to quenching or merge until only the PLE max at 365 nm is recognizable. The multiple peaks at cryogenic temperatures hint at the diversity of Sb(III) environments present within this structure, suggesting their mutual involvement in the observed spectra.

The dT-PL spectra were then measured by exciting at each of the PLE peak positions listed above as they evolved with temperature (Figure 4.1d; Figure 8.34). Excitation at the PLE max was used to measure the PL spectra in Figure 4.1d as a function of temperature. These spectra exhibit three discernable trends: PL intensity saturation below 40 K, a PL redshift with decreasing temperature, and PL broadening as temperature increases.

The integrated PL intensity of these spectra could be fit with an Arrhenius model containing two activation energies to investigate the quenching of each peak with temperature (Figure 8.35). While an exact description for these energies (<30 meV and >200 meV) cannot be given, we suggest that the large activation energy is related to thermal quenching of the STE state and the <30 meV may be the activation energy that corresponds to transfer between different triplet sates of the Sb^{3+} cation, as previously determined for $Cs_3Bi_2Cl_9$.[119]

The PL redshift with decreasing temperature occurs concomitantly with an increasing Stokes shift (1.21 eV at RT to 1.43 eV at 12 K) and maybe the result of an altered lone-pair stereoactivity.[306] This same behavior is observed in the dT-PL spectra originating from 290 nm and 330 nm excitation (Figure 8.34).

To probe these observations, the FWHM of the three sets of dT-PL spectra were fit with the Toyozawa model to determine the phonon energy associated with the observed temperature dependent broadening (Figure 4.7,Figure 4.8).

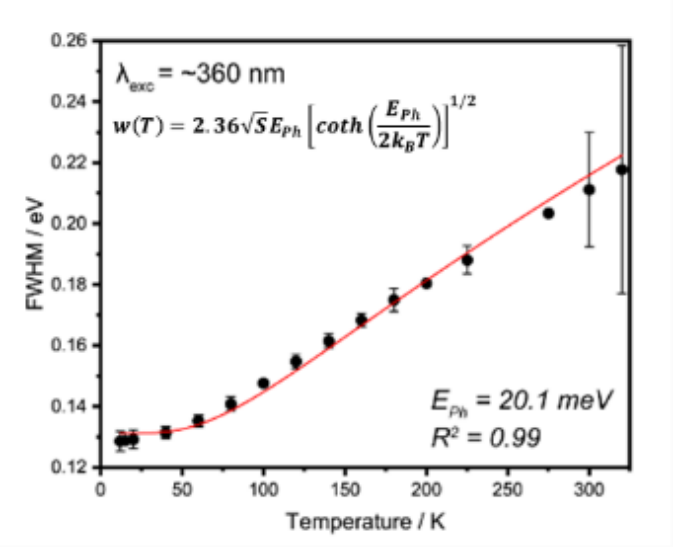

Figure 4.7. Temperature dependent broadening data from $Rb_7Sb_3Cl_{16}$ (excitation at PLE max) fitted with the Toyozawa model.

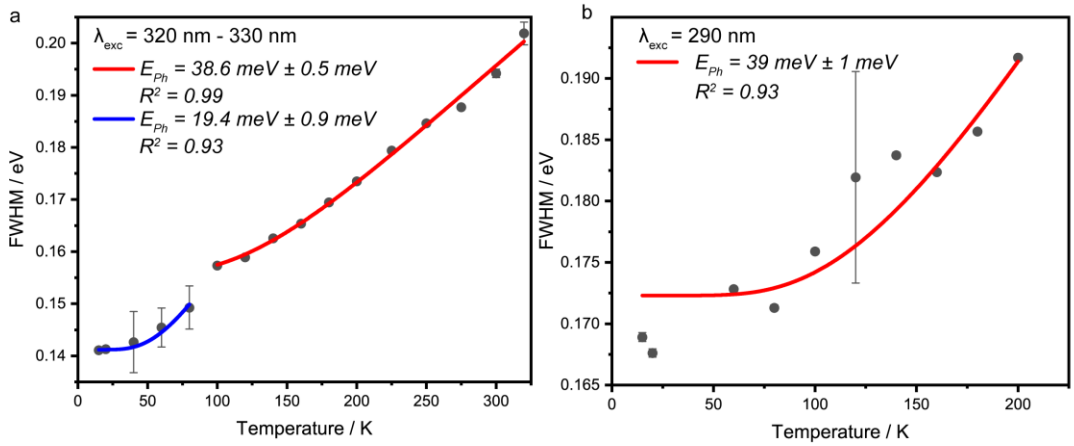

Figure 4.8. Temperature dependent broadening data from $Rb_7Sb_3Cl_{16}$ fitted with the Toyozawa model with excitation at a) 320 nm to 330 nm and at b) 290 nm.

An energy of 20.1±0.5 meV (*ca.* 165 cm^{-1}) was extracted from the broadening of the main emission peak (*ca.* 360 nm excitation). The same analysis, when applied to the dT-PL spectra at 290 nm excitation, reveals a higher effective phonon energy of 39±1 meV while the dT-PL spectra at 330 nm excitation is discontinuous and requires two phonon energies of 19.4±0.9 meV and 38.6±0.5 meV to model, suggesting the overlap of features associated with both $[Sb_2Cl_{10}]^{4-}$ dimers and $[SbCl_6]^{3-}$ octahedra (Figure 4.8). The agreement of these energies implies that there are two distinct emission features with characteristic phonon energies near 39 meV and 20 meV; however,

these effective phonon energies represent an average energy and are not always the result of a single vibrational mode. Nevertheless, they can be often correlated to the Raman spectrum of a material.

The Raman spectrum for $Rb_7Sb_3Cl_{16}$ is quite complex, as there are vibrational modes from both the octahedral and dimeric units with additional peak splitting due to the bent dimers that break the D_{2h} symmetry of a perfect dimer unit (Figure 8.36). Therefore, while a small peak at 160 cm^{-1} (19.8 meV) and the most intense peak at 306 cm^{-1} (37.9 meV) match the energies extracted from the Toyozawa fits of FWHM vs. T from the dT-PL spectra, the large number of vibrational modes precludes any definite identification of the structural origin for these features.

These observations are further corroborated by PL-PLE maps measured at 12 K, 100 K, and 200 K (Figure 4.9). At the lowest temperature, a diagonal trend in the map can be observed indicating the presence of two distinct, yet overlapped, bands. As the temperature increased, these features continued to overlap and then fade until only a single peak in the PL-PLE map could be observed. We consider that the blue-shifted and quicker-to-quench band likely originates from the octahedral $[SbCl_6]^{3-}$ units.

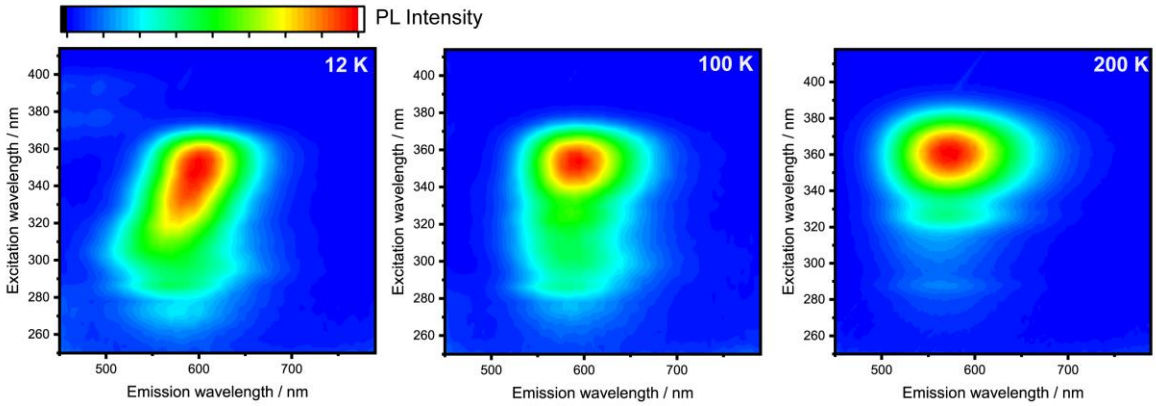

Figure 4.9. PL-PLE maps for $Rb_7Sb_3Cl_{16}$ measured at 12 K, 100 K, and 200 K.

With these observations in mind, we propose a qualitative CC diagram for $Rb_7Sb_3Cl_{16}$ (Figure 4.1e). Unlike previous models for STE-emitters, it includes two ground states and two excited states. The two separate ground states were drawn to reflect the suspected contribution of both the $[Sb_2Cl_{10}]^{4-}$ dimers and $[SbCl_6]^{3-}$ octahedra, while the separate excited states are based on the existence of two strongly overlapped emission peaks at cryogenic temperatures and indicate the STEs that may form on these isolated structural features. The wavy lines that originate from the intersection of ground and excited states represent thermally activated (phonon-assisted) quenching processes which compete with radiative recombination at temperatures near to RT.

As depicted in the CC diagram, the spectral features originating from $[Sb_2Cl_{10}]^{4-}$ dimers

and $[SbCl_6]^{3-}$ octahedra may have different lifetime-temperature behaviors. Therefore, dT-time-resolved PL (dT-TRPL) was measured from RT to 12 K (Figure 4.1f). While RT TRPL demonstrates a monoexponential trace similar to those observed in other STE emitting systems (Figure 4.10),[284] the average lifetime becomes biexponential as the temperature decreases indicating the existence of two different radiative processes. This behavior occurs concomitantly with the average lifetime becoming strongly wavelength dependent (Figure 4.10c).

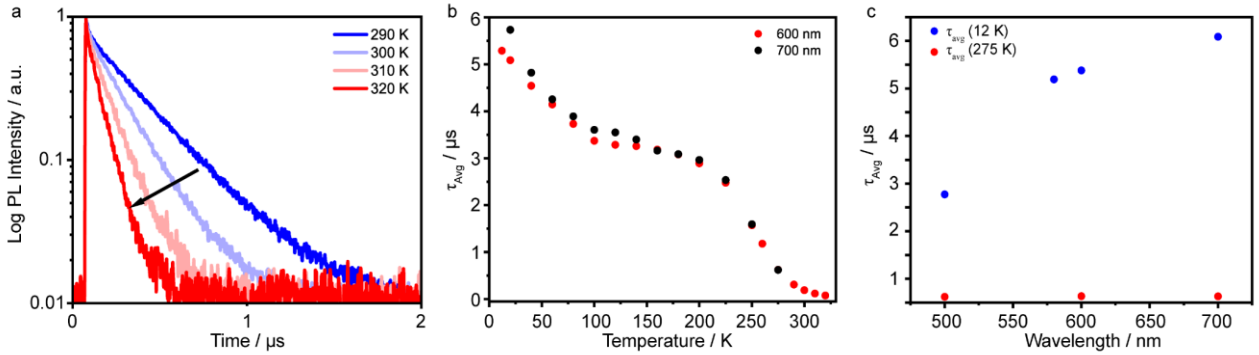

Figure 4.10. TRPL of $Rb_7Sb_3Cl_{16}$ a) TRPL of $Rb_7Sb_3Cl_{16}$ measured at various temperatures close to RT. b) Average, intensity-weighted, lifetime values for $Rb_7Sb_3Cl_{16}$ measured at two different emission wavelengths. c) Average, intensity-weighted, lifetime values for $Rb_7Sb_3Cl_{16}$ measured at different wavelengths and at different temperatures.

These two observations are similarly tied to the efficient radiative recombination of STEs at both $[SbCl_6]^{3-}$ octahedra and $[Sb_2Cl_{10}]^{4-}$ dimers at low temperatures. We investigated this observation further by performing a time-resolved emission spectroscopy (TRES) experiment (Figure 4.11). The psuedocolor 2D TRES intensity plot closely matches the RT steady state PL spectrum. Upon close inspection, a small, very fast component can be identified with very weak blueshifted PL further indicating that these are two non-interacting, monoexponential processes that have spectral overlap thus supporting the hypothesis that two emissive centers may exist except that one clearly dominates in intensity.

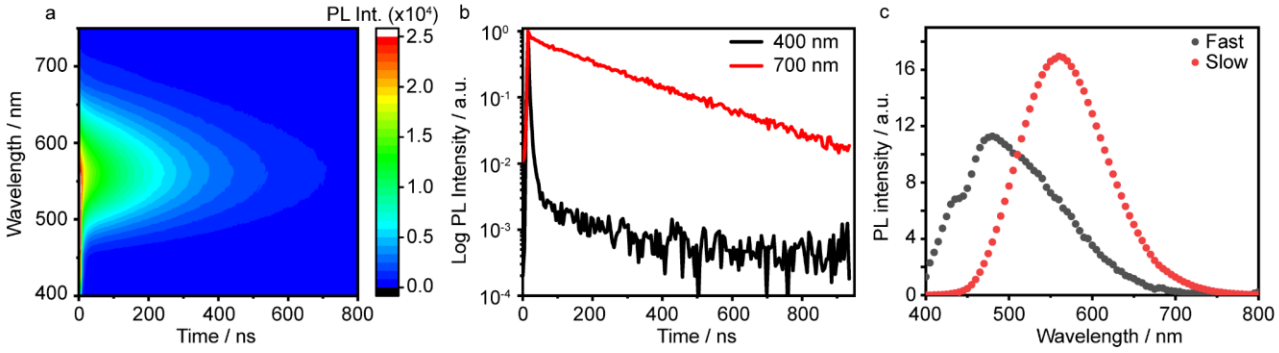

Figure 4.11. TRES for $Rb_7Sb_3Cl_{16}$: a) 2D TRES plot, c) lifetime slices at 400 nm and 700 nm,

b) spectral slices of the fast (<50 ns) and slow components from the TRES experiment.

This strong dependence of the PL lifetime on temperature has been previously demonstrated to be a general feature of other 0D and 1D Sn-halides, and showcases such materials as exceptional thermometric agents.[284] The outstanding suitability of such materials towards thermometry and thermography stems from three main factors: the very steep dependence of their PL lifetime on temperature, the fact that these PL lifetime values fall in an easy-to-measure range that spans several nanoseconds to several microseconds, and the intrinsic nature of the PL lifetime as it is only affected by temperature and remains unaltered by other factors such as impurities or partial degradation. Therefore, the average lifetime versus temperature behavior of $Rb_7Sb_3Cl_{16}$ was evaluated to screen its potential thermometric performance. By comparing the integrated PL intensity with the average lifetime, two distinct temperature-sensitive regimes can be identified: radiative-nonradiative competition (quenching) near RT and radiative only (non-quenching) below 100 K. The quenching regime behaves analogously to Sn-based STE emitters, with the PL-intensity and average lifetime varying directly due to competition between radiative and non-radiative channels.[284] The non-quenching regime demonstrates temperature-dependent lifetimes without a significant decrease in PL intensity, indicating a direct variation in the radiative lifetime. This feature has been previously observed in Bi(III) based systems and is attributed to a change in the emission characteristics due to transfer between different luminescent triplet states. In both regimes (cryogenic temperatures and close to RT), the observed lifetime shifts may be significant enough to have potential applications in ROT. Furthermore, $Rb_7Sb_3Cl_{16}$ exhibits excellent thermal stability with complete reversibility in PL intensity and PL lifetime up to 150 °C (423 K; Figure 8.37).

The FOM for this application is the specific thermometric sensitivity, where higher specific sensitivities indicate greater thermometric precision as smaller thermal deviations are required to alter the average PL lifetime. These can be calculated using the following formula:

$$\alpha = -\frac{d\tau}{dT}\frac{1}{\tau} \quad (1)$$

where α is the specific sensitivity in inverse temperature, τ is the average PL lifetime, and T is the temperature.[278, 284] The specific thermometric sensitivity for $Rb_7Sb_3Cl_{16}$ is shown in Figure 8.38. Although the non-quenching regime (T < 100 K) yields rather low values for α (≤ 0.01 K^{-1}), α exceeds 0.06 K^{-1} near RT, equaling that of the exceptional Sn-halide-based STE thermographic materials[284] and highlighting the potential of this compound as a stable inorganic thermometric material.

Given this excellent thermal sensitivity, we sought to determine which structural feature ($[SbCl_6]^{3-}$ octahedra or $[Sb_2Cl_{10}]^{4-}$ dimer) was responsible for, or dominant in, the observed RT PL. From the dT-PL/PLE/TRPL and Raman experiments, we could already infer that both

structural units within the $Rb_7Sb_3Cl_{16}$ structure contribute to its PL. To help determine which Sb-site in $Rb_7Sb_3Cl_{16}$ can be assigned to the PL and PLE max for this material, we performed density functional theory (DFT) calculations of the partial density of states (DOS) and compared the energies of these transitions (Figure 4.12a). The disorder in the complex $Rb_7Sb_3Cl_{16}$ structure was unable to be modeled through a tripled supercell along the *c*-axis, as the resulting structure was too large to utilize in computational studies. A new ordered model was therefore generated in Materials Studio from the 230 K $Rb_7Sb_3Cl_{16}$ structure, maintaining the original unit cell size and using the other partially ordered layer as a template to arrange the disordered $[Sb_2Cl_{10}]^{4-}$ dimers.

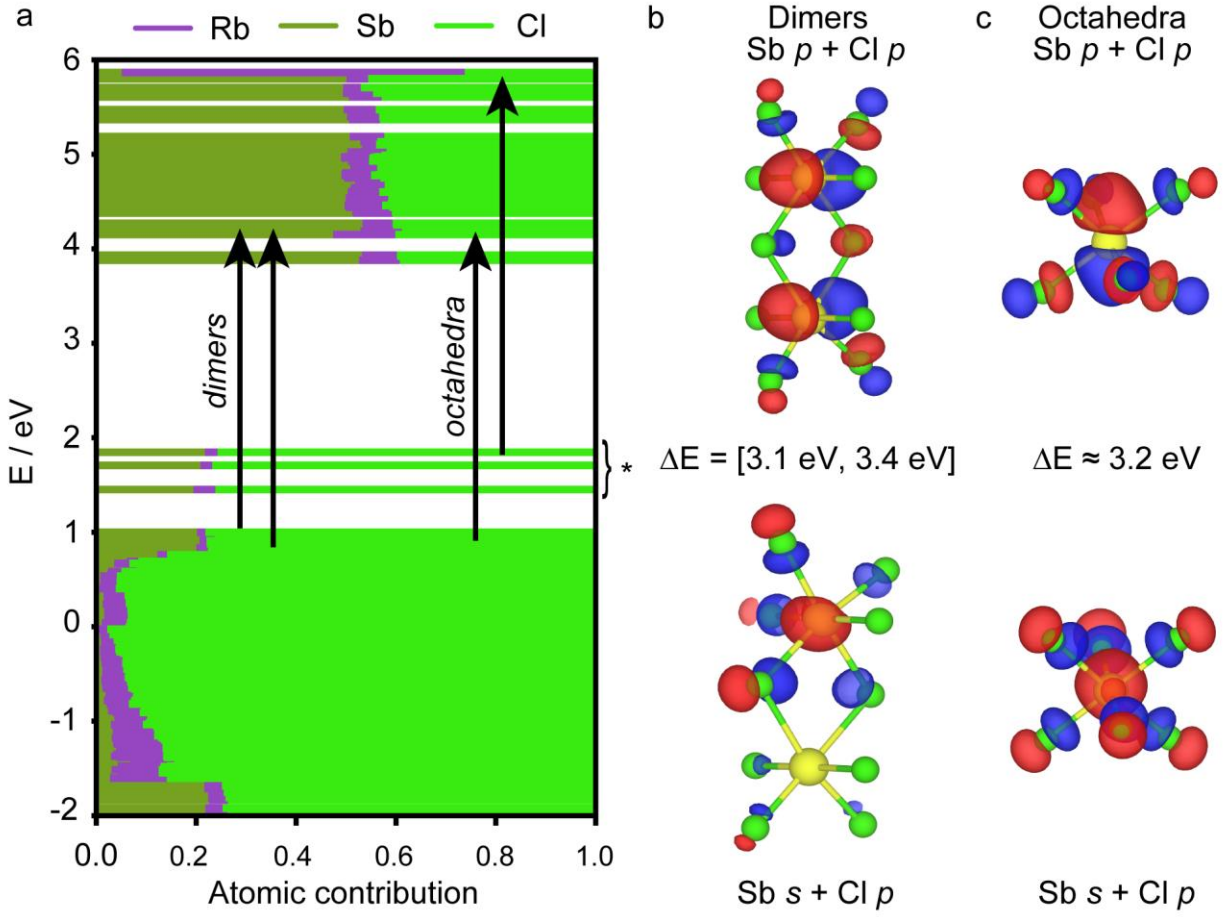

Figure 4.12. (a) Partial density of states for $Rb_7Sb_3Cl_{16}$. (b) Occupied (lower) and unoccupied (higher) molecular orbitals belonging to $[Sb_2Cl_{10}]^{4-}$ dimers. (c) Occupied (lower) and unoccupied (higher) molecular orbitals belonging to $[SbCl_6]^{3-}$ octahedra.

The electronic states were found to be localized on both the $[SbCl_6]^{3-}$ octahedra and the $[Sb_2Cl_{10}]^{4-}$ dimers, with no states near the HOMO-LUMO gap extending over incongruent structural features (Figure 4.12b,c). The states near the valence band/HOMO are comprised of Sb *5s* and Cl *4p* orbitals, whereas the conduction band/LUMO consists primarily of Sb *5p*, Cl *4p* orbitals (corresponding to an *sp* to *p* allowed transition). As is the case with other main-group metal halides,[307-308] the alkali cation (Rb^+, purple) does not significantly contribute to the DOS

near the bandgap.

Unexpectedly, the DFT calculations indicated that both $[Sb_2Cl_{10}]^{4-}$ dimers and $[SbCl_6]^{3-}$ octahedra had energetically feasible transitions lying close to one another. Although most low-energy transitions belong to the $[Sb_2Cl_{10}]^{4-}$ dimers, the HOMO is octahedral. While our model is far from definitive, it suggests that $[Sb_2Cl_{10}]^{4-}$ dimers are the predominant source of PL and therefore that the mutual optical activity, especially at low temperatures, is likely to be the result of numerous possible transitions occurring on effectively isolated structural features.

The inability to effectively distinguish between these sites computationally inspired us to take a chemical approach and investigate the $Rb_7Bi_{3-x}Sb_xCl_{16}$ family – where optical changes could, ideally, be tracked back to discrete structural modifications. Previously, it was reported that $Rb_7Bi_3Cl_{16}$ exhibits blue PL when prepared as NCs.[174] Given the observation of bright STE emission from single crystals in other 0D systems as well as in $Rb_7Sb_3Cl_{16}$, we expected that we would be able to study these same optical properties in single crystals of $Rb_7Bi_3Cl_{16}$.

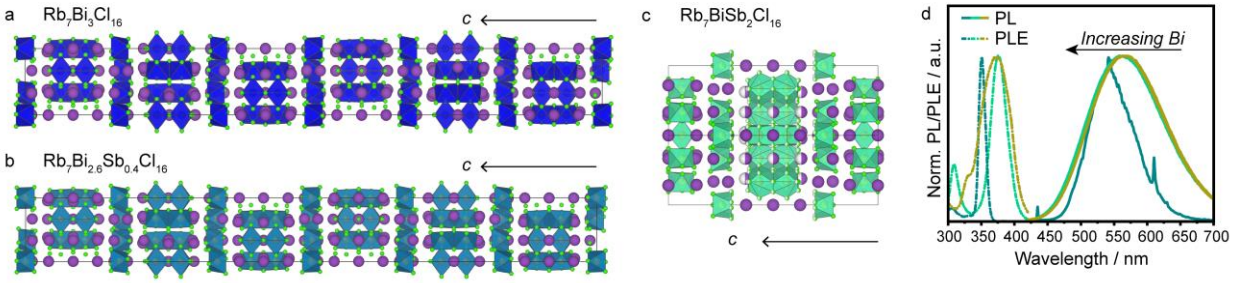

Figure 4.13. (a) The crystal structure of $Rb_7Bi_3Cl_{16}$ as viewed along the [100] axis contains Bi dimers and octahedra (blue with green chlorine atoms) separated by Rb^+ cations (purple). (b) The crystal structure of $Rb_7Bi_{2.6}Sb_{0.4}Cl_{16}$ as viewed along the [100] axis contains mixed Sb/Bi dimers and octahedra (cerulean with green chlorine atoms) separated by Rb^+ cations (purple). (c) The crystal structure of $Rb_7BiSb_2Cl_{16}$ as viewed along [110] contains mixed Sb/Bi dimers and octahedra (aquamarine with green chlorine atoms) separated by Rb^+ cations (purple). (d) The normalized RT PL (solid) and PLE (dashed) spectra of $Rb_7Bi_{3-3x}Sb_{3x}Cl_{16}$.

Single crystals of the $Rb_7Bi_3Cl_{16}$ phase were grown solvothermally from a solution containing a 1:1 ratio of Rb:Bi to avoid the formation of the Rb_3BiCl_6 phase. Although the structure was confirmed to have similar motifs to that of its Sb-analogue (bismuth chloride dimers and octahedra), it was observed to have additional superstructure reflections in the diffractograms that were not fully described by the disordered model isostructural to the Sb-endmember (Figure 8.39; Table 8.32-Table 8.35). Instead, the $Rb_7Bi_3Cl_{16}$ phase crystallizes in the *R*-3*c* space group, with a tripled *c*-axis to yield unit cell parameters of $a = b = 13.10250(10)$ Å and $c = 102.9084(17)$ Å (Figure 4.13a). As shown in Figure 8.39, the unwrapped images of the diffraction pattern exhibit weak superstructure that remains unaccounted for with the $P3_1c$ space group, which results in a disordered structure. Furthermore, the *R*-3*c* solution accounts for these weak points and has lower

correlation matrix values than the disordered solution.

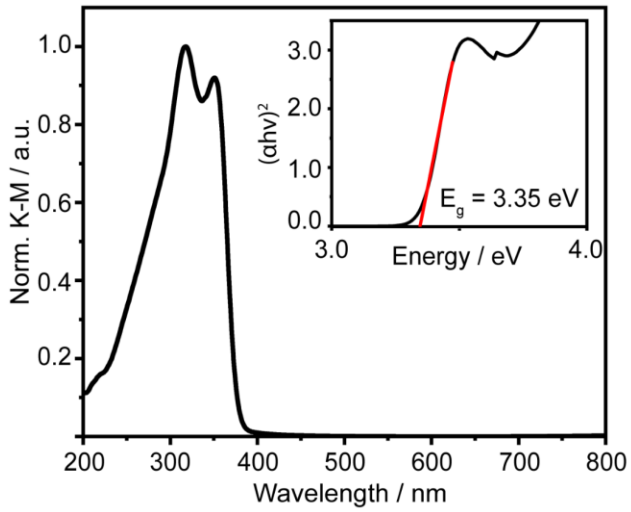

Figure 4.14. Absorption spectra of $Rb_7Bi_3Cl_{16}$ with Tauc plot shown in the inset. The absorption spectrum was measured in diffuse reflectance and recalculated using the K-M transformation.

Contrary to the Sb-analogue, $Rb_7Bi_3Cl_{16}$ did not exhibit PL under blue or UV-excitation at RT although it is a direct-gap semiconductor analogous to $RbSb_3Cl_{16}$ (Figure 4.14). Furthermore, pattern matching the solved structure confirms the product to be phase pure $Rb_7Bi_3Cl_{16}$, ruling out the possibility of any parasitic impurities such as Rb_3BiCl_6 that might absorb UV light without re-emission (Figure 8.40-Figure 8.43). By cooling $Rb_7Bi_3Cl_{16}$ to 12 K, red PL centered at 610 nm was observed; however, the PL rapidly quenched and red-shifted with increasing temperature until it had completely vanished around 200 K (Figure 4.15; Figure 8.44). The observed red PL also suggests that $[Bi_2Cl_{10}]^{4-}$ dimers, rather than $[BiCl_6]^{3-}$ octahedra (which should emit blue), are key to the observed luminescence.[182]

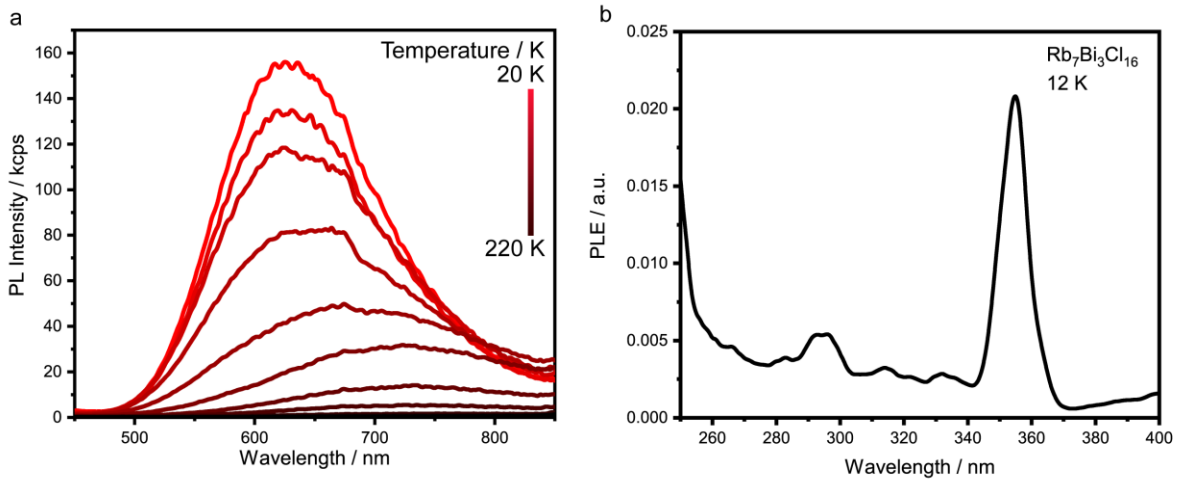

Figure 4.15. a) dT-PL for $Rb_7Bi_3Cl_{16}$ and b) PLE at 12 K

Furthermore, the PLE exhibits a much simpler spectrum than $Rb_7Sb_3Cl_{16}$ with only one major peak at 355 nm and a smaller feature located around 290 nm. We attributed these two features to the bismuth-chloride dimers and octahedra, respectively, and suppose that their relatively weak intensity is due to a low-temperature quenching regime (radiative/non-radiative competition) for this material. We confirmed this with dT-TRPL and found that the center of the quenching regime was at ~100 K (Figure 4.16; Figure 8.45). As the observed emission was still firmly within the quenching regime at these temperatures, no wavelength dependence in the PL lifetime was observed as in $Rb_7Sb_3Cl_{16}$.

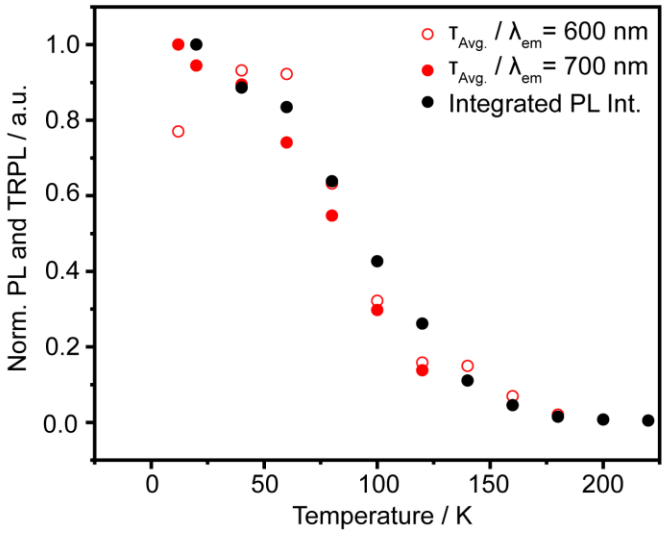

Figure 4.16. Normalized PL lifetime and PL intensity vs. temperature for $Rb_7Bi_3Cl_{16}$.

By characterizing the two compositional endmembers, we could see that the Bi^{3+} effectively acts as a "knock-out element" for RT PL. Any changes to the RT PL and PLE spectra should therefore be related to the changing environment around Sb.

Two intermediate compositions containing both Sb and Bi were then prepared (additional synthetic information can be found in the Supplementary Information). The Sb-rich composition, $Rb_7BiSb_2Cl_{16}$, was found to be isostructural with $Rb_7Sb_3Cl_{16}$ with the Bi atoms forming a solid solution with partial occupancy of both the octahedra and dimer sites (Figure 4.13b; Figure 8.46; Table 8.36-Table 8.39). The Bi-rich compound, $Rb_7Bi_{2.6}Sb_{0.4}Cl_{16}$, on the other hand, exhibits a fully ordered structure isostructural to $Rb_7Bi_3Cl_{16}$ (Figure 4.13c; Figure 8.47; Table 8.40-Table 8.43).

These four structures, although visually dissimilar based on unit cell parameters alone, all constitute a single isostructural "7-3-16" structure family. The three-fold rotational symmetry that masquerades itself as disorder in the dimer layer of the Sb-rich and Sb-only structures is unmasked in the Bi-rich and Bi-only phases. Furthermore, these materials adhere to Vegard's law (when axis tripling is accounted for) and suggest a solid-solution between Sb and Bi (Figure 8.48).

Although it had been expected that these two cations, having different sizes (0.76 Å for Sb^{3+} and 1.03 Å for Bi^{3+}),[309] might occupy different sites within these structures, the structure solutions indicated similar alloying across all sites. This was also strongly supported by solid-state nuclear magnetic resonance (ssNMR) experiments. ^{87}Rb was selected as the nuclei of choice as ^{85}Rb, ^{121}Sb, ^{123}Sb and ^{209}Bi all possess large quadrupolar moments, and the multitude of different chlorine species (even in the compositional endmember materials) excluded ^{35}Cl and ^{37}Cl. The 1D

experiments (Figure 8.49) for $Rb_7Sb_3Cl_{16}$ and $Rb_7Bi_3Cl_{16}$ exhibit signals that are broadened by a second order quadrupole interaction. The mixed materials, however, only show broad overlapping signals. To improve the resolution, multi-quantum-magic-angle spinning (MQMAS) experiments were used (Figure 8.50). This technique effectively separates the anisotropic quadrupole interaction from the isotropic chemical shift thus allowing for the identification of individual species (*i.e.* atomic environments). The mixed-metal materials exhibit signals around 70 ppm that are spread along the chemical shift axis and are not present in the spectra of $Rb_7Sb_3Cl_{16}$ or $Rb_7Bi_3Cl_{16}$. This chemical shift distribution supports the formation of a solid solution due to the stochastic distribution of Sb and Bi among all crystallographic sites.

Optically, the substitution of Sb^{3+} with Bi^{3+} quenches the emission of these materials, and blueshifts both the PL and PLE with respect to $Rb_7Sb_3Cl_{16}$ (Figure 4.13d). Concomitant to the blueshift of the Bi-rich PLE spectrum, the width of the PLE peak sharply narrows. This is possibly related to the quenching of any mixed $[Bi_{2-x}Sb_{2x}Cl_{10}]^{4-}$ ($x \leq 1$) dimers as the alloying with Bi would be expected to decrease phonon energies and therefore lead to lower quenching temperatures.

These two materials were then investigated by dT-PL/PLE/TRPL; their specific sensitivities were also determined and compared to both $Rb_7Sb_3Cl_{16}$ and $Rb_7Bi_3Cl_{16}$ (Figure 4.17-Figure 4.21). Analogously to $Rb_7Bi_3Cl_{16}$, the PLE spectra of both $Rb_7BiSb_2Cl_{16}$ and $Rb_7Bi_{2.6}Sb_{0.4}Cl_{16}$ exhibit fewer peaks vis-à-vis $Rb_7Sb_3Cl_{16}$. Furthermore, they both feature a prominent PLE max around 355 nm and a second weaker feature around 300 nm-320 nm (Figure 4.17,Figure 4.19). Excitation at these two set of wavelengths results in two separate emission bands, with similar emission energies but different intensities (Figure 4.18, Figure 4.20Figure 4.21). As a result, the intensity ratios between these two sets of wavelengths are both emission wavelength and temperature dependent (Figure 8.51). By comparing the excitation-peak intensity ratios with temperature, an inverse relationship between high energy and low energy transitions could be observed for the Sb-rich phase. However, this relationship is not observed in the Bi-rich phase, indicating that energy transfer between high and low energy transitions is unlikely, which is in agreement with the computational prediction that there are no viable dimer-to-octahedra transitions near the HOMO-LUMO gap for $Rb_7Sb_3Cl_{16}$ (Figure 8.52; Figure 4.12).[272] A more plausible interpretation is that the higher and lower energy excitation peaks are respectively associated with octahedral and dimer environments.

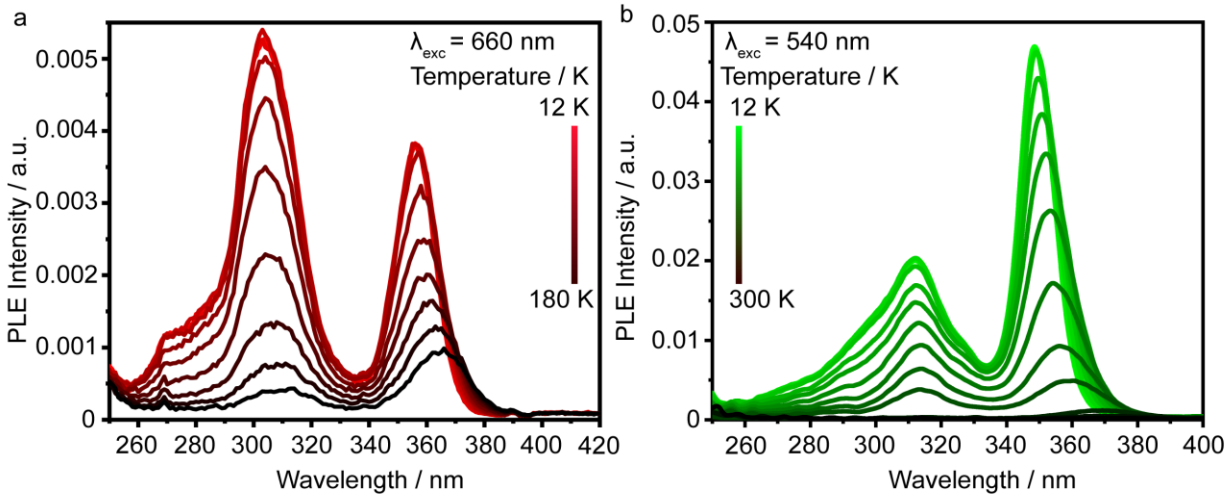

Figure 4.17. dT-PLE spectra for $Rb_7BiSb_2Cl_{16}$. Measured by detecting light emitted at a) 660 nm and b) 540 nm

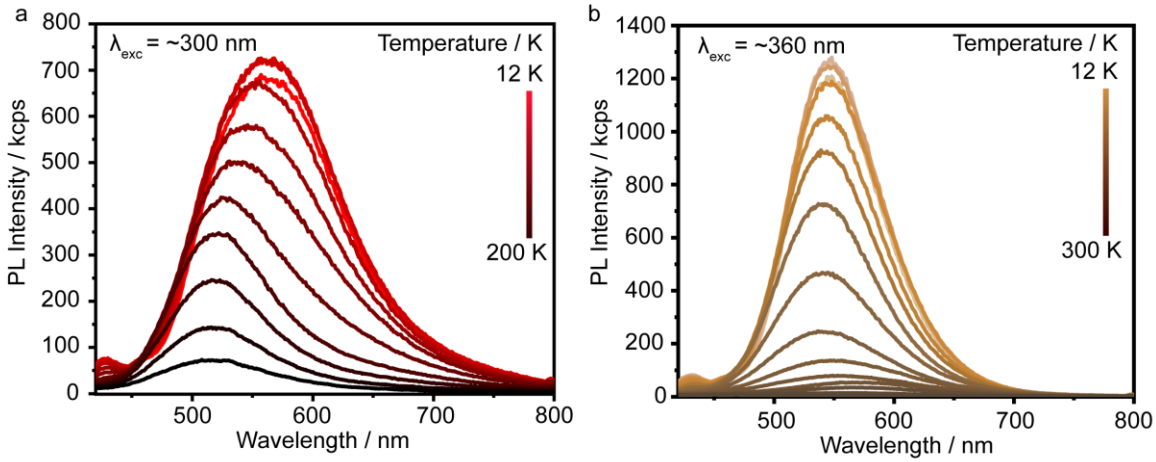

Figure 4.18. dT-PL spectra for $Rb_7BiSb_2Cl_{16}$. Measured by exciting at a) 300 nm and b) 360 nm

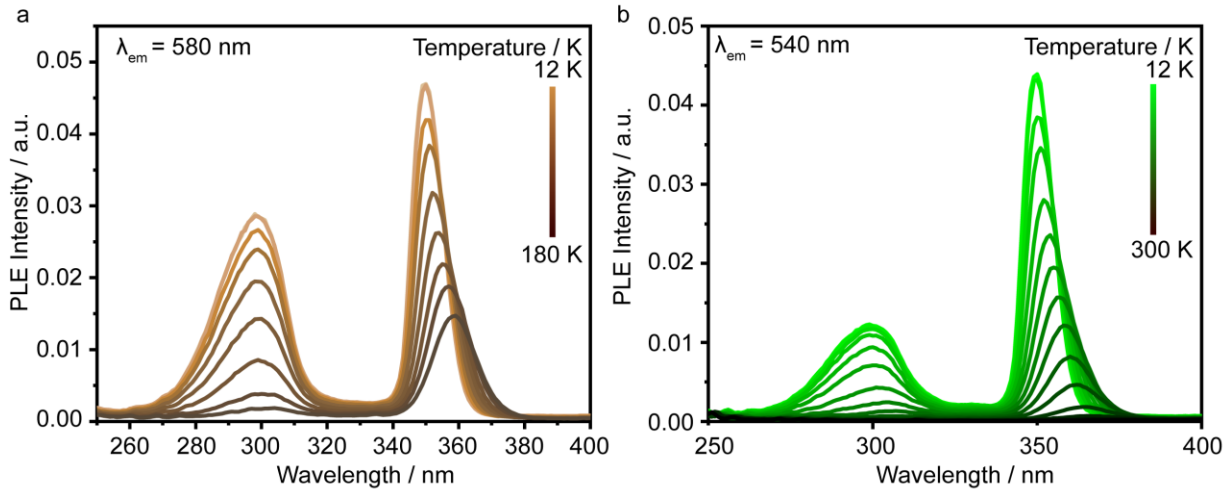

Figure 4.19. dT-PLE spectra for $Rb_7Bi_{2.6}Sb_{0.4}Cl_{16}$. Measured by detecting light emitted at a) 580 nm and b) 540 nm.

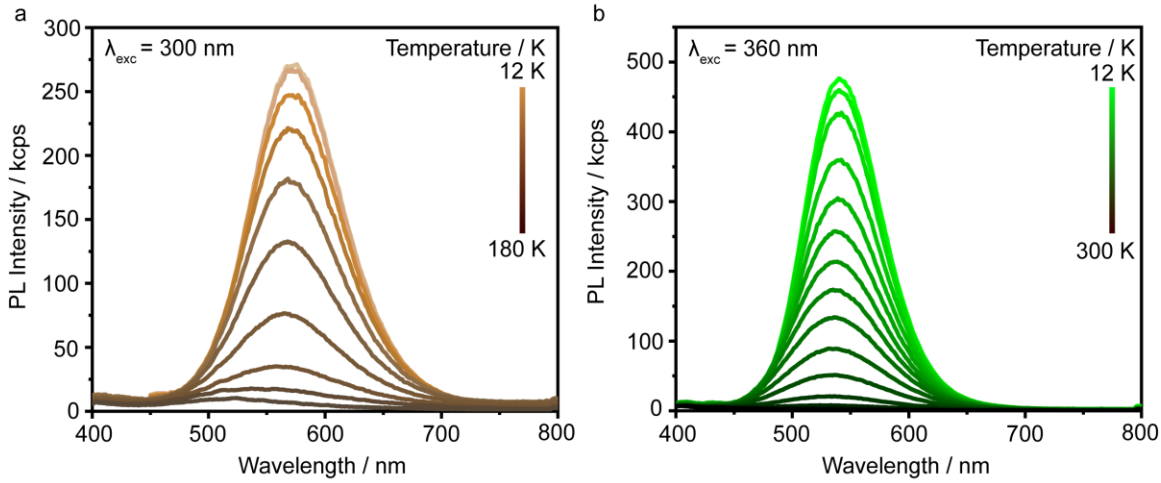

Figure 4.20. dT-PL spectra for $Rb_7Bi_{2.6}Sb_{0.4}Cl_{16}$. Measured by exciting at a) 300 nm and b) 360 nm.

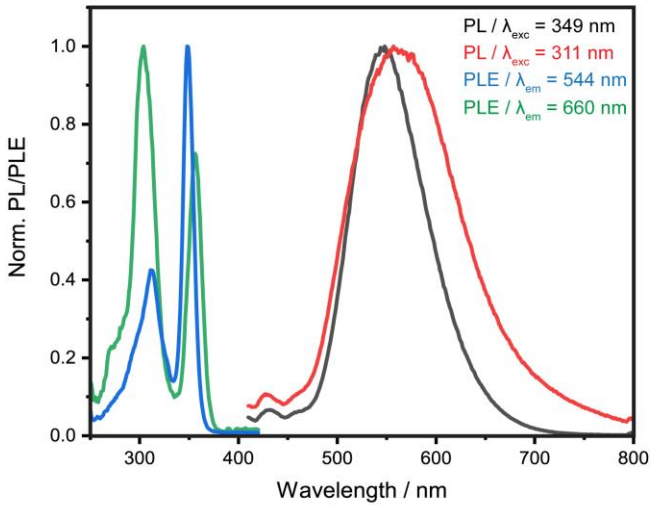

Figure 4.21. 12 K PL and PLE comparison for $Rb_7BiSb_2Cl_{16}$.

The comparison of PL and PLE spectra of all materials at 12 K demonstrates that the mixed-metal materials have larger band gaps than the compositional endmembers (Figure 4.22,Figure 4.23). However, the PL for both substituted materials is blue shifted from both $Rb_7Sb_3Cl_{16}$ and $Rb_7Bi_3Cl_{16}$, suggesting that they emit from a similar structural feature. By comparing the PL and PLE spectra at 200 K, we can see $Rb_7Bi_3Cl_{16}$ has already quenched, indicating that any $[BiCl_6]^{3-}$ octahedra or $[Bi_2Cl_{10}]^{4-}$ dimers should be optically silent. Therefore, we expect mixed-Sb/Bi dimers to be dark as well; this leaves the Sb-octahedra as the source of the weak and blue-shifted emission which is observed in the mixed-metal systems, especially the Bi-rich $Rb_7Bi_{2.6}Sb_{0.4}Cl_{16}$. While the PLE shows that the peak position for the mixed-metals matches that of $Rb_7Sb_3Cl_{16}$ (agrees with previous PL/PLE maps), the PL demonstrates a monotonic shift in peak emission wavelength with the Bi-rich phase having the most blue-shifted emission as a result of weak $[SbCl_6]^{3-}$ octahedra emission. This agrees with our assignment of $[Sb_2Cl_{10}]^{4-}$ dimer-centered emission as the predominant source of PL in $Rb_7Sb_3Cl_{16}$ at RT.

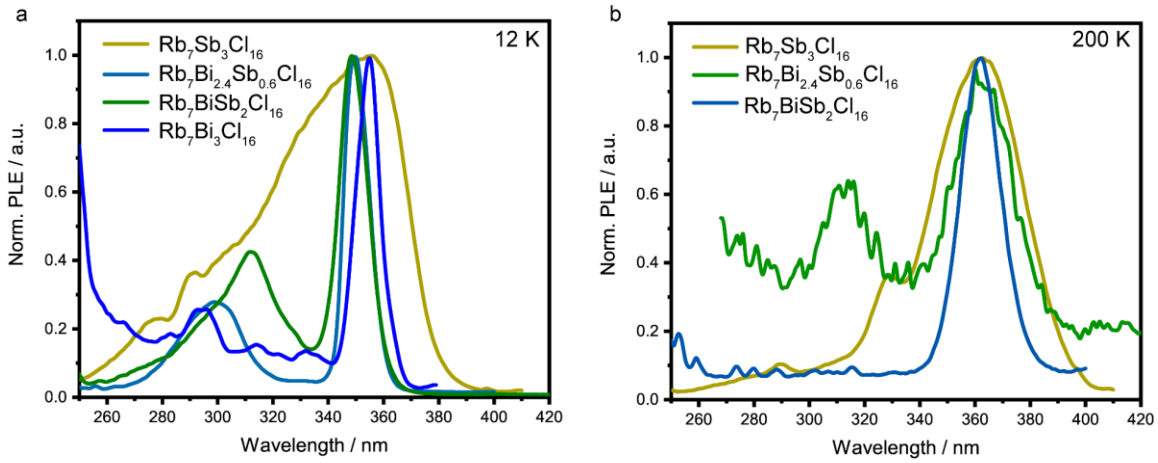

Figure 4.22. PLE comparisons for the $Rb_7Bi_{3-3x}Sb_{3x}Cl_{16}$ family at a) 12 K and b) 200 K.

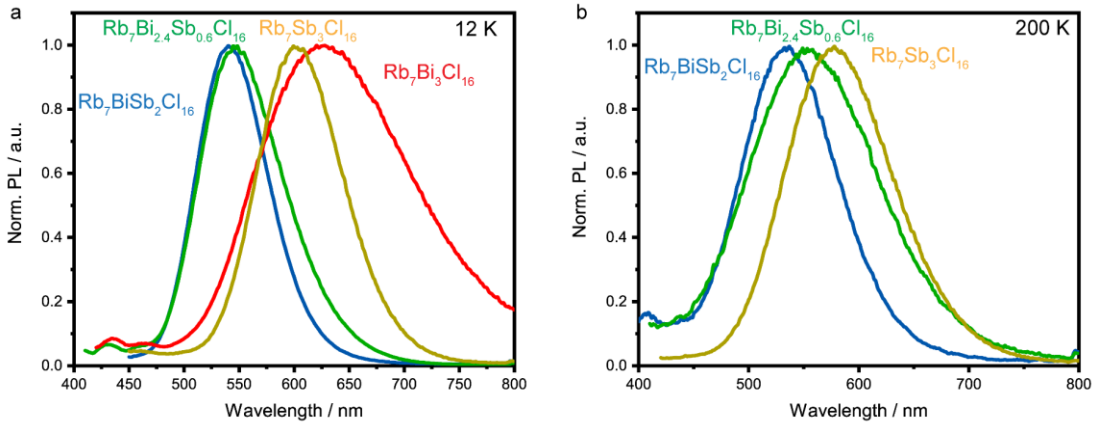

Figure 4.23. PL comparisons for the $Rb_7Bi_{3-3x}Sb_{3x}Cl_{16}$ family at a) 12 K and b) 200 K.

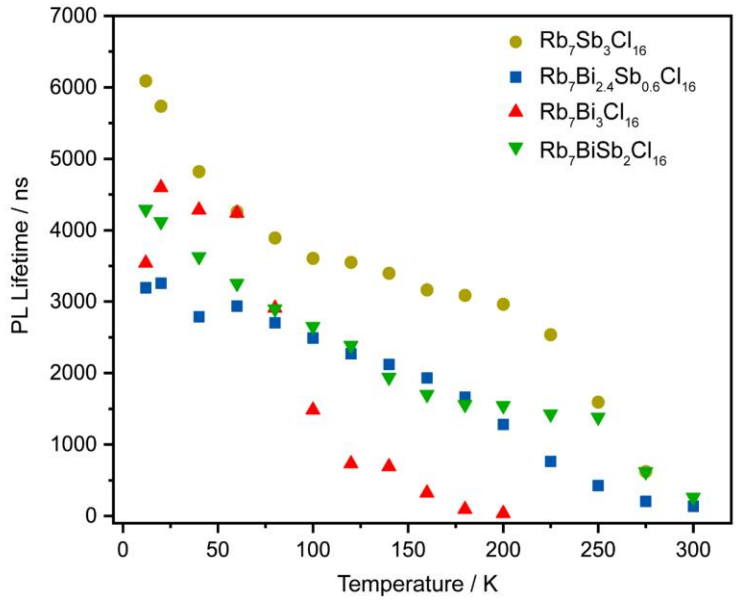

Figure 4.24. Average PL lifetimes with respect to temperature for the $Rb_7Bi_{3-3x}Sb_{3x}Cl_{16}$ family.

To judge the potential of these substituted materials as thermometric luminophores, as well to determine whether Sb/Bi alloying is an effective way to alter the thermometric sensitivity regime, the PL lifetimes of the two mixed-metal materials were measured to determine their specific sensitivities. In both cases, the mixed-metal compositions demonstrate lifetimes that are intermediate between those of $Rb_7Sb_3Cl_{16}$ and $Rb_7Bi_3Cl_{16}$ (Figure 4.24). However, the additional Bi^{3+} in these structures appears to quench the emission without increasing the steepness of the lifetime vs. temperature curve. This widening of the quenching regime (radiative vs. nonradiative competition) decreases specific sensitivity values, showing that the Sb/Bi substitution does not lend itself towards thermographic utilization (Figure 8.53)

Given the increased Bi content of these materials, as well as previous works on the use of low-dimensional materials as detectors, we characterized the electronic properties and measured the X-ray photoresponse of $Rb_7Sb_3Cl_{16}$ and $Rb_7Bi_{2.6}Sb_{0.4}Cl_{16}$, which had yielded the largest crystals (Figure 8.54-Figure 8.56). As expected from their 0D structure, these materials exhibit very low conductivities (hundreds of pS cm^{-1}). These materials also demonstrate a weak photocurrent response under X-ray illumination, with $Rb_7Sb_3Cl_{16}$ having a $\mu\tau$ product of $1.3x10^{-5}$ cm^2 S^{-1} V^{-1} (Figure 8.55), on par with that of the pnictogen $A_3M_2I_9$ compounds.[308] The Bi rich structure has an improved X-ray photoconductivity with a $\mu\tau$ of $1.75x10^{-3}$ cm^2 S^{-1} V^{-1} (Figure 8.56).

As a final example of the numerous synthetic possibilities for this system, we also explored the substitution of Rb^+ for K^+. This resulted in the formation of a related 0D structure; however,

the main product phase was KCl with only small amounts (~3-5%) of $K_7Sb_3Cl_{16}$.

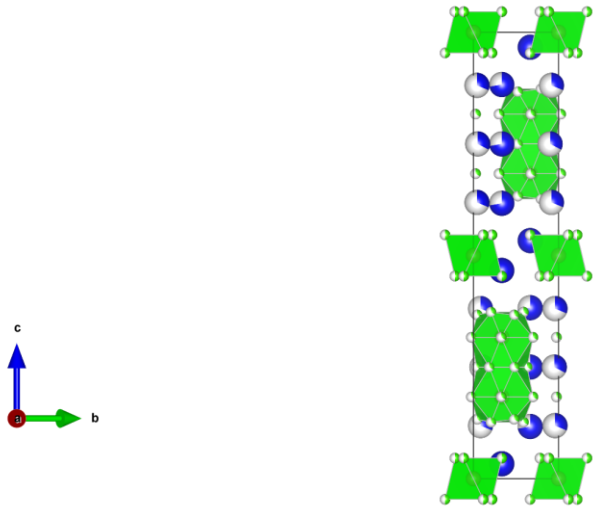

Figure 4.25. Structure of $K_7Sb_3Cl_{16}$ at 298 K.

This material was found to crystallize in a *P*6$_3$/*mmc* space group, and also contains an ordered octahedral layer and a disordered dimeric layer (Figure 4.25,Figure 4.26; Table 8.44-Table 8.47). The disordered *P*6$_3$*mmc* solution is an acceptable model for this structure, but ultimately not the most correct solution. There is insufficient data to satisfactorily apply a more ordered model to this data as was done for $Rb_7Bi_3Cl_{16}$. However, this data set shows the same features that led us to the adoption of the larger, ordered model as described for $Rb_7Bi_3Cl_{16}$.

This phase also exhibits RT PL, which is centered at 590 nm with a Stokes shift of 1.2 eV and a FWHM of 0.53 eV (Figure 4.27). This indicates an unexpected reversal in the trend observed in Chapter 2 for the effect of the A-cation on the PL from a 0D metal-halide. As a brief reminder, the substitution of Cs with Rb or K in Cs_4SnBr_6 blue shifts the PL without altering the PLE. Here, the substitution of Rb with K redshifts the PL. This may be explained by our suggestion that the dimers are the emissive species at RT. Since we expect the local environment surrounding the octahedra in $K_7Sb_3Cl_{16}$ to be shrunk compared to those of $Rb_7Sb_3Cl_{16}$, we would expect the result in the same trend as in Cs_4SnBr_6 if octahedra were more emissive.

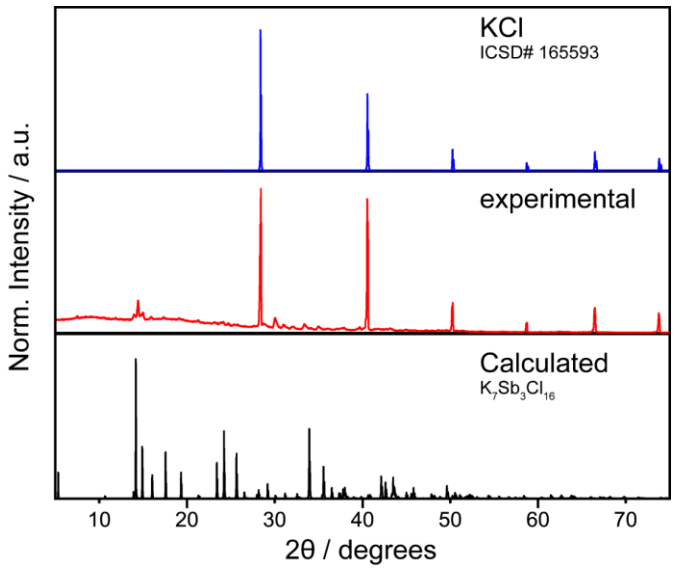

Figure 4.26. PXRD of $K_7Sb_3Cl_6$. The synthesis of $K_7Sb_3Cl_{16}$ typically resulted in the presence of large quantity of KCl; however, KCl is a non-emissive salt under UV excitation and therefore does not interfere in the investigation of optical properties such as PL.

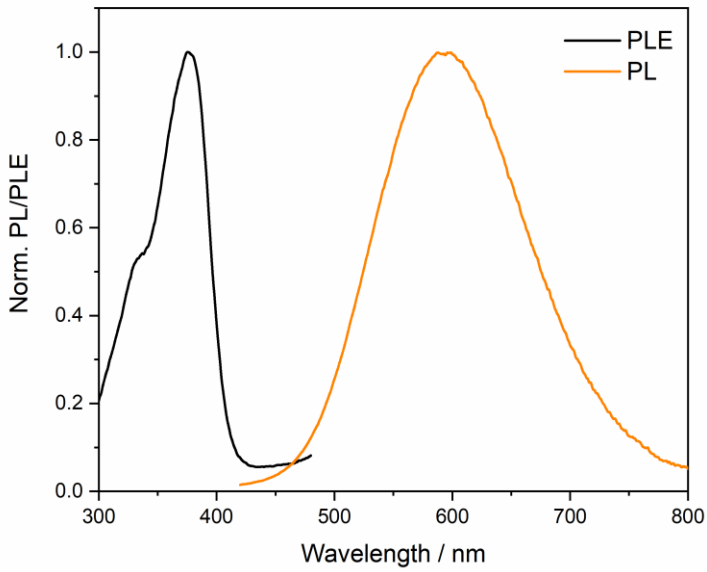

Figure 4.27. PL and PLE of $K_7Sb_3Cl_6$ at 298 K.

Analogously to $Rb_7Sb_3Cl_{16}$, this phase exhibits similar temperature dependent properties and is another promising thermometric luminophore. dT-PLE and dT-PL measurements both demonstrate the same features that were previously discussed for $Rb_7Sb_3Cl_{16}$, such as increasing PL intensity with decreasing temperatures, decreased FWHM, a redshift in the PL, and a blueshift in the PLE (Figure 4.28,Figure 4.29). These trends were not explored further but are expected to have strong similarities to those of the Rb-analogue.

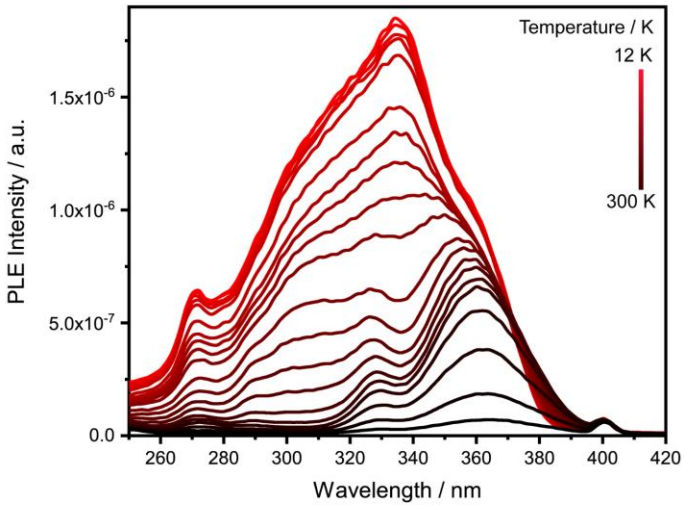

Figure 4.28. dT-PLE of $K_7Sb_3Cl_6$.

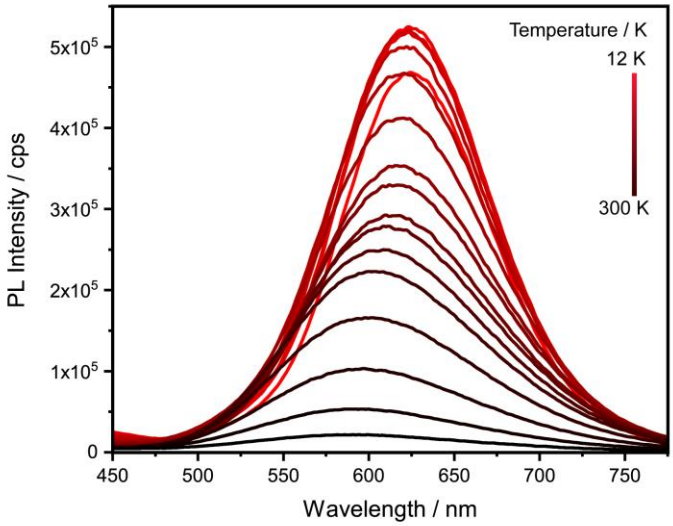

Figure 4.29. dT-PL of $K_7Sb_3Cl_6$.

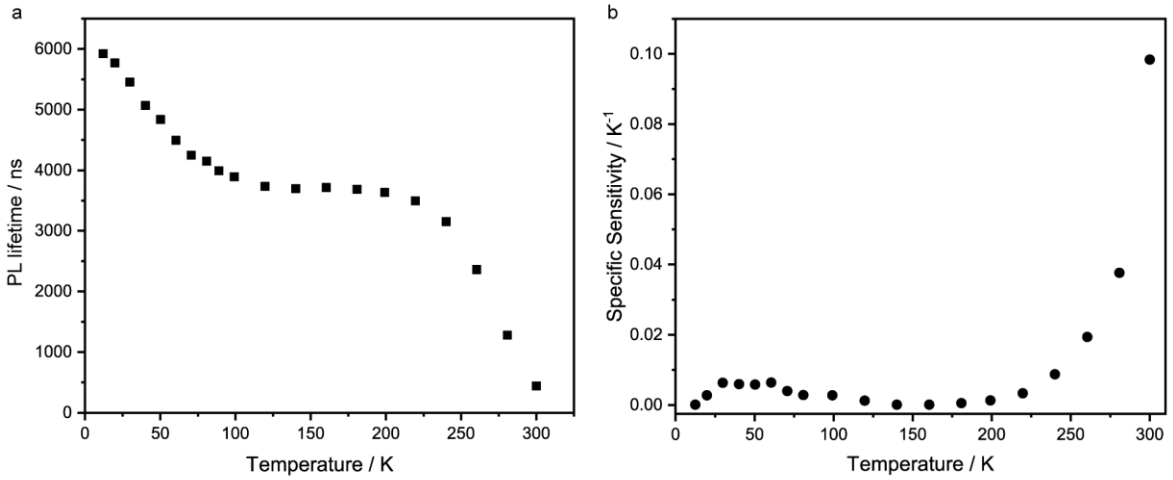

Figure 4.30. dT-TRPL of $K_7Sb_3Cl_6$. a) Average lifetime with temperature. b) specific sensitivity.

To determine whether such a material could also serve as a potential thermometric material, the dT-TRPL was measured and the specific sensitivity was determined (Figure 4.30). The same two-region trend was observed from fitting the dT-TRPL data for this phase just as in $Rb_7Sb_3Cl_{16}$ The specific sensitivity for the RT region may in fact reach values of up to 0.1 K^{-1}, which may be some of the best sensitivities for RT thermoluminophores.

Finally, we subjected several of our samples, as well as $Rb_3Sb_2I_9$, to X-ray excitation in an effort to determine whether these could also function as scintillator materials, similar to the $(bmpip)_2SnBr_4$ and $(bmpip)_2PbBr_4$ (bmpip = 1-butyl-1-methyl-piperidinium) samples demonstrated previously in our group (Figure 4.31).[172]

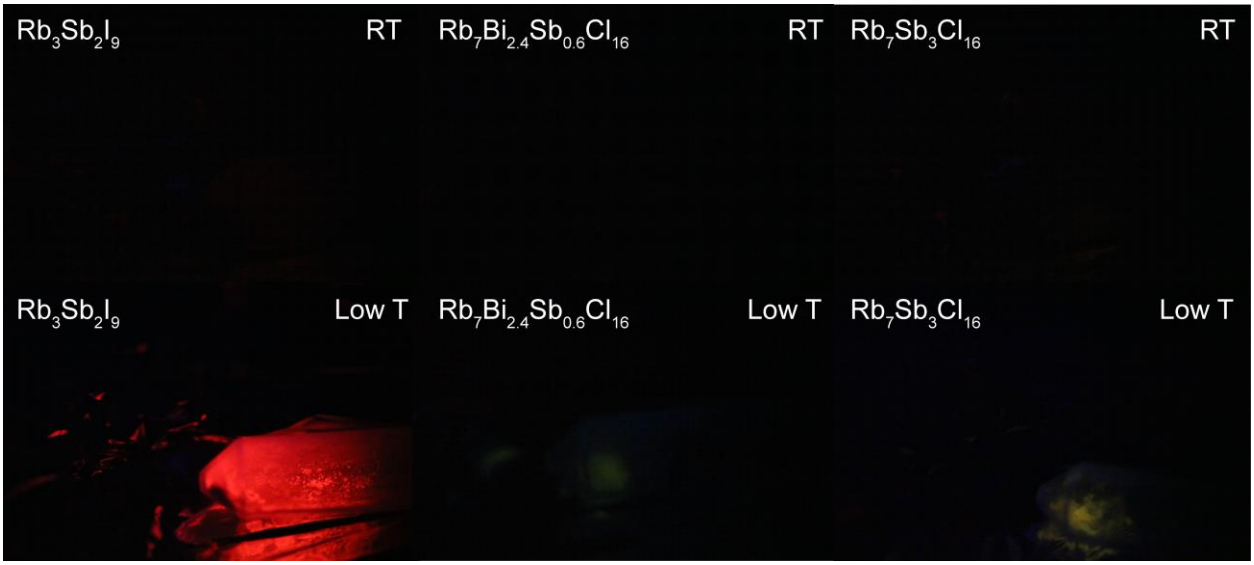

Figure 4.31. X-ray scintillation images of $Rb_3Sb_2I_9$, $Rb_7Bi_{2.4}Sb_{0.6}Cl_{16}$, and $Rb_7Sb_3Cl_{16}$ at various temperatures.

To our disappointment, no RT scintillation could be observed; however, visible scintillation could be captured upon cooling with liquid nitrogen. Unsurprisingly, the scintillation intensity rapidly decreased as the samples warmed to RT, mirroring their behavior under UV excitation. While cryogenic scintillation is increasingly researched as an application, it requires, preferably, materials with fast decay times.[310] Low-dimensional materials, as we have shown previously, exhibit increasing PL lifetimes with decreasing temperature, which makes them less than ideal for this application.

4.5. Conclusion

In summary, through the synthesis and substitutional investigation of the $Rb_7Bi_{3x}Sb_{3-3x}Cl_{16}$ material family, we found three RT luminescent 0D Sb-halides that exhibit excellent thermographic sensitivities around RT while remaining oxidatively stable. Furthermore, through a combination of DFT analysis and temperature dependent optical studies, we find evidence suggesting that the efficient RT PL originates from the structures' edge-shared $[Sb_2Cl_{10}]^{4-}$ dimers. This structural motif has not received significant attention to date, but these results show that such dimers may be an excellent coordination to target for the discovery of luminescent 0D pnictogen-halides.

Chapter 5. Intervalent and mixed-valent zero-dimensional metal-halides of the $Rb_{23}Sb^{III}_{7-x}Bi^{III}_{x}Sb^{V}_{2}Cl_{54}$ family ($x \leq 3.5$)

Excerpts and figures from this chapter may appear in the upcoming manuscript:

Benin, B.M.;[#] McCall, K. M.;[#] Wörle, M.; Borgeaud dit Advocat, D.; Sakhatskyi, K.; Yakunin, S.; Kovalenko, M.V., "Intervalent and mixed-valent zero-dimensional metal-halides in the $Rb_{23}M^{III}_{7}Sb^{V}_{2}Cl_{54}$ family (M^{III} = Sb, Bi)", *manuscript in preparation* **2020**.

5.1. Abstract

The results of the previous chapters demonstrated that zero-dimensional metal-halides exhibit unique properties, promising for optoelectronic applications such as thermometry and thermography. While previous publications have also demonstrated the utility of such materials in high-energy excitation applications such as X-ray scintillation, the vast majority of optoelectronic applications use blue (~450 nm) excitation sources. However, most 0D metal-halides have sub-400 nm excitation maxima with only weak 450-460 nm absorption. Therefore, finding suitable strategies to narrow the band gap of these materials are required. One obvious possibility is of course to substitute with heavier halides such as Br^- or I^-. This strategy, while easy to implement, is hindered by decreased luminescence quenching temperatures and concomitantly lower PLQY values.

One potential solution that we sought to investigate was through the use of 0D mixed-valent materials. These tend to have broad absorption bands that extend into the visible range, giving many of these materials red or even black colors. Given this strong visible absorption, we were determined to see if any such materials may be luminescent at any temperature as no reports existed on the topic. Furthermore, we identified an open question within the literature regarding the existence and structure of the "$Rb_4Sb^{III}Sb^{V}Cl_{12}$" and "$Rb_{2.67}SbCl_6$" phases.

Therefore, we synthesized this phase and found the correct stoichiometry to be $Rb_{23}Sb^{III}_{7}Sb^{V}_{2}Cl_{54}$, with an orthorhombic structure (*Cmcm*) and red color. No low temperature PL was observed; however, we were able to discover a series of new materials once the Sb^{III} was partially or even fully substituted with Bi^{III}. These instead crystallize in a trigonal crystal system with a *R*32 space group. Incidentally, this belongs to one of the piezoelectric space groups and suggests that these phases may exhibit piezoelectricity or second harmonic generation. To confirm this space group, we performed SHG measurements and found strong evidence of its existence. Regarding optical properties, the charge transfer bands for these materials blue shift as the amount of Bi^{III} increases compared to the Sb-only phases, but still no PL was observed at any temperature

down to 12 K.

5.2. Introduction

Vacancy-ordered double perovskites are a well-known 0D system in which octahedra are separated by regular vacancies.[311-312] This structure can be derived from the 3D $AM^{II}X_3$ halide perovskite through the splitting of the M^{II} site into a combination of vacancies and M^{IV} octahedra, where every other site is occupied to yield a 0D cluster compound consisting of $M^{IV}X_6$ octahedra and A-site cations arranged in an antifluorite structure. In these systems, the metal-halide octahedra typically have M^{IV} metal centers with an overall formula of $A_2M^{IV}X_6$ (A = K, Rb, Cs; M^{IV} = Sn,[188, 190] Te,[115] Pb,[313] Ti,[187] Pd,[196] Pt,[313] Hf,[227-228] Zr;[229] X = Cl, Br, I).[314] Several main group metal halides with this structure type were luminescent, including the series Cs_2TeX_6, with the most efficient luminescence found in the chloride analogue, as expected.[315] However, the first main group metal chloride with a low bandgap was the intensely colored indigo Cs_2SbCl_6, first reported in 1882.[316] The strong color of these compounds was unexpected because undoped, low-dimensional ternary chlorides containing either pnictogen (III) or pnictogen (V) metal-centers, tend to be colorless both in solution and in the solid state.

The intial reports on such phases described the blue-black Cs_2SbCl_6 and, later, the black Cs_2SbBr_6, as containing a tetravalent Sb cation, however this oxidation state is unknown for Sb. Hence it was proposed that the M^{IV} site was shared by M^{III} and MV octahedra to generate a mixed-valent ordered double perovskite structure with the formula $A_4M^{III}M^{V}X_{12}$, often written as $A_2M^{III}{}_{0.5}M^{V}{}_{0.5}X_6$ to maintain the connection to the parent structure type.[317-319] Magnetic measurements later demonstrated these materials to be diamagnetic, thereby confirming the mixed-valent composition $Cs_4Sb^{III}Sb^{V}X_{12}$,[320] and the optical features of this mixed valency, based on optical measurements, were first described in 1963 by Peter Day.[321]

These materials were intensely investigated in the 20th century as a prototypical example of this charge-transfer in the solid state, due in part to their optical properties lying in the visible spectrum.[322]

At this point, a growing library of mixed-valent materials began to develop with groups investigating the structure and properties associated with various combinations of Sb^{V} and Bi^{III}, In^{III}, Tl^{III}, Fe^{III}, and Rh^{III} as well as bromides and chlorides.[317, 321-325] This allowed for comparative studies based on optical and electrical properties as well as structures. It was demonstrated that the charge transfer occurs from the ns^2 orbital of the M^{III} cation to the $5s^0$ orbtial of the Sb^{V} cation thereby explaining the shift in the charge transfer band, and the change from a Robin-Day type II to type I system, as the M^{III} cation changes from Sb and Bi to In and Tl.[321-322, 326] Additionally, it was shown that the intensity of the charge-transfer band was at its maximum intensity when the $[M^{III}]:[M^{V}] = 1$ in both the solid state as well as in solution.[322]

The through-space or outer-sphere nature of the energy transfer was supported by both electrical conductivity and resistivity measurements as well as structural analysis. These materials

form disconnected structures with nearly cubic symmetry, and the phases all tend to adopt either cubic structures, in which M^{III} and Sb^{V} sites are identical, or tetragonal structures with unique sites for M^{III} and Sb^{V} (Figure 5.1; Table 5.1).[325] Importantly, given that these are 0D structures there are no extended paths or chains through the structure for charge transfer; additionally, there are no aggregates such as dimers or timers that could provide an inner-sphere charge transfer mechansim.[322, 327] This mechanism was further supported with the observation of high resistivities (10^6-10^9 Ωcm) and negligible photoconductivity.[323, 328-329]

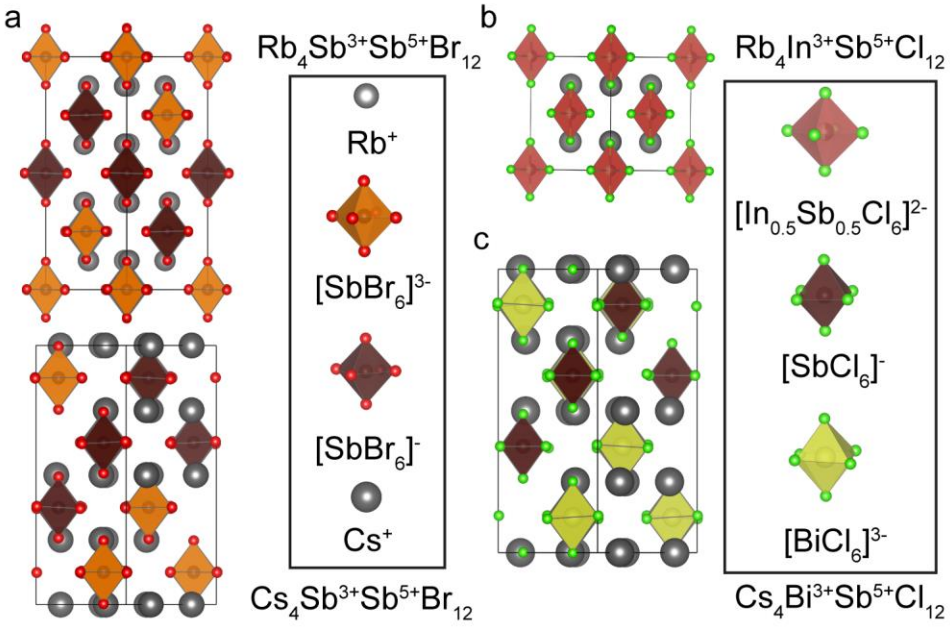

Figure 5.1. Previously reported mixed-valent metal halides at RT: a) $(Rb/Cs)_4Sb^{3+}Sb^{5+}Br_{12}$; b) $Rb_4InSbCl_{12}$; c) $Cs_4BiSbCl_{12}$.

Table 5.1. Known $A_4M^{III}Sb^{V}X_{12}$ phases.

Composition	*Space group*	*T (K)*	*a*	*c*	*Abs. max (nm)*	*Ref.*
$Cs_4Sb^{III}Sb^{V}Cl_{12}$	$I4_1/amd$	298	10.4650 (2)	21.0095 (7)	540.5	326, 330-331
$Cs_4Bi^{III}Sb^{V}Cl_{12}$	$I4_1/amd$	298	10.4928 (2)	21.1017 (6)	417	330-331
$Cs_4In^{III}Sb^{V}Cl_{12}$	Fm3m	4.7	9.9093 (1)	-	590	326, 330
$Rb_4In^{III}Sb^{V}Cl_{12}$	Fm3m	4.7	10.0613 (1)	-	-	330
$Rb_4Sb^{III}Sb^{V}Br_{12}$	$I4_1/amd$	4.7	10.706 (3)	21.695 (22)	"black"	317, 324
$Cs_4Sb^{III}Sb^{V}Br_{12}$	$I4_1/amd$	300	10.842 (3)	21.91(15)	"black"	320, 330, 332
$(NH_4)_4Sb^{III}Sb^{V}Br_{12}$	$I4_1/amd$	-	10.66	21.52	1053	317, 331, 333
"$Rb_4Sb^{III}Sb^{V}Cl_{12}$*"*	-	298	10.14 (2)	-	510.2	317, 326, 331

Although there is a large body of work related to the structures and properties of this

material family, the structure and properties of the Rb-Sb^{III}-Bi^{III}-Sb^{V}-Cl phases remain underexplored. While the tetragonal $Rb_4Sb^{III}Sb^{V}Br_{12}$ is known (Table 5.1),[323-324] the corresponding chloride has been observed to be either cubic,[317] cubic yet slightly disordered,[320] or to decompose into a reportedly monoclinic $Rb_{2.67}SbCl_6$ phase for which the structure is unknown.[327, 330] Furthermore, no reports exist on $Rb_4Bi^{III}Sb^{V}Cl_{12}$ or any related phase.

Herein we present that the cubic $Rb_4Sb^{III}Sb^{V}Cl_{12}$ is unstable and that the monoclinic $Rb_{2.67}SbCl_6$ phase is instead most correctly described as the red, orthorhombic $Rb_{23}Sb^{III}_7Sb^{V}_2Cl_{54}$. Additionally, this composition serves as a template for substitution with Bi^{3+} to generate a series of new structures within the $Rb_{23}Sb^{III}_{7-x}Bi^{III}_xSb^{V}_2Cl_{54}$ ($x \leq 3.5$) family, which exhibit very large, trigonal unit cells ($V \approx 16{,}000$ Å^3), tunable charge transfer bands, and second harmonic generation (SHG).

5.3. Experimental Methods

For detailed experimental details regarding materials, synthetic procedures, and characterization techniques, see chapter 7. Materials and Methods.

5.4. Results and Discussion

Red, hexagonal plates of $Rb_{23}Sb^{III}_7Sb^{V}_2Cl_{54}$ were grown solvothermally from an HCl solution (Figure 5.2a). The crystals tend to grow together and stack, resulting in varying color intensities. Previously, two phases, the cubic $Rb_4Sb^{III}Sb^{V}Cl_{12}$ and the monoclinic $Rb_{2.67}SbCl_6$ (a stoichiometry of $Rb_{24}Sb_9Cl_{54}$, which is not far off the true stoichiometry), were reported to form in the Rb-$Sb^{III/V}$-Cl compositional space. While the former was suggested to be cubic, it was also reported to decompose spontaneously at RT to the monoclinic phase, which was observed to grow as hexagonal platelets. At first glance, this agrees with the appearance of our crystals except that ours do not interact with polarized light, which would suggest a higher symmetry axis such as that found in a nearly cubic system. By measuring single crystal XRD, we were surprised to discover that the material adopts an orthorhombic structure with the *Cmcm* space group (a = 22.2915 Å, b = 12.8759 Å, c = 36.9787 Å; Figure 5.2b; Table 8.48-Table 8.51).

This structure significantly deviates from those observed for other M^{III}-Sb^{V} systems, in which the structures adopt a cubic or tetragonal unit cell with all octahedra effectively aligned along one of the unit cell axes (Figure 5.1a). The octahedra in $Rb_{23}Sb^{V}_7Sb^{III}_2Cl_4$, on the other hand, arrange into layers stacked along c, still comprised of 0D octahedra separated by Rb^+, but the octahedral orientation shifts across each layer in a repeating ABCABC stacking sequence. In this stacking, the CA layers resemble a slice of the tetragonal A_2MX_6 structure while the B layers (comprised entirely of $Sb^{III}Cl_6$ octahedra) pack along a different orientation, and while the A and C layers mirror each other across individual ABC blocks, adjacent ABC-ABC blocks have flipped orientation such that the octahedra zigzag along the c-axis *i.e.* they form a disconnected, corrugated

chain (best viewed along the (210) plane; Figure 5.2b). Within these zig-zagged layers the $[SbCl_6]^-$ octahedra occupy unique sites surrounded by six $[SbCl_6]^{3-}$ octahedra, with an average Sb···Sb distance of 7.48 Å with no Rb cations directly between them (Figure 5.3). The octahedra are clearly distinguished by size and shape, with the Sb^V octahedra being mostly undistorted (shortest Sb-Cl bond of 2.303 (16) Å vs. a longest Sb-Cl bond of 2.355 (16) Å), with an average Sb-Cl bond length of 2.3388 Å. In contrast, the lower charge of Sb^{III} results in a larger octahedron with an average Sb-Cl bond length of 2.6398 Å; moreover, the $5s^2$ lone pair of the Sb^{3+} cation is stereoactive and distorts the octahedron, resulting in three shorter bonds (2.499-2.528 Å) and three longer bonds (2.747-2.795 Å; Figure 5.4). The Sb^{III}-Cl bond lengths correlate well with those found for the $[SbCl_6]^{3-}$ octahedra in $Rb_7Sb_3Cl_{16}$ (average bond length = 2.6373 Å), but the octahedra in $Rb_{23}Sb^V_7Sb^{III}_2Cl_4$ are slightly more distorted than those in $Rb_7Sb_3Cl_{16}$ suggesting greater lone-pair stereoactivity.[334]

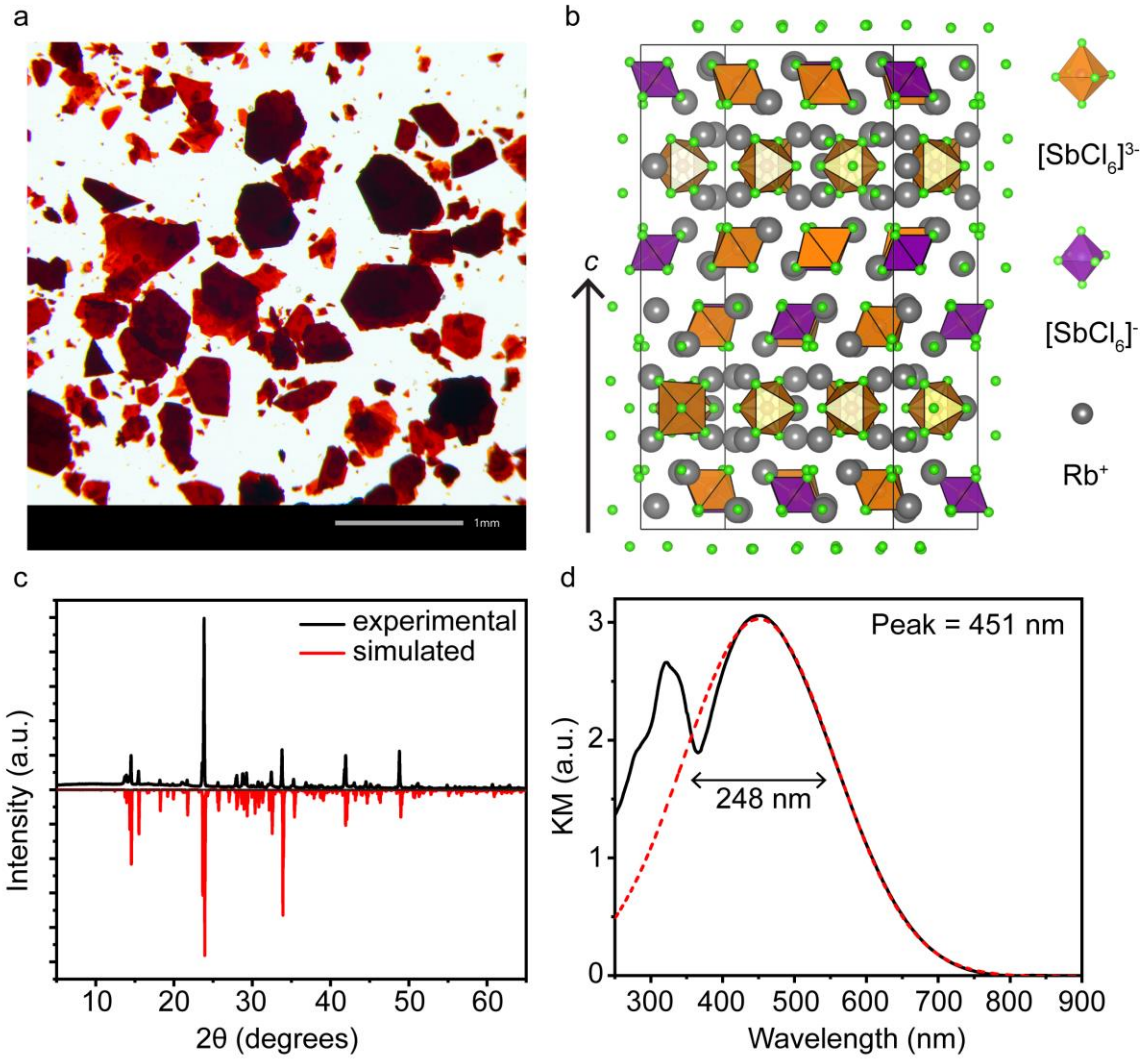

Figure 5.2. Structure and KM spectrum for $Rb_{23}Sb^{III}_{7}Sb^{V}_{2}Cl_{54}$. a) Photo of the crystalline material obtained from a typical solvothermal synthesis; scale bar is 1 mm in length. b) The unit cell viewed along the (210) plane; $[SbCl_6]^{3-}$ octahedra (orange), $[SbCl_6]^{-}$ octahedra (purple), rubidium cations (grey). c) PXRD pattern comparing the measured pattern (black) with that of the simulated patterns for $Rb_{23}Sb^{III}_{7}Sb^{V}_{2}Cl_{54}$ (red) and $RbSbCl_6$ (blue). d) KM transformed diffuse reflectance spectrum with the absorption edge roughly fit with a gaussian peak to estimate the peak width and position.

The deeply colored appearance of these crystals arises from charge transfer that is expected to occur from the $5s^2$ state of the Sb^{III} to the $5s^0$ of the Sb^{V}.[335] While clearly separated, this distance is within reason for outer sphere electron transfer[336] as distances of up to 20 Å can be surmounted in biological systems through this process.[337] However, the rates of electron transfer typically have an inverse exponential dependence.[338] For this reason, the shortest donor-acceptor distance, or in this case $Sb^{III}\cdots Sb^{V}$ distance, is likely to be more important. While the $Sb^{III}\cdots Sb^{V}$ distance within

a pseudo-layer is *ca.* 7.42 A, the $Sb^{III}\cdots Sb^{V}$ distance between layers containing Sb^{V} cations can be as low as 7.072 (3) A (Figure 5.5a). Additionally, the octahedra between these two layers are aligned with respect to one-another whereas they appear to have different orientations when compared with the Sb^{III}-only layer.

This seems to arise as a cooperative effect from the lone-pair stereoactivity in the Sb^{III} octahedra which expresses itself away from the Sb^{V} layers towards the Sb^{III}-only layers. This expansion appears to push the Sb^{V} octahedra slightly out of the plane, closer to one-another, and closer to the adjacent layer's Sb^{III}-octahedra. This is further shown by highlighting the bonds lengthened by lone-pair expression in Figure 5.5b.

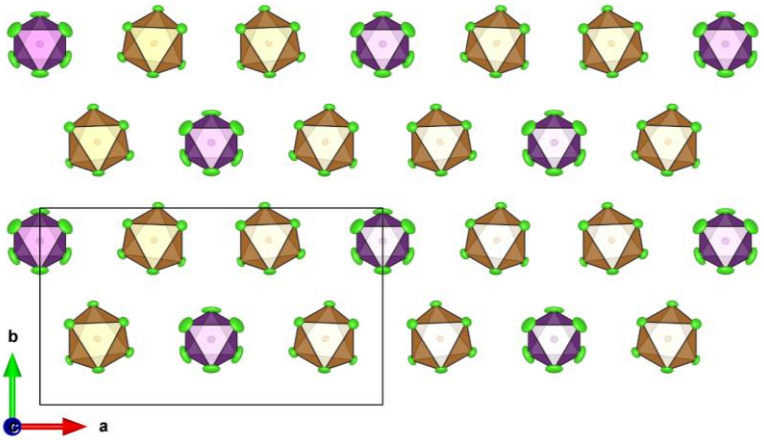

Figure 5.3. Single layer of 0D $[SbCl_6]^{3-}$ and $[SbCl_6]^{-}$ octahedra viewed along the *c*-axis.

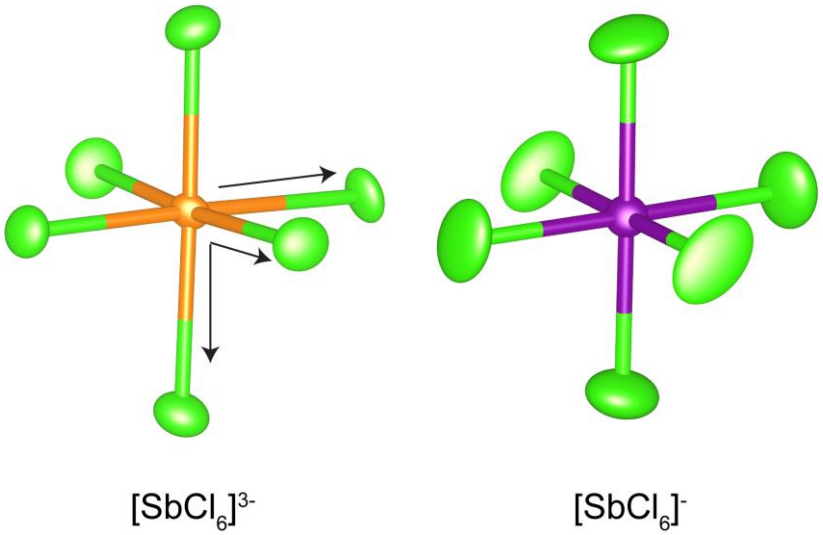

Figure 5.4. Comparison of $[SbCl_6]^{3-}$ and $[SbCl_6]^{-}$ octahedra.

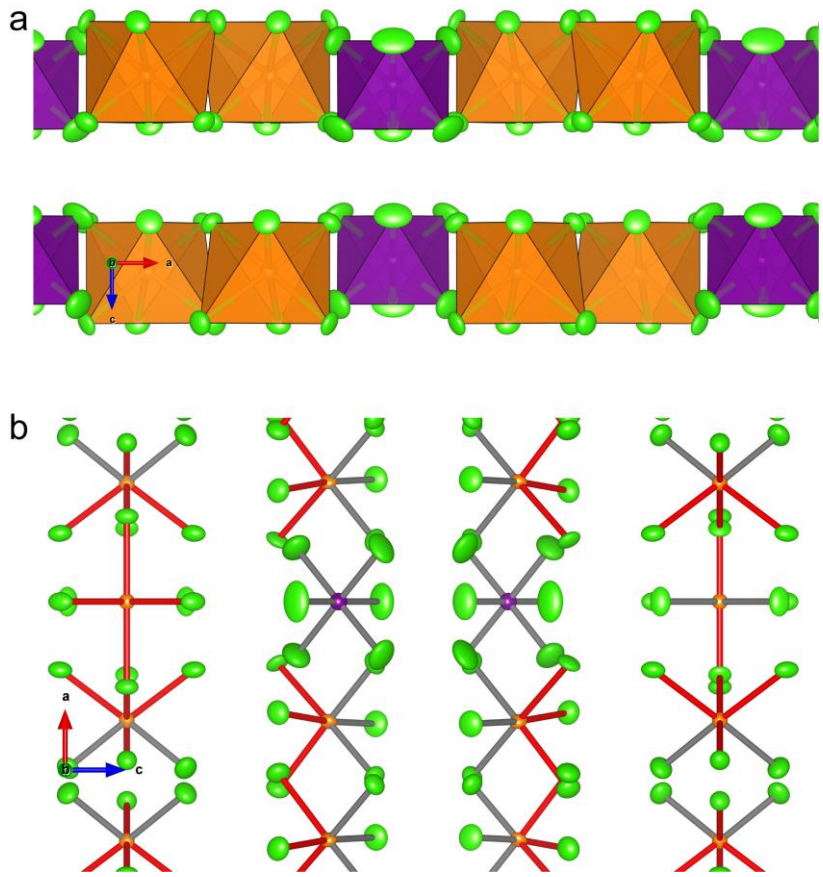

Figure 5.5. $[SbCl_6]^-$ and $[SbCl_6]^{3-}$ layer environments. a) Polyhedra viewed along the b-axis. b) The same section of the structure shown in a ball-and-stick fashion. Sb-Cl bonds shorter than 2.6 Å are grey whereas Sb-Cl bonds longer than 2.6 Å are red.

Powder XRD (PXRD) demonstrates that the measured crystals of $Rb_{23}Sb^{III}_7Sb^{V}_2Cl_{54}$ were representative of the entire reaction (Figure 5.2c). However, in our initial attempts to synthesize single crystals of $Rb_{23}Sb^{III}_7Sb^{V}_2Cl_{54}$, it became evident that the choice of oxidant during the synthesis plays a crucial role in obtaining a phase-pure product. Nitric acid, for example, is known to be a powerful oxidant. When used for the synthesis of $Rb_{23}Sb^{III}_7Sb^{V}_2Cl_{54}$, it results in large, colorless rods as a side product. These were found to be the $RbSbCl_6$ phase (Figure 5.7; Table 8.52-Table 8.55). To avoid this over oxidation, the oxidant was substituted for H_2O_2, which could be more readily decomposed.

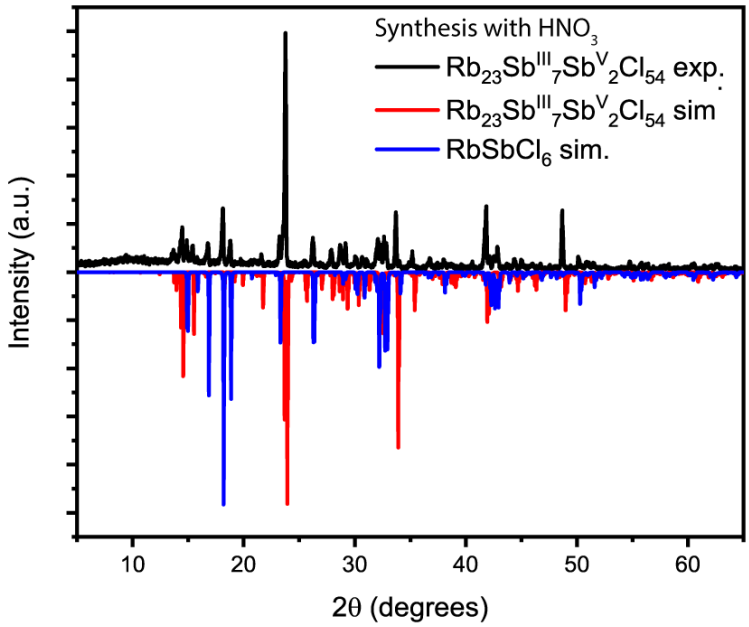

Figure 5.6. PXRD of $Rb_{23}Sb_9Cl_{54}$ synthesized with HNO_3 as the oxidant.

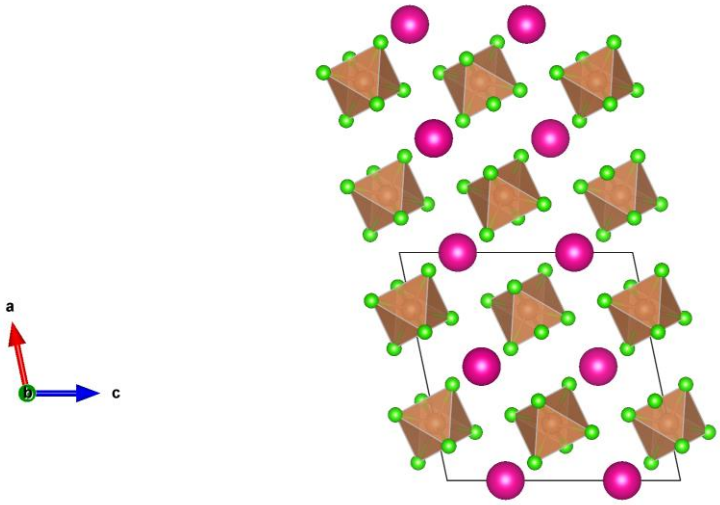

Figure 5.7. Crystal structure of $RbSbCl_6$.

Given that the previously mentioned and published mixed-valent structures all exhibited either cubic or tetragonal unit cells at RT, we created a structure field diagram to observe how this new orthorhombic structure could be related to the other known compositions. This was prepared by comparing the A/X and B/X size ratios for different symmetries and compositions (Figure 5.8a).[339] Based on this diagram it is clear that $Rb_{23}Sb^{III}_7Sb^{V}_2Cl_{54}$ occupies an otherwise empty region distinct from the other cubic and tetragonal phases.

By further substituting Sb^{3+} with Bi^{3+}, we sought to investigate the otherwise empty

compositional space above this orthorhombic structure as well as to observe how the charge transfer band would be altered by the expected change in unit cell size, octahedral separation, and electronic configuration.

Our initial attempts were centered on obtaining Sb^{3+} rich phases and occasionally resulted in crystals with a dirty, metallic appearance. Upon closer examination, it became clear that two phases were present and that $Rb_7BiSb_2Cl_{16}$ crystals had nucleated and served as a substrate for the growth of smaller, red crystals (Figure 5.8b).[334]

These red crystals have a strong absorption band in the visible regime, unlike that of either pure Sb(III) or Sb(V) materials, suggesting that this was another mixed-valent composition (Figure 5.8c) Furthermore, the peak absorption wavelength in the visible range was centered at roughly 450 nm. This is considerably blue shifted from that measured for $Rb_{23}Sb^{III}_7Sb^{V}_2Cl_{54}$, further implying that a mixed Sb^{III}/Bi^{III} phase was grown.

The structure of this material was determined by single crystal X-ray diffraction on a crystal similar to that shown in Figure 5.8b. This material was found to crystallize in a trigonal crystal system with the *R*32 space group with an unexpectedly large unit cell ($a = b$ = 12.95670 (10) Å, c = 111.7130(14) Å, V = 16241.4 (3) $Å^3$) for a fully inorganic material (Figure 5.8d; Table 8.56-Table 8.58). We determined the stoichiometry to be $Rb_{23}Bi_{2.50}Sb_{6.50}Cl_{54}$. Unlike the $Rb_7Bi_{3-3x}Sb_{3x}Cl_{16}$ family of structures, which contain edge-shared dimers, the structural units within this phase are restricted to ordered and disordered octahedra of varying sizes depending on their composition and oxidation state. The smallest of these octahedra are again those containing only Sb^{5+}, which have nearly the same average bond length of *ca.* 2.33 Å as those in the $Rb_{23}Sb^{III}_7Sb^{V}_2Cl_{54}$ phase. The other octahedra increase according to their Sb^{3+}:Bi^{3+} ratio with the largest units being Bi^{3+} rich. The overall structure appears to have several repeating layers, one three-layer block resembling that of $Rb_{23}Sb^{III}_7Sb^{V}_2Cl_{54}$ and a second three-layer block with disordered octahedra sandwiched by octahedra with large thermal parameters, these units arrange into disconnected zig zags similar to $Rb_{23}Sb^{III}_7Sb^{V}_2Cl_{54}$ (Figure 5.8e,f). The largest, Bi^{3+} rich octahedra create layers between which the smaller octahedral layers are found; additionally, these Bi-rich layers serve as turning points for the superstructure corrugation.

Given the apparent solid solution that exists amongst the M^{3+} octahedra between Sb^{3+} and Bi^{3+}, we synthesized several additional materials with full and variable Bi^{3+} substitution. These samples were found to crystallize in the same trigonal space group as the mixed-metal samples, with the lattice parameters following Vegard's law (Figure 5.9a; Table 8.59-Table 8.62).

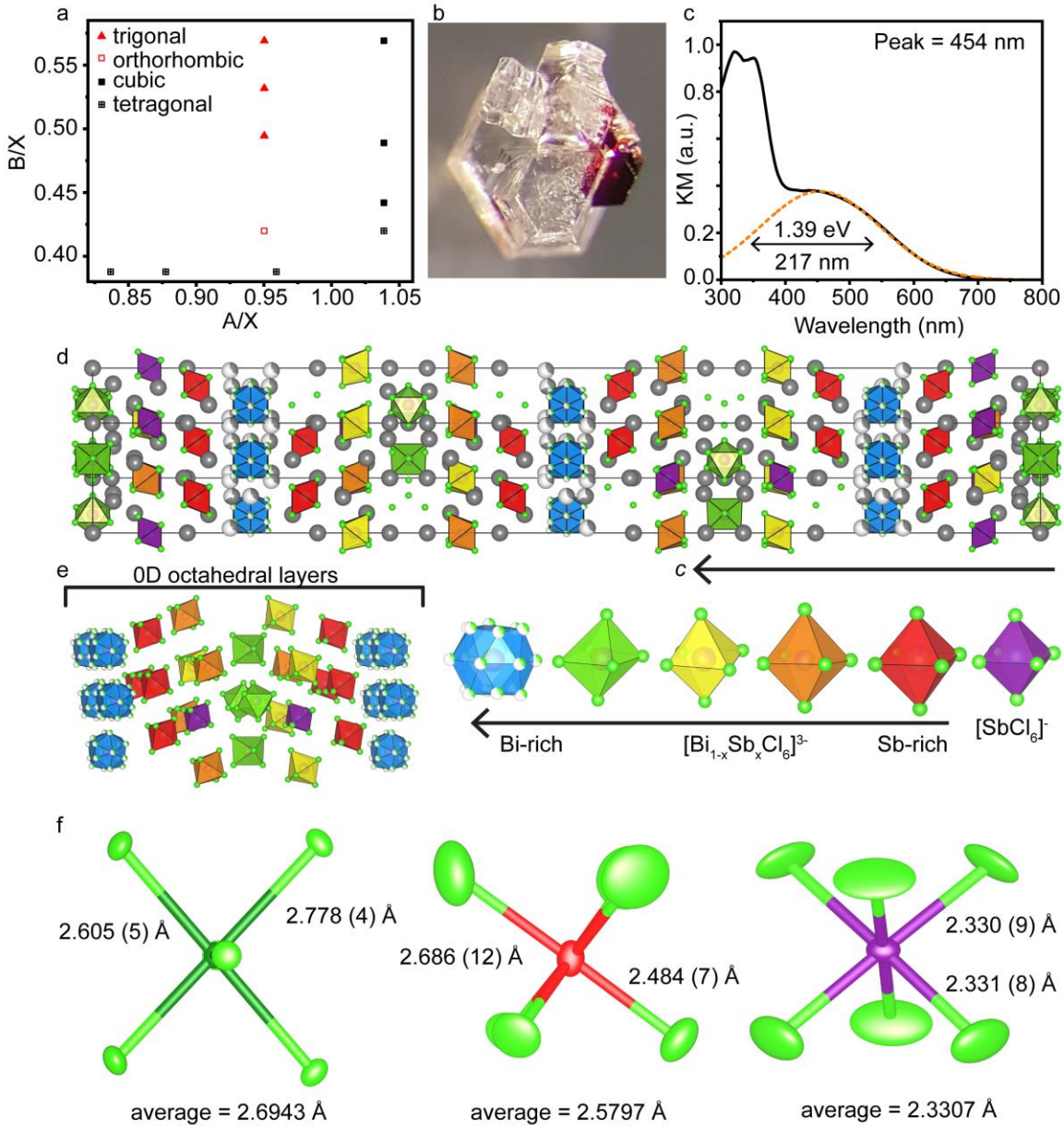

Figure 5.8. Structural and optical properties of the $Rb_{23}Bi_{2.50}Sb^{III}_{4.50}Sb^{V}_{2}Cl_{54}$ phase. a) Structure field diagram of known mixed-valent metal-halide phases and $Rb_{23}Bi_{7-x}Sb_xSb^{V}_{2}Cl_{54}$ phases. b) optical image of the red, $Rb_{23}Bi_{2.50}Sb^{III}_{4.50}Sb^{V}_{2}Cl_{54}$. c) KM spectrum for $Rb_{23}Bi$ Sb $Sb^{V}_{2}Cl_{54}$ with 3 contributing sub-peaks. d) the unit cell of $Rb_{23}Bi_{2.50}Sb^{III}_{4.50}Sb^{V}_{2}Cl_{54}$ displayed along the (210) plane. e) an alternative view on 1/3rd of the unit cell to demonstrate the 0D layers and the individual octahedra it comprises. f) Comparison of Bi-rich, Sb-rich, and Sb^{V} octahedra.

Structurally, very little changes between the Bi^{3+} only, Bi^{3+} rich, and Bi^{3+} poor samples. The Sb^{5+} octahedra remain in the same position and the overall superstructure corrugation is still observable. The changes to composition are, however, enough to affect the energy of the charge

transfer band that gives these phases their intense colors (Figure 5.9b). For example, $Rb_{23}Bi_7Sb_2Cl_{54}$ is a light-yellow crystal (inset image in Figure 5.9a); this can also be observed from the KM spectra measured for a series of compositions in the $Rb_{23}Bi_{7-x}Sb^{III}_xSb_2Cl_{54}$ series (Figure 5.9b).

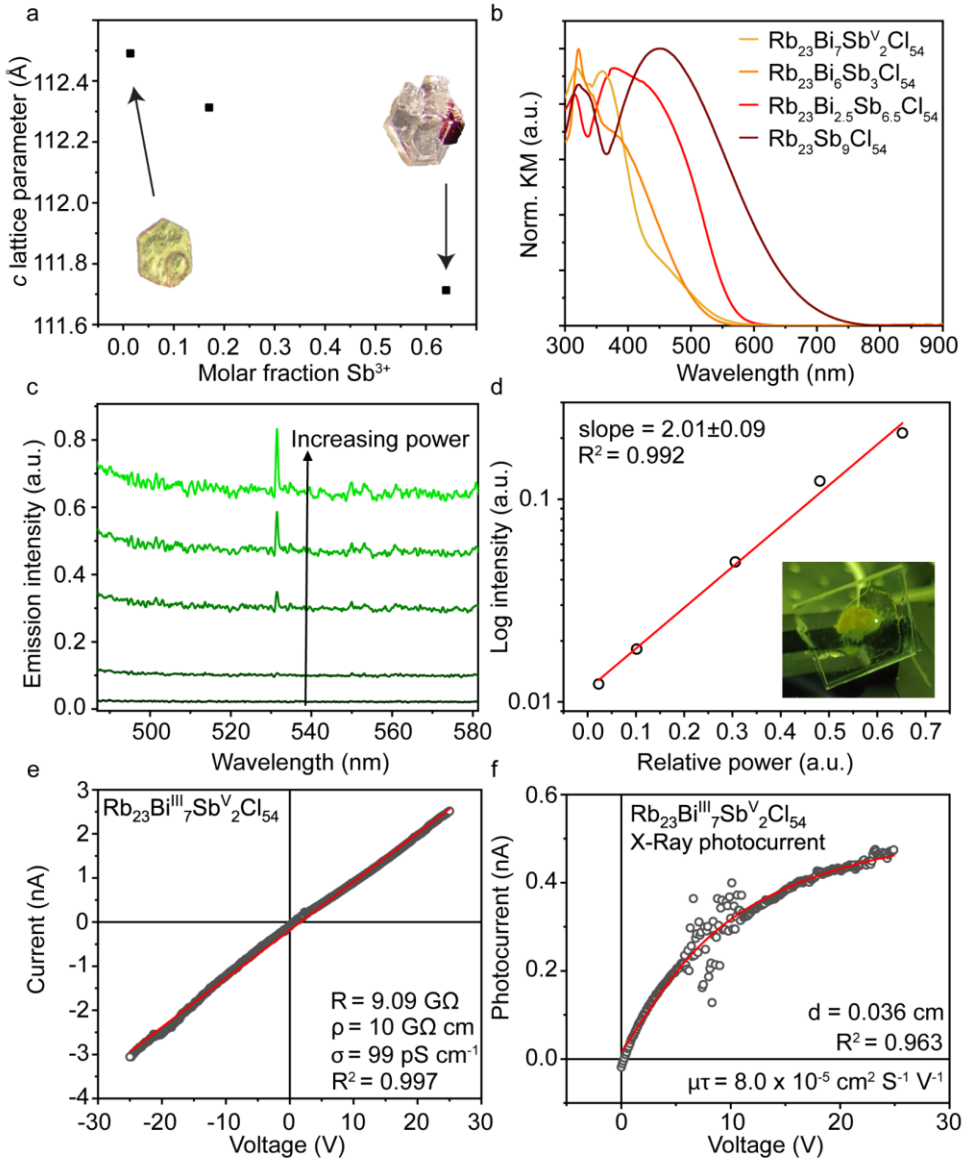

Figure 5.9. Tunability, resistivity, X-ray photoconductivity and SHG: a) compositional tunability in the $Rb_{23}Bi_{7-x}Sb_xSb^V_2Cl_{54}$ family, inset images are of measured crystals; b) KM spectra of various members of the $Rb_{23}Bi_{7-x}Sb_xSb^V_2Cl_{54}$ family with differing Bi^{3+}:Sb^{3+} ratios; c) SHG spectra with increasing laser power; d) Power dependent SHG intensity measurement; inset photo demonstrates SHG; e) I-V curve for $Rb_{23}Bi_7Sb^V_2Cl_{54}$; f) X-ray photoconductivity.

From these, it can be concluded that Bi^{3+}-Sb^{5+} and Sb^{3+}-Sb^{5+} charge transfer interactions occur at visibly different energies, and this can be further illustrated by comparing the gaussian fits for each charge transfer band (Figure 5.10). Although a peak shift is observed, the broadness and overlap of these peaks precludes any determination of the individual contributions of each transition to the overall spectral shape.

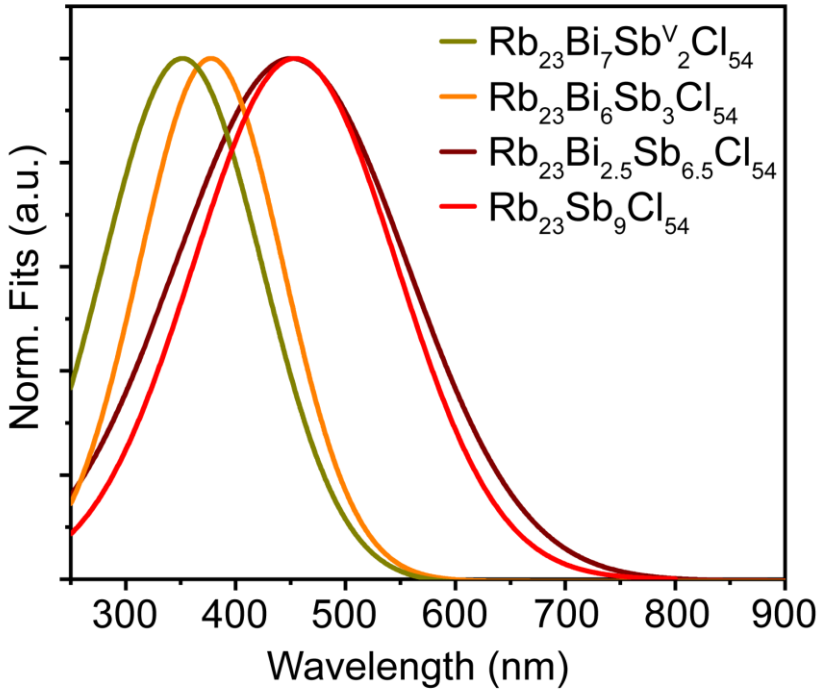

Figure 5.10. Charge-transfer band tunability.

Given the unusually large structure of the structures in the $Rb_{23}Bi_{7-x}Sb^{III}_xSb_2Cl_{54}$ series, we measured second harmonic generation (SHG) to check whether we had correctly ascribed the *R*32 space group to $Rb_{23}Bi_7Sb^V_2Cl_{54}$. Briefly, the *R*32 space group is one of the piezoelectric space groups, which simply implies that the unit cell is polar with an intrinsic dipole moment. Effects such as piezoelectricity and SHG are related to the symmetry of the structure rather than the chemical composition and hence serve as a good check for noncentrosymmetry in a structure. SHG, specifically, is a process in which some photons entering a material are effectively upconverted from frequency, ω, to 2ω while conserving the total energy *i.e.* the number of photons is halved after conversion. Experimentally, for the fundamental emission from a YAG:Nd laser, this appears as 1.064 μm → 532 nm conversion where the invisible IR beam becomes green.

To examine this property, we exposed a polycrystalline powder of $Rb_{23}Bi_7Sb^V_2Cl_{54}$ to a 1.064 μm laser pulse. A powder is well suited as it contains all possible crystal orientations thus

there will be some grains where crystal axes orient towards the incident beam according to a phase-matched condition, required for the SHG process. While scanning the focused laser beam across the sample, some areas would produce visible green spots. Spectrally, this SHG emission occurs as a sharp line located exactly at 532 nm (Figure 5.9c). Furthermore, the intensity of this peak is expected to have a quadratic power dependence. When log(intensity) was plotted against power, a line with a slope of 2 was found further confirming the presence of non-centrosymmetry in $Rb_{23}Bi_7Sb_2Cl_{54}$ (Figure 5.9d).[340-341]

Having confirmed the structures of these materials and having observed charge-transfer band tunability, we turned our attention towards potential applications for these materials. Previously, Day et al. had characterized the electrical properties for several $A_4M^{III}M^{V}X_{12}$ phases and investigated photoconductivity as well as photocatalysis.[328] They found that all the phases that they investigated were highly resistive with conductivity that increased with temperature, effectively identifying these materials as wide-gap semiconductors. However, no significant photoconductivity or changes under O_2 or H_2 were observed (Table 5.2).

Additionally, we considered the utility of these phases in X-ray detection. In several recent reports, highly resistive metal-halides such as the 0D $Cs_3Bi_2I_9$ or the 2D $(NH_4)_3Bi_2I_9$ have been presented as possible alpha-particle and X-ray detector materials, respectively.[308, 342-343] The benefit of using low-dimensional and 0D materials of this type with high resistivities is that these will have very low noise under bias as a result of their intrinsically high resistivity.[118, 334]

I-V curves were only measured for $Rb_{23}Bi_7Sb^{V}_2Cl_{54}$ as single crystals of suitable size could not be grown for other compositions. This material was found to be very resistive ($1.0x10^{10}$ Ωcm), as expected from previously reported values (Figure 5.9e). While slightly less resistive than other mixed-valent materials, the resistivity is on par with values measured for other pnictogen-halide based low-dimensional materials such as $Rb_7Sb_3Cl_{16}$ or the $A_3M_2X_9$ series.

Table 5.2. Reported resistivities for mixed-valent $A_4M^{III}M^{V}X_{12}$ materials.

Composition	*R (Ωcm)*	*Ref.*
$Cs_4Bi^{III}Sb^{V}Cl_{12}$	$6.06x10^{14}$	328
$Cs_4Sb^{III}Sb^{V}Cl_{12}$	$2.74x10^{11}$	328
$Cs_4In^{III}Sb^{V}Cl_{12}$	$1.06x10^{15}$	328
$Rb_4Sb_2Cl_{12}$	$3.3x10^{12}$	328
$(NH_4)_4Sb^{III}Sb^{V}Br_{12}$	$1x10^{7}$	323

Exposing a single crystal of $Rb_{23}Bi_7Sb^{V}_2Cl_{54}$, with a thickness of 0.36 mm, to X-rays resulted in a measurable photoresponse that could be fit with the Hecht model (Figure 5.9f). Doing so yields a μτ product of $8.0x10^{-5}$ cm^2 s^{-1} V^{-1}. Surprisingly, this is only 10x lower than the best-to-date μτ product reported for $Cs_3Bi_2I_9$.[308, 343] Photoconductivity was also examined, but again no significant response could be detected.

Considering the existence of the visible charge transfer band, we further examined if any

of these materials exhibited PL. While no reports have indicated that M^{III}/Sb^{V} mixed-valent materials exhibit any PL, previous studies on Wolfram's red salt (WRS), $[Pt^{II}(C_2H_5NH_2)_4][Pt^{IV}(C_2H_5NH_2)_4Cl_2]Cl_4 \bullet 4H_2O$, and *N*,*N*-dimethylaminobenzylidene-1,3-indandione (DMABI) have found evidence of emission from localized self-trapped charge-transfer excitons (STCTEs). In the case of DMABI, this was observed around 2.5 eV at RT; whereas, WRS exhibited an emission peak around 1.15 eV at 4.2 K.[344-345] In both cases, the emission was reported to be very weak (<0.1% for DMABI).[346]

As no visible PL was observed in our materials down to 12 K, we also examined the possibility of IR emission at 77 K. Samples were cooled in a cryostat and illuminated with a Xe lamp. An IR detector ($In_{1-x}Ga_xAs$) was utilized with several long pass filters to exclude scattered light from the lamp. No emission was observed from any $Rb_{23}Bi_{7-x}Sb_xSb^{V}_2Cl_{54}$ samples. Given the lack of visible emission in these systems, we also investigated the dilution of Sb^{3+} centers with both In^{3+} and Bi^{3+} by targeting the $Rb_{23}Bi_{7-x-y}In_xSb_ySb^{V}_2Cl_{54}$ system. One reaction incidentally yielded a new oxychloride phase, Rb_2SbCl_5O (Figure 5.11; Table 8.63-Table 8.66). Aside from this, pure phases seldom formed, and no PL was observed down to 77 K in all cases.

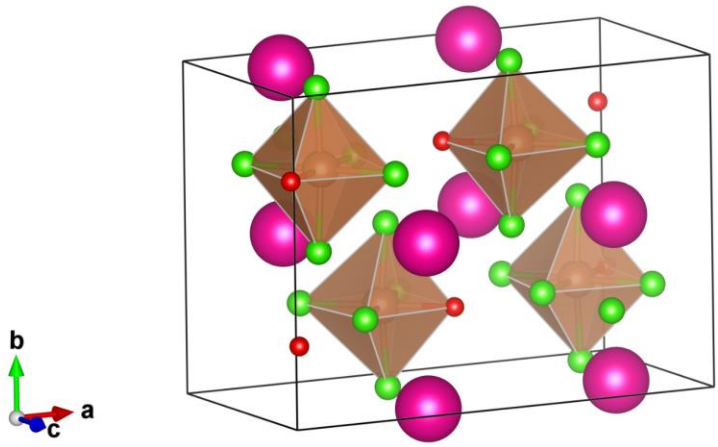

Figure 5.11. Unit cell of Rb_2SbCl_5O.

5.5. Conclusion

After over a century of research on the $A_4M^{III}M^{V}X_{12}$ family, new phases can still be discovered within this compositional space. We demonstrated that the combination of Rb, Sb^{III}, Sb^{V}, and Cl results in the orthorhombic $Rb_{23}Sb^{III}_7Sb^{V}_2Cl_{54}$, while the addition of Bi^{III} generates a family of $Rb_{23}Bi^{III}_{7-x}Sb^{III}_xSb^{V}_2Cl_{54}$ ($x \leq 7$) materials that crystallize in the non-centrosymmetric *R*32

space group. This non-centrosymmetry was confirmed by the observation of SHG with a 1064 nm laser.

Going further, we examined the possibility of using such mixed-valent phases for X-ray detection. A clear photoresponse was observed with a μτ product of 8.0×10^{-5} cm^2 s^{-1} V^{-1}. These results clearly indicate that further studies on the use of such mixed-valent materials in high-energy radiation detection applications are warranted. While the exact benefit of the intervalent or metal-metal charge transfer is not yet certain, it may be possible that the rate with which carriers are able to hop or move through a material is improved through the expected outer-sphere electron transfer mechanism as compared to single oxidation state low-dimensional materials.

Chapter 6. Summary and Outlook

6.1. Summary

In summary, this dissertation has served to present several new additions to the growing family of luminescent, lead-free metal-halides. We have focused specifically on 0D materials, which were previously a relatively unexplored compositional space in terms of optical properties and applications. First, by demonstrating that the $Cs_{4-x}A_xSn(Br_{1-y}I_y)_6$ (A=Rb, K; $x\leq1$; $y\leq1$) family are tunable, luminescent STE emitters. Second, by showcasing the ability of these materials as well as hybrid organic-inorganic 0D materials and 1D lead-free metal halides to act as extremely temperature sensitive phosphors for time-resolved remote-optical thermography. Third, by expanding the catalogue of oxidatively stable 0D metal-halides with the discovery of the fully inorganic $Rb_7Bi_{3-3x}Sb_{3x}Cl_{16}$ family of materials and demonstrating their potential as thermographic luminophores. Finally, by reinvestigating the field of low-dimensional mixed valent materials to discover the $Rb_{23}Bi^{III}_{7-x}Sb^{III}_xSb^V_2Cl_{54}$ ($x\leq7$) series of materials.

6.2. Outlook

By exploring all of these different materials, we have demonstrated the unique optical properties exhibited by 0D metal-halides. While our research, as well as the research of other members in the Kovalenko group, has shed light on applications where these materials have proven useful (*e.g.* thermometry and scintillation), there is still room for further exploration. One way that we can consider novel applications of these materials may be to grade material properties against application requirements (Table 6.1).

In doing so, we can rationalize why certain applications are not ideal and where material improvements can be focused. For example, literature reports still attempt to sell the dream of 0D metal-halide based SSL, the current state of the field is far from any useful transition towards lighting.

Table 6.1. New and potential applications for 0D metal-halides.

Application	*Broad PL*	*Large Stokes Shift*	*Temp. dep. PL lifetime*	*Long RT PL lifetime*	*Temp. dep. PLQY*	*λ_{exc} <400 nm*
SSL	+	+	–	~	–	–
Thermometry	~	~	+	~	~	~
X-ray Scint.	~	+	~	–	–	~
Neutron im.	~	+	~	~	–	~
Solar conc.	~	+	~	~	–	–
FLQR codes	+	+	~	~	–	~
"STED"	~	+	+	~	+	–

Of course, this is not without a reason. 0D metal halides, as mentioned in Section 1.4.5.2, have several highly sought after optical characteristics when it comes to solid state lighting: broadband and tunable PL and large Stokes shifts that would minimize self-absorption. In addition, their long PL lifetimes, which would be a drawback in some applications, is not a problem for lighting. However, for all their promise, the hopes of these materials as white-light phosphors are still marred by several, currently inescapable, characteristics: their strongly temperature dependent optical properties, and their predominantly UV excitation maxima.

In fact, heating these 0D metal-halide phosphors by only 10 °C can reduce their PLQY by to 25% or 30% depending on composition, and since the surface of an LED may reach temperatures of up to 70 °C, this thermal quenching represents a significant hurdle. This effect disqualifies any remaining 0D metal-halides in our current library of known materials from participating as a useful SSL phosphor. Furthermore, the majority of commercially available excitation sources are currently blue LEDs rather than violet or UV.

For any significant contribution towards SSL phosphor materials, future 0D metal-halides would need to be designed with high temperature quenching regimes (ideally above 70° C) and blue (440-460 nm) PLE maxima. As of writing in 2020, no material fits this stringent set of requirements.

Alternatively, X-ray scintillation and thermometry/thermography as demonstrated by the Kovalenko group are either less affected by such characteristics or even make use of them. So what about new or previously unexplored research directions? Where might 0D metal-halides fit in the future? Table 6.1 also includes the same properties-requirements analysis for several potentially fruitful applications in optoelectronic research.

To start, we can consider more imaging or scintillation related applications. Obviously, γ radiation can be detected by a scintillator, but the lighter elements that compose most luminescent

0D metal-halides are not ideal for this. Instead, elements such as Cs, Tl, Pb, Bi, and I should be utilized. Instead, neutron imaging via recoil protons could be an excellent application with the use of NCs of these materials as self-absorption is generally an unwanted and parasitic process. Therefore, the large Stokes shifts of these materials would be useful. Furthermore, most of the other properties of 0D metal-halides would not be detrimental.

6.2.1. Luminescent solar concentrators

Another application that could utilize some of the properties of 0D materials, when prepared as NCs, without being bogged down by their electrical shortcomings is the luminescent solar concentrator.[347-349] This technology relies on luminescent materials to concentrate indirect or diffusely scattered light in the environment onto a solar cell. Since their conception, these devices have predominantly used organic dyes as luminophores as a result of their typically high PLQYs. Such devices have so far demonstrated PCEs of up to 3.4% (with organic dyes and Si) although the theoretical maximum is as high as 26.8% thus illustrating the importance of additional factors in luminophore choice and LSC construction.[350-353] The general requirements for ideal luminophores include broad spectral absorption with high absorption efficiency (large absorption coefficients), large Stokes shifts (minimal absorption/emission overlap), high PLQY, and matched emission wavelength and PV spectral response (*i.e.* 1.1 eV for Si or 1.4 eV for GaAs).[352, 354]

Given these demanding requirements, few luminophores are able to satisfy all criteria. While dye molecules have shown promising performance, they tend to have non-negligible emission/absorption overlap, narrow absorption bands, and limited photostability. Various quantum dots (*e.g.* CdSe/CdS, CdSe/ZnS, $CuInS_2$ and perovskite NCs have also been recently utilized in this system, and while these have achieved efficiencies up to 9%, they too suffer from similar drawbacks as well as decreased solubility in the host matrix.[353, 355-361] Therefore, 0D metal-halides with PLQY's of up to 90% and large Stokes shifts may be promising contenders in this field. No reports have currently shown a working 0D-based luminescent solar concentrator, and any attempts will require a broader library of 0D, luminescent metal-halides as our current materials share many of the drawbacks of molecular dyes and quantum dots: narrow absorption bands, limited visible absorption, potentially decreased matrix solubility, and non-PV-resonant emission energy. Furthermore, $Rb_7Sb_3Cl_{16}$ is currently the only 0D metal-halide for which the absorption coefficient has been reported (~150 cm^{-1}), and it may not be large enough for this application.[334] However, the lack of investigation on this topic precludes any further general statements except that meaningful research on the topic of LSCs will require this value to be measured and considered.

The final two future applications are also best served by NCs, but they also make use of the greatest number of material features without being detrimentally affected by other shortcomings. The first of these is fluorescent-lifetime encoded security tags or quick read codes.

6.2.2. Fluorescent-lifetime encoded security tags

The essence of this application is in creating covert security features to protect consumer items from counterfeiting by printing an image or code with two NC inks that exhibit unicolor emission but have measurably different PL lifetimes. At the time of writing, this has been effectively demonstrated once with carbon dots.[362] Although carbon dots have excellent stability, their emission is likely permanent defect related, and this may hinder batch-to-batch reproducibility as well as scalability (hydrothermally synthesized). We have recently submitted a manuscript detailing the use of perovskite NC with ethylene diamine inclusions as alternatives for this same purpose. However, in this work we found it difficult to achieve truly unicolor emission due to varying FWHMs of the emission peaks from the two different nanocrystal compositions. Therefore, 0D metal-halide NCs could provide a remedy to the problems faced in both situations. First, it has been demonstrated in this dissertation that 0D metal-halides have intrinsic, structurally and compositionally determined emission wavelengths and emission lifetimes. In some cases, such as $Cs_{4-x}A_xSn(Br_{1-y}I_y)_6$ these properties can be varied almost independently *e.g.* by compensating the blueshift from K addition by adding a small amount of I, a green-emitting powder could be generated with a similar emission wavelength to Cs_4SnBr_6 but with faster emission. In addition to this, and solving the problem faced by perovskite NCs, STE emitting 0D materials have intrinsically broad emission that would render decoding an image via color settings difficult, if not impossible.

The final application, which we have already conducted some preliminary studies towards, is the use of 0D metal-halides as stimulated emission depletion microscopy (STED)-like fluorophores.

6.2.3. "STED" microscopy and FLIM-nanoscopy

STED microscopy is a super resolution microscopy technique that allows for sub-250 nm resolution thus enabling imaging of cellular organelles, cytoskeletal features such as actin, or viruses.[363-365] Typically, this is achieved through the use of a 2-laser system; one laser for excitation and one for depletion.[366] The depletion laser is donut shaped and aligned to the excitation beam; this laser effectively depletes any fluorophores in its path. The remaining pinhole leftover from this 2-beam arrangement is abbe diffraction unlimited and has been demonstrated to result in resolutions down to 20-30 nm.[364]

0D STE-emitting metal-halides may be useful due to their large Stokes shifts, which significantly inhibit re-excitation by the depletion laser and allows for a broader selection of depletion laser wavelengths to be utilized.

Our initial studies found that the depletion process that plays a role in normal STED is instead a quenching process for 0D metal-halides akin to what we observed in Chapter 3 (Figure 6.1). In other words, we found that the STED depletion laser heats the 0D metal-halide resulting

in localized quenching. This was demonstrated with a powder film of $(TMEDA)_4SnI_6$.

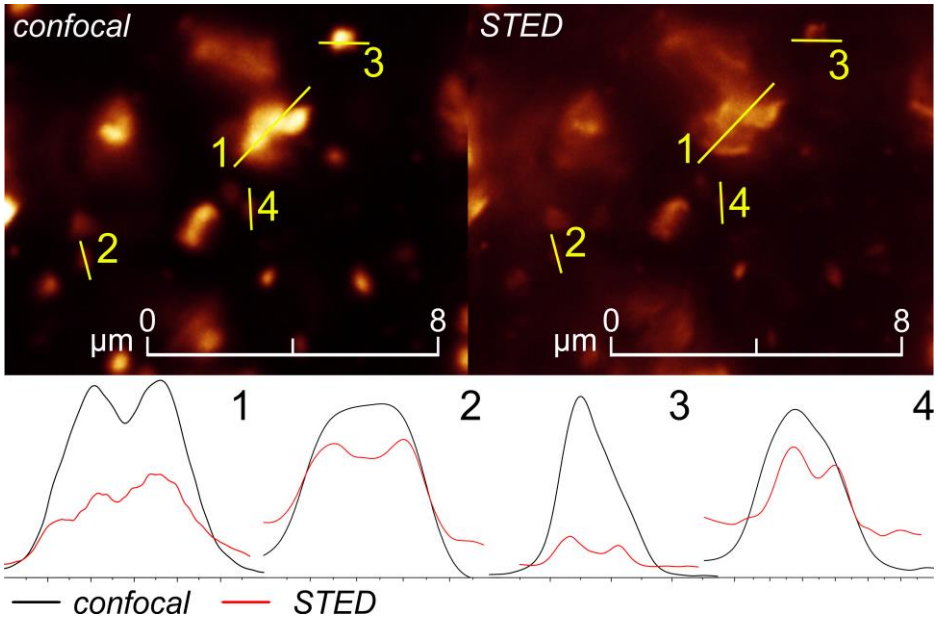

Figure 6.1. Confocal and STED comparison of a group of $(TMEDA)_4SnI_6$ crystals. The spectra numbered 1-4 correspond to the numbered yellow lines. The sample was excited with a continuous wave (CW) 405 nm laser and depleted with a 592 nm CW laser

This can be observed by comparing the intensity spectra along various lines in images taken in both confocal and STED configurations (yellow-lines and spectra numbered 1-4). Initial results indicate that these materials are able to act as fluorophores for STED imaging. Already, with a commercial system we were able to observe an improvement in the resolution with the ability to discern closely spaced crystallites (Figure 6.1). Furthermore, preliminary studies have shown that these materials, like semiconductors, are stable under excitation and can be reversibly excited and depleted for numerous cycles without bleaching. In contrast, commercially available dyes tend to require packaging in dark containers and storage in dark, refrigerated environments. From an initial perspective, 0D metal-halide fluorophores appear to combine the benefits of traditional molecular dyes with the robust stability of bulk semiconductors.

An added benefit of this approach that we noticed whilst measuring is that this local thermal depletion can be achieved with very little power. This could be of benefit if samples are potentially sensitive to the heating effects of the depletion laser. During the course of these initial studies, we still faced several issues that require further investigation: limited blue absorption and large particle sizes with high polydispersity. This first challenge may or may not be important depending on the samples being investigated and the STED-imaging system being utilized. Our commercial system was limited to 405 nm excitation, but systems exist with 355 nm excitation and great customizability. The second challenge, however, is critical for moving towards a true proof-of-

concept for STED and towards another potential spin-off — FLIM nanoscopy.

This would be effectively a super-resolution microscopy form of thermography. This approach would require a 2-laser STED system in which the excitation laser could also be pulsed and synced to a TCSPC system. This could yield diffraction unlimited thermal images with which modern circuits, composed of billions of nanometric transistors could be potentially investigated. This concept could be potentially extended towards biological studies if future materials or morphologies were found to be stable in biological media.

Given these widely differing applications that could be approached utilizing these materials, I believe that these materials have only just begun to be explored. Furthermore, materials discovery within the solid-state and materials chemistry communities is needed to find compositions that can answer the many requirements of applications yet unfulfilled by our current materials library.

Chapter 7. Materials and Methods

7.1. Materials

Cesium bromide (CsBr, 99%), cesium chloride (CsCl, 99.9%), and rubidium bromide (RbBr, 99.8%) were purchased from ABCR. Cesium bromide (CsBr, 99%) and tin (II) bromide ($SnBr_2$, 99.2%) were purchased from Alfa Aesar. Tin (II) iodide (SnI_2, 99%) was purchased from STREM Chemicals, Inc. Cesium iodide (CsI, 99.9%), rubidium chloride (RbCl, 99+%), and hydrogen peroxide (H_2O_2, >30%) were purchased from ACROS. Potassium bromide (KBr), silver bromide (AgBr), and antimony (III) oxide (Sb_2O_3, >98%) were purchased from Fluka. Sodium bromide (NaBr, ≥99.5%), potassium chloride (KCl, ≥99.5%), nitric acid (HNO_3, ≥65%), antimony (III) oxide (Sb_2O_3, 99%), and bismuth (III) oxide (Bi_2O_3, 99.9%) were purchased from Sigma Aldrich. Hydrochloric acid (HCl, 37%) was purchased from VWR. Indium (III) oxide (In_2O_3, 99.999%) was purchased from Koch-Light Laboratories.

All chemicals were stored and handled, and all manipulations were performed, under ambient conditions. All chemicals were used as received without further purification

Pyrex tubes (DURAN®) were purchased from Schott AG (12.00 ± 0.16 mm outer diameter with 1.50 ± 0.07 mm thickness). These were made into ampules and sealed using an oxygen-hydrogen flame.

Stainless steel autoclaves from Parr instruments and Amar Equipments were utilized with PTFE containers for all solvothermal syntheses

7.2. Synthetic procedures

7.2.1. Cs_4SnBr_6 synthesis

CsBr and $SnBr_2$ were mixed in a 4.5:1 molar ratio, mortared, and pressed together into a pellet (> 5 tons of pressure, 12 mm die). The pellet was then sealed under vacuum (10^{-2} – 10^{-3} mbar) in a Pyrex tube and heated to 350 °C for 60 hours. The tube was opened in the glovebox, and the above process was repeated once more. The previously reported pseudo-binary phase diagram shows that Cs_4SnBr_6 undergoes a peritectic decomposition when heated above 380°C. Accordingly, cooling a melt with this composition, the resulting product consists of a mixture of CsBr, $CsSnBr_3$, and Cs_4SnBr_6. Therefore, a phase pure synthesis of Cs_4SnBr_6 can only be achieved by annealing a solid mixture of CsBr and $SnBr_2$.

7.2.2. $Cs_{4-x}A_xSn(Br_{1-y}I_y)_6$ (A = Rb, K; x ≤ 1, y ≤ 1) synthesis

The synthesis of mixed cation, mixed anion, or mixed cation and anion phases was conducted using the same general procedure as above. *For A-site substitution:* CsBr was replaced with RbBr or KBr. The total, molar quantity of Cs, Rb, and K was at least 4.5x that of Sn. *For X-site substitution:* iodide was introduced into the system by exchanging CsBr for CsI. In the case of Cs_4SnI_6, $SnBr_2$ was replaced with SnI_2. Briefly, mortared samples were pressed at pressures >5 tons in an Ar-filled glovebox, sealed in evacuated Pyrex tubes, and heated to 350 °C. This was repeated at least twice until a visually off-white material was obtained after grinding. Further heating is possible, but not necessary after this point. Single crystals were grown by subjecting a previously prepared sample of Cs_4SnBr_6 to additional heating cycles. The length of each heating cycle was extended to 100 hrs. Through this approach small crystals, 20-40 microns in size, were successfully grown.

7.2.3. $Rb_7Sb_3Cl_{16}$ synthesis

In a typical synthesis, Sb_2O_3 (1.5 mmol) was dissolved in HCl (5 mL) while stirring. Once a clear solution was obtained, RbCl (7 mmol) was added directly to the Sb_2O_3/HCl solution and the autoclave was sealed and placed into a muffle furnace. The autoclave was then heated to 160 °C at 50 °C/hr and kept at this temperature for 24 hours before cooling to RT at a rate of 5 °C/hr. The contents of the reaction were then separated by vacuum filtration without washing.

7.2.4. $K_7Sb_3Cl_{16}$ synthesis

In a typical synthesis, Sb_2O_3 (1.5 mmol) was dissolved in HCl (5 mL) while stirring. Once a clear solution was obtained, KCl (7 mmol) was added directly to the Sb_2O_3/HCl solution and the autoclave was sealed and placed into a muffle furnace. The autoclave was then heated to 160 °C at 50 °C/hr and kept at this temperature for 24 hours before cooling to RT at a rate of 5 °C/hr. The contents of the reaction were then separated by vacuum filtration without washing.

7.2.5. $Rb_7Bi_3Cl_{16}$ synthesis

In a typical synthesis, Bi_2O_3 (1.5 mmol) was dissolved in HCl (5 mL) while stirring. Once a clear solution was obtained, RbCl (3 mmol) was added directly to the Bi_2O_3/HCl solution and the autoclave was sealed and placed into a muffle furnace. The autoclave was then heated to 160 °C at 50 °C/hr and kept at this temperature for 24 hours before cooling to RT at a rate of 5 °C/hr. The contents of the reaction were then separated by vacuum filtration without washing.

7.2.6. $Rb_7Bi_{3-3x}Sb_{3x}Cl_{16}$ synthesis

Sb_2O_3 and Bi_2O_3 were combined in the desired ratio (total of 1.5 mmol combined) and dissolved in HCl (5 mL) while stirring. Once a clear solution was obtained, RbCl (7 mmol) was added directly to the Sb_2O_3/Bi_2O_3/HCl solution and the autoclave was sealed and placed into a muffle furnace. The autoclave was then heated to 160 °C at 50 °C/hr and kept at this temperature for 24 hours before cooling to RT at a rate of 2-5°C/hr (slower rates gave larger crystals). The contents of the reaction were then separated by vacuum filtration without washing.

7.2.7. $Rb_{23}Bi^{III}_{7-x}Sb^{III}_xSb^V_2Cl_{54}$ synthesis

The synthesis of $Rb_{23}Bi^{III}_{7-x}Sb^{III}_xSb^V_2Cl_{54}$ was adapted from previous reports.[332] To control the Bi^{III}:Sb^{III} ratio and to retain the stoichiometry with Sb^V several solutions are utilized. The first solution, containing Sb(V), is prepared by dissolving the appropriate amount of Sb_2O_3 in HCl (typically 1 mL, 0.6 M in Sb^{3+}). Once a clear solution was observed, the Sb(III) was oxidized to Sb(V) by the addition of a large molar excess of H_2O_2. As the oxidant is added, the solution changes color to yellow, indicating the coexistence of Sb(III) and Sb(V). To ensure complete oxidation, the solution was heated to 80-100 °C. After 20-30 min the solution becomes nearly colorless, indicating the successful oxidation of Sb(III) to Sb(V). This solution was then left to cool to RT.

At this time two additional solutions were prepared, one containing Sb_2O_3 and Bi_2O_3 (their relative ratio determined by the desired stoichiometry) dissolved in HCl (2 mL, 1.04 M in Sb^{3+}/Bi^{3+}) and another containing RbCl dissolved in HCl (4 mL, 1.71 M). The solution containing Sb(III)/Bi(III) was added to the Sb(V) solution to again produce a yellow solution; this additional step allows for more precise control of the Sb(III) amount in the reaction.

This solution, containing Sb(III)/Bi(III) and Sb(V), was then slowly pipetted into the RbCl/HCl solution resulting in the formation of a colored or white (most likely Rb_3BiCl_6) precipitate. In the case of the white precipitate, the solution was again heated until all the precipitate had redissolved. Once a clear solution was once again obtained, the solution was allowed to slowly cool to RT to obtain powders varying in color from yellow to dark red depending on the Sb(III):Bi(III) ratio.

To obtain single crystals, the powders were not separated from the mother liquor. Instead, the entire mixture was added to a Teflon lined autoclave and heated to 160 °C at 50 °C h^{-1}. This temperature was held for 48 h before cooling back to RT at 2-5 °C h^{-1}.

The resulting crystals could be separated from the mother liquor by vacuum filtration. To ensure that they were dry enough for storage, the crystals were kept under dynamic vacuum for a minimum of 30 minutes or until they were visibly dry and free flowing.

7.3. Structural Characterization

7.3.1. Powder X-ray Diffraction

Powder diffraction patterns were collected on a STADI P diffractometer (STOE & Cie GmbH, Darmstadt, Germany) in transmission mode (Debye-Scherrer geometry). The diffractometer is equipped with a silicon strip MYTHEN 1K detector (Fa. DECTRIS) and a curved Ge (111)-monochromator ($CuK\alpha_1$, λ=1.54056 Å).

7.3.2. Single-Crystal X-ray Diffraction

Single-crystal X-ray diffraction measurements were conducted on Bruker Smart, Bruker Smart Apex 2, Oxford Xcalibur S, and a Bruker D8 Venture each equipped with a molybdenum sealed tube X-ray source (MoKα; λ=0.71073 Å) and graphite monochromators. Crystals were tip-mounted with paraffin oil or Lithelen high vacuum grease

Absorption correction was performed with Multi-scan *CrysAlis PRO* 1.171.39.31d (Rigaku Oxford Diffraction, 2017). Empirical absorption correction using spherical harmonics, implemented in SCALE3 ABSPACK scaling algorithm. Data was processed and refined with *CrysAlis PRO* 1.171.39.31d (Rigaku OD, 2017), *SHELXS*,[367] XL,[367] and Olex2.[368]

7.3.3. Scanning Electron Microscopy and Energy-Dispersive X-ray Spectroscopy

Scanning electron microscopy (SEM) of the as-obtained sample was done on a Quanta 200F microscope (Thermo Fisher Scientific) operated at an acceleration voltage V_{acc} = 20 kV. Energy-dispersive X-ray spectroscopy (EDS) was performed with an Octane SDD detector (EDAX, Ametec) attached to the microscope column. For spectra recording and quantification (ZAF correction), the software Gemini (EDAX) was used.

7.3.4. ^{87}Rb NMR

^{87}Rb solid-state Magic Angle Spinning (MAS) NMR was measured on a 16.4 T Bruker Avance III HD spectrometer (Bruker Biospin, Fällanden, Switzerland). The instrument was equipped with a 2.5 mm double-channel solid-state probe head. The spinning frequency was set to 20 kHz. Chemical shifts were referenced to RbCl in D_2O (0.01 M).

For the 1D spectra, a one pulse experiment was used with an excitation pulse of 1 µs. Between 128 and 1024 transients were acquired with a recycle delay of 0.5 s.

The 2D multi quantum MAS (MQMAS) spectra were acquired using a Bruker 3Q MAS pulse program for odd half integer spin nuclei, using 3 pulses with full echo acquisition (mp3qdfs). The 90-degree pulse was set to 4.1 µs and 2048 transients were acquired. To cover the whole

spectral range, the transmitter offset was set to 25 and 75 ppm. Variable echo build up times (15 and 60 rotor cycles) were used to detect a full echo of fast and slow relaxing species.

7.4. Optical characterization

7.4.1. UV-Vis Diffuse Reflectance Measurements

Diffuse reflectance spectra of microcrystalline powders were collected using a Jasco V670 spectrophotometer equipped with an integrating sphere (ILN-725). The absorption spectra were then calculated using a KM transformation.

7.4.2. RT PL and PLE Measurements

RT PL and PLE spectra were measured using a Fluorolog iHR 320 Horiba Jobin Yvon spectrofluorometer equipped with a Xe lamp and a photomultiplier tube. Samples were measured while held between quartz slides.

7.4.3. Absolute PLQY measurements

Absolute values of the PLQY were measured on a Quantaurus-QY C13534-11 Series spectrometer from Hamamatsu with an integrating sphere. The sample was filled in the quartz petri dish and placed in the bottom of the sphere. Excitation was scanned from 300 to 400 nm with a 10 nm step.

7.4.4. RT TRPL

TRPL traces were recorded with a 355 nm excitation source (a frequency-tripled, picosecond Nd:YAG laser, Duetto from Time-Bandwidth). Scattered laser emission was filtered out using dielectric long-pass filters with edges at 400 nm. Measurements were performed using a time-correlated single photon counting (TCSPC) setup, equipped with a SPC-130-EM counting module (Becker & Hickl GmbH) and an IDQ-ID-100-20-ULN avalanche photodiode (Quantique) for recording the decay traces. The average radiative lifetimes were determined as $\tau_{avg} = (\sum_{i=1}^{2} \tau_i^2 \cdot A_i) / (\sum_{i=1}^{2} \tau_i \cdot A_i)$ where A_i and τ_i are the corresponding amplitudes and exponential decay parameters in a bi-exponential analysis

7.4.5. Absorption Coefficient determination

The absorption coefficient of $Rb_7Sb_3Cl_{16}$ was measured from a single crystal, which was

taped to a 1 mm round, metallic aperture. This was placed in front of the integrating sphere of a Jasco V770 spectrometer. The crystal's thickness was measured using optical microscopy in both white light and fluorescence modes from a side view of the platelet shaped crystal (Figure 8.33).

7.4.6. dT-PL, dT-PLE, dT-TRPL, TRES, dW-PL Measurements

7.4.6.1. $Cs_{4-x}A_xSn(Br_{1-y}I_y)_6$ (A = Rb, K; x ≤ 1, y ≤ 1)

Temperature-dependent PL spectra were obtained by exciting the sample with a 355 nm pulsed laser. The sample was mounted in a helium exchange cryostat and the PL was analyzed by a 0.5m monochromator coupled to a nitrogen-cooled CCD camera. PL and PLE spectra were measured using a Fluorolog iHR 320 Horiba Jobin Yvon spectrofluorometer equipped with a Xe lamp and a photomultiplier tube. Samples were measured while held between quartz slides. Variable temperature spectra were measured in a Joule–Thomson cryostat (MMR Technologies) operated in the temperature range of 78-300 K. PL emission could be recorded with a heating rate of approximately 5 K/min.

7.4.6.2. $Rb_7Bi_{3-3x}Sb_{3x}Cl_{16}$ and $K_7Sb_3Cl_{16}$

dT-PL, PLE, and TRPL traces were measured from 320 K to 12 K on a FluoTime 300 spectrometer from PicoQuant Gmbh that was equipped with a TimeHarp 260 PICO counting unit, which was coupled with a CS204, closed cycle helium cryostat from Advanced Research Systems for temperature variation.

PL and PLE spectra were measured using a Xe lamp coupled to a monochromator. TRPL traces were recorded using a frequency tripled Nd:YAG laser (355 nm wavelength, a power density of about 0.1 mW cm^{-2}, a pulse duration of 10 ps). Scattered light from the excitation source was suppressed with a 400 nm longpass filter placed before the emission monochromator. The average radiative lifetimes were determined as intensity weighted average lifetimes.

TRES studies were performed using the above system in the TRPL configuration with a built-in TRES wizard.

Powder dependent PL studies were performed by manually varying the excitation intensity of the 355 nm laser. A range of average excitation powers from 2 μW to 2 mW was used.

7.4.7. Raman

Raman spectroscopy was conducted using a Thermo Scientific DXR 2 confocal Raman microscope with 455 nm laser excitation. Each sample was measured in the range of 77.6 cm^{-1} to 3773.6 cm^{-1}, no peaks were observed above 500 cm^{-1}

7.4.8. DFT calculations

7.4.8.1. $Cs_{4-x}A_xSn(Br_{1-y}I_y)_6$ (A = Rb, K; x ≤ 1, y ≤ 1)

Calculations were carried out at the DFT level as implemented in the cp2k quantum chemistry code. A single 1x1x1 unit cell containing 66 atoms was constructed for all materials involved. A mixed plane-wave and Gaussian basis set approach was used to describe the wave function and electronic density, respectively. The kinetic energy cutoff of the plane-wave basis was set to 400 Rydberg, while a double-ζ basis set plus polarization functions was employed to describe the molecular orbitals. DOS, emission and excitation energies were calculated using Perdew-Burke-Ernzerhof (PBE) exchange-correlation functional. Scalar relativistic effects have been accounted for by using effective core potential functions in the basis set. Spin-orbit coupling effects were not included. The optical excitation and emission energies were obtained by computing the total energy differences between the ground state and excited-state structures, at the ground state and excited state geometries respectively. Excited state geometry optimizations were performed with unrestricted Kohn-Sham calculations for a triplet multiplicity with fixed lattice parameters, optimized for the ground state geometry. We assume that the triplet energy and structure are qualitatively similar to the excited state singlet. Calculations with lattice relaxation for the ground state geometry optimization were performed to account for statistical disorder in the experimental crystal structures. External pressure applied for cell optimization was 100 bar. Atomic coordinates were optimized until the force reached 0.023 eV/ Å. Calculation for structures at different temperatures were performed without geometry relaxation on the lattices obtained from single crystal X-ray diffraction

7.4.8.2. $Rb_7Bi_{3-3x}Sb_{3x}Cl_{16}$ and $K_7Sb_3Cl_{16}$

Calculations were carried out at the DFT level as implemented in the cp2k quantum chemistry code. Using the experimentally determined and disordered $Rb_7Sb_3Cl_{16}$ structure, a *P*1 unit cell with parameters $a = c = 12.9655$, $c = 34.1932$ containing 248 atoms was constructed by ordering the disordered dimer layer with the ordered layer as a template. A mixed plane-wave and Gaussian basis set approach was used to describe the wave function and electronic density, respectively. The kinetic energy cutoff of the plane-wave basis was set to 400 Rydberg, while a double-ζ basis set plus polarization functions was employed to describe the molecular orbitals. DOS, emission and excitation energies were calculated using Perdew-Burke-Ernzerhof (PBE) exchange-correlation functional. Scalar relativistic effects have been accounted for by using effective core potential functions in the basis set. Spin-orbit coupling effects were not included. Unit cell parameters were taken from experimental data and not relaxed, whereas atomic coordinates were optimized until the force reached 0.023 eV/ Å

7.4.9. Conductivity and X-ray photoconductivity measurements

I-V measurements were recorded with a Keithley 236 source measurement unit. For the characterization with X-rays, the Keithley 237 source measurement unit was used to apply a bias voltage while X-rays were generated using the Mini–X Amptek X-ray tube with an accelerating voltage of 50 kV and a X-ray tube current of 50 μA.

Chapter 8. Appendix

8.1. Appendix to Chapter 2

When measuring the powder pattern of polycrystalline samples obtained with shorter tempering time, no other phases except Cs_4SnBr_6 and CsBr were observed (when ratios of $CsBr:SnBr_2 \geq 4.5:1$ are used). The powder pattern was measured at RT and refined using the General Structure Analysis System (GSAS) with EXPGUI and GSASII.[369-370] Weight fractions of 92.5% and 7.5% were found for Cs_4SnBr_6 and CsBr, respectively (reflections arising from CsBr are indicated by blue asterisks; Fig. S1, 2).

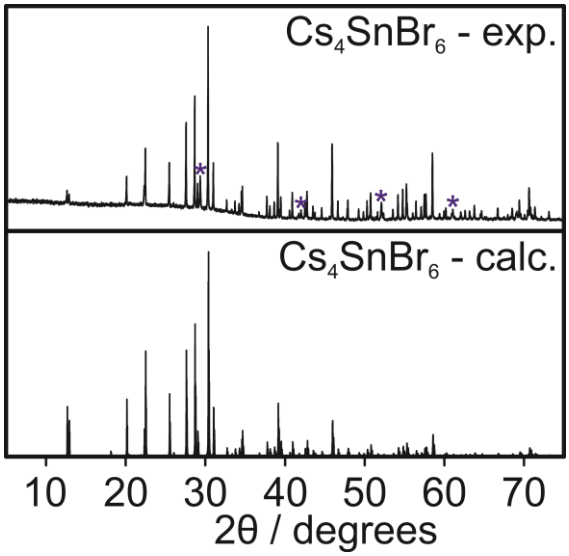

Figure 8.1. Experimental and calculated powder patterns of Cs_4SnBr_6. The experimental powder pattern collected from Cs_4SnBr_6 demonstrates that a typical reaction produces a majority of Cs_4SnBr_6 with a side product of CsBr (denoted by blue asterisks). This is expected given the slight excess of CsBr used in the initial reaction mixture. The Cs_4SnBr_6 diffraction pattern was calculated in Vesta using the experimentally determined structure of Cs_4SnBr_6.

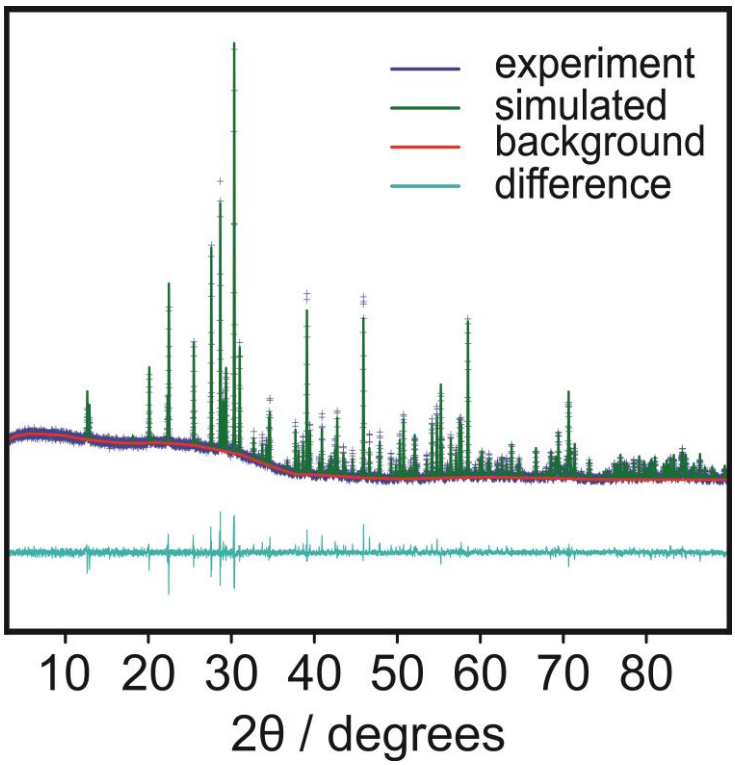

Figure 8.2. Refinement of Cs_4SnBr_6. The unit cell constants of Cs_4SnBr_6 at RT were determined through Rietveld refinement using GSASII.

Table 8.1. Refinement of Cs4SnBr6.

Sample	**Cs_4SnBr_6**
Temperature	298 K
Formula Weight	1129.73
Crystal System	trigonal
Space Group	*R-3c*
Color	Colorless
a (Å)	13.676354
c (Å)	17.271424
Volume (Å3)	2797.69
Z	6.0
F(000)	2880.0
ρ_{calc} (g cm^{-3})	4.023
Radiation	Cu Kα (λ = 1.54184 Å)
2θ for data collection (°)	3.03–90.02
2θ step (°)	0.01
Data/restraints/para-meters	8700/0/49
Rp	0.034
Rwp	0.046
Rexp	0.037
$\chi 2$	1.610
Sample	Cs4SnBr6
Temperature	298 K

Table 8.2. Fractional atomic coordinates and isotropic or equivalent isotropic displacement parameters (Å2) for Cs4SnBr6.

Atom	**Wyckoff Symbol**	**X**	**Y**	**Z**	**Uiso*/Ueq**
Sn1	*6b*	0	0	0	0.0199 (5)*
Cs1	*18e*	0.37525 (12)	0	1/4	0.0199 (5)*
Cs2	*6a*	0	0	1/4	0.0199 (5)*
Br1	*36f*	0.14145 (17)	0.50449 (19)	0.06624 (10)	0.0199 (5)*

Table 8.3. Variable temperature diffraction data for Cs_4SnBr_6.

	Cs_4SnBr_6		
Temperature (K)	272.98 (10)	199.99 (10)	100.00 (10)
Formula Weight	1129.79	1129.77	1129.77
Crystal System	trigonal	trigonal	trigonal
Space Group	*R*-3*c*	*R*-3*c*	*R*-3*c*
a (Å)	13.6687 (3)	13.6191 (2)	13.5598 (2)
c (Å)	17.2597 (5)	17.2184 (4)	17.1628 (3)
γ/°	120	120	120
Volume (Å^3)	2792.67 (16)	2765.80 (10)	2732.91 (9)
F(000)	2880.0	2880.0	2880
ρ_{calc} (g cm^{-3})	4.031	4.070	4.119
Radiation	Cu *K*α (λ = 1.54184 Å)	Cu *K*α (λ = 1.54184 Å)	Cu *K*α (λ = 1.54184 Å)
2θ for data collection (°)	12.694–159.126	12.73–158.642	12.776–159.604
μ (mm^{-1})	85.81	86.644	87.687
Crystal Size (mm^3)	0.047 0.037 0.025	0.047 0.037 0.025	0.047 0.037 0.025
Index Ranges	-17 ≤ h ≤ 16 -17 ≤ k ≤ 17 -21 ≤ l ≤ 21	-12 ≤ h ≤ 17 -17 ≤ k ≤ 17 -21 ≤ l ≤ 21	-13 ≤ h ≤ 17 -17 ≤ k ≤ 15 -21 ≤ l ≤ 21
Reflections Collected	19422	14101	14021
Independent Reflections	683 [R_{int} = 0.0678, R_{sigma} = 0.0155]	675 [R_{int} = 0.0568, R_{sigma} = 0.0152]	667 [R_{int} = 0.0601, R_{sigma} = 0.0166]
Data/restraints/parameters	683/0/19	675/0/19	667/0/19
Goodness-of-fit on F^2	1.164	1.255	1.124
Final R indexes [I>=2σ (I)]	R_1 = 0.0242 wR_2 = 0.0596	R_1 = 0.0243 wR_2 = 0.0648	R_1 = 0.0257 wR_2 = 0.0678
Final R indexes [all data]	R_1 = 0.0244 wR_2 = 0.0596	R_1 = 0.0245 wR_2 = 0.0650	R_1 = 0.0258 wR_2 = 0.0678
Largest diff. peak/hole (e Å-3)	0.70/-1.79	0.76/-1.54	1.03/-1.37

The lattice parameters were determined to be larger than those previously reported[149] with $a = b$ = 13.6687(3) and c = 17.2597(5) at 273 K but in close agreement with recent computational predictions.[237]

Table 8.4. Fractional atomic coordinates and equivalent isotropic displacement parameters ($Å^2×10^3$) for Cs_4SnBr_6 at 273 K.

Atom	Wyckoff Symbol	*X*	*y*	*z*	U(eq)[a]
Cs1	*18e*	0.62487(3)	0	1/4	30.40(15)
Cs2	*6a*	0	0	1/4	41.6(2)
Sn1	*6b*	0	0	0	18.38(18)
Br1	*36f*	0.69510 (5)	0.52439 (5)	0.23286 (3)	31.33(17)

[a] U_{eq} is defined as 1/3 of the trace of the orthogonalised U_{IJ} tensor.

Table 8.5. Anisotropic displacement parameters ($Å^2×10^3$) for Cs_4SnBr_6 at 273 K

Atom	U11	U22	U33	U23	U13	U12
Cs1	30.0(2)	26.4(2)	33.6(3)	-5.37(16)	-2.69(8)	13.19(12)
Cs2	52.6(3)	52.6(3)	19.6(4)	0	0	26.29(17)
Sn1	18.8(2)	18.8(2)	17.5(3)	0	0	9.41(11)
Br1	34.8(3)	32.0(3)	31.4(3)	2.2(2)	0.2(2)	19.8(2)

[a] The anisotropic displacement factor exponent takes the form: $-2\pi^2[h^2a^{*2}U_{11}+2hka^*b^*U_{12}+\ldots]$.

Table 8.6. Fractional atomic coordinates and equivalent isotropic displacement parameters ($Å^2×10^3$) for Cs_4SnBr_6 at 200 K

Atom	Wyckoff Symbol	*x*	*Y*	*z*	U(eq)[a]
Cs1	*18e*	0.62475 (3)	0	1/4	20.21(16)
Cs2	*6a*	0	0	1/4	27.8(2)
Sn1	*6b*	0	0	0	12.06(19)
Br1	*36f*	0.69512 (5)	0.52482 (5)	0.23270 (3)	21.26(18)

[a] U_{eq} is defined as 1/3 of the trace of the orthogonalised U_{IJ} tensor.

Table 8.7. Anisotropic displacement parameters ($Å^2×10^3$) for Cs_4SnBr_6 at 200 K.

Atom	U11	U22	U33	U23	U13	U12
Cs1	20.1(2)	17.8(2)	21.9(3)	-3.56(15)	-1.78(8)	8.89(12)
Cs2	35.5(3)	35.5(3)	12.6(4)	0	0	17.73(16)
Sn1	12.5(2)	12.5(2)	11.2(4)	0	0	6.25(12)
Br1	23.7(3)	21.8(3)	21.1(3)	1.5(2)	0.2(2)	13.5(2)

[a] The Anisotropic displacement factor exponent takes the form: $-2\pi^2[h^2a^{*2}U_{11}+2hka^*b^*U_{12}+\ldots]$.

Table 8.8. Fractional atomic coordinates and equivalent isotropic displacement parameters ($Å^2×10^3$) for Cs_4SnBr_6 at 100 K.

Atom	Wyckoff Symbol	x	y	z	U(eq)[a]
Cs1	*18e*	0.62455 (3)	0	1/4	8.67(17)
Cs2	*6a*	0	0	1/4	12.3(2)
Sn1	*6b*	0	0	0	4.9(2)
Br1	*36f*	0.69516 (4)	0.52533 (4)	0.23256 (3)	9.54(18)

[a] U_{eq} is defined as 1/3 of of the trace of the orthogonalised U_{IJ} tensor.

Table 8.9. Anisotropic displacement parameters ($Å^2×10^3$) for Cs_4SnBr_6 at 100 K.

Atom	U11	U22	U33	U23	U13	U12
Cs1	8.5(2)	7.5(2)	9.7(3)	-1.69(14)	-0.85(7)	3.76(12)
Cs2	15.7(3)	15.7(3)	5.6(4)	0	0	7.84(14)
Sn1	5.0(3)	5.0(3)	4.7(4)	0	0	2.49(13)
Br1	10.2(3)	9.8(3)	9.9(3)	0.65(18)	0.18(19)	6.0(2)

[a] The Anisotropic displacement factor exponent takes the form: $-2\pi^2[h^2a^{*2}U_{11}+2hka^*b^*U_{12}+\ldots]$.

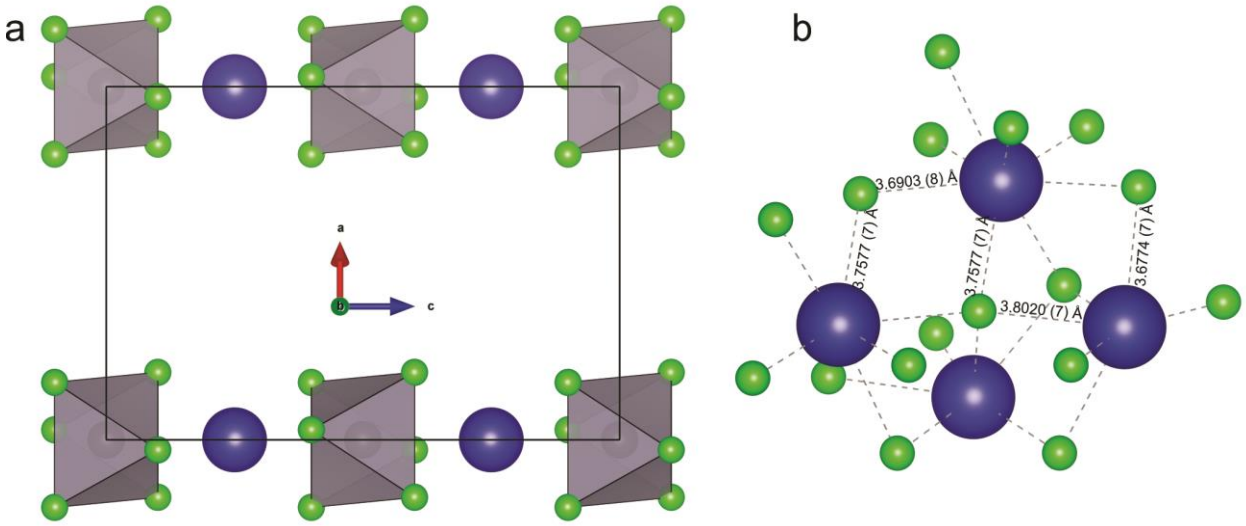

Figure 8.3. Distinct crystallographic positions of Cs. Views of the Cs_4SnBr_6 structure demonstrating the two distinct crystallographic positions of Cs within the structure. (a) Cs(2) cations are located between $[SnBr_6]^{4-}$ octahedra in six-fold coordination with an average Cs-Br bond length of 3.5520 (3) Å. The Sn-Sn distance along the c-axis is 8.6299 (3) Å. (b) Cs(1) is found between the columns formed by $[SnBr_6]^{4-}$ octahedra and Cs(2). It is in an eight-coordinate position with Cs-Br bond lengths ranging from 3.6774 (7) Å to 3.8020 (7) Å.

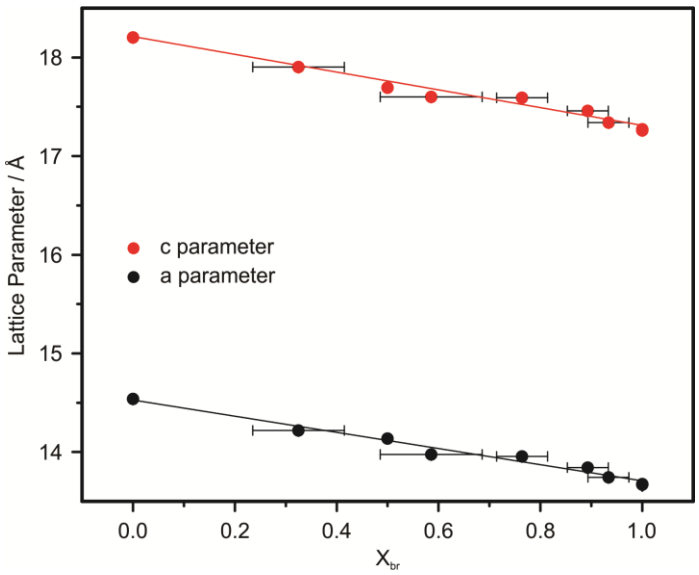

Figure 8.4. Bromide and iodide substitution. The substitution of bromide for iodide results in a linear change in the a and c lattice parameters. This is in agreement with Vegard's law and suggests a solid solution exists between Br and I on these general positions. The R^2 value for the linear fit of lattice parameter vs. molar fraction of bromide is 0.98 for both the *a* and *c* parameters.

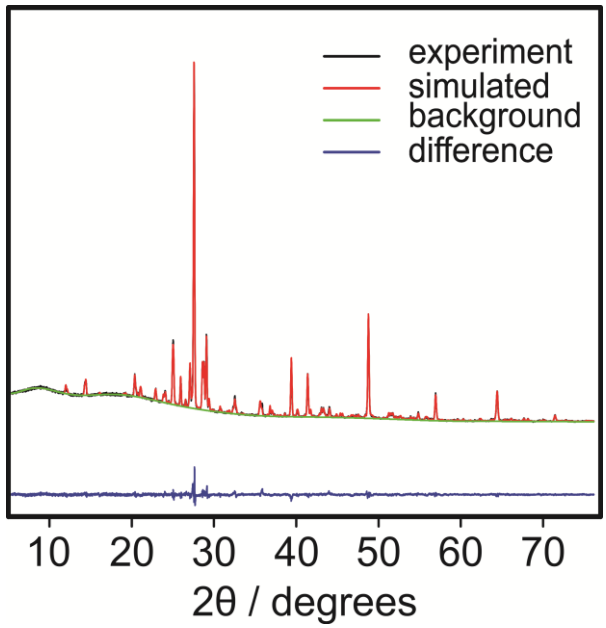

Figure 8.5. Refinement of Cs_4SnI_6. The crystal structure of Cs_4SnI_6 was determined through Rietveld refinement using GSAS and EXPGUI.

Table 8.10. Refinement of Cs_4SnI_6.

Sample	**Cs_4SnI_6**
Temperature	298 K
Formula Weight	1411.73
Crystal System	trigonal
Space Group	*R-3c*
Color	Black
a (Å)	14.5315 (4)
c (Å)	18.1571 (8)
Volume (Å3)	3028.52
Z	6.0
F(000)	3528
ρ_{calc} (g cm^{-3})	4.222
Radiation	Cu Kα (λ = 1.54184 Å)
2θ for data collection (°)	5.01–75.00
2θ step (°)	0.01
Data/restraints/para-meters	7000/0/43
Rp	0.028
Rwp	0.037
Rexp	0.029
Goodness-of-fit on F2	0.05787
χ2	1.638
(Δ/σ)max	0.06

Table 8.11. Fractional atomic coordinates and isotropic or equivalent isotropic displacement parameters (Å^2) for Cs_4SnI_6.

Atom	**Wyckoff Symbol**	**X**	**Y**	**Z**	**Uiso*/Ueq**
Sn1	*6b*	0	0	0	0.0729 (15)*
Cs1	*18e*	0.3787 (4)	0	1/4	0.0729 (15)*
Cs2	*6a*	0	0	1/4	0.0729 (15)*
I1	*36f*	0.1404 (4)	0.5044 (5)	0.0641 (2)	0.0729 (15)*

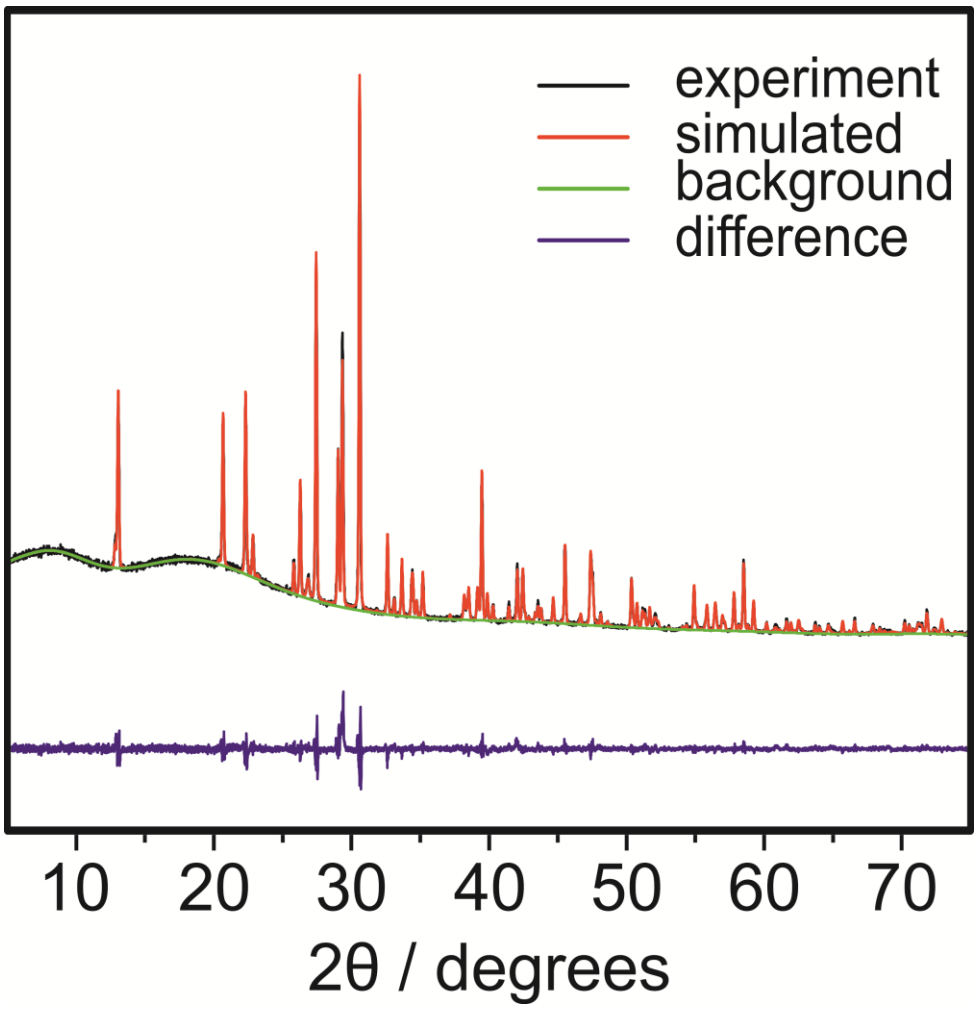

Figure 8.6. Refinement of $Cs_{3.2}K_{0.8}SnBr_6$. The crystal structure of $Cs_{3.2}K_{0.8}SnBr_6$ was determined through Rietveld refinement using GSAS and EXPGUI.

Table 8.12. Refinement of $Cs_{3.2}K_{0.8}SnBr_6$.

Sample	**$Cs_{3.20}K_{0.80}SnBr_6$**
Temperature	298 K
Formula Weight	1054.92
Crystal System	trigonal
Space Group	*R*-3*c*
Color	Colorless
a (Å)	13.79233 (8)
c (Å)	16.45368 (17)
Volume (Å^3)	2710.62 (3)
Z	6.0
F(000)	2708
ρ_{calc} (g cm^{-3})	3.877
Radiation	Cu *K*α (λ = 1.54184 Å)
2θ for data collection (°)	5.00–75.99
2θ step (°)	0.01
Data/restraints/para-meters	7100/0/24
R_p	0.033
R_{wp}	0.049
R_{exp}	0.030
$R(F^2)$	0.07058
χ^2	2.560
$(\Delta/\sigma)_{max}$	0.68

Table 8.13. Fractional atomic coordinates and isotropic or equivalent isotropic displacement parameters (Å^2) for $Cs_{3.2}K_{0.8}SnBr_6$.

Atom	**Wyckoff Symbol**	**X**	**Y**	**Z**	**Uiso*/Ueq**	**Occ. (<1)**
Cs1	*18e*	0.37804 (11)	x	3/4	0.05625*	
Sn2	*6b*	1/3	2/3	2/3	0.05625*	
Cs3	*6a*	2/3	1/3	0.58333	0.05625*	0.20243
Br4	*36f*	0.36230 (15)	0.50857 (16)	0.55817 (8)	0.05625*	
K5	*6a*	2/3	1/3	0.58333	0.05625*	0.79755

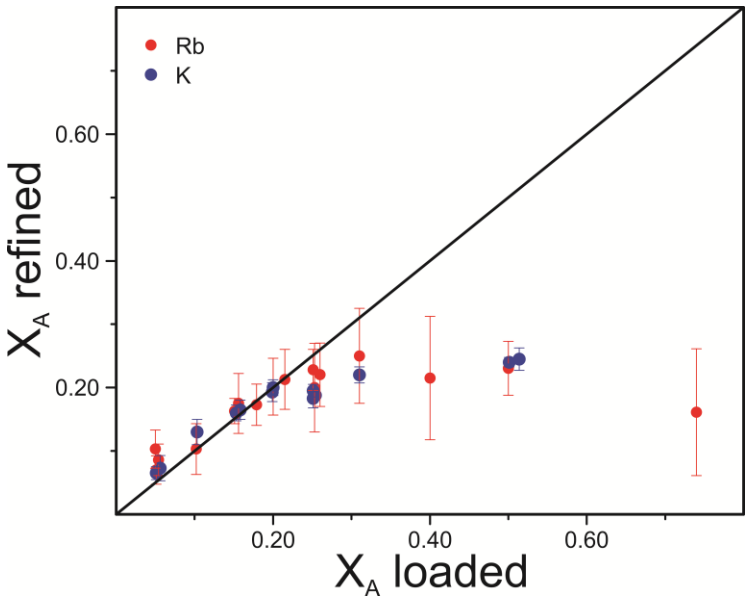

Figure 8.7. Limited A-site substitution.

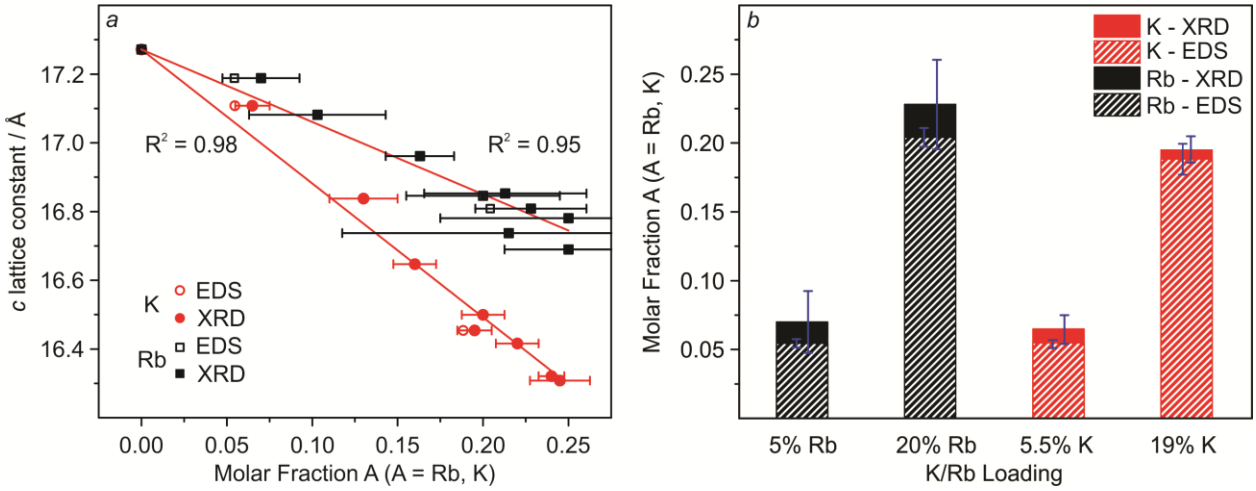

Figure 8.8. Expanded view of the *c*-lattice parameter's dependence on A-site occupancy. (a) For both K- and Rb- substitution, a linear change in the *c*-lattice parameter with the molar fraction of K and Rb ions is observed with R^2 values of 0.98 and 0.95, respectively. Error bars represent the standard uncertainty as calculated from the Rietveld refinement by GSAS. (b) The composition as determined by EDS is compared with that determined by Rietveld refinement.

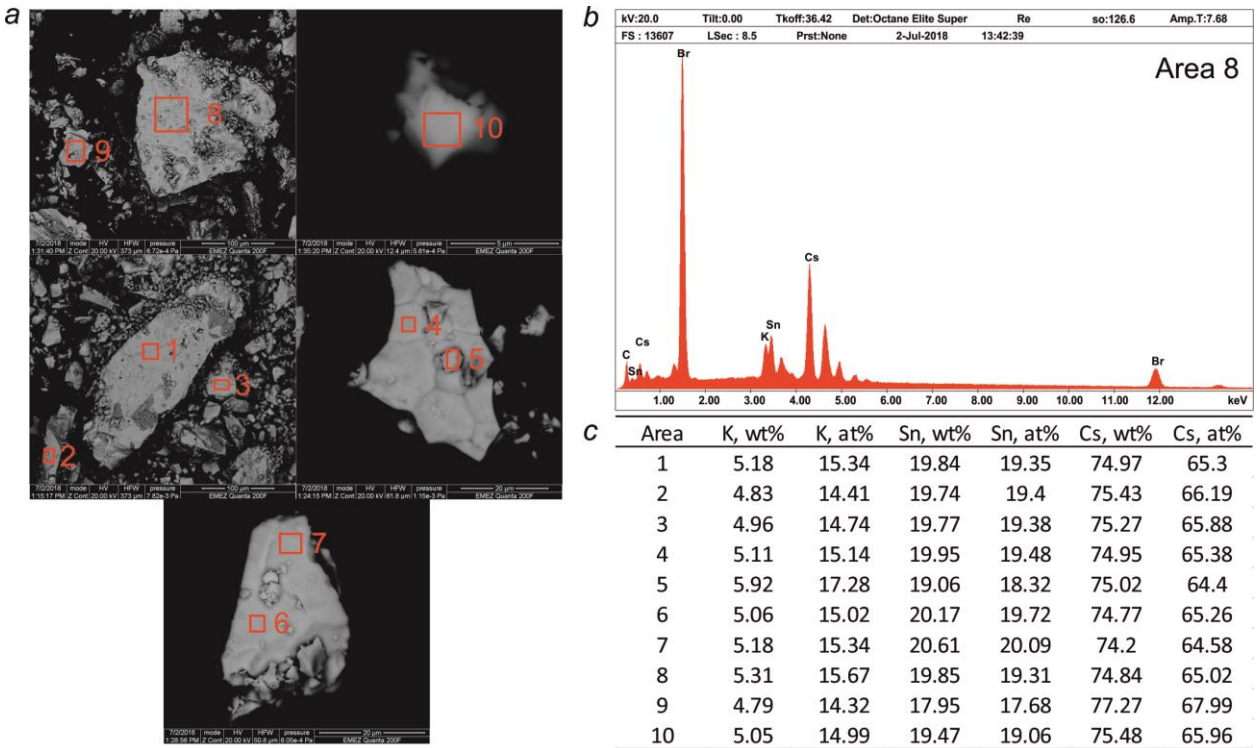

c

Area	K, wt%	K, at%	Sn, wt%	Sn, at%	Cs, wt%	Cs, at%
1	5.18	15.34	19.84	19.35	74.97	65.3
2	4.83	14.41	19.74	19.4	75.43	66.19
3	4.96	14.74	19.77	19.38	75.27	65.88
4	5.11	15.14	19.95	19.48	74.95	65.38
5	5.92	17.28	19.06	18.32	75.02	64.4
6	5.06	15.02	20.17	19.72	74.77	65.26
7	5.18	15.34	20.61	20.09	74.2	64.58
8	5.31	15.67	19.85	19.31	74.84	65.02
9	4.79	14.32	17.95	17.68	77.27	67.99
10	5.05	14.99	19.47	19.06	75.48	65.96

Figure 8.9. SEM and EDS of $Cs_{3.2}K_{0.8}SnBr_6$. (a) SEM images obtained from $Cs_{3.2}K_{0.8}SnBr_6$. (b) The EDS spectrum measured from the region marked with the number 8. (c) The K, Sn, and Cs weight percent (wt%) and atomic percent (at%) as measured in 10 regions (individually marked in subfigure a). This same process was repeated for all 4 points presented in Figure 8.8.

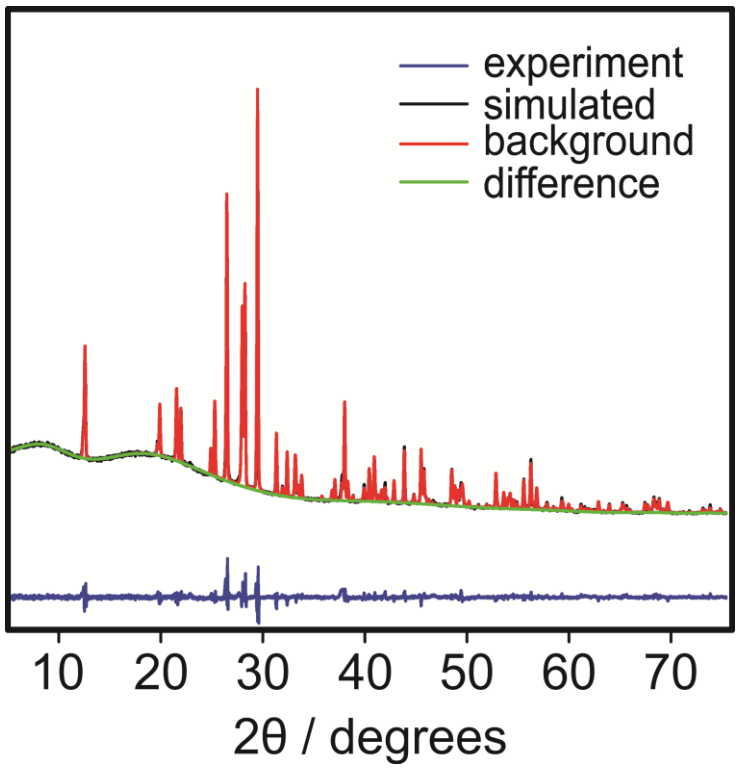

Figure 8.10. Refinement of $Cs_{3.2}K_{0.8}SnBr_3I_3$. The crystal structure of $Cs_{3.2}K_{0.8}SnBr_3I_3$ was determined through Rietveld refinement using GSAS and EXPGUI.

Table 8.14. Refinement of $Cs_{3.2}K_{0.8}SnBr_3I_3$.

Sample	**$Cs_{3.28}K_{0.72}SnBr_{2.85}I_{3.15}$**
Temperature	298 K
Formula Weight	1209.61
Crystal System	trigonal
Space Group	*R-3c*
Color	pale yellow
a (Å)	14.28389 (9)
c (Å)	17.11201 (19)
Volume (Å3)	3023.604 (33)
Z	6.0
F(000)	3064
ρ_{calc} (g cm^{-3})	3.986
Radiation	Cu Kα (λ = 1.54184 Å)
2θ for data collection (°)	5.01–75.44
2θ step (°)	0.01
Data/restraints/para-meters	7045/0/7
Rp	0.029
Rwp	0.044
Rexp	0.024
R(F2)	0.09110
$\chi 2$	3.349
(Δ/σ)max	0.03

Table 8.15. Fractional atomic coordinates and isotropic or equivalent isotropic displacement parameters (Å^2) for $Cs_{3.2}K_{0.8}SnBr_3I_3$.

Atom	Wyckoff Symbol	X	Y	Z	Uiso*/Ueq	Occ. (<1)
Cs1	*18e*	0.38179 (12)	0	1/4	0.0607 (4)*	
Sn2	*6b*	0	0	0	0.0607 (4)*	
Cs3	*6a*	0	0	1/4	0.0607 (4)*	0.27543
Br4	*36f*	0.14407 (12)	0.50868 (14)	0.05804 (7)	0.0607 (4)*	0.47572
K5	*6a*	0	0	1/4	0.0607 (4)*	0.72457
I6	*36f*	0.14406 (12)	0.50867 (14)	0.05804 (7)	0.0607 (4)*	0.52428

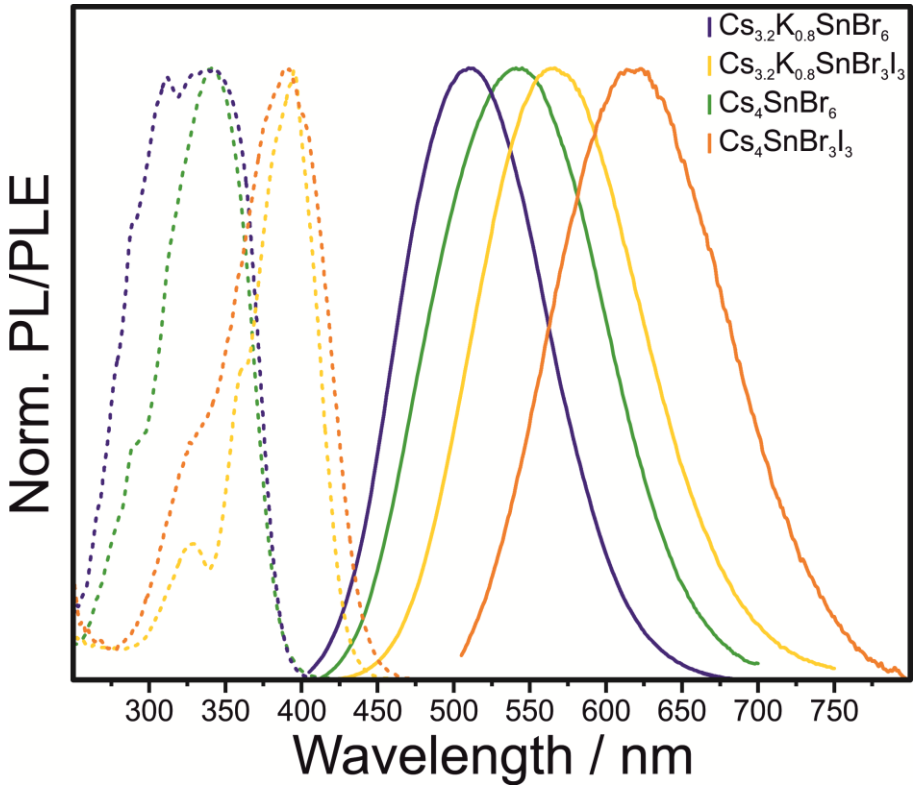

Figure 8.11. RT PL spectra of samples measured at Low T. PL and PLE spectra of the four samples that were used for temperature dependent PL measurements down to 6 K. These spectra were measured at RT.

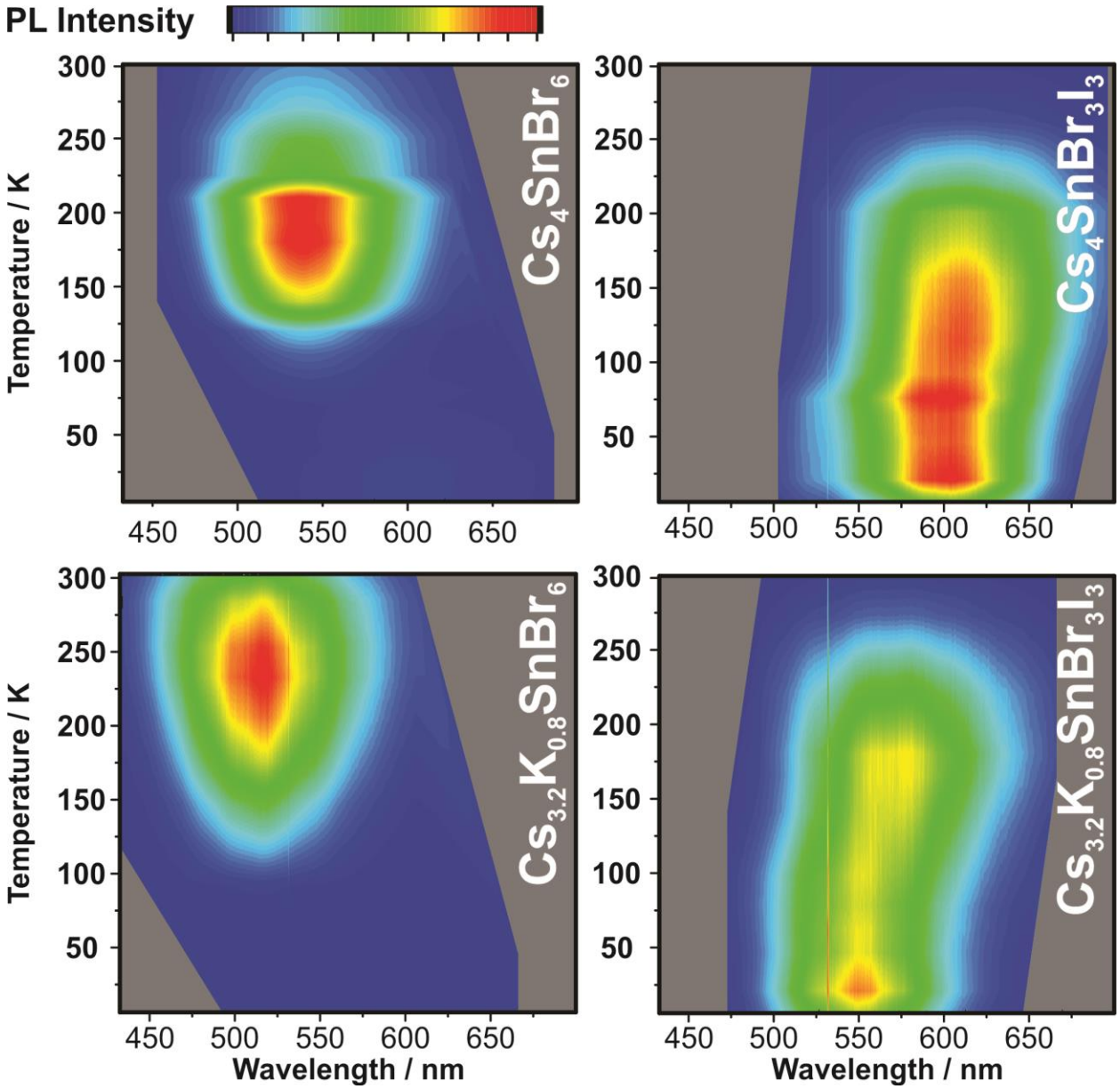

Figure 8.12. Temperature dependent PL spectra. Temperature dependent PL spectra collected from 300 K to 6 K with a 355 nm excitation laser. The composition which corresponds to the spectra is written in the right corner of each graph.

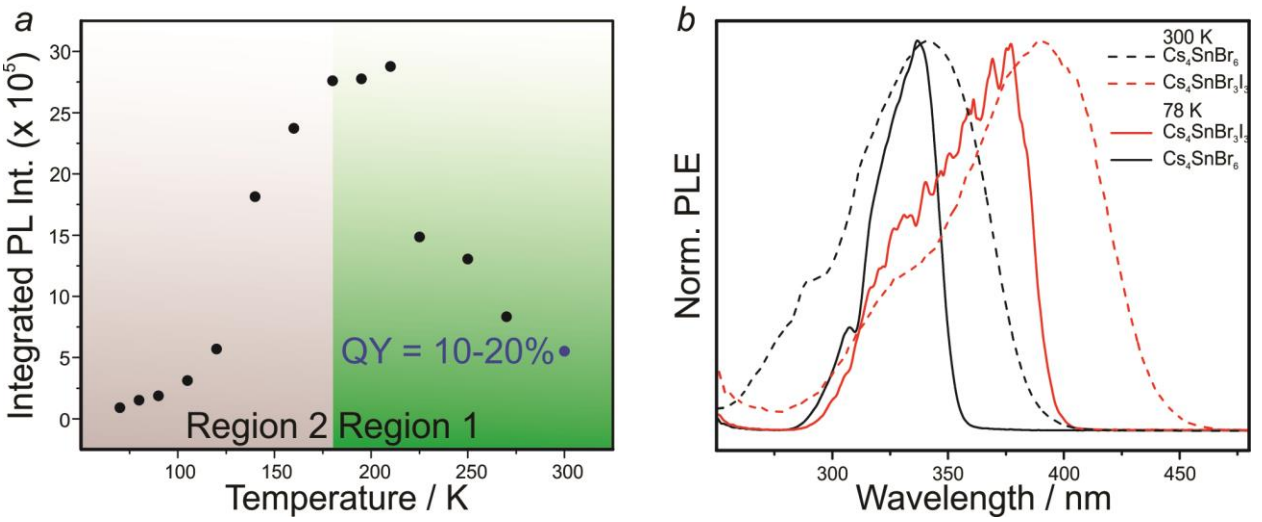

Figure 8.13. Temperature dependence of PL intensity and temperature dependent excitation spectra: (a) The integrated PL intensity of Cs_4SnBr_6 plotted against temperature (excitation at 355 nm), (b) PLE vs. Temperature for Cs_4SnBr_6 (black) and $Cs_4SnBr_3I_3$ (red) at 300 K (dashed) and 78 K (solid).

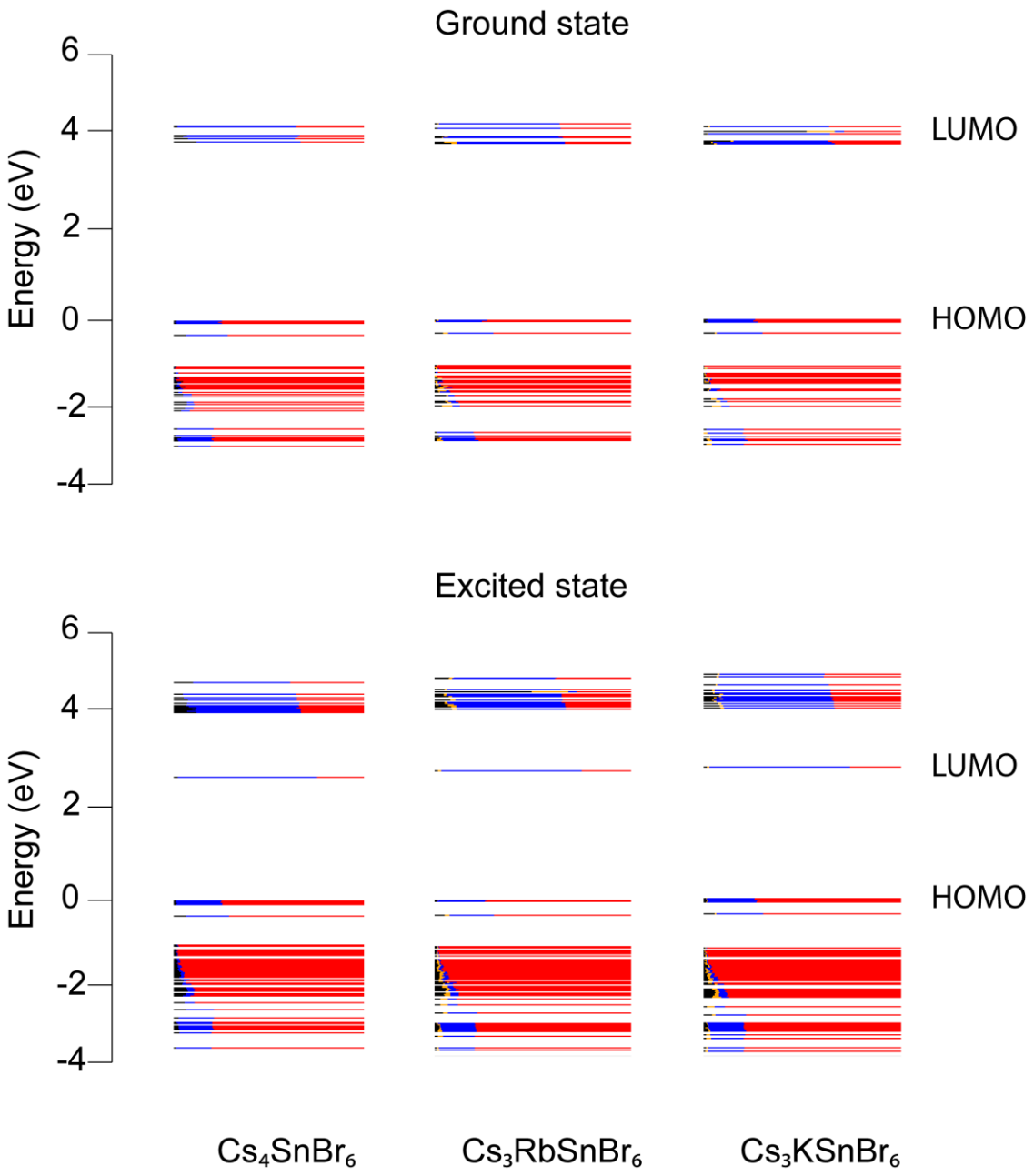

Figure 8.14. Frontier orbitals (HOMO and LUMO) for ground and excited states of A_4SnBr_6. Color-code: black – Cs, orange – Rb/K, blue – Sn, red – Br. Molecular orbitals for ground and excited state obtained from single-point calculations on optimized ground and excited state geometry. The values of HOMO-LUMO gap from single-point calculations are not reliable and are omitted. The LUMO in excited state comprises exclusively Sn-5p and Br-4p orbitals from distorted $SnBr_6$ octahedron As discussed, the contribution of A-site cation to the band edge is negligible (black and orange). HOMO is comprised of Sn s-orbitals and Br p-orbitals, whereas Sn-p orbitals and Br p-orbitals contribute to the LUMO.

Table 8.16. Comparison of calculated energies (eV) for three different approaches: lattice fixed at experimental values, lattice optimization for the ground state only, and the lattice optimized for both ground and excited states; g-e – difference in total energies of ground and excited states. In general, lattice relaxation facilitates the convergence of the excited state geometry but underestimates the real emission and excitation energies

	No lattice optimization		Lattice optimization - ground state		Lattice optimization - both states	
	g-e (eV)	Emission (eV)	g-e (eV)	Emission (eV)	g-e (eV)	Emission (eV)
Cs_4SnBr_6	2.9	2.3	2.9	2.25	2.9	2.15
$Cs_3RbSnBr_6$	3.0	2.4	2.9	2.3	2.9	2.2
Cs_3KSnBr_6	3.0	2.4	2.9	2.4	2.9	2.3

Table 8.17. Bond distances (Å) for axial and equatorial Sn-Br bonds in the optimized ground and excited state geometries.

Compound	Ground state		Excited state	
	Axial (Å)	Equatorial (Å)	Axial (Å)	Equatorial (Å)
Cs_4SnBr_6	3.049	3.049	3.658	2.88
$Cs_3RbSnBr_6$	3.042	3.042	3.603	2.88
Cs_3KSnBr_6	3.035	3.035	3.567	2.88

As a general trend, the axial Sn-Br bond is elongated depending on the cation, whereas equatorial bond decreases to the same value regardless the composition.

Table 8.18. Bond distances (Å) for excited and ground state, calculated emission and absorption energies for Cs_4SnBr_6 at different temperatures (273, 200, and 100 K).

Temperature (K)	c/a ratio	Axial bond (Å)		Equatorial bond (Å)		Calculated Emission (eV)	Calculated Absorption (eV)
		Ground	Excited	Ground	Excited		
273	1.263	3.000	3.562	3.000	2.880	2.33	3.55
200	1.264	2.990	3.550	2.990	2.881	2.34	3.54
100	1.266	2.985	3.538	2.985	2.878	2.34	3.53

The relative change in Sn-Br bond distance is much smaller than for different compositions. The calculations were performed with lattice parameters fixed at experimental values and relaxing only atomic positions.

8.2. Appendix to Chapter 3

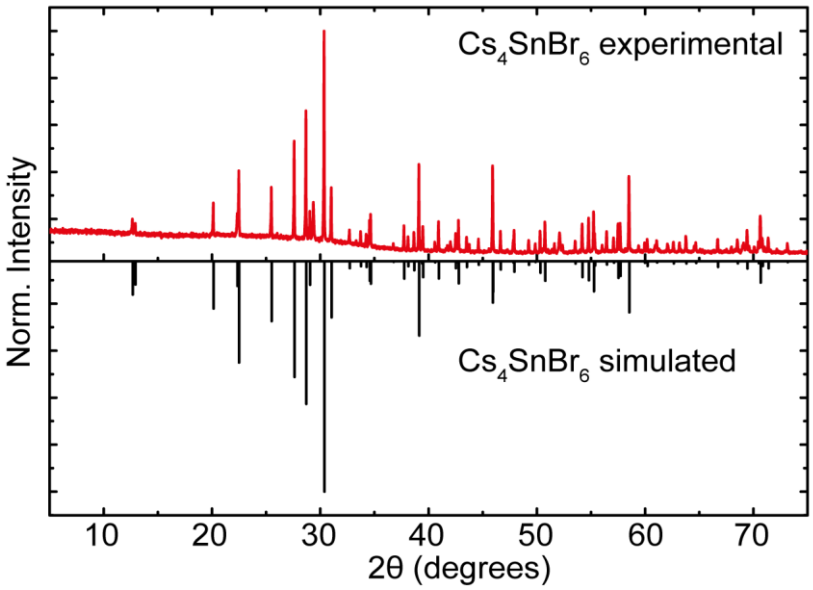

Figure 8.15. Powder X-ray diffraction pattern of Cs_4SnBr_6.

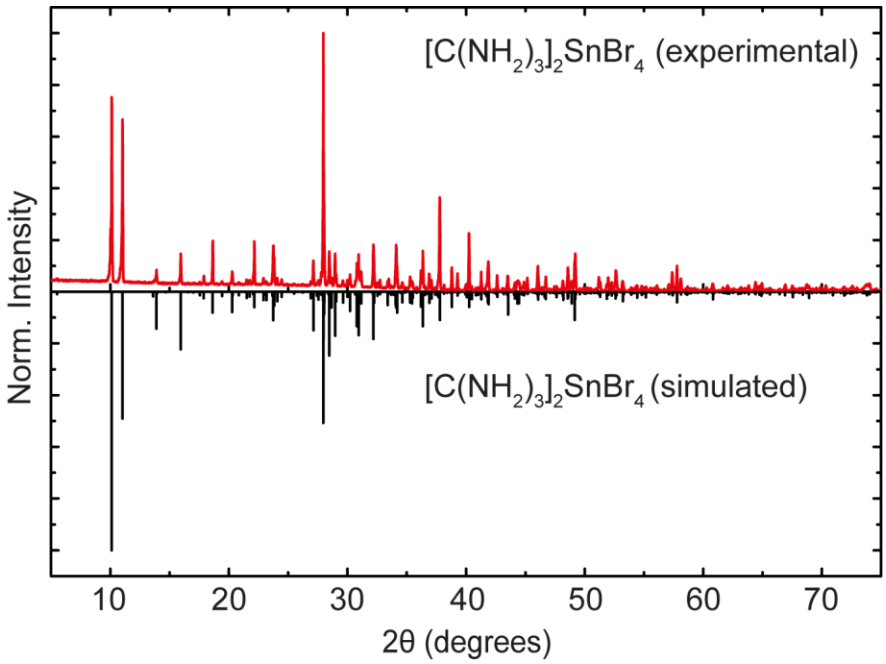

Figure 8.16. Powder X-ray diffraction pattern of $[C(NH_2)_3]_2SnBr_4$.

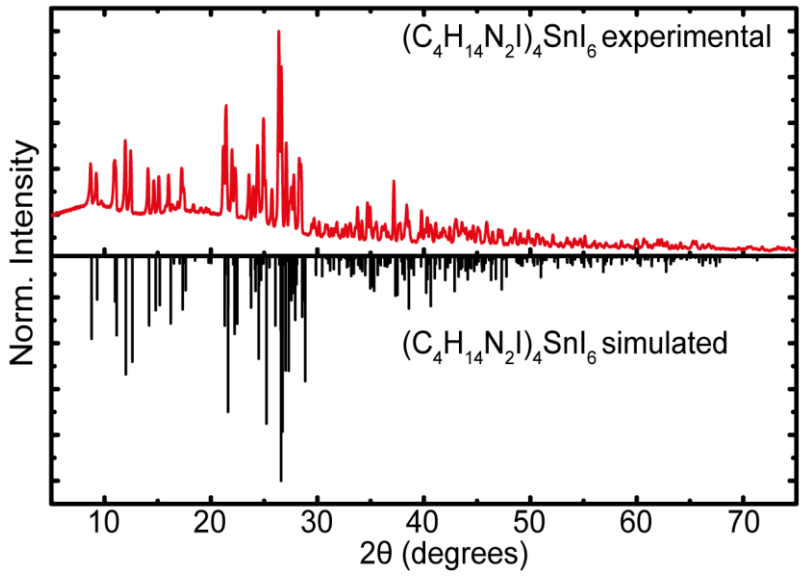

Figure 8.17. Powder X-ray diffraction pattern of $(C_4H_{14}N_2I)_4SnI_6$.

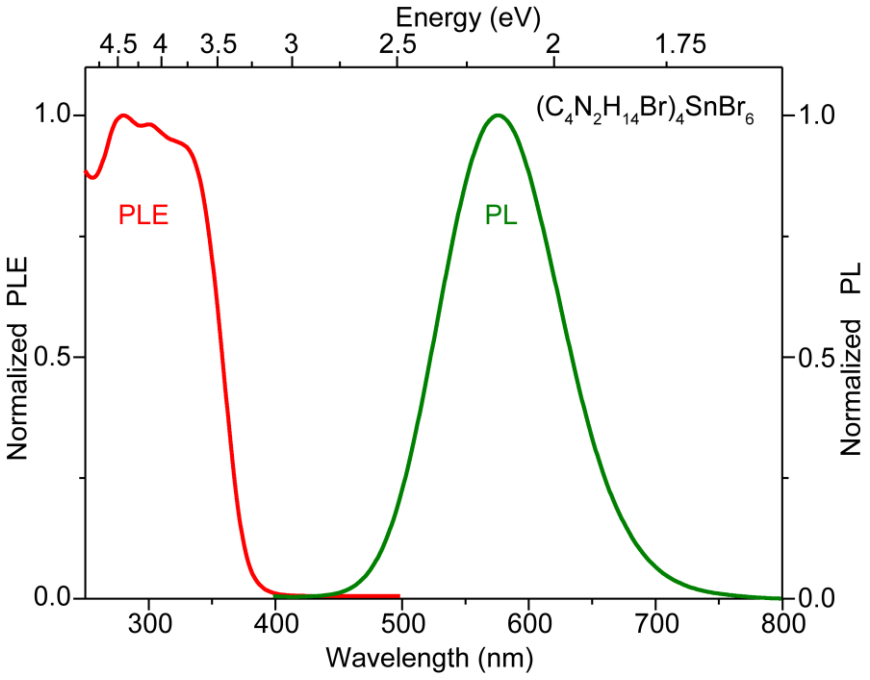

Figure 8.18. Optical characterization of $(C_4N_2H_{14}Br)_4SnBr_6$: PLE (red) and PL (green) spectra.

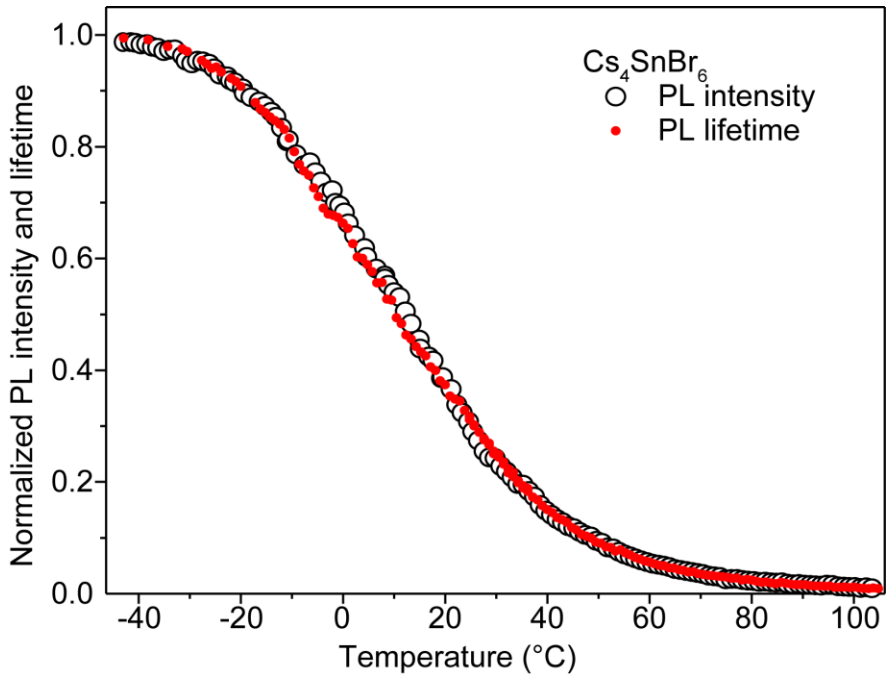

Figure 8.19. Temperature dependence of Cs_4SnBr_6 PL emission lifetime and intensity

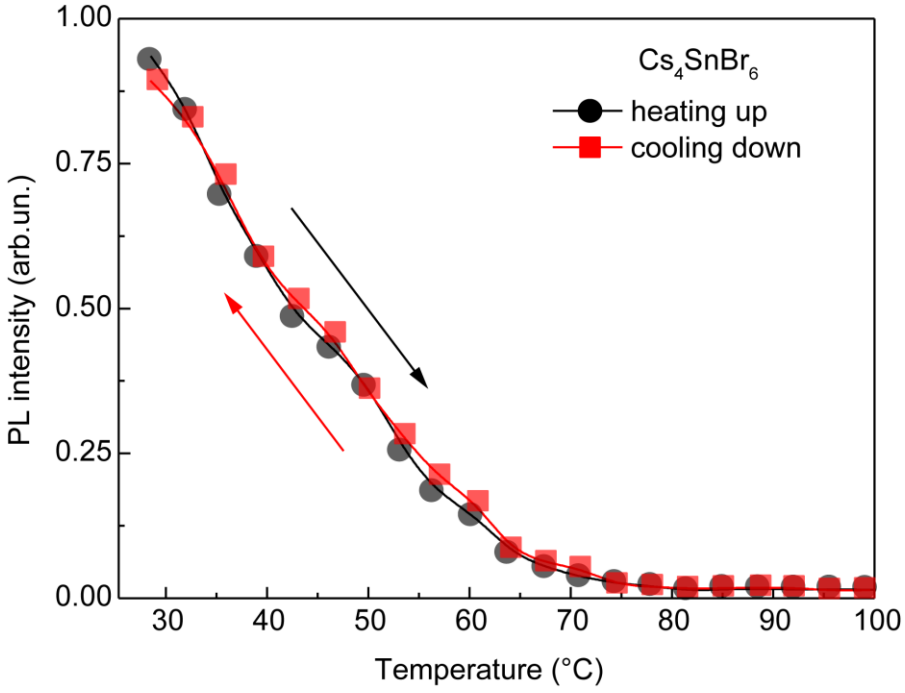

Figure 8.20. Reversible thermal quenching for Cs_4SnBr_6 PL emission.

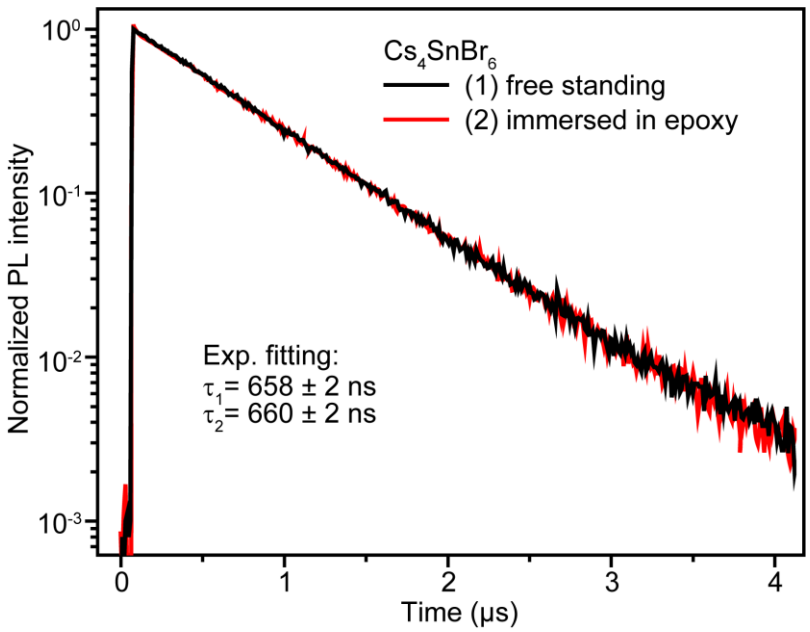

Figure 8.21. Effect of surrounding on time-resolved PL traces for Cs_4SnBr_6.

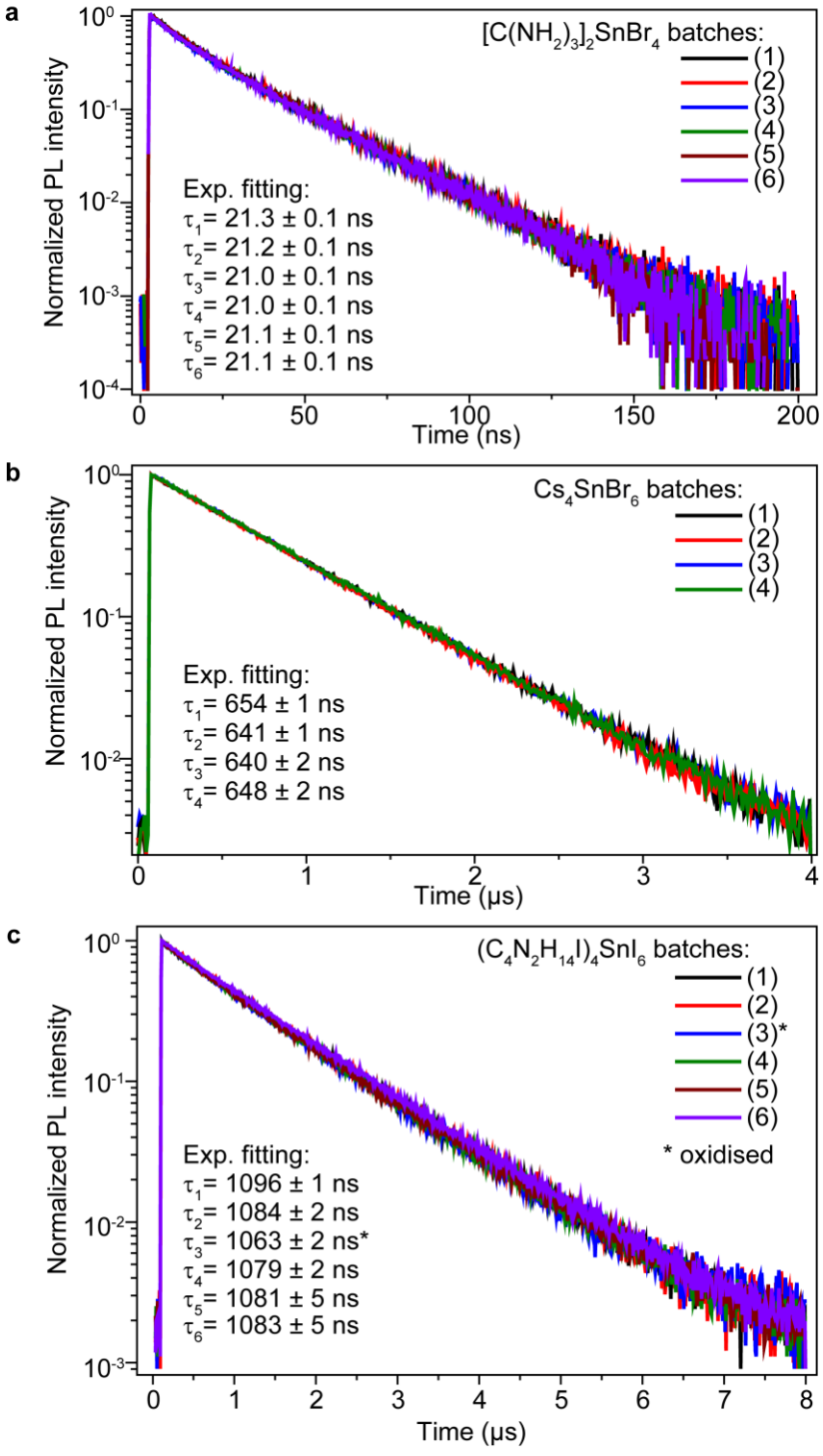

Figure 8.22. Time-resolved PL traces for several batches of (a) $[C(NH_2)_3]_2SnBr_4$, (b) Cs_4SnBr_6, (c) $(C_4N_2H_{14}I)_4SnI_6$. Measured lifetimes vary mostly as a result of RT fluctuation.

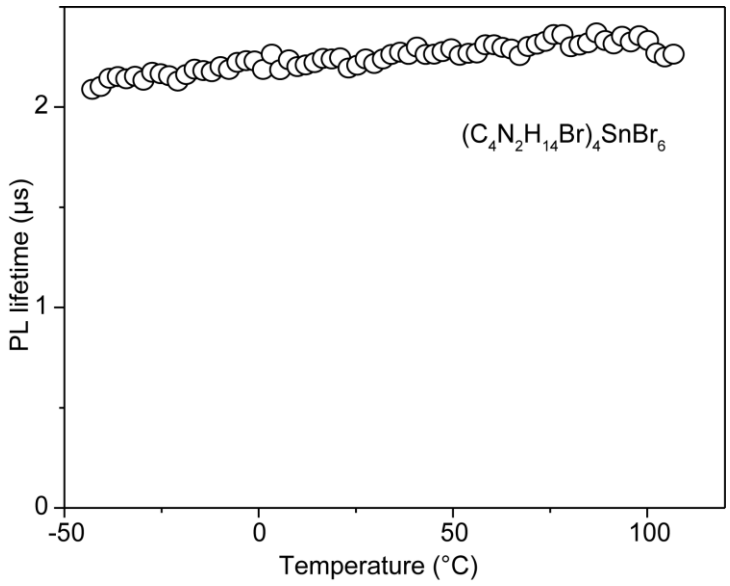

Figure 8.23. PL lifetime temperature dependence for $(C_4N_2H_{14}Br)_4SnBr_6$.

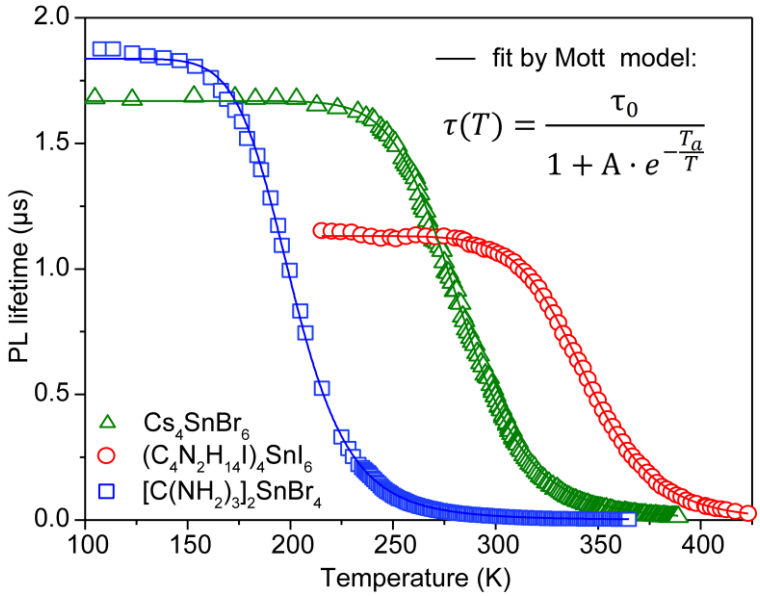

Figure 8.24. Fitting by the Mott model. PL lifetime temperature dependence for $[C(NH_2)_3]_2SnBr_4$ (blue squares), Cs_4SnBr_6 (green triangles), $(C_4N_2H_{14}I)_4SnI_6$ (red circles) by fitting with an Mott model (colored lines): $\tau(T) = \frac{\tau_0}{1+A \cdot e^{-\frac{T_a}{T}}}$.

Table 8.19. Fitting parameters for the Mott model.

Composition	τ_0	A	T_a	E_a	Temperature sensitivity range
	ns		K	eV	ºC (K)
Cs_4SnBr_6	1669	$1.9\ 10^7$	4759	0.41	-30 – 40 (243 - 323)
$[C(NH_2)_3]_2SnBr_4$	1837	$1.5\ 10^6$	2863	0.25	-100 – 30 (173 - 243)
$(C_4N_2H_{14}I)_4SnI_6$	1131	$5.7\ 10^8$	6945	0.6	40 – 110 (313 - 383)

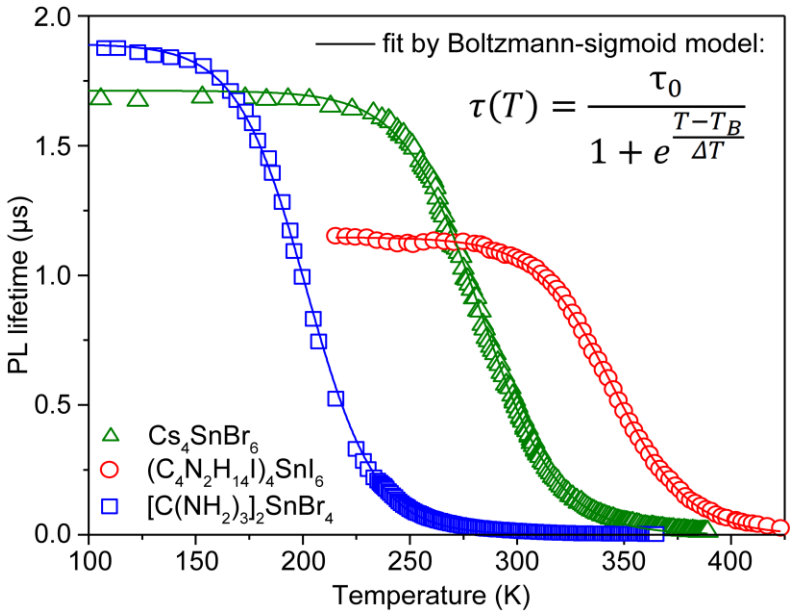

Figure 8.25. Fitting by the Boltzmann-sigmoid model. PL lifetime temperature dependence for $[C(NH_2)_3]_2SnBr_4$ (blue squares), Cs_4SnBr_6 (green triangles), $(C_4N_2H_{14}I)_4SnI_6$ (red circles) by fitting with the Boltzmann-sigmoid model (colored lines): $\tau(T) = \frac{\tau_0}{1+e^{\frac{T-T_B}{\Delta T}}}$.

Table 8.20. Fitting parameters for Boltzmann-sigmoid model. Temperature sensitivity ranges are determined as $T_B \pm 2\Delta T$

Composition	τ_0	T_B	ΔT	Temperature sensitivity range	E_{ph}
	ns	K	K	ºC (K)	meV
Cs_4SnBr_6	1711	281	18	-30 – 40 (243 - 323)	24
$[C(NH_2)_3]_2SnBr_4$	1892	205	17	-100 – 30 (173 - 243)	18
$(C_4N_2H_{14}I)_4SnI_6$	1146	345	18	40 – 110 (313 - 383)	30

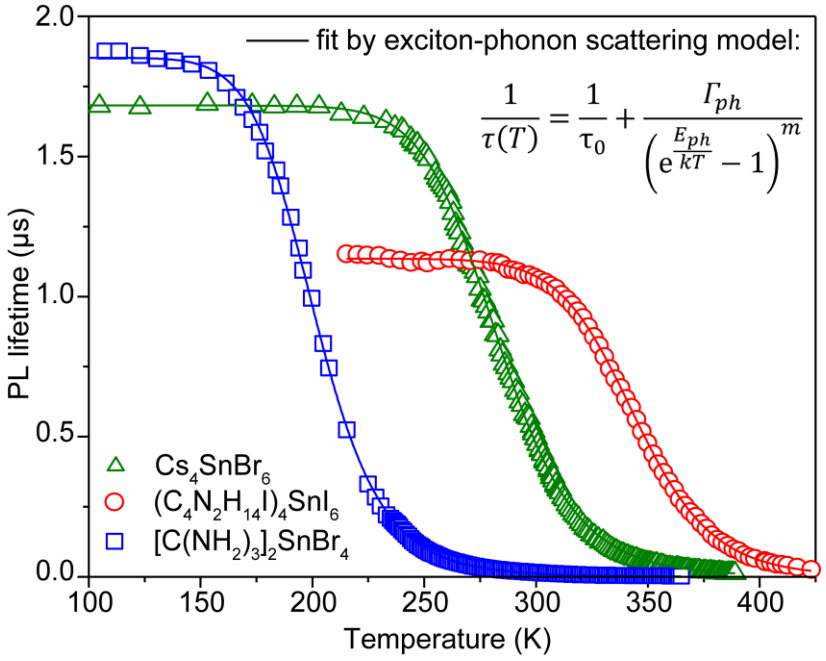

Figure 8.26. Fitting by the exciton-phonon scattering model. PL lifetime temperature dependence for $[C(NH_2)_3]_2SnBr_4$ (blue squares), Cs_4SnBr_6 (green triangles), $(C_4N_2H_{14}I)_4SnI_6$ (red circles) by fitting with the exciton-phonon scattering model (colored lines): $\frac{1}{\tau(T)} = \frac{1}{\tau_0} + \frac{\Gamma_{ph}}{\left(e^{\frac{E_{ph}}{kT}} - 1\right)^m}$.

Table 8.21. Fitting parameters for the exciton-phonon scattering model.

Composition	τ_0	Γ_{ph}	E_{ph}		m	Temperature sensitivity range
	ns	10^{-6} s^{-1}	meV	K		°C (K)
Cs_4SnBr_6	1681	0.053	21.3	247	10.7	-30 – 40 (243 - 323)
$[C(NH_2)_3]_2SnBr_4$	1851	0.03	15.6	181	8.7	-100 – 30 (173 - 243)
$(C_4N_2H_{14}I)_4SnI_6$	1135	0.13	25.2	292	13	40 – 110 (313 - 383)

Figure 8.27. Photographs of the depth standard for ToF imaging in Figure 3.8.

Note 8.1. Key specifications of ToF-FLI image sensor used in the setup:

- Number of pixels: 256 x 256 pixels
- Maximum frame rate at full resolution: 100 fps
- Analog outputs (no on-chip ADC)
- Pixel size: 6.3 x 6.3 µm → Active area size 1.6 mm x 1.6 mm
- Maximum demodulation frequency: 4 x 20 MHz = 80 MHz
- Quantum efficiency (QE): 0.43@600nm, 0.21@800nm, 0.14@850nm
- Fill factor: 14 %
- Dark current: 40 e-
- Pixel saturation capacitance: 9 ke-
- Maximum SNR: 39.9 dB
- Dynamic range: 49.9 dB
- Detailed description of image sensor architecture can be found in Supplementary Ref. [283].

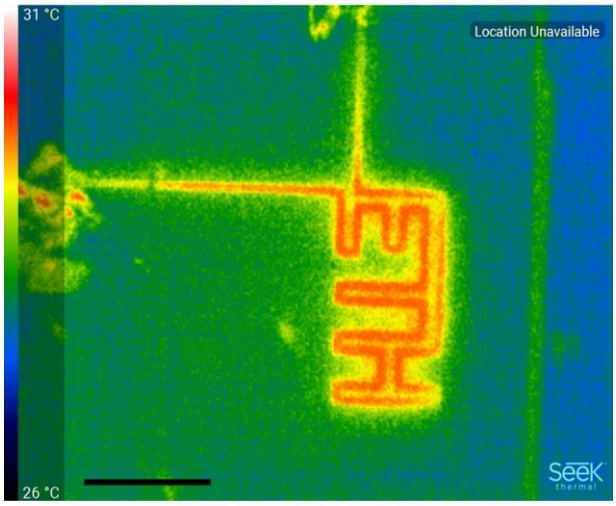

Figure 8.28. A thermographic image of a patterned ITO glass slide with a bolometric camera. The sample was heated with a passing electrical current and acquired with a commercial LWIR bolometry camera equipped with a ZnSe lensed macro-objective. Scale bar is 3 mm.

8.3. Appendix to Chapter 4

Table 8.22. Crystal data and structure refinement comparison for $Rb_7Sb_3Cl_{16}$ at 300 K, 230 K, and 100 K

Empirical formula	$Rb_7Sb_3Cl_{16}$	$Rb_7Sb_3Cl_{16}$	$Rb_7Sb_3Cl_{16}$
Formula weight	1530.74	1530.74	1530.74
Temperature	**300 K**	**230(2) K**	**100(2) K**
Wavelength	0.71073 Å	0.71073 Å	0.71073 Å
Crystal system	Hexagonal	Hexagonal	Hexagonal
Space group	*P*-62*m*	*P*-62*m*	*P*-62*m*
Unit cell dimensions	a = 12.9802(4) Å, α = 90° b = 12.9802(4) Å, β = 90° c = 34.2522(11) Å, γ = 120°	a = 12.9655(2) Å, α = 90° b = 12.9655(2) Å, β = 90° c = 34.1932(8) Å, γ = 120°	a = 12.8570(2) Å, α = 90° b = 12.8570(2) Å, β = 90° c = 34.1574(5) Å, γ = 120°
Volume	4997.8(3) $Å^3$	4977.93(19) $Å^3$	4889.84(17) $Å^3$
Z	6	6	6
Density (calculated)	3.052 g/cm^3	3.064 g/cm^3	3.119 g/cm^3
Absorption coefficient	13.855 mm^{-1}	13.910 mm^{-1}	14.161 mm^{-1}
F(000)	4104	4104	4104
Crystal size	0.241 x 0.187 x 0.03 mm^3	0.232 x 0.214 x 0.034 mm^3	0.201 x 0.168 x 0. 084 mm^3
θ range for data collection	1.784 to 31.572°	1.787 to 30.507°	1.789 to 30.497°
Index ranges	-18<=h<=18, -18<=k<=18, -49<=l<=49	-18<=h<=18, -18<=k<=18, -48<=l<=48	-18<=h<=18, -18<=k<=18, -50<=l<=50
Reflections collected	59312	297301	251406
Independent reflections	5798 [R_{int} = 0.0908]	5524 [R_{int} = 0.1190]	5426 [R_{int} = 0.1172]
Completeness to θ = 25.242°	99.9%	99.9%	99.9%
Refinement method	Full-matrix least-squares on F^2	Full-matrix least-squares on F^2	Full-matrix least-squares on F^2
Data / restraints / parameters	5798 / 0 / 218	5524 / 0 / 218	5426 / 0 / 208
Goodness-of-fit	1.093	1.216	1.109
Final R indices [I > 2σ(I)]	R_{obs} = 0.0818, wR_{obs} = 0.2226	R_{obs} = 0.0546, wR_{obs} = 0.1492	R_{obs} = 0.0802, wR_{obs} = 0.2347
R indices [all data]	R_{all} = 0.1037, wR_{all} = 0.2385	R_{all} = 0.0559, wR_{all} = 0.1505	R_{all} = 0.0825, wR_{all} = 0.2370
Largest diff. peak and hole	6.468 and -2.562 e·$Å^{-3}$	2.429 and -1.820 e·$Å^{-3}$	3.967 and -3.597 e·$Å^{-3}$
Absolute structure	Refined as inversion twin	Refined as inversion twin	Refined as inversion twin
Absolute structure parameter	0.46(4)	0.50(3)	0.50(3)

$R = \Sigma||F_o|-|F_c|| / \Sigma|F_o|$, $wR = \{\Sigma[w(|F_o|^2 - |F_c|^2)^2] / \Sigma[w(|F_o|^4)]\}^{1/2}$ and $w=1/[\sigma^2(Fo^2)+(0.1415P)^2+17.7772P]$ where $P=(Fo^2+2Fc^2)/3$

Table 8.23. Atomic coordinates (x10^4) and equivalent isotropic displacement parameters (Å^{2}x10^3) for $Rb_7Sb_3Cl_{16}$ at 300 K with estimated standard deviations in parentheses.

Label	x	y	z	Occupancy	U_{eq}*
Sb(1)	-6677(1)	0	-656(1)	1	26(1)
Sb(2)	-13257(1)	0	-2499(1)	1	26(1)
Sb(4)	-10000	0	-4340(1)	1	23(1)
Sb(3)	-16666.67	-3333.33	-4337(1)	1	24(1)
Rb(2)	-3333.33	3333.33	0	1	34(1)
Rb(3)	-13333.33	3333.33	-1328(1)	1	35(1)
Rb(1)	-2789(2)	0	0	1	32(1)
Rb(4)	-12882(2)	0	-1309(1)	1	39(1)
Rb(7)	-10000	0	-2909(2)	1	49(1)
Rb(5)	-13333.33	3333.33	-2805(1)	1	62(1)
Rb(6)	-16661(2)	0	-2152(2)	1	65(1)
Rb(8)	-13334(2)	-3334(2)	-3674(2)	0.6667	32(1)
Rb(11)	-13307(3)	-3307(3)	-5000	0.6667	38(2)
Cl(4)	-5542(3)	2370(4)	-664(1)	1	33(1)
Cl(7)	-13047(5)	1737(5)	-2013(2)	1	51(2)
Cl(6)	-11593(5)	0	-2123(2)	1	54(2)
Cl(1)	-5456(6)	0	-1230(2)	1	66(2)
Rb(10)	-13813(5)	0	-3674(2)	0.3333	34(2)
Rb(9)	-13403(4)	-488(4)	-3688(2)	0.3333	34(1)
Cl(3)	-8076(7)	0	0	1	64(3)
Cl(2)	-8092(6)	0	-1146(3)	1	68(2)
Cl(9)	-13319(6)	-1645(7)	-2944(2)	1	79(2)
Cl(5)	-5231(8)	0	0	1	81(4)
Cl(8)	-15037(7)	0	-2916(3)	1	107(4)
Cl(16)	-15479(11)	-1018(10)	-4337(3)	0.3333	34(2)
Cl(12)	-12344(9)	-1087(10)	-4332(3)	0.3333	31(2)
Cl(13)	-14287(10)	-2113(12)	-4329(3)	0.3333	35(2)
Rb(12)	-13370(5)	-578(5)	-5000	0.3333	36(2)
Rb(13)	-13845(6)	0	-5000	0.3333	36(2)
Cl(14)	-15445(14)	-2074(15)	-3802(6)	0.3333	71(5)
Cl(15)	-16666(9)	-1872(14)	-3900(6)	0.3333	66(5)
Cl(18)	-15270(20)	-3370(14)	-5000	0.3333	88(11)
Cl(11)	-11453(14)	-1453(14)	-3870(6)	0.3333	49(4)
Cl(10)	-11241(13)	0	-3824(6)	0.3333	53(5)
Cl(19)	-11480(20)	-1480(20)	-5000	0.3333	104(18)
Cl(20)	-11390(20)	0	-5000	0.3333	87(14)
Cl(17)	-16590(20)	-4760(20)	-5000	0.3333	102(13)

*U_{eq} is defined as one third of the trace of the orthogonalized U_{ij} tensor.

Table 8.24. Anisotropic displacement parameters ($Å^2x10^3$) for $Rb_7Sb_3Cl_{16}$ at 300 K with estimated standard deviations in parentheses.

Label	U_{11}	U_{22}	U_{33}	U_{12}	U_{13}	U_{23}
Sb(1)	28(1)	28(1)	20(1)	14(1)	-1(1)	0
Sb(2)	26(1)	29(1)	23(1)	15(1)	1(1)	0
Sb(4)	24(1)	24(1)	22(1)	12(1)	0	0
Sb(3)	23(1)	23(1)	27(1)	11(1)	0	0
Rb(2)	40(2)	40(2)	21(2)	20(1)	0	0
Rb(3)	44(1)	44(1)	18(1)	22(1)	0	0
Rb(1)	32(1)	30(2)	35(2)	15(1)	0	0
Rb(4)	52(2)	37(2)	24(1)	18(1)	0(1)	0
Rb(7)	58(2)	58(2)	30(2)	29(1)	0	0
Rb(5)	69(2)	69(2)	47(2)	35(1)	0	0
Rb(6)	60(2)	37(2)	88(3)	19(1)	-2(2)	0
Rb(8)	31(2)	31(2)	32(2)	14(2)	-2(1)	-2(1)
Rb(11)	34(2)	34(2)	42(3)	16(2)	0	0
Cl(4)	33(2)	34(2)	29(2)	14(2)	0(2)	2(2)
Cl(7)	91(3)	46(2)	32(2)	45(2)	11(2)	-1(2)
Cl(6)	51(2)	104(5)	25(2)	52(3)	-1(2)	0
Cl(1)	70(3)	95(6)	41(3)	47(3)	17(2)	0
Rb(10)	37(2)	24(3)	37(3)	12(2)	-3(2)	0
Rb(9)	30(2)	34(2)	37(2)	16(2)	-2(2)	2(2)
Cl(3)	36(3)	33(4)	121(9)	16(2)	0	0
Cl(2)	59(3)	39(3)	99(5)	20(2)	-46(4)	0
Cl(9)	132(6)	70(4)	68(3)	74(4)	-11(3)	-32(3)
Cl(5)	52(4)	112(10)	100(8)	56(5)	0	0
Cl(8)	71(3)	202(12)	93(6)	101(6)	-20(4)	0
Cl(16)	37(5)	32(5)	34(4)	19(4)	-2(4)	-3(4)
Cl(12)	25(4)	25(5)	35(4)	6(4)	0(4)	0(4)
Cl(13)	25(4)	44(6)	35(4)	18(5)	0(4)	-5(5)
Rb(12)	27(3)	25(3)	52(4)	11(2)	0	0
Rb(13)	26(3)	28(4)	53(5)	14(2)	0	0
Cl(14)	52(8)	58(8)	100(13)	27(8)	-40(9)	-39(9)
Cl(15)	29(6)	50(8)	109(13)	13(5)	7(6)	-44(9)
Cl(18)	54(13)	19(8)	190(30)	19(8)	0	0
Cl(11)	44(6)	44(6)	66(11)	27(7)	20(8)	20(8)
Cl(10)	39(6)	60(11)	67(12)	30(6)	19(7)	0
Cl(19)	23(8)	23(8)	270(60)	13(9)	0	0
Cl(20)	32(9)	45(16)	190(50)	22(8)	0	0
Cl(17)	68(17)	34(10)	210(40)	29(11)	0	0

The anisotropic displacement factor exponent takes the form: $-2\pi^2[h^2a^{*2}U_{11} + ... + 2hka^*b^*U_{12}]$

Table 8.25. Selected bond lengths [Å] for $Rb_7Sb_3Cl_{16}$ at 300 K with estimated standard deviations in parentheses.

Label	Distances
Sb(1)-Cl(4)	2.665(4)
Sb(1)-Cl(1)	2.525(6)
Sb(1)-Cl(3)	2.890(6)
Sb(1)-Cl(2)	2.487(6)
Sb(2)-Rb(4)	4.105(2)
Sb(2)-Cl(7)	2.705(5)
Sb(2)-Cl(6)	2.515(7)
Sb(2)-Rb(10)	4.090(6)
Sb(2)-Rb(9)	4.113(5)
Sb(2)-Cl(9)	2.591(6)
Sb(2)-Cl(8)	2.715(9)
Sb(4)-Cl(12)	2.638(10)
Sb(4)-Cl(11)	2.479(17)
Sb(4)-Cl(10)	2.390(17)
Sb(3)-Cl(16)	2.603(11)
Sb(3)-Cl(13)	2.675(11)
Sb(3)-Cl(14)	2.440(15)
Sb(3)-Cl(15)	2.417(13)
Rb(2)-Rb(1)	4.7199(16)
Rb(2)-Cl(4)	3.371(3)
Rb(2)-Cl(5)	3.7590(8)
Rb(3)-Rb(4)	4.6477(15)
Rb(3)-Cl(7)	3.273(5)
Rb(1)-Cl(5)	3.170(10)
Rb(4)-Cl(7)	3.379(5)
Rb(4)-Cl(6)	3.252(6)
Rb(7)-Cl(6)	3.395(6)
Rb(7)-Cl(9)	3.733(6)
Rb(7)-Cl(10)	3.52(2)
Rb(5)-Cl(7)	3.545(5)
Rb(5)-Cl(8)	3.7665(9)
Rb(6)-Cl(8)	3.360(11)
Rb(8)-Cl(9)	3.321(6)
Rb(8)-Cl(12)	3.387(11)
Rb(8)-Cl(13)	3.322(12)
Rb(8)-Cl(11)	2.531(18)
Rb(11)-Cl(13)	3.357(11)
Rb(11)-Cl(18)	2.51(3)
Rb(11)-Cl(19)	2.37(3)
Rb(10)-Rb(9)	1.011(8)
Rb(10)-Cl(8)	3.046(12)
Rb(10)-Cl(16)	2.954(12)
Rb(10)-Cl(13)	3.353(12)
Rb(10)-Cl(14)	2.495(16)
Rb(10)-Cl(15)	3.349(13)
Rb(10)-Cl(10)	3.377(18)
Rb(9)-Cl(9)	2.990(9)
Rb(9)-Cl(16)	3.290(12)
Rb(9)-Cl(12)	2.901(11)
Rb(9)-Cl(13)	2.857(12)

Rb(9)-Cl(14)	2.441(16)
Rb(9)-Cl(11)	3.396(7)
Rb(9)-Cl(10)	2.591(17)
Cl(16)-Rb(12)	3.378(12)
Cl(16)-Rb(13)	2.931(11)
Cl(16)-Cl(14)	2.30(2)
Cl(16)-Cl(15)	2.03(2)
Cl(12)-Cl(13)	2.185(17)
Cl(12)-Rb(12)	2.886(11)
Cl(12)-Cl(11)	2.147(18)
Cl(12)-Cl(10)	2.25(2)
Cl(13)-Rb(12)	2.880(11)
Cl(13)-Rb(13)	3.399(12)
Cl(13)-Cl(14)	2.37(2)
Rb(12)-Rb(13)	1.186(10)
Rb(12)-Cl(18)	3.205(18)
Rb(12)-Cl(19)	3.203(8)
Rb(12)-Cl(20)	2.28(3)
Rb(13)-Cl(20)	3.18(3)
Cl(14)-Cl(15)	1.76(2)
Cl(18)-Cl(17)	1.76(3)
Cl(11)-Cl(10)	1.772(13)
Cl(19)-Cl(20)	1.869(18)

Table 8.26. Atomic coordinates (x10^4) and equivalent isotropic displacement parameters (Å^{2}x10^3) for $Rb_7Sb_3Cl_{16}$ at 230(2) K with estimated standard deviations in parentheses.

Label	x	y	z	Occupancy	U_{eq}*
Sb(1)	6676(1)	0	5657(1)	1	26(1)
Sb(2)	10000	3252(1)	7500(1)	1	24(1)
Sb(3)	10000	0	9342(1)	1	20(1)
Sb(4)	6666.67	3333.33	9340(1)	1	20(1)
Rb(1)	2786(2)	0	5000	1	26(1)
Rb(2)	6666.67	3333.33	5000	1	31(1)
Rb(3)	6666.67	3333.33	6328(1)	1	28(1)
Rb(4)	10000	2884(2)	6310(1)	1	31(1)
Rb(5)	10000	0	7912(1)	1	40(1)
Rb(6)	6666.67	3333.33	7806(1)	1	53(1)
Rb(7)	10000	6674(2)	7154(2)	1	64(1)
Rb(8)	10000	6661(2)	8677(1)	0.6667	33(1)
Rb(9)	10000	3833(4)	8678(2)	0.3333	32(1)
Rb(10)	9532(3)	2940(4)	8693(1)	0.3333	33(1)
Rb(11)	10000	3848(5)	10000	0.3333	33(2)
Rb(12)	9418(4)	2789(4)	10000	0.3333	33(1)
Rb(13)	10000	6696(3)	10000	0.6667	32(1)
Cl(1)	7909(2)	2371(2)	5663(1)	1	27(1)
Cl(2)	5457(4)	0	6230(2)	1	52(2)
Cl(3)	8109(4)	0	6134(2)	1	55(2)
Cl(4)	8077(5)	0	5000	1	58(2)
Cl(5)	5212(5)	0	5000	1	75(3)

Cl(6)	8255(3)	3032(4)	7015(1)	1	41(1)
Cl(7)	10000	1586(3)	7123(2)	1	43(1)
Cl(8)	8359(6)	1671(5)	7951(2)	1	83(2)
Cl(9)	10000	5053(6)	7923(2)	1	115(4)
Cl(10)	7868(12)	3368(10)	8770(4)	0.3333	55(3)
Cl(11)	8117(10)	4787(10)	8880(5)	0.3333	64(4)
Cl(12)	8555(10)	0	8845(4)	0.3333	39(2)
Cl(13)	10000	1237(10)	8801(4)	0.3333	48(3)
Cl(14)	8912(8)	1255(8)	9331(2)	0.3333	32(2)
Cl(15)	7894(9)	2189(8)	9329(2)	0.3333	34(2)
Cl(16)	8991(7)	4474(8)	9341(2)	0.3333	33(2)
Cl(17)	8063(14)	4704(14)	10000	0.3333	63(5)
Cl(18)	8156(14)	3404(16)	10000	0.3333	78(7)
Cl(19)	10000	8532(16)	10000	0.3333	65(7)
Cl(20)	8600(16)	8600(16)	10000	0.3333	67(8)

*U_{eq} is defined as one third of the trace of the orthogonalized U_{ij} tensor.

Table 8.27. Anisotropic displacement parameters ($Å^2x10^3$) for $Rb_7Sb_3Cl_{16}$ at 230(2) K with estimated standard deviations in parentheses.

Label	U_{11}	U_{22}	U_{33}	U_{12}	U_{13}	U_{23}
Label	U_{11}	U_{22}	U_{33}	U_{12}	U_{13}	U_{23}
Sb(1)	29(1)	28(1)	21(1)	14(1)	-1(1)	0
Sb(2)	28(1)	23(1)	23(1)	14(1)	0	1(1)
Sb(3)	19(1)	19(1)	21(1)	10(1)	0	0
Sb(4)	18(1)	18(1)	25(1)	9(1)	0	0
Rb(1)	22(1)	24(1)	33(1)	12(1)	0	0
Rb(2)	35(1)	35(1)	23(2)	17(1)	0	0
Rb(3)	32(1)	32(1)	19(1)	16(1)	0	0
Rb(4)	28(1)	37(1)	25(1)	14(1)	0	0(1)
Rb(5)	47(1)	47(1)	28(2)	23(1)	0	0
Rb(6)	59(1)	59(1)	42(2)	30(1)	0	0
Rb(7)	34(1)	56(2)	95(2)	17(1)	0	-4(2)
Rb(8)	35(2)	35(1)	30(2)	18(1)	0	1(1)
Rb(9)	27(2)	34(2)	34(2)	14(1)	0	1(2)
Rb(10)	36(2)	41(2)	30(2)	25(2)	-4(2)	-5(2)
Rb(11)	25(3)	26(2)	47(4)	12(2)	0	0
Rb(12)	27(2)	27(2)	46(3)	14(2)	0	0
Rb(13)	34(2)	30(2)	32(2)	17(1)	0	0
Cl(1)	31(2)	27(2)	26(1)	15(1)	-2(1)	0(1)
Cl(2)	49(2)	66(3)	48(3)	33(2)	16(2)	0
Cl(3)	45(2)	31(2)	85(4)	16(1)	-36(2)	0
Cl(4)	29(2)	24(3)	119(7)	12(2)	0	0
Cl(5)	39(3)	89(7)	113(8)	45(3)	0	0
Cl(6)	36(2)	68(2)	29(2)	34(2)	-1(2)	10(2)
Cl(7)	77(3)	38(2)	26(2)	39(2)	0	-4(2)
Cl(8)	71(3)	56(2)	75(3)	-5(2)	31(3)	20(2)
Cl(9)	218(11)	72(3)	103(5)	109(6)	0	-15(3)
Cl(10)	56(6)	50(6)	58(6)	25(5)	21(5)	0(5)

Cl(11)	41(5)	47(6)	117(11)	31(5)	35(6)	46(7)
Cl(12)	34(4)	28(5)	51(6)	14(2)	-10(5)	0
Cl(13)	64(9)	39(4)	48(7)	32(5)	0	8(5)
Cl(14)	26(4)	32(4)	38(3)	14(3)	2(3)	3(3)
Cl(15)	40(4)	28(4)	40(4)	21(3)	2(4)	-1(3)
Cl(16)	30(4)	30(4)	38(4)	13(3)	6(3)	2(3)
Cl(17)	35(7)	38(7)	128(17)	27(6)	0	0
Cl(18)	30(7)	48(9)	160(20)	25(6)	0	0
Cl(19)	22(7)	29(6)	140(20)	11(4)	0	0

The anisotropic displacement factor exponent takes the form: $-2\pi^2[h^2a^{*2}U_{11} + ... + 2hka^*b^*U_{12}]$.

Table 8.28. Selected bond lengths [Å] for $Rb_7Sb_3Cl_{16}$ at 230(2) K with estimated standard deviations in parentheses.

Label	Distances
Sb(1)-Cl(1)	2.664(3)
Sb(1)-Cl(2)	2.517(5)
Sb(1)-Cl(3)	2.471(5)
Sb(1)-Cl(4)	2.890(5)
Sb(1)-Cl(5)	2.942(5)
Sb(2)-Rb(4)	4.0967(19)
Sb(2)-Rb(9)	4.095(5)
Sb(2)-Rb(10)	4.112(4)
Sb(2)-Cl(6)	2.703(3)
Sb(2)-Cl(7)	2.515(4)
Sb(2)-Cl(8)	2.597(5)
Sb(2)-Cl(9)	2.745(7)
Sb(3)-Cl(12)	2.528(13)
Sb(3)-Cl(13)	2.448(13)
Sb(3)-Cl(14)	2.634(8)
Sb(4)-Cl(10)	2.481(11)
Sb(4)-Cl(11)	2.454(11)
Sb(4)-Cl(15)	2.664(8)
Sb(4)-Cl(16)	2.610(8)
Rb(1)-Cl(5)	3.145(7)
Rb(2)-Rb(3)	4.5402(18)
Rb(2)-Cl(1)	3.362(2)
Rb(2)-Cl(5)	3.7529(6)
Rb(3)-Rb(4)	4.6406(10)
Rb(3)-Cl(1)	3.365(3)
Rb(3)-Cl(2)	3.8041(9)
Rb(3)-Cl(6)	3.274(3)
Rb(4)-Cl(1)	3.299(3)
Rb(4)-Cl(3)	3.3456(17)
Rb(4)-Cl(6)	3.375(3)
Rb(4)-Cl(7)	3.250(4)
Rb(5)-Cl(7)	3.391(5)
Rb(5)-Cl(8)	3.722(6)
Rb(5)-Cl(12)	3.701(15)
Rb(5)-Cl(13)	3.437(15)
Rb(6)-Cl(6)	3.536(4)

Rb(6)-Cl(8)	3.799(6)
Rb(6)-Cl(9)	3.7648(10)
Rb(6)-Cl(10)	3.638(14)
Rb(7)-Cl(9)	3.367(9)
Rb(8)-Cl(9)	3.316(8)
Rb(8)-Cl(11)	2.533(11)
Rb(8)-Cl(16)	3.348(9)
Rb(9)-Rb(10)	1.005(6)
Rb(9)-Cl(9)	3.027(10)
Rb(9)-Cl(10)	2.537(13)
Rb(9)-Cl(11)	3.315(10)
Rb(9)-Cl(13)	3.393(14)
Rb(9)-Cl(15)	3.339(10)
Rb(9)-Cl(16)	2.939(9)
Rb(10)-Cl(8)	2.991(7)
Rb(10)-Cl(10)	2.497(14)
Rb(10)-Cl(12)	3.402(5)
Rb(10)-Cl(13)	2.592(13)
Rb(10)-Cl(14)	2.903(9)
Rb(10)-Cl(15)	2.852(9)
Rb(10)-Cl(16)	3.280(9)
Rb(11)-Rb(12)	1.191(8)
Rb(11)-Cl(16)	2.917(9)
Rb(11)-Cl(17)	3.214(13)
Rb(11)-Cl(18)	2.161(16)
Rb(12)-Cl(14)	2.882(9)
Rb(12)-Cl(15)	2.869(9)
Rb(12)-Cl(18)	2.149(16)
Rb(13)-Cl(16)	3.365(9)
Rb(13)-Cl(17)	2.548(17)
Rb(13)-Cl(19)	2.38(2)
Cl(10)-Cl(11)	1.743(16)
Cl(10)-Cl(15)	2.460(16)
Cl(10)-Cl(16)	2.429(16)
Cl(11)-Cl(16)	2.097(16)
Cl(12)-Cl(13)	1.761(10)
Cl(12)-Cl(14)	2.207(14)
Cl(13)-Cl(14)	2.306(15)
Cl(14)-Cl(15)	2.192(12)
Cl(17)-Cl(18)	1.75(2)
Cl(19)-Cl(20)	1.861(13)
Sb(1)-Cl(1)	2.664(3)

Table 8.29. Atomic coordinates ($x10^4$) and equivalent isotropic displacement parameters ($Å^2x10^3$) for $Rb_7Sb_3Cl_{16}$ at 100(2) K with estimated standard deviations in parentheses.

Label	x	y	z	Occupancy	U_{eq}*
Sb(1)	3303(2)	10000	5663(1)	1	15(1)
Sb(2)	0	6743(1)	7500(1)	1	15(1)
Sb(3)	3333.33	6666.67	9331(1)	1	12(1)
Sb(4)	0	10000	9337(1)	1	13(1)
Rb(1)	7196(2)	10000	5000	1	16(1)
Rb(2)	3333.33	6666.67	5000	1	16(1)
Rb(3)	-3333.33	3333.33	6325(1)	1	17(1)
Rb(4)	0	7115(2)	6318(1)	1	20(1)
Rb(5)	-3333.33	3333.33	7800(1)	1	34(1)
Rb(6)	-3349(2)	6651(2)	7156(2)	1	40(1)
Rb(7)	0	10000	7913(2)	1	26(1)
Rb(8)	0	6187(5)	8673(2)	0.3333	15(2)
Rb(9)	475(4)	7082(5)	8688(2)	0.3333	16(1)
Rb(10)	3339(2)	10000	8675(1)	0.6667	13(1)
Rb(11)	3312(3)	10000	10000	0.6667	12(1)
Rb(12)	6175(6)	10000	10000	0.3333	15(2)
Rb(13)	7184(6)	10551(5)	10000	0.3333	15(2)
Cl(1)	4735(9)	10000	5000	1	70(5)
Cl(2)	1890(9)	10000	5000	1	95(8)
Cl(3)	2079(4)	7616(4)	5666(1)	1	17(1)
Cl(4)	4546(7)	10000	6228(3)	1	41(2)
Cl(5)	1912(7)	10000	6164(3)	1	54(3)
Cl(6)	0	8423(6)	7131(2)	1	40(2)
Cl(7)	-1765(5)	5212(5)	7011(2)	1	32(1)
Cl(8)	0	4942(7)	7918(3)	1	98(5)
Cl(9)	1651(8)	8342(7)	7949(2)	1	71(3)
Cl(10)	0	8745(14)	8805(7)	0.3333	32(4)
Cl(11)	1467(14)	10000	8823(6)	0.3333	26(3)
Cl(12)	1112(10)	8736(9)	9333(3)	0.3333	14(2)
Cl(13)	2078(10)	7825(10)	9329(3)	0.3333	14(2)
Cl(14)	3353(11)	8128(18)	8854(7)	0.3333	54(6)
Cl(15)	4522(17)	7899(16)	8771(6)	0.3333	45(4)
Cl(16)	4537(10)	9028(9)	9344(3)	0.3333	15(2)
Cl(17)	6599(19)	11883(19)	10105(5)	0.1667	15(4)
Cl(18)	5220(20)	11890(20)	9915(7)	0.1667	27(6)
Cl(19)	1490(30)	10000	10000	0.3333	48(8)

*U_{eq} is defined as one third of the trace of the orthogonalized U_{ij} tensor.

Table 8.30. Anisotropic displacement parameters ($Å^2x10^3$) for $Rb_7Sb_3Cl_{16}$ at 100(2) K with estimated standard deviations in parentheses.

Label	U_{11}	U_{22}	U_{33}	U_{12}	U_{13}	U_{23}
Sb(1)	18(1)	17(1)	9(1)	8(1)	0(1)	0
Sb(2)	18(1)	16(1)	12(1)	9(1)	0	0(1)
Sb(3)	12(1)	12(1)	13(1)	6(1)	0	0
Sb(4)	14(1)	14(1)	10(1)	7(1)	0	0
Rb(1)	20(1)	18(2)	8(1)	9(1)	0	0
Rb(2)	23(2)	23(2)	2(2)	12(1)	0	0
Rb(3)	21(1)	21(1)	8(1)	11(1)	0	0
Rb(4)	20(1)	28(1)	8(1)	10(1)	0	0(1)
Rb(5)	44(2)	44(2)	13(2)	22(1)	0	0
Rb(6)	24(1)	24(1)	75(3)	14(2)	-4(2)	-4(2)
Rb(7)	32(2)	32(2)	15(2)	16(1)	0	0
Rb(8)	14(3)	19(2)	11(2)	7(2)	0	-1(2)
Rb(9)	17(2)	23(2)	15(2)	15(2)	3(2)	3(2)
Rb(10)	14(2)	13(2)	12(2)	6(1)	-1(1)	0
Rb(11)	8(2)	10(2)	20(2)	5(1)	0	0
Rb(12)	8(2)	5(3)	30(4)	2(2)	0	0
Rb(13)	10(2)	12(3)	23(3)	6(2)	0	0
Cl(1)	27(4)	37(6)	150(17)	18(3)	0	0
Cl(2)	20(4)	12(4)	250(30)	6(2)	0	0
Cl(3)	25(2)	22(2)	6(2)	14(2)	1(2)	1(2)
Cl(4)	38(3)	37(4)	47(4)	18(2)	-15(3)	0
Cl(5)	37(3)	22(3)	97(7)	11(2)	42(4)	0
Cl(6)	93(6)	39(2)	7(2)	47(3)	0	0(2)
Cl(7)	32(2)	30(2)	9(2)	-2(2)	2(2)	-4(2)
Cl(8)	207(17)	57(4)	80(7)	104(8)	0	18(4)
Cl(9)	56(4)	46(4)	58(4)	-14(3)	-31(4)	-19(3)
Cl(10)	36(10)	21(6)	45(11)	18(5)	0	-3(6)
Cl(11)	20(5)	30(9)	31(8)	15(4)	7(6)	0
Cl(12)	11(4)	8(4)	21(4)	5(3)	1(3)	2(3)
Cl(13)	12(4)	10(4)	25(4)	9(3)	-1(4)	-1(4)
Cl(14)	6(5)	46(10)	100(16)	7(6)	-10(6)	25(10)
Cl(15)	38(9)	28(7)	72(12)	17(7)	20(9)	21(8)
Cl(16)	13(4)	7(4)	25(5)	5(4)	0(4)	1(3)

The anisotropic displacement factor exponent takes the form: $-2\pi^2[h^2a^{*2}U_{11} + ... + 2hka^*b^*U_{12}]$.

Table 8.31. Selected bond lengths [Å] for $Rb_7Sb_3Cl_{16}$ at 100(2) K with estimated standard deviations in parentheses.

Label	Distances
Sb(1)-Cl(3)	2.655(4)
Sb(1)-Cl(4)	2.506(8)
Sb(1)-Cl(5)	2.474(8)
Sb(2)-Rb(4)	4.068(3)
Sb(2)-Rb(8)	4.068(6)
Sb(2)-Rb(9)	4.094(5)
Sb(2)-Cl(6)	2.503(7)
Sb(2)-Cl(7)	2.710(5)
Sb(2)-Cl(8)	2.721(9)
Sb(2)-Cl(9)	2.593(7)
Sb(3)-Cl(14)	2.477(19)
Sb(3)-Cl(15)	2.466(18)
Sb(3)-Cl(16)	2.630(10)
Sb(4)-Cl(10)	2.43(2)
Sb(4)-Cl(11)	2.579(18)
Sb(4)-Cl(12)	2.648(10)
Rb(1)-Rb(2)	4.6633(18)
Rb(1)-Cl(1)	3.164(13)
Rb(2)-Cl(1)	3.7271(12)
Rb(2)-Cl(3)	3.352(3)
Rb(3)-Rb(4)	4.6012(15)
Rb(3)-Cl(7)	3.243(5)
Rb(4)-Cl(3)	3.285(4)
Rb(4)-Cl(5)	3.310(3)
Rb(4)-Cl(6)	3.247(6)
Rb(4)-Cl(7)	3.346(5)
Rb(5)-Cl(7)	3.507(5)
Rb(5)-Cl(8)	3.7340(13)
Rb(6)-Cl(6)	3.732(2)
Rb(6)-Cl(7)	3.403(6)
Rb(7)-Cl(6)	3.355(7)
Rb(7)-Cl(10)	3.45(2)
Rb(7)-Cl(11)	3.63(2)
Rb(8)-Rb(9)	0.998(8)
Rb(8)-Cl(8)	3.034(14)
Rb(8)-Cl(10)	3.32(2)
Rb(8)-Cl(13)	3.313(12)
Rb(9)-Cl(9)	2.973(10)
Rb(9)-Cl(10)	2.533(19)
Rb(9)-Cl(11)	3.336(7)
Rb(9)-Cl(12)	2.883(11)
Rb(9)-Cl(13)	2.826(11)
Rb(9)-Cl(14)	3.293(13)
Rb(10)-Cl(9)	3.282(7)
Rb(10)-Cl(11)	2.458(18)
Rb(10)-Cl(12)	3.354(11)
Rb(10)-Cl(13)	3.303(11)
Rb(10)-Cl(14)	2.492(19)
Rb(10)-Cl(16)	3.329(11)
Rb(11)-Cl(16)	3.323(11)

Rb(11)-Cl(18)	2.46(3)
Rb(11)-Cl(19)	2.35(4)
Rb(12)-Rb(13)	1.125(10)
Rb(12)-Cl(16)	2.897(11)
Rb(12)-Cl(17)	2.23(2)
Rb(12)-Cl(18)	3.24(2)
Rb(13)-Cl(17)	2.22(2)
Cl(10)-Cl(11)	1.767(13)
Cl(10)-Cl(12)	2.31(2)
Cl(11)-Cl(12)	2.270(18)
Cl(12)-Cl(13)	2.090(15)
Cl(13)-Cl(14)	2.20(2)
Cl(14)-Cl(15)	1.69(2)
Cl(14)-Cl(16)	2.17(2)
Cl(15)-Cl(16)	2.43(2)
Cl(17)-Cl(18)	1.89(3)

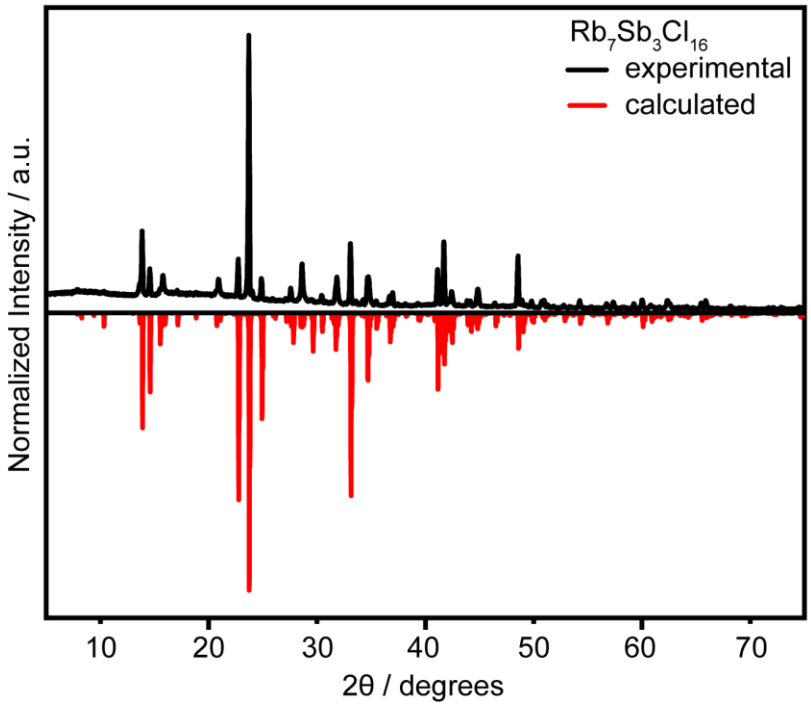

Figure 8.29. Experimental and calculated powder patterns of $Rb_7Sb_3Cl_{16}$. The $Rb_7Sb_3Cl_{16}$ diffraction pattern was calculated in Vesta using the experimentally determined structure of $Rb_7Sb_3Cl_{16}$.

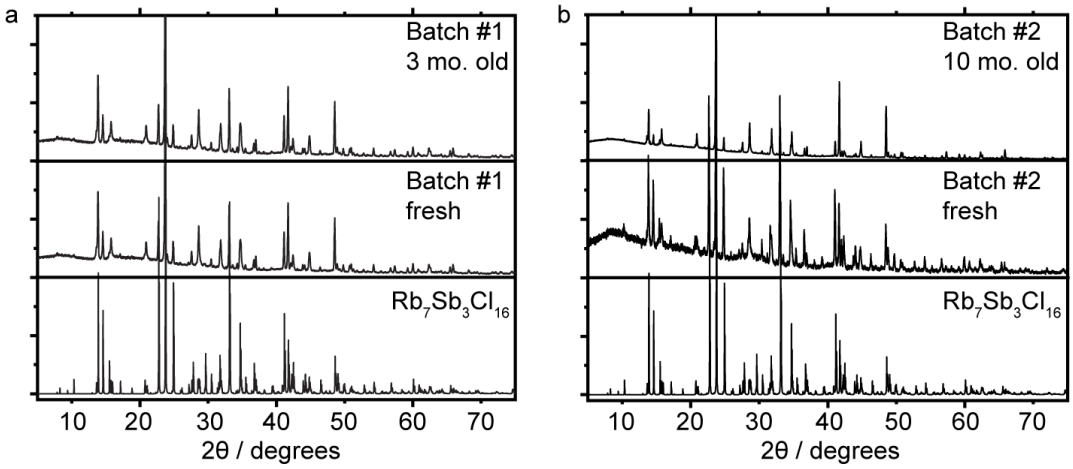

Figure 8.30. Structural stability of $Rb_7Sb_3Cl_{16}$. Two separate batches (a) and (b) were measured each after several months and no new phases were observed, supporting the oxidative stability of this material.

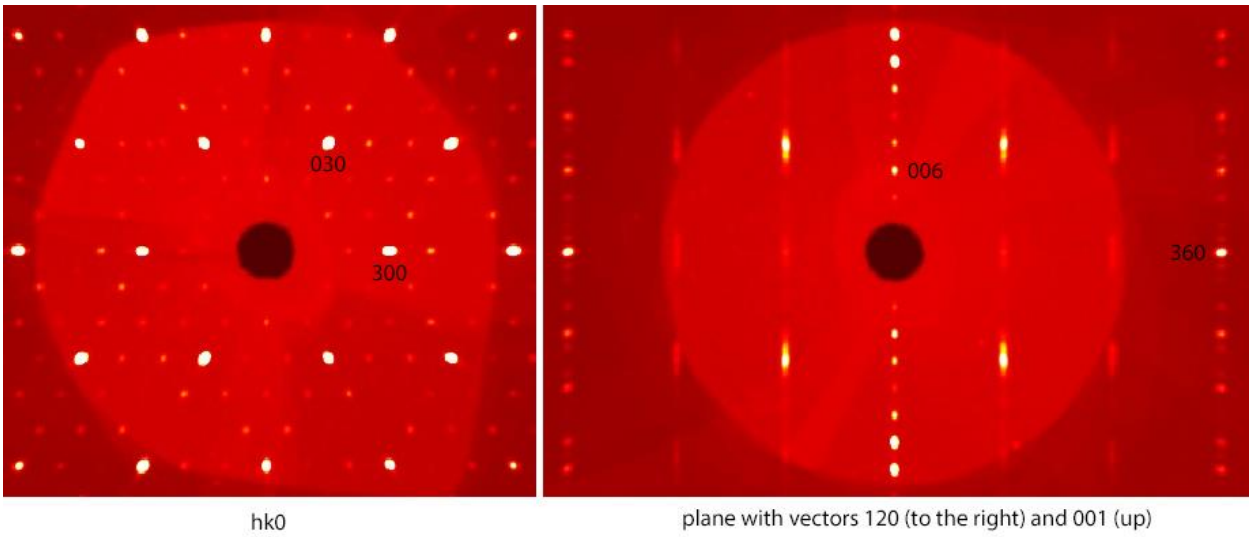

Figure 8.31. Unwrapped images from the 230 K diffraction experiment for $Rb_7Sb_3Cl_{16}$. The left panel demonstrates the six-fold symmetry present in the structure looking at the *ab* plane. The right image looks at the *c* axis and clearly demonstrates the combination of ordered and disordered units present in the structure. The discrete and well-resolved lines represent the ordered layers while the smeared lines in between are the disordered layers

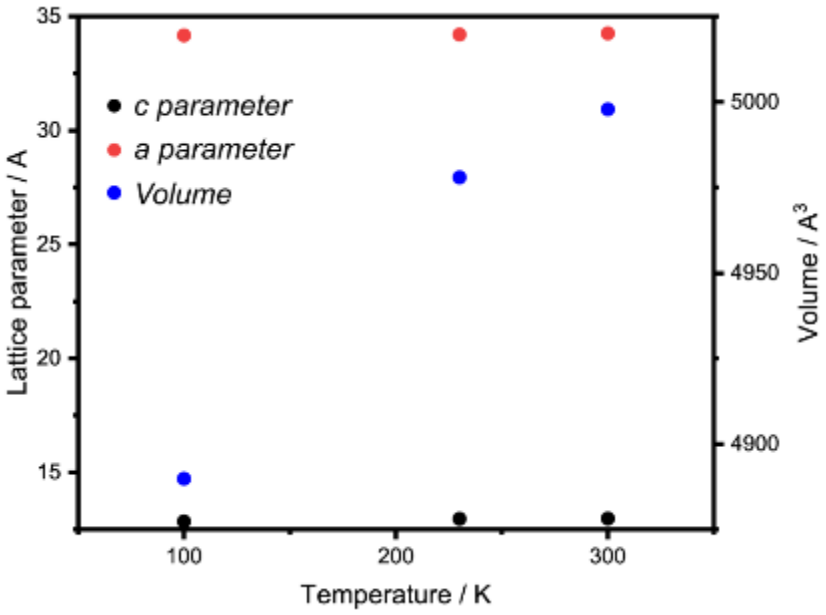

Figure 8.32. Lattice parameters and unit cell volume with temperature

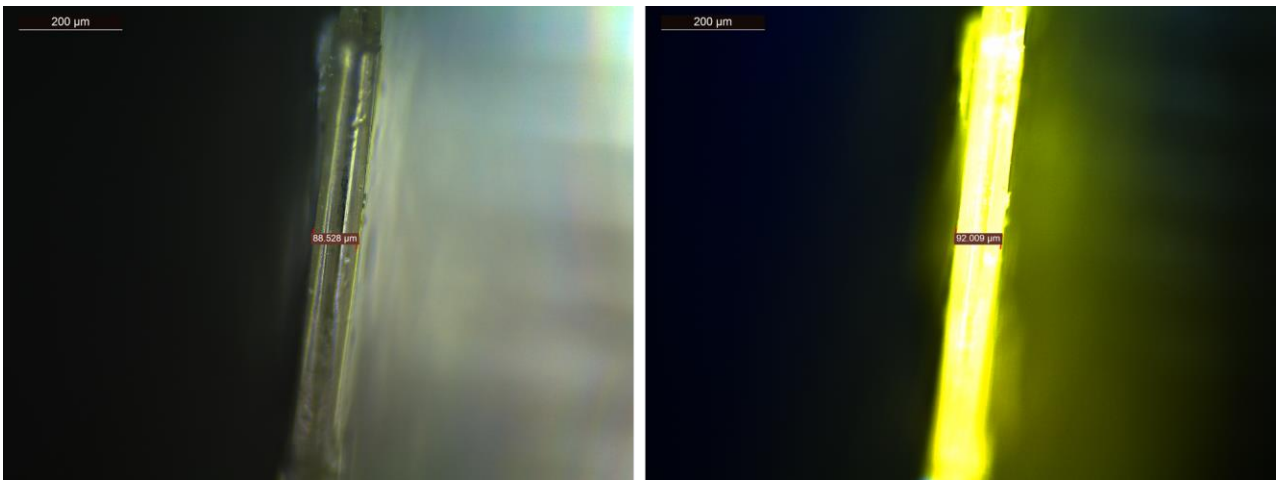

Figure 8.33. Side view of the single crystal of $Rb_7Sb_3Cl_{16}$ in white light (left) and fluorescence (right) mode used to measure the absorption coefficient. Scale bars are 200 µm.

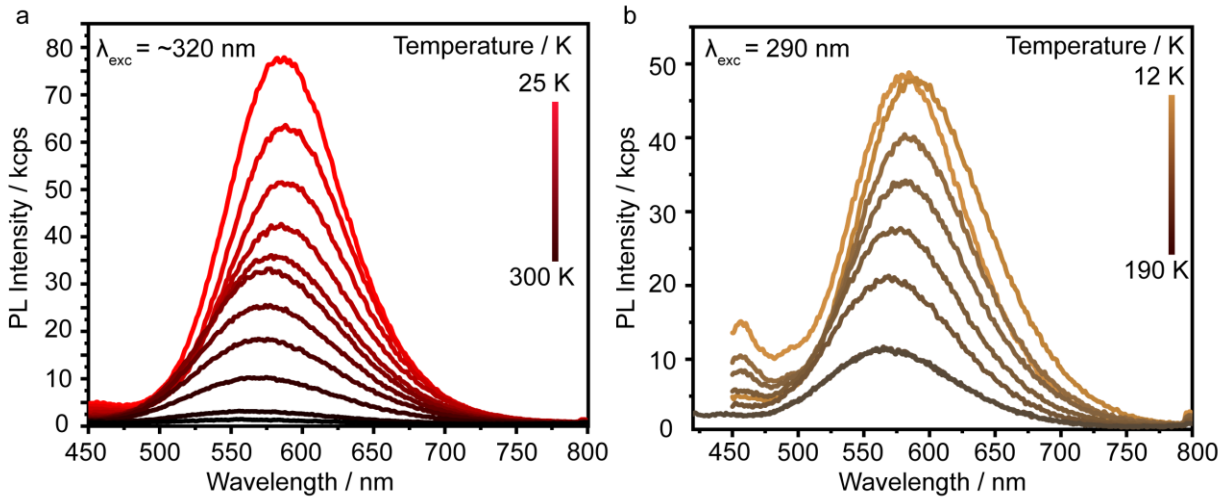

Figure 8.34. dT-PL spectra of $Rb_7Sb_3Cl_{16}$ with excitation at a) 320 nm and b) 290 nm.

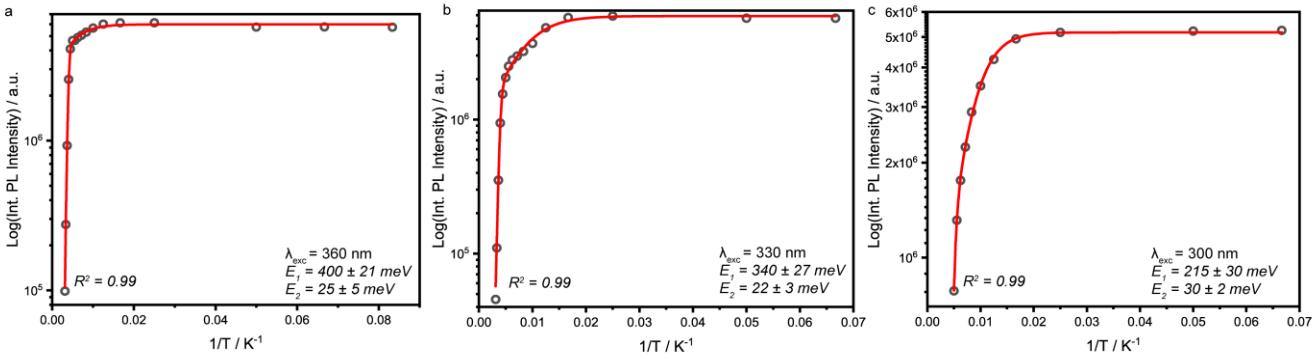

Figure 8.35. Arrhenius fits for the integrated PL-intensity of $Rb_7Sb_3Cl_{16}$ with two activation energies at a) 360 nm excitation, b) 330 nm excitation, and c) 300 nm excitation. The following formula was used during the fitting: $I_t = \frac{I_0}{1+C_1 e^{\frac{-E_1 T}{k_B 1000}} + C_2 e^{\frac{-E_2 T}{k_B 1000}}}$

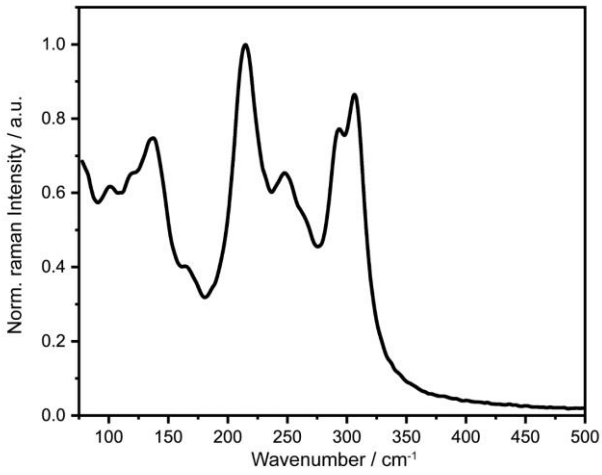

Figure 8.36. Raman spectra of $Rb_7Sb_3Cl_{16}$.

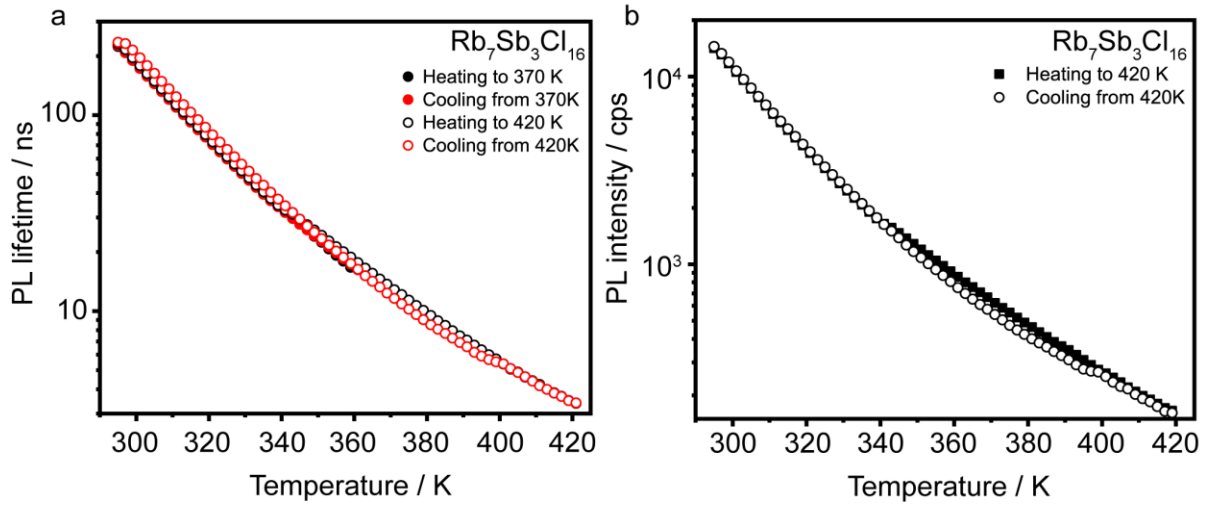

Figure 8.37. Thermal stability of $Rb_7Sb_3Cl_{16}$: a) PL lifetime as a function of temperature, b) PL intensity as a function of temperature. Lifetime and intensity were measured as separate runs.

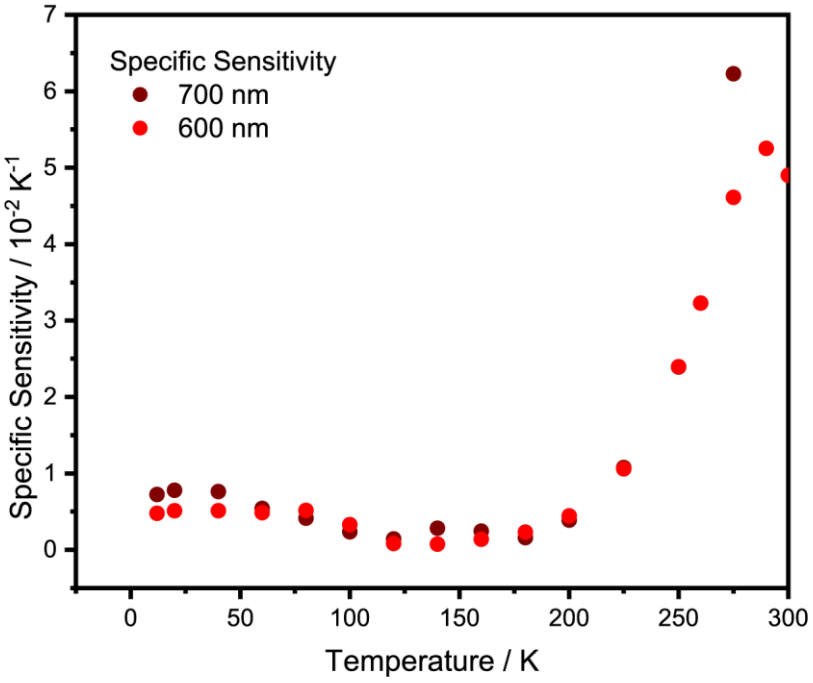

Figure 8.38. Specific sensitivities (α) calculated for $Rb_7Sb_3Cl_{16}$ at two different wavelengths with respect to T according to the formula, $\alpha = -\frac{dt}{dT}\frac{1}{t}$.

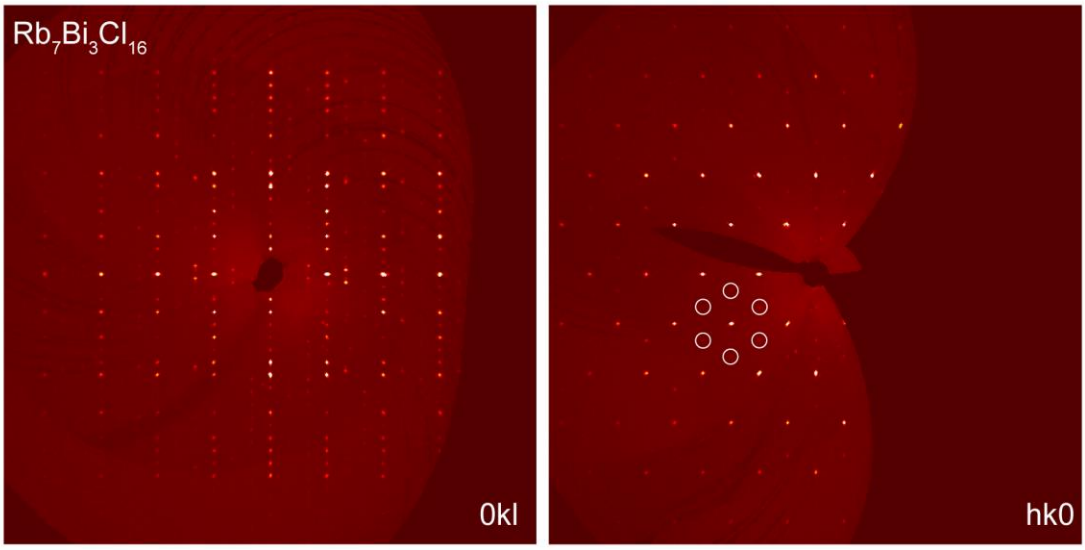

Figure 8.39. 0kl and hk0 unwrapped images for $Rb_7Bi_3Cl_{16}$.

Table 8.32. Crystal data and structure refinement for $Rb_7Bi_3Cl_{16}$ at 298 K.

Empirical formula	$Rb_7Bi_3Cl_{16}$
Formula weight	1792.43
Temperature	298 K
Wavelength	0.71073 Å
Crystal system	Hexagonal
Space group	*R*-3*c*
Unit cell dimensions	a = 13.10250(10) Å, α = 90° b = 13.10250(10) Å, β = 90° c = 102.9084(17) Å, γ = 120°
Volume	15299.9(3) $Å^3$
Z	18
Density (calculated)	3.502 g/cm^3
Absorption coefficient	26.700 mm^{-1}
F(000)	14040
Crystal size	0.071 x 0.058 x 0.04 mm^3
θ range for data collection	1.806 to 29.574°
Index ranges	-18<=h<=18, -13<=k<=18, -142<=l<=142
Reflections collected	60200
Independent reflections	4792 [R_{int} = 0.0878]
Completeness to θ = 25.242°	99.9%
Refinement method	Full-matrix least-squares on F^2
Data / restraints / parameters	4792 / 0 / 121
Goodness-of-fit	1.051
Final R indices [I > 2σ(I)]	R_{obs} = 0.0387, wR_{obs} = 0.0696
R indices [all data]	R_{all} = 0.0811, wR_{all} = 0.0778
Largest diff. peak and hole	1.180 and -1.552 e·$Å^{-3}$
Absolute structure	Refined with twin
Absolute structure parameter	0.206(3)

$R = \Sigma||F_o|-|F_c|| / \Sigma|F_o|$, $wR = \{\Sigma[w(|F_o|^2 - |F_c|^2)^2] / \Sigma[w(|F_o|^4)]\}^{1/2}$ and $w=1/[\sigma^2(Fo^2)+(0.0079P)^2+146.9450P]$

where $P=(Fo^2+2Fc^2)/3$

Table 8.33. Atomic coordinates ($x10^4$) and equivalent isotropic displacement parameters ($Å^2x10^3$) for $Rb_7Bi_3Cl_{16}$ at 298 K with estimated standard deviations in parentheses

Label	x	y	z	Occupancy	U_{eq}^*
Bi(1)	6666.67	3333.33	4980(1)	1	23(1)
Bi(2)	3331(1)	3351(1)	4385(1)	1	26(1)
Bi(3)	0	0	5000	1	22(1)
Rb(1)	9546(1)	6209(1)	5385(1)	1	35(1)
Rb(2)	9975(1)	6697(1)	4882(1)	1	61(1)
Rb(3)	6666.67	3333.33	4590(1)	1	40(1)
Rb(4)	6666.67	3333.33	4165(1)	1	36(1)
Rb(5)	3333.33	-534(1)	4166.67	1	34(1)
Rb(6)	0	0	4596(1)	1	40(1)

Cl(1)	8101(2)	5160(2)	5121(1)	1	56(1)
Cl(2)	8572(2)	3769(2)	4827(1)	1	47(1)
Cl(3)	5722(2)	4610(2)	4382(1)	1	34(1)
Cl(4)	3338(2)	4827(2)	4546(1)	1	58(1)
Cl(5)	3323(3)	2078(2)	4576(1)	1	58(1)
Cl(6)	3333.33	4749(2)	4166.67	1	35(1)
Cl(7)	3333.33	1924(2)	4166.67	1	50(1)
Cl(8)	932(2)	2211(2)	4385(1)	1	35(1)
Cl(9)	80(3)	1702(2)	4846(1)	1	49(1)

*U_{eq} is defined as one third of the trace of the orthogonalized U_{ij} tensor.

Table 8.34. Anisotropic displacement parameters ($Å^2x10^3$) for $Rb_7Bi_3Cl_{16}$ at 298 K with estimated standard deviations in parentheses.

Label	U_{11}	U_{22}	U_{33}	U_{12}	U_{13}	U_{23}
Bi(1)	23(1)	23(1)	21(1)	12(1)	0	0
Bi(2)	25(1)	28(1)	23(1)	13(1)	1(1)	-1(1)
Bi(3)	22(1)	22(1)	22(1)	11(1)	0	0
Rb(1)	36(1)	43(1)	29(1)	22(1)	-1(1)	-2(1)
Rb(2)	66(1)	43(1)	58(1)	16(1)	3(1)	-1(1)
Rb(3)	47(1)	47(1)	25(1)	24(1)	0	0
Rb(4)	42(1)	42(1)	26(1)	21(1)	0	0
Rb(5)	28(1)	31(1)	40(1)	14(1)	-1(1)	-1(1)
Rb(6)	47(1)	47(1)	26(1)	23(1)	0	0
Cl(1)	56(2)	48(2)	40(2)	8(2)	-13(2)	-16(2)
Cl(2)	36(2)	67(2)	40(2)	28(2)	6(1)	-7(2)
Cl(3)	30(2)	39(2)	33(1)	16(1)	1(1)	2(1)
Cl(4)	38(2)	53(2)	81(2)	21(2)	-1(2)	-35(2)
Cl(5)	77(2)	55(2)	43(2)	36(2)	-1(2)	15(2)
Cl(6)	29(2)	32(2)	43(2)	14(1)	2(2)	1(1)
Cl(7)	86(3)	39(2)	39(2)	43(2)	-1(2)	0(1)
Cl(8)	32(2)	35(2)	34(1)	14(1)	0(1)	0(1)
Cl(9)	82(2)	39(2)	37(2)	39(2)	-5(2)	5(1)

The anisotropic displacement factor exponent takes the form: $-2\pi^2[h^2a^{*2}U_{11} + ... + 2hka^*b^*U_{12}]$.

Table 8.35. Selected bond lengths [Å] for $Rb_7Bi_3Cl_{16}$ at 298 K with estimated standard deviations in parentheses.

Label	Distances
Bi(1)-Rb(2)	4.4871(10)
Bi(1)-Rb(3)	4.0144(13)
Bi(1)-Cl(1)	2.621(2)
Bi(1)-Cl(2)	2.762(2)
Bi(2)-Cl(3)	2.714(2)
Bi(2)-Cl(4)	2.544(2)
Bi(2)-Cl(5)	2.578(2)
Bi(2)-Cl(6)	2.8957(17)
Bi(2)-Cl(7)	2.9218(18)
Bi(2)-Cl(8)	2.723(2)
Bi(3)-Rb(6)	4.1545(12)
Bi(3)-Cl(9)	2.694(2)
Rb(1)-Cl(1)	3.195(2)
Rb(2)-Cl(1)	3.348(3)
Rb(2)-Cl(2)	3.371(3)
Rb(3)-Rb(4)	4.3724(16)
Rb(3)-Cl(2)	3.325(2)
Rb(3)-Cl(3)	3.315(2)
Rb(3)-Cl(5)	3.837(3)
Rb(4)-Cl(3)	3.373(2)
Rb(4)-Cl(7)	3.7974(3)
Rb(5)-Cl(7)	3.220(3)
Rb(6)-Cl(5)	3.815(3)
Rb(6)-Cl(8)	3.328(2)
Rb(6)-Cl(9)	3.370(2)

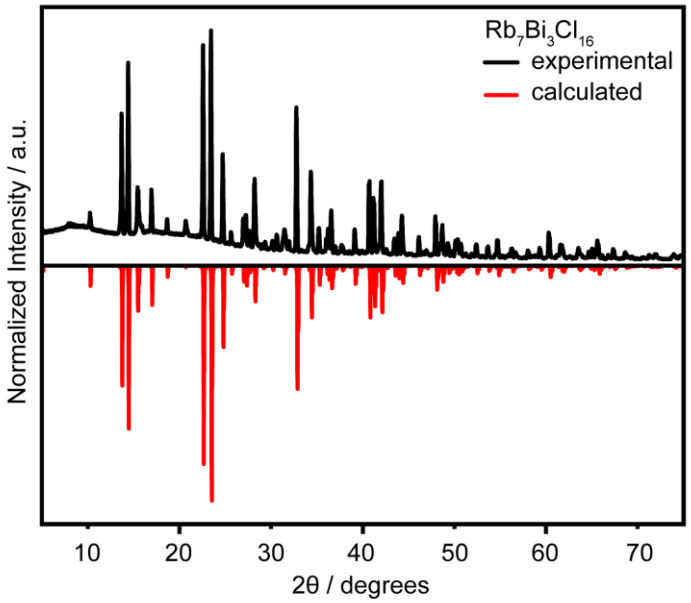

Figure 8.40. Experimental and calculated powder patterns of $Rb_7Bi_3Cl_{16}$. The diffraction pattern was calculated in Vesta using the experimentally determined structure of $Rb_7Bi_3Cl_{16}$.

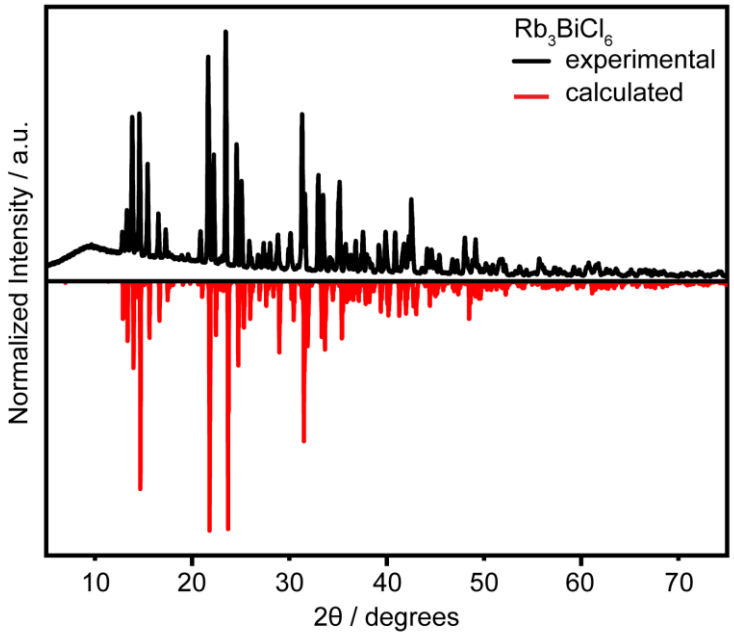

Figure 8.41. . Experimental and calculated powder patterns of Rb_3BiCl_6. The Rb_3BiCl_6 diffraction pattern was calculated in Vesta using the experimentally determined structure of Rb_3BiCl_6.

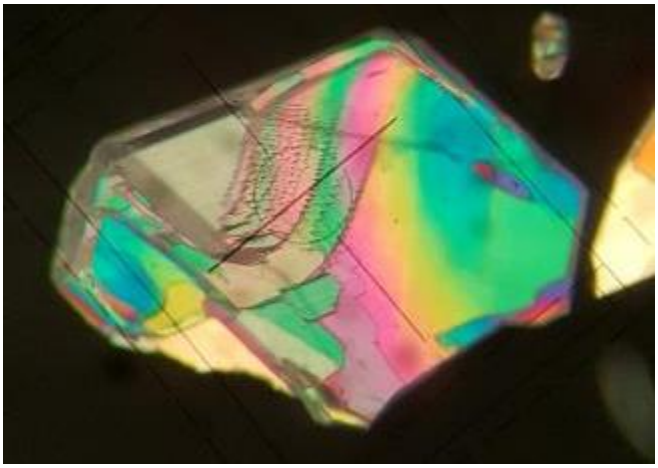

Figure 8.42. Photos of Rb_3BiCl_6 crystals under polarized light. Their interaction with polarized light also them to be more easily separated from crystals of $Rb_7Bi_3Cl_{16}$ system, which grow as thin platelets (like the $Rb_7Sb_3Cl_{16}$ system) and do not rotate polarized light indicating that their high symmetry axis must be oriented perpendicular to the large, flat face of the platelet.

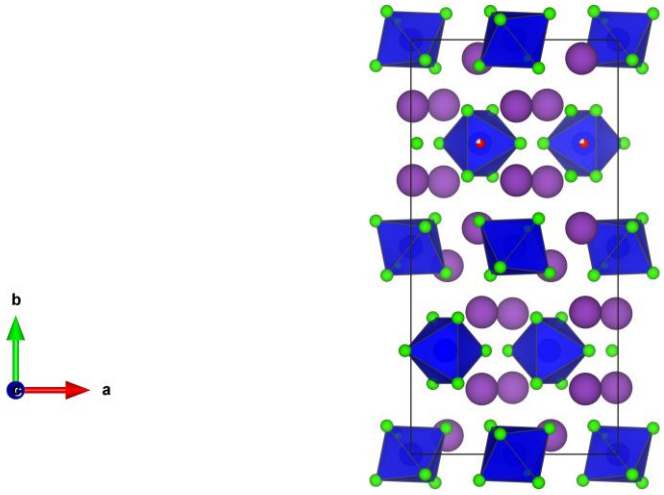

Figure 8.43. Structure of Rb_3BiCl_6 at 298 K.

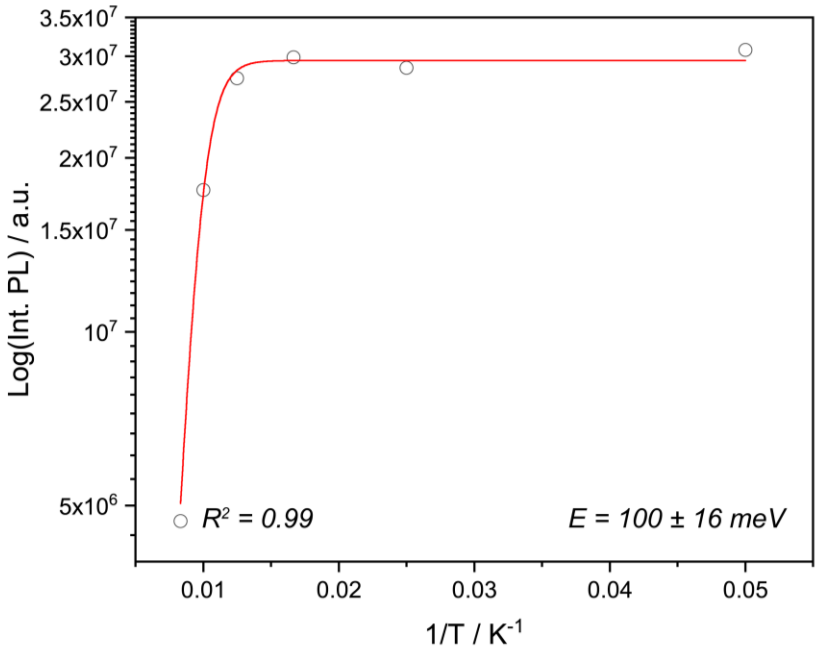

Figure 8.44. Arrhenius plot of PL intensity vs. T for $Rb_7Bi_3Cl_{16}$. The activation energy of *ca.* 100 meV is much lower than that determined for the pure-Sb and agrees with the experimental observation that this material is quenched at far lower temperatures then $Rb_7Sb_3Cl_{16}$.

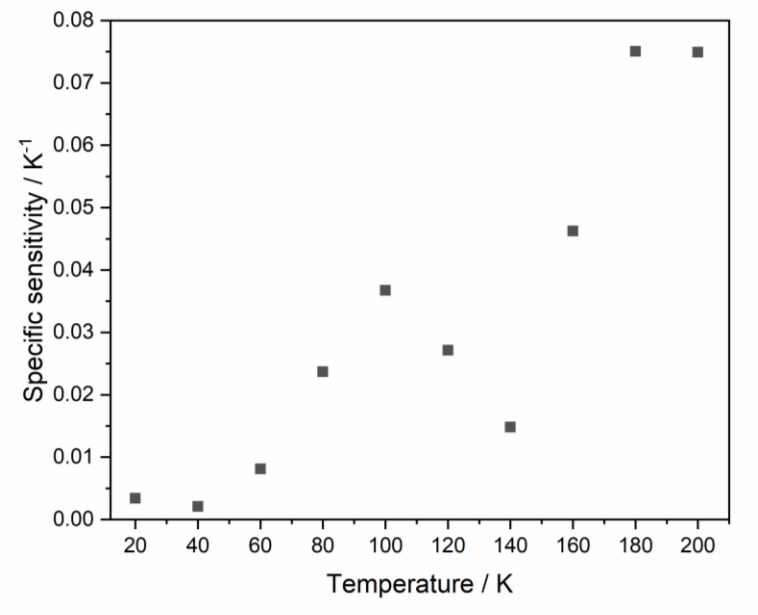

Figure 8.45. Specific sensitivity of $Rb_7Bi_3Cl_{16}$.

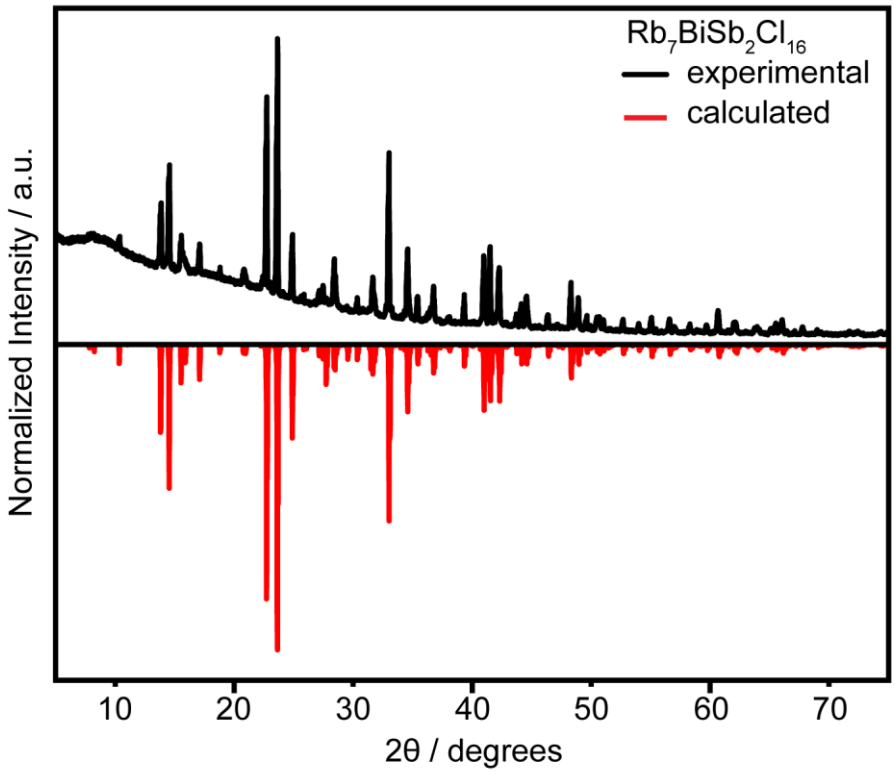

Figure 8.46. Experimental and calculated powder patterns of $Rb_7BiSb_2Cl_{16}$. The $Rb_7BiSb_2Cl_{16}$ diffraction pattern was calculated in Vesta using the experimentally determined structure of $Rb_7BiSb_2Cl_{16}$.

Table 8.36. Crystal data and structure refinement for $Rb_7Sb_{2.07}Bi_{0.93}Cl_{16}$ at 296(3) K.

Empirical formula	$Rb_7Sb_{2.07}Bi_{0.93}Cl_{16}$
Formula weight	1612.15
Temperature	296(3) K
Wavelength	0.71073 Å
Crystal system	Hexagonal
Space group	*P*-62*m*
Unit cell dimensions	a = 13.0332(2) Å, α = 90° b = 13.0332(2) Å, β = 90° c = 34.1956(5) Å, γ = 120°
Volume	5030.40(17) $Å^3$
Z	6
Density (calculated)	3.193 g/cm^3
Absorption coefficient	17.904 mm^{-1}
F(000)	4283
Crystal size	0.375 x 0.3 x 0.188 mm^3
θ range for data collection	1.804 to 35.484°
Index ranges	-21<=h<=21, -21<=k<=20, -54<=l<=54
Reflections collected	149507
Independent reflections	8103 [R_{int} = 0.0844]
Completeness to θ = 25.242°	99.8%
Refinement method	Full-matrix least-squares on F^2
Data / restraints / parameters	8103 / 0 / 186
Goodness-of-fit	1.054
Final R indices [I > 2σ(I)]	R_{obs} = 0.0539, wR_{obs} = 0.1651
R indices [all data]	R_{all} = 0.0712, wR_{all} = 0.1798
Largest diff. peak and hole	4.582 and -1.702 e·$Å^{-3}$

$R = \Sigma||F_o|-|F_c|| / \Sigma|F_o|$, $wR = \{\Sigma[w(|F_o|^2 - |F_c|^2)^2] / \Sigma[w(|F_o|^4)]\}^{1/2}$ and $w=1/[\sigma^2(Fo^2)+(0.0813P)^2+39.1137P]$

where $P=(Fo^2+2Fc^2)/3$

Table 8.37. Atomic coordinates (x10^4) and equivalent isotropic displacement parameters ($Å^2$x10^3) for $Rb_7Sb_{2.07}Bi_{0.93}Cl_{16}$ at 296(3) K with estimated standard deviations in parentheses.

Label	x	y	z	Occupancy	U_{eq}^*
Rb(1)	6622(2)	10000	2149(1)	1	58(1)
Rb(2)	6683(2)	6683(2)	2843(1)	1	57(1)
Rb(3)	7114(2)	7114(2)	1345(1)	1	34(1)
Rb(4)	6666.67	3333.33	1290(1)	1	42(1)
Rb(5)	6666.67	3333.33	0	1	38(1)
Rb(6)	7202(2)	7202(2)	0	1	33(1)
Rb(7)	3332(2)	3875(3)	5000	0.5	37(1)
Rb(8)	3333.33	6666.67	5000	0.5	36(2)
Rb(9)	10000	10000	5000	1	38(1)
Rb(10)	3333.33	6666.67	3707(2)	0.5	34(1)
Rb(11)	10000	10000	3709(1)	1	41(1)

Rb(12)	6222(2)	9553(2)	3658(1)	0.5	35(1)
Cl(1)	4838(5)	8408(4)	2914(2)	1	71(2)
Cl(2)	5148(5)	6927(5)	2017(1)	1	59(2)
Cl(3)	8071(6)	9602(6)	2999(2)	0.5	48(2)
Cl(4)	8427(6)	8427(6)	2128(2)	1	130(5)
Cl(5)	1893(5)	1893(5)	1143(2)	1	66(2)
Cl(6)	4554(5)	4554(5)	1228(2)	1	63(2)
Cl(7)	4437(3)	2073(3)	663(1)	1	36(1)
Cl(8)	4748(7)	4748(7)	0	1	69(3)
Cl(9)	1912(6)	1912(6)	0	1	57(2)
Cl(10)	5232(10)	6657(7)	5000	0.5	63(4)
Cl(11)	6680(15)	8109(12)	5000	0.5	86(6)
Cl(12)	4303(5)	5407(6)	4338(2)	0.5	36(2)
Cl(13)	7764(5)	9023(5)	4341(2)	0.5	36(2)
Cl(14)	5216(9)	6669(7)	3864(3)	0.5	66(3)
Cl(15)	6666(8)	7899(8)	3797(3)	0.5	64(2)
Bi(01)	3333.33	6666.67	2480(1)	0.408(10)	24(1)
Bi(02)	10000	10000	2551(1)	0.327(13)	24(1)
Bi(03)	3312(1)	3312(1)	657(1)	0.171(9)	24(1)
Bi(04)	6656(1)	6656(1)	4343(1)	0.381(10)	28(1)
Sb(1)	3333.33	6666.67	2480(1)	0.592(10)	24(1)
Sb(2)	10000	10000	2551(1)	0.673(13)	24(1)
Sb(3)	3312(1)	3312(1)	657(1)	0.829(9)	24(1)
Sb(4)	6656(1)	6656(1)	4343(1)	0.619(10)	28(1)

*U_{eq} is defined as one third of the trace of the orthogonalized U_{ij} tensor.

Table 8.38. Anisotropic displacement parameters ($Å^2x10^3$) for $Rb_7Sb_{2.07}Bi_{0.93}Cl_{16}$ at 296(3) K with estimated standard deviations in parentheses.

Label	U_{11}	U_{22}	U_{33}	U_{12}	U_{13}	U_{23}
Rb(1)	66(2)	40(2)	58(2)	20(1)	2(1)	0
Rb(2)	56(2)	56(2)	46(2)	18(1)	0(1)	0(1)
Rb(3)	44(1)	44(1)	21(1)	26(1)	-2(1)	-2(1)
Rb(4)	53(1)	53(1)	19(1)	26(1)	0	0
Rb(5)	46(2)	46(2)	21(1)	23(1)	0	0
Rb(6)	35(1)	35(1)	31(1)	19(1)	0	0
Rb(7)	27(2)	28(2)	56(2)	13(2)	0	0
Rb(8)	38(2)	38(2)	32(2)	19(1)	0	0
Rb(9)	41(2)	41(2)	33(2)	20(1)	0	0
Rb(10)	39(2)	39(2)	26(2)	19(1)	0	0
Rb(11)	43(2)	43(2)	35(2)	22(1)	0	0
Rb(12)	34(2)	38(2)	36(1)	20(2)	1(1)	-1(1)
Cl(1)	69(3)	43(2)	63(2)	-3(2)	15(2)	-15(2)
Cl(2)	62(2)	105(3)	37(2)	62(3)	-10(2)	-21(2)
Cl(3)	31(3)	66(4)	47(3)	25(3)	7(2)	-6(3)
Cl(4)	113(4)	113(4)	34(3)	-42(5)	-15(2)	-15(2)
Cl(5)	59(3)	59(3)	97(5)	43(3)	41(3)	41(3)
Cl(6)	68(3)	68(3)	40(2)	23(3)	-15(2)	-15(2)
Cl(7)	38(2)	42(2)	29(1)	21(2)	0(1)	0(2)
Cl(8)	49(4)	49(4)	85(6)	6(4)	0	0

Cl(9)	42(3)	42(3)	91(6)	24(4)	0	0
Cl(10)	39(5)	26(5)	122(12)	15(4)	0	0
Cl(11)	112(14)	41(6)	125(13)	53(8)	0	0
Cl(12)	27(2)	37(3)	42(2)	16(2)	0(2)	0(2)
Cl(13)	33(3)	28(3)	38(2)	9(2)	-2(2)	1(2)
Cl(14)	62(5)	55(5)	82(6)	31(4)	-39(5)	-2(4)
Cl(15)	69(6)	53(4)	76(6)	35(4)	2(4)	22(4)
Bi(01)	22(1)	22(1)	29(1)	11(1)	0	0
Bi(02)	25(1)	25(1)	22(1)	12(1)	0	0
Bi(03)	27(1)	27(1)	18(1)	14(1)	1(1)	1(1)
Bi(04)	28(1)	28(1)	28(1)	13(1)	-1(1)	-1(1)
Sb(1)	22(1)	22(1)	29(1)	11(1)	0	0
Sb(2)	25(1)	25(1)	22(1)	12(1)	0	0
Sb(3)	27(1)	27(1)	18(1)	14(1)	1(1)	1(1)
Sb(4)	28(1)	28(1)	28(1)	13(1)	-1(1)	-1(1)

The anisotropic displacement factor exponent takes the form: $-2\pi^2[h^2a^{*2}U_{11} + ... + 2hka^*b^*U_{12}]$.

Table 8.39. Bond lengths [Å] for $Rb_7Sb_{2.07}Bi_{0.93}Cl_{16}$ at 296(3) K with estimated standard deviations in parentheses.

Label	Distances
Rb(1)-Cl(1)	3.426(5)
Rb(1)-Cl(2)	3.498(5)
Rb(1)-Cl(3)	3.642(8)
Rb(1)-Cl(4)	3.816(2)
Rb(1)-Bi(01)	4.4619(15)
Rb(2)-Cl(2)	3.564(4)
Rb(2)-Cl(3)	3.339(7)
Rb(2)-Cl(4)	3.337(8)
Rb(2)-Cl(15)	3.632(11)
Rb(2)-Bi(01)	4.5280(13)
Rb(2)-Bi(02)	4.437(2)
Rb(3)-Rb(4)	4.6670(11)
Rb(3)-Rb(6)	4.6004(14)
Rb(3)-Cl(2)	3.359(4)
Rb(3)-Cl(4)	3.179(6)
Rb(3)-Cl(6)	3.360(7)
Rb(4)-Rb(5)	4.4130(18)
Rb(4)-Cl(6)	3.8130(10)
Rb(4)-Cl(7)	3.313(3)
Rb(5)-Cl(7)	3.392(3)
Rb(5)-Cl(8)	3.7767(8)
Rb(6)-Cl(8)	3.198(9)
Rb(7)-Rb(8)	3.637(4)
Rb(7)-Cl(10)	3.210(10)
Rb(7)-Cl(12)	2.860(6)
Rb(8)-Cl(10)	2.480(12)
Rb(8)-Cl(12)	3.389(6)
Rb(9)-Cl(13)	3.388(6)
Rb(10)-Rb(12)	3.767(3)

Rb(10)-Cl(1)	3.450(5)
Rb(10)-Cl(12)	3.320(6)
Rb(10)-Cl(14)	2.510(9)
Rb(11)-Cl(3)	3.344(7)
Rb(11)-Cl(13)	3.328(6)
Rb(12)-Cl(1)	3.042(5)
Rb(12)-Cl(3)	3.275(6)
Rb(12)-Cl(13)	3.373(6)
Rb(12)-Cl(14)	3.379(8)
Rb(12)-Cl(15)	2.541(9)
Cl(1)-Bi(01)	2.597(5)
Cl(1)-Sb(1)	2.597(5)
Cl(2)-Bi(01)	2.723(4)
Cl(2)-Sb(1)	2.723(4)
Cl(3)-Bi(02)	2.764(6)
Cl(3)-Sb(2)	2.764(6)
Cl(4)-Bi(02)	2.508(6)
Cl(4)-Sb(2)	2.508(6)
Cl(5)-Bi(03)	2.486(5)
Cl(5)-Sb(3)	2.486(5)
Cl(6)-Bi(03)	2.535(5)
Cl(6)-Sb(3)	2.535(5)
Cl(7)-Bi(03)	2.670(3)
Cl(7)-Sb(3)	2.670(3)
Cl(8)-Bi(03)	2.925(6)
Cl(9)-Bi(03)	2.896(5)
Cl(9)-Sb(3)	2.896(5)
Cl(10)-Cl(11)	1.890(19)
Cl(10)-Bi(04)	2.916(8)
Cl(11)-Bi(04)	2.930(8)
Cl(12)-Cl(14)	2.191(11)
Cl(12)-Bi(04)	2.659(6)
Cl(12)-Sb(4)	2.659(6)
Cl(13)-Cl(15)	2.359(12)
Cl(13)-Bi(04)	2.673(6)
Cl(13)-Sb(4)	2.673(6)
Cl(14)-Cl(15)	1.779(13)
Cl(14)-Bi(04)	2.498(8)
Cl(14)-Sb(4)	2.498(8)
Cl(15)-Bi(04)	2.467(8)
Cl(15)-Sb(4)	2.467(8)

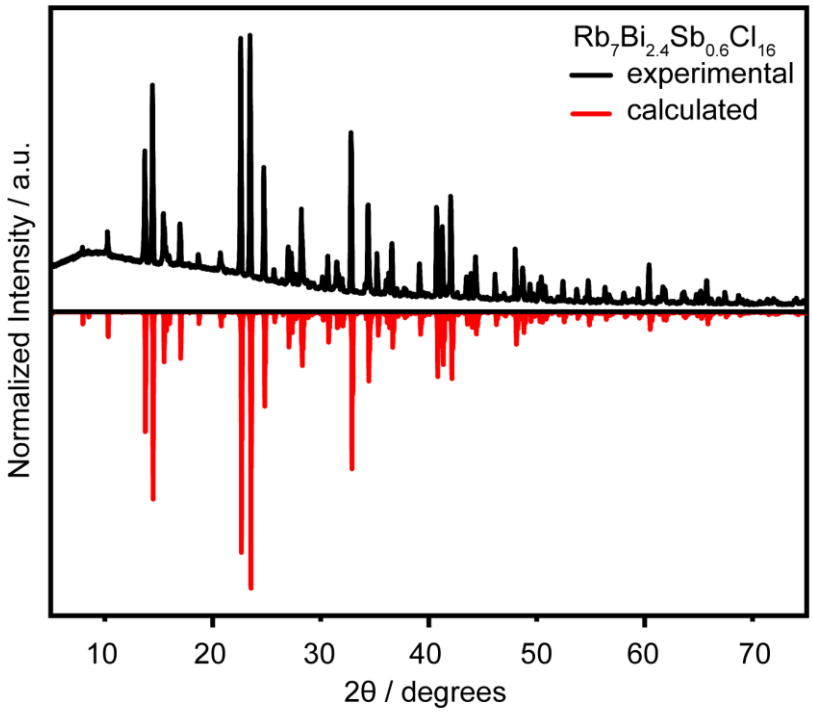

Figure 8.47. Experimental and calculated powder patterns of $Rb_7Bi_{2.4}Sb_{0.6}Cl_{16}$. The $Rb_7Bi_{2.4}Sb_{0.6}Cl_{16}$ diffraction pattern was calculated in Vesta using the experimentally determined structure of $Rb_7Bi_{2.4}Sb_{0.6}Cl_{16}$.

Table 8.40. Crystal data and structure refinement for $Rb_7Bi_{2.41}Sb_{0.59}Cl_{16}$ at 300 K.

Empirical formula	$Rb_7Bi_{2.41}Sb_{0.59}Cl_{16}$
Formula weight	1740.72
Temperature	300 K
Wavelength	0.71073 Å
Crystal system	Hexagonal
Space group	*R*-3*c*
Unit cell dimensions	a = 13.08950(10) Å, α = 90° b = 13.08950(10) Å, β = 90° c = 102.8418(13) Å, γ = 120°
Volume	15259.7(3) $Å^3$
Z	18
Density (calculated)	3.410 g/cm^3
Absorption coefficient	24.171 mm^{-1}
F(000)	13699
Crystal size	0.203 x 0.124 x 0.076 mm^3
θ range for data collection	1.188 to 33.775°
Index ranges	-20<=h<=20, -20<=k<=20, -160<=l<=159
Reflections collected	223325
Independent reflections	6819 [R_{int} = 0.0764]
Completeness to θ = 25.242°	100%
Refinement method	Full-matrix least-squares on F^2
Data / restraints / parameters	6819 / 0 / 123
Goodness-of-fit	1.070
Final R indices [I > 2σ(I)]	R_{obs} = 0.0269, wR_{obs} = 0.0473
R indices [all data]	R_{all} = 0.0623, wR_{all} = 0.0556
Largest diff. peak and hole	0.807 and -1.667 e·$Å^{-3}$

$R = \Sigma||F_o|-|F_c|| / \Sigma|F_o|$, $wR = \{\Sigma[w(|F_o|^2 - |F_c|^2)^2] / \Sigma[w(|F_o|^4)]\}^{1/2}$ and $w=1/[\sigma^2(Fo^2)+(0.0183P)^2+53.8518P]$

where $P=(Fo^2+2Fc^2)/3$

Table 8.41. Atomic coordinates ($x10^4$) and equivalent isotropic displacement parameters ($Å^2x10^3$) for $Rb_7Bi_{2.41}Sb_{0.59}Cl_{16}$ at 300 K with estimated standard deviations in parentheses.

Label	x	y	z	Occupancy	U_{eq}^*
Bi(1)	0	0	5000	0.917(4)	22(1)
Bi(2)	3333.33	6666.67	5019(1)	0.879(3)	24(1)
Bi(3)	3351(1)	3331(1)	5615(1)	0.758(2)	26(1)
Rb(3)	6211(1)	9550(1)	4615(1)	1	35(1)
Rb(5)	-538(1)	3333.33	5833.33	1	35(1)
Rb(6)	0	0	5832(1)	1	39(1)
Rb(4)	3333.33	6666.67	5409(1)	1	41(1)
Rb(1)	0	0	5404(1)	1	41(1)
Rb(2)	6723(1)	6695(1)	4883(1)	1	61(1)
Cl(4)	4602(1)	5709(1)	5617(1)	1	36(1)
Cl(9)	2220(1)	944(1)	5614(1)	1	36(1)
Cl(7)	4750(1)	3333.33	5833.33	1	40(1)

Cl(1)	1702(1)	88(2)	5154(1)	1	49(1)
Cl(3)	4810(1)	6232(1)	5172(1)	1	48(1)
Cl(8)	4816(1)	3336(1)	5455(1)	1	62(1)
Cl(6)	1912(1)	3333.33	5833.33	1	56(1)
Cl(2)	5150(1)	8096(1)	4878(1)	1	58(1)
Cl(5)	2088(1)	3323(2)	5424(1)	1	60(1)
Sb(3)	3351(1)	3331(1)	5615(1)	0.242(2)	26(1)
Sb(1)	0	0	5000	0.083(4)	22(1)
Sb(2)	3333.33	6666.67	5019(1)	0.121(3)	24(1)

*U_{eq} is defined as one third of the trace of the orthogonalized U_{ij} tensor.

Table 8.42. Anisotropic displacement parameters ($Å^2x10^3$) for $Rb_7Bi_{2.41}Sb_{0.59}Cl_{16}$ at 300 K with estimated standard deviations in parentheses.

Label	U_{11}	U_{22}	U_{33}	U_{12}	U_{13}	U_{23}
Bi(1)	23(1)	23(1)	21(1)	11(1)	0	0
Bi(2)	24(1)	24(1)	22(1)	12(1)	0	0
Bi(3)	28(1)	26(1)	23(1)	13(1)	1(1)	-1(1)
Rb(3)	42(1)	37(1)	31(1)	23(1)	3(1)	1(1)
Rb(5)	32(1)	29(1)	43(1)	14(1)	0(1)	1(1)
Rb(6)	44(1)	44(1)	29(1)	22(1)	0	0
Rb(4)	48(1)	48(1)	27(1)	24(1)	0	0
Rb(1)	48(1)	48(1)	26(1)	24(1)	0	0
Rb(2)	79(1)	44(1)	58(1)	28(1)	-4(1)	-1(1)
Cl(4)	40(1)	32(1)	36(1)	19(1)	-1(1)	-1(1)
Cl(9)	36(1)	32(1)	38(1)	14(1)	0(1)	-1(1)
Cl(7)	34(1)	31(1)	53(1)	15(1)	0(1)	0(1)
Cl(1)	39(1)	81(1)	38(1)	37(1)	-4(1)	4(1)
Cl(3)	47(1)	68(1)	42(1)	39(1)	-14(1)	-6(1)
Cl(8)	54(1)	38(1)	88(1)	19(1)	35(1)	-2(1)
Cl(6)	42(1)	89(2)	52(1)	44(1)	-1(1)	-1(1)
Cl(2)	49(1)	58(1)	42(1)	7(1)	17(1)	12(1)
Cl(5)	58(1)	77(1)	48(1)	37(1)	-15(1)	2(1)
Sb(3)	28(1)	26(1)	23(1)	13(1)	1(1)	-1(1)
Sb(1)	23(1)	23(1)	21(1)	11(1)	0	0
Sb(2)	24(1)	24(1)	22(1)	12(1)	0	0

The anisotropic displacement factor exponent takes the form: $-2\pi^2[h^2a^{*2}U_{11} + ... + 2hka^*b^*U_{12}]$.

Table 8.43. Selected bond lengths [Å] for $Rb_7Bi_{2.41}Sb_{0.59}Cl_{16}$ at 300 K with estimated standard deviations in parentheses.

Label	Distances
Bi(1)-Rb(1)	4.1492(6)
Bi(1)-Cl(1)	2.6881(9)
Bi(2)-Cl(3)	2.7626(9)
Bi(2)-Cl(2)	2.6085(10)
Bi(3)-Cl(4)	2.6960(9)
Bi(3)-Cl(9)	2.7080(9)
Bi(3)-Cl(7)	2.8944(8)
Bi(3)-Cl(8)	2.5302(10)
Bi(3)-Cl(6)	2.9294(9)
Bi(3)-Cl(5)	2.5641(10)
Rb(3)-Rb(2)	4.9483(6)
Rb(3)-Cl(2)	3.1981(10)
Rb(5)-Rb(6)	4.7547(3)
Rb(5)-Cl(6)	3.2071(14)
Rb(6)-Rb(1)	4.4079(7)
Rb(6)-Cl(9)	3.3780(9)
Rb(6)-Cl(6)	3.79226(15)
Rb(4)-Cl(4)	3.3138(9)
Rb(4)-Cl(3)	3.3287(11)
Rb(4)-Cl(5)	3.8346(13)
Rb(4)-Sb(2)	4.0077(6)
Rb(1)-Cl(9)	3.3265(9)
Rb(1)-Cl(1)	3.3626(11)
Rb(1)-Cl(5)	3.8139(13)
Rb(1)-Sb(1)	4.1492(6)
Rb(2)-Cl(3)	3.7393(12)
Rb(2)-Cl(2)	3.3739(14)
Cl(4)-Sb(3)	2.6960(9)
Cl(9)-Sb(3)	2.7080(9)
Cl(7)-Sb(3)	2.8944(8)
Cl(1)-Sb(1)	2.6881(9)
Cl(3)-Sb(2)	2.7626(9)
Cl(8)-Sb(3)	2.5302(10)
Cl(2)-Sb(2)	2.6085(9)
Cl(5)-Sb(3)	2.5641(10)

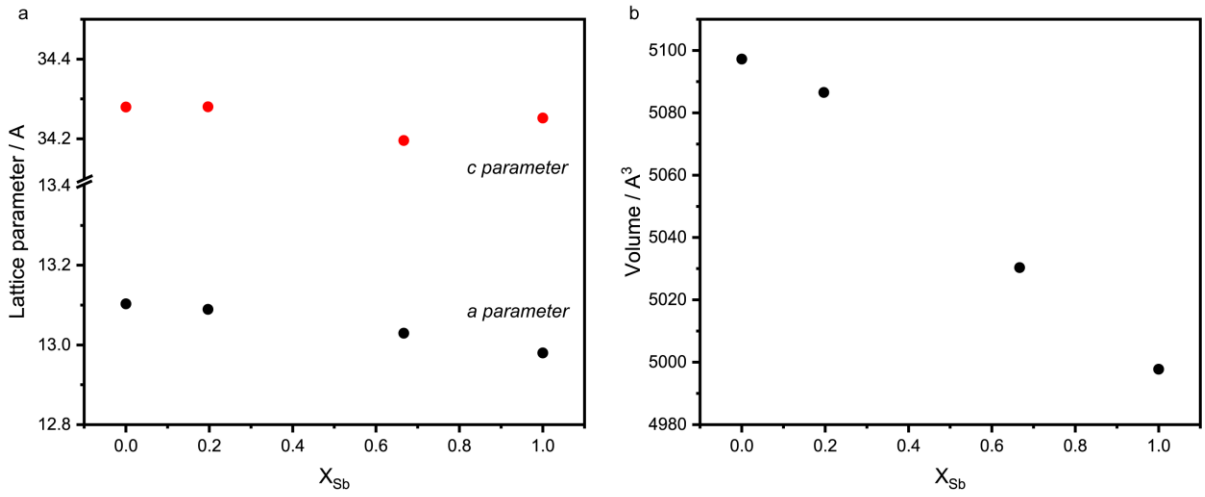

Figure 8.48. Vegard's law for the $Rb_7Bi_{3-3x}Sb_{3x}Cl_{16}$ family. a) lattice parameter a is strongly affected while c stays relatively constant. b) The volume follows a linear trend in agreement with Vegard's law.

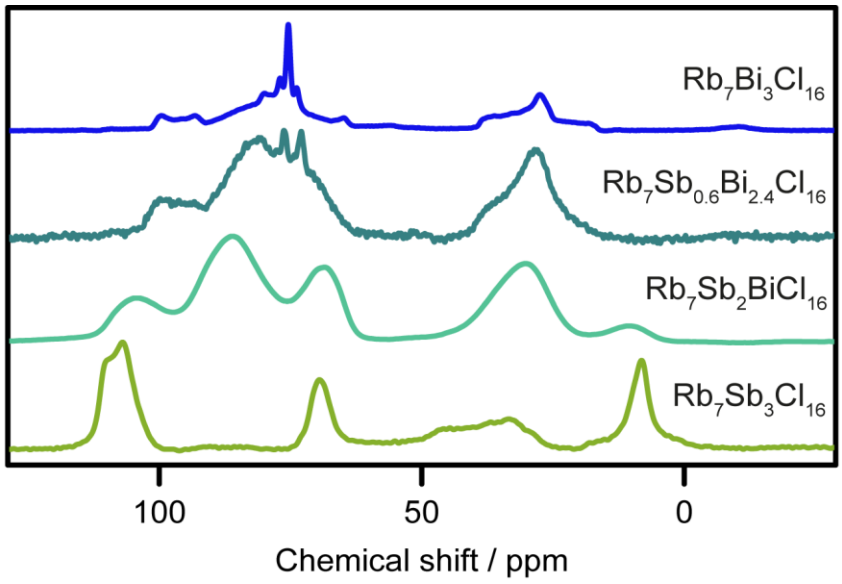

Figure 8.49. 1D ^{87}Rb NMR spectra for the $Rb_7Bi_{3-3x}Sb_{3x}Cl_{16}$ family

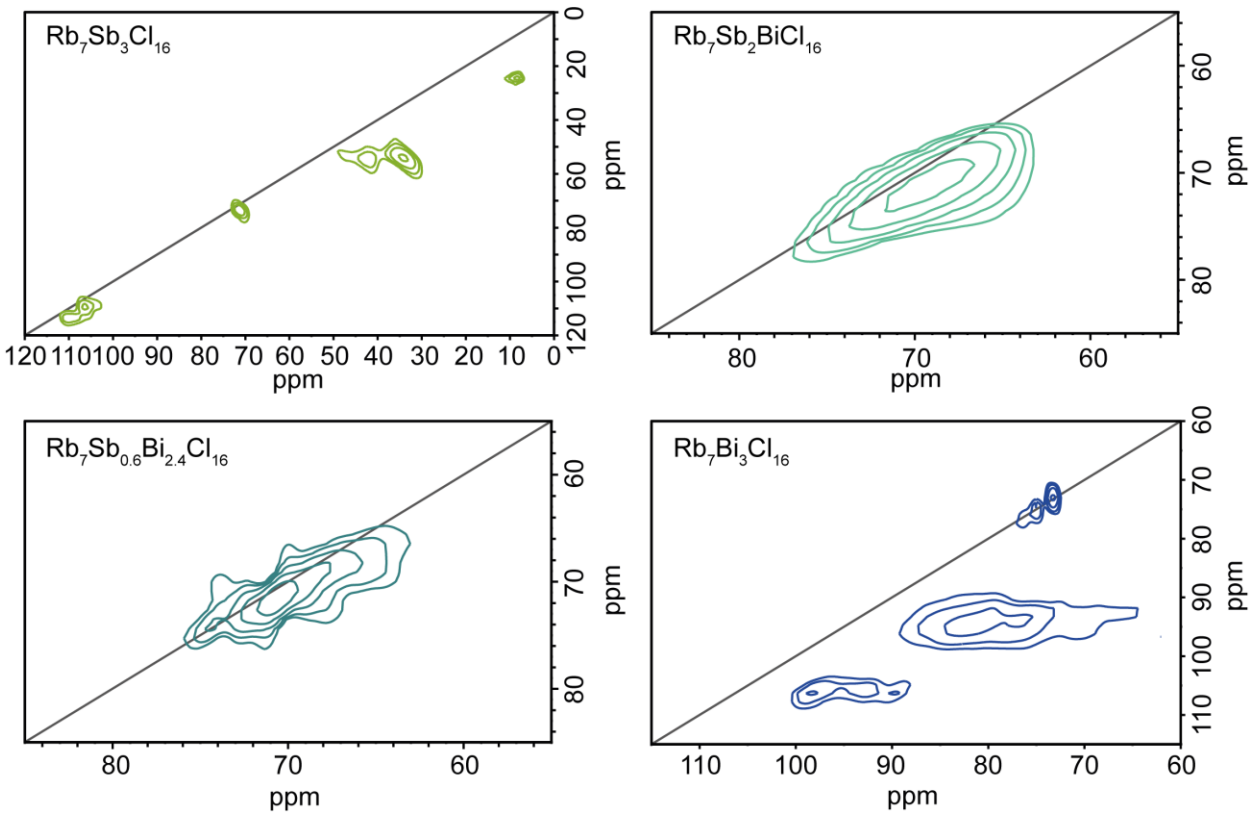

Figure 8.50. MQMAS ^{87}Rb NMR spectra for the $Rb_7Bi_{3-3x}Sb_{3x}Cl_{16}$ family.

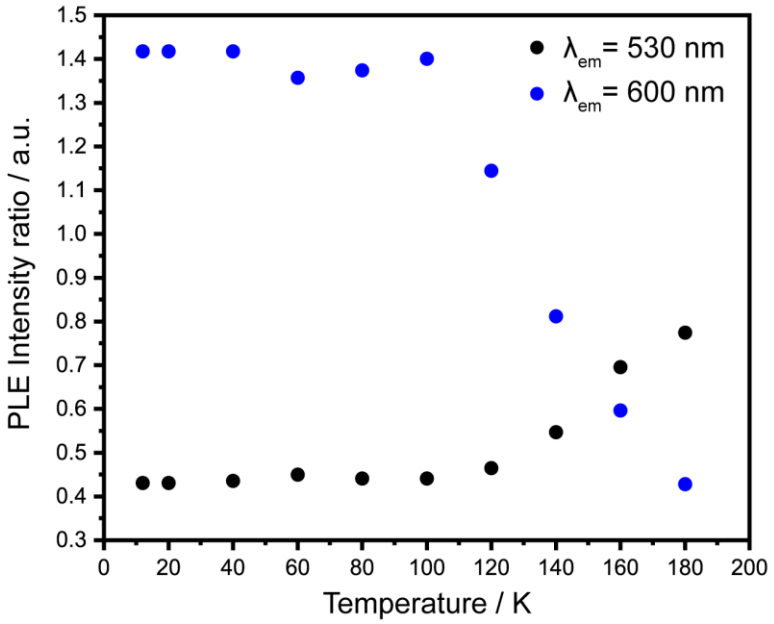

Figure 8.51. PLE peak intensity ratio as a function of temperature for $Rb_7BiSb_2Cl_{16}$.

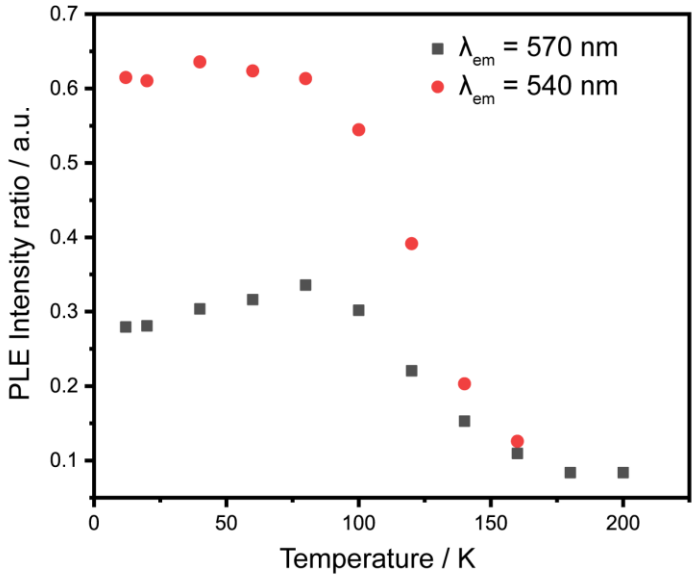

Figure 8.52. PLE peak intensity ratio as a function of temperature for $Rb_7Bi_{2.6}Sb_{0.4}Cl_{16}$.

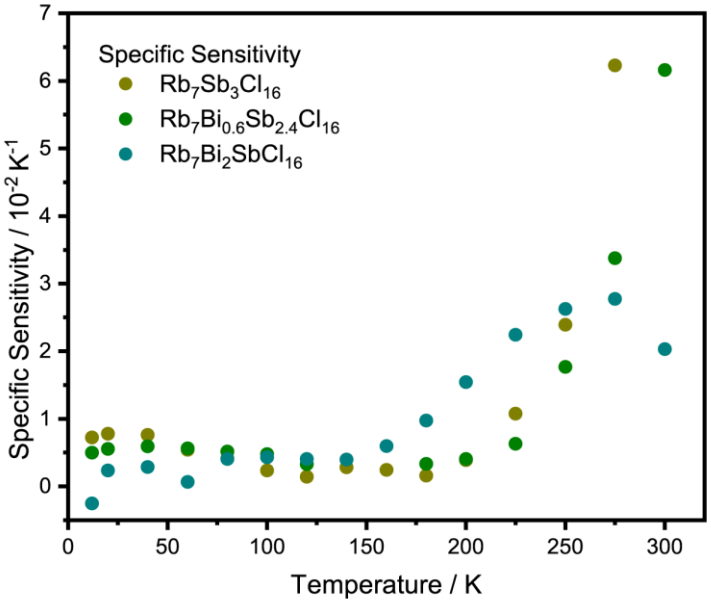

Figure 8.53. Specific sensitivity values for the $Rb_7Bi_{3-3x}Sb_{3x}Cl_{16}$ family.

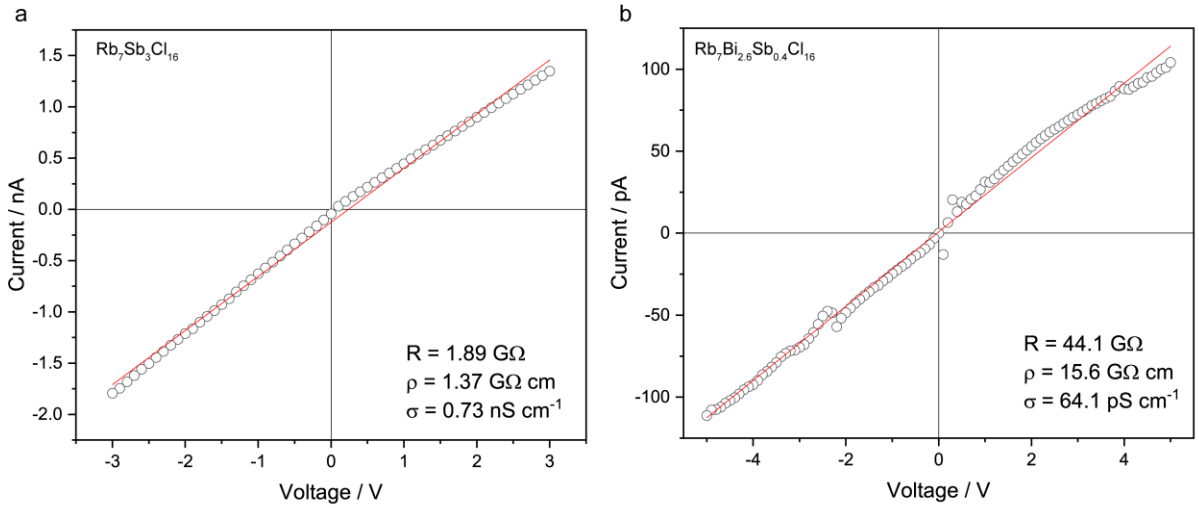

Figure 8.54. I-V curves for a) $Rb_7Sb_3Cl_{16}$ and b) $Rb_7Bi_{2.6}Sb_{0.4}Cl_{16}$.

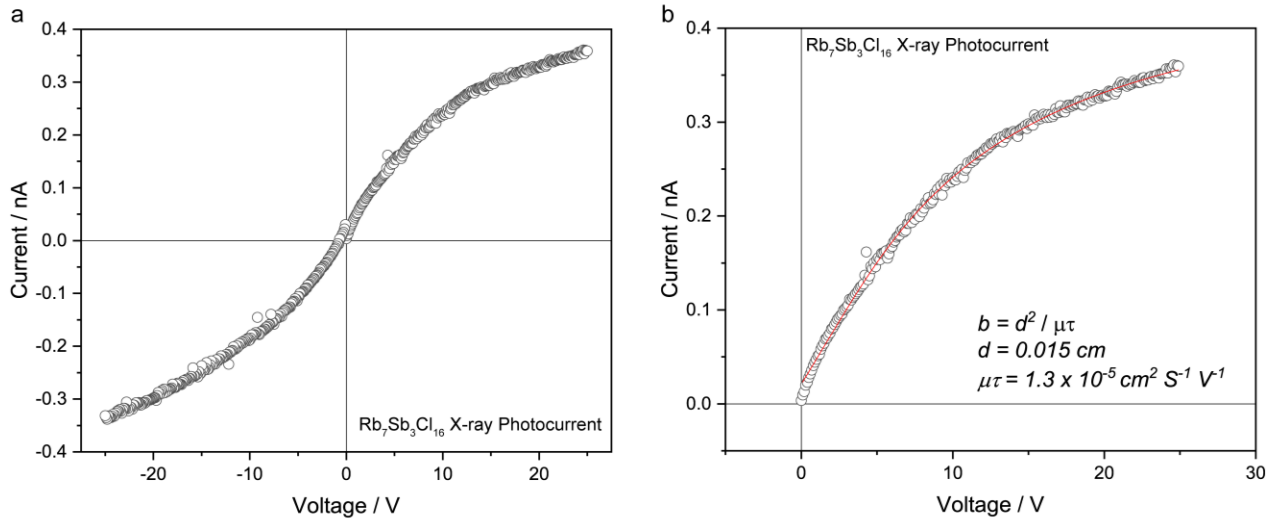

Figure 8.55. a) X-ray photoconductivity of $Rb_7Sb_3Cl_{16}$ and b) fitting with the Hecht equation to determine the μτ product.

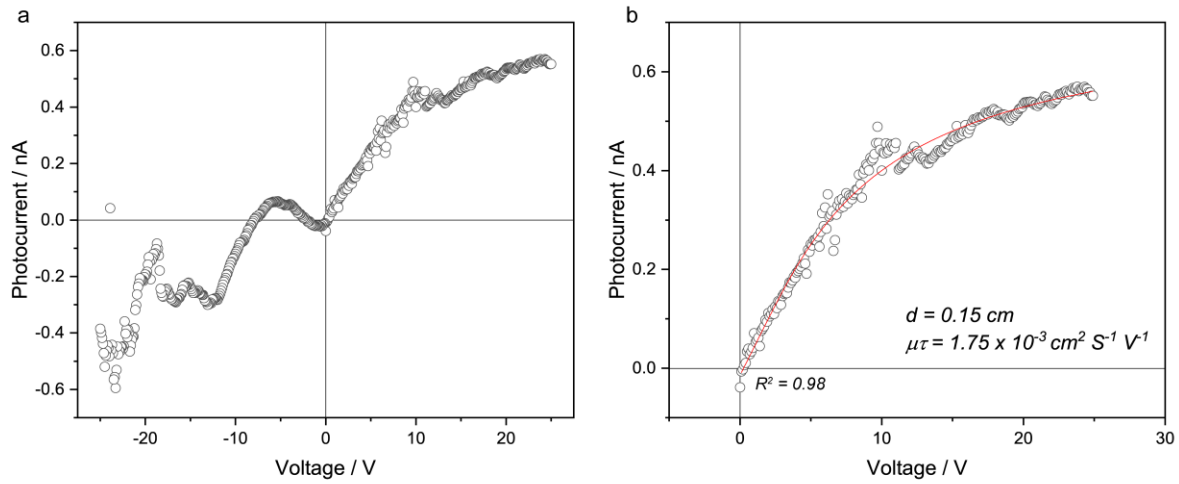

Figure 8.56. a) X-ray photoconductivity of $Rb_7Bi_{2.6}Sb_{0.4}Cl_{16}$ and b) fitting with the Hecht equation to determine the μτ product.

Table 8.44. Crystal data and structure refinement for $K_7Sb_3Cl_{16}$ at 298.4(7) K.

Empirical formula	$K_7Sb_3Cl_{16}$
Formula weight	1206.35
Temperature	298.4(7) K
Wavelength	0.71073 Å
Crystal system	Hexagonal
Space group	$P6_3/mmc$
Unit cell dimensions	a = 7.3434(4) Å, α = 90° b = 7.3434(4) Å, β = 90° c = 33.143(2) Å, γ = 120°
Volume	1547.8(2) $Å^3$
Z	2
Density (calculated)	2.588 g/cm^3
Absorption coefficient	4.918 mm^{-1}
F(000)	1116
Crystal size	0.115 x 0.094 x 0.037 mm^3
θ range for data collection	2.458 to 33.335°
Index ranges	-6<=h<=9, -4<=k<=10, -33<=l<=50
Reflections collected	5651
Independent reflections	1161 [R_{int} = 0.0849]
Completeness to θ = 25.242°	99.8%
Refinement method	Full-matrix least-squares on F^2
Data / restraints / parameters	1161 / 0 / 66
Goodness-of-fit	1.171
Final R indices [I > 2σ(I)]	R_{obs} = 0.0673, wR_{obs} = 0.1104
R indices [all data]	R_{all} = 0.1118, wR_{all} = 0.1236
Largest diff. peak and hole	0.703 and -0.987 e·$Å^{-3}$

$R = \Sigma||F_o|-|F_c|| / \Sigma|F_o|$, $wR = \{\Sigma[w(|F_o|^2 - |F_c|^2)^2] / \Sigma[w(|F_o|^4)]\}^{1/2}$ and $w=1/[\sigma^2(Fo^2)+16.4487P]$ where $P=(Fo^2+2Fc^2)/3$

Table 8.45. Atomic coordinates (x10^4) and equivalent isotropic displacement parameters ($Å^2$x10^3) for $K_7Sb_3Cl_{16}$ at 298.4(7) K with estimated standard deviations in parentheses.

Label	x	y	z	Occupancy	U_{eq}^*
Sb(1)	10000	10000	5000	1	32(1)
Sb(2)	3333.33	6666.67	6832(1)	1	27(1)
K(1)	6666.67	3333.33	4666(2)	1	78(2)
K(2)	6666.67	3333.33	6170(2)	0.722(16)	69(3)
K(3)	-415(7)	415(7)	6189(2)	0.313(6)	48(3)
K(4)	6666.67	3333.33	7500	0.72(2)	84(5)
K(5)	991(19)	495(10)	7500	0.323(9)	49(4)
Cl(1)	11147(9)	13336(8)	4538(2)	0.5	80(2)
Cl(2)	6994(8)	6739(9)	6833(2)	0.3333	40(2)
Cl(3)	4777(10)	5223(10)	6332(4)	0.3333	74(3)

Cl(4)	2061(9)	4122(18)	6268(3)	0.3333	72(3)
Cl(5)	4811(10)	5189(10)	7500	0.3333	60(4)
Cl(6)	1851(10)	3700(20)	7500	0.3333	66(4)

*U_{eq} is defined as one third of the trace of the orthogonalized U_{ij} tensor.

Table 8.46. Anisotropic displacement parameters ($Å^2x10^3$) for $K_7Sb_3Cl_{16}$ at 298.4(7) K with estimated standard deviations in parentheses

Label	U_{11}	U_{22}	U_{33}	U_{12}	U_{13}	U_{23}
Sb(1)	29(1)	29(1)	38(1)	15(1)	0	0
Sb(2)	27(1)	27(1)	26(1)	14(1)	0	0
K(1)	67(2)	67(2)	100(4)	34(2)	0	0
K(2)	89(4)	89(4)	30(3)	44(2)	0	0
K(3)	39(3)	39(3)	38(3)	-3(3)	6(2)	-6(2)
K(4)	106(7)	106(7)	40(5)	53(4)	0	0
K(5)	74(8)	39(4)	46(6)	37(4)	0	0
Cl(1)	96(6)	46(2)	96(3)	35(3)	37(3)	23(3)
Cl(2)	32(3)	51(3)	40(2)	23(3)	2(2)	0(2)
Cl(3)	62(5)	62(5)	86(7)	22(5)	23(3)	-23(3)
Cl(4)	66(5)	75(7)	79(7)	38(4)	-24(3)	-49(6)
Cl(5)	39(5)	39(5)	105(11)	22(6)	0	0
Cl(6)	58(7)	28(7)	100(11)	14(3)	0	0

The anisotropic displacement factor exponent takes the form: $-2\pi^2[h^2a^{*2}U_{11} + ... + 2hka^*b^*U_{12}]$.

Table 8.47. Bond lengths [Å] for $K_7Sb_3Cl_{16}$ at 298.4(7) K with estimated standard deviations in parentheses

Label	Distances
Sb(1)-Cl(1)	2.643(5)
Sb(2)-Cl(2)	2.662(5)
Sb(2)-Cl(3)	2.473(10)
Sb(2)-Cl(4)	2.473(9)
K(2)-Cl(2)	3.247(7)
K(2)-Cl(3)	2.464(11)
K(3)-Cl(4)	2.415(11)
K(4)-Cl(5)	2.360(13)
K(5)-Cl(5)	3.175(10)
K(5)-Cl(6)	2.110(13)
Cl(2)-Cl(3)	2.198(11)
Cl(3)-Cl(4)	1.750(8)
Cl(5)-Cl(6)	1.883(9)

8.4. Appendix to Chapter 5

Table 8.48. Crystal data and structure refinement for $Rb_{23}Sb_9Cl_{54}$ at 293(2) K.

Empirical formula	$Rb_{23}Sb_9Cl_{54}$
Formula weight	4975.86
Temperature	293(2) K
Wavelength	0.71073 Å
Crystal system	Orthorhombic
Space group	*Cmcm*
Unit cell dimensions	a = 22.2915(7) Å, α = 90° b = 12.8759(4) Å, β = 90° c = 36.9787(13) Å, γ = 90°
Volume	10613.7(6) $Å^3$
Z	4
Density (calculated)	3.114 g/cm^3
Absorption coefficient	14.113 mm^{-1}
F(000)	8912
Crystal size	0.113 x 0.06 x 0.02 mm^3
θ range for data collection	1.652 to 31.672°
Index ranges	-32<=h<=32, -18<=k<=18, -53<=l<=48
Reflections collected	69501
Independent reflections	9072 [R_{int} = 0.1384]
Completeness to θ = 25.242°	100%
Refinement method	Full-matrix least-squares on F^2
Data / restraints / parameters	9072 / 0 / 217
Goodness-of-fit	1.256
Final R indices [I > 2σ(I)]	R_{obs} = 0.1735, wR_{obs} = 0.3678
R indices [all data]	R_{all} = 0.2150, wR_{all} = 0.3900
Largest diff. peak and hole	5.463 and -2.556 e·$Å^{-3}$

$R = \Sigma||F_o|-|F_c|| / \Sigma|F_o|$, $wR = \{\Sigma[w(|F_o|^2 - |F_c|^2)^2] / \Sigma[w(|F_o|^4)]\}^{1/2}$ and $w=1/[\sigma^2(Fo^2)+(0.1068P)^2+2014.6614P]$ where $P=(Fo^2+2Fc^2)/3$

Table 8.49. Atomic coordinates (x10^4) and equivalent isotropic displacement parameters (Å^{2}x10^3) for $Rb_{23}Sb_9Cl_{54}$ at 293(2) K with estimated standard deviations in parentheses.

Label	x	y	z	Occupancy	U_{eq}*
Sb(01)	5000	27(3)	2500	1	23(1)
Sb(02)	6657(2)	5002(2)	2500	1	22(1)
Sb(03)	3326(1)	-1644(2)	800(1)	1	25(1)
Sb(04)	10000	8325(2)	4285(1)	1	30(1)
Rb(05)	5000	-3775(3)	1854(2)	1	31(1)
Rb(06)	8557(2)	6905(2)	3150(1)	1	33(1)
Rb(07)	8335(2)	3338(3)	3094(1)	1	43(1)
Rb(08)	6797(2)	5135(3)	3821(1)	1	50(1)
Rb(09)	5000	-212(6)	1179(2)	1	66(2)
Rb(0A)	5000	-3162(4)	479(2)	1	55(2)
Rb(0B)	3274(2)	1583(4)	397(2)	1	60(1)
Rb(0C)	5000	3341(6)	2500	1	48(2)
Cl(0D)	6190(5)	103(8)	2500	1	38(2)
Cl(0E)	7216(5)	3181(9)	2500	1	39(2)
Cl(0F)	4142(5)	-891(7)	409(3)	1	50(2)
Cl(0G)	2393(4)	-2340(7)	1223(3)	1	52(2)
Cl(0H)	4141(4)	-2741(6)	1229(3)	1	43(2)
Cl(0I)	2554(4)	-784(7)	412(2)	1	44(2)
Cl(0J)	6023(5)	6726(7)	2500	1	36(2)
Cl(0K)	5000	1429(9)	3059(4)	1	44(3)
Cl(0L)	5953(4)	4285(6)	3062(2)	1	40(2)
Cl(0M)	3450(5)	97(6)	1223(3)	1	48(2)
Cl(0N)	3293(5)	-3236(6)	401(3)	1	51(2)
Cl(0O)	7324(5)	5670(8)	2996(3)	1	53(2)
Cl(0P)	5000	-1324(8)	1999(3)	1	50(3)
Cl(0Q)	10000	6827(11)	4650(5)	1	79(6)
Cl(0R)	10745(7)	9063(13)	4646(4)	1	90(4)
Cl(0S)	10000	9795(10)	3930(5)	1	90(7)
Cl(0T)	9248(7)	7548(14)	3929(4)	1	97(5)

*U_{eq} is defined as one third of the trace of the orthogonalized U_{ij} tensor.

Table 8.50. Anisotropic displacement parameters (Å^{2}x10^3) for $Rb_{23}Sb_9Cl_{54}$ at 293(2) K with estimated standard deviations in parentheses.

Label	U_{11}	U_{22}	U_{33}	U_{12}	U_{13}	U_{23}
Sb(01)	26(2)	16(2)	27(2)	0	0	0
Sb(02)	26(2)	16(1)	25(2)	-2(1)	0	0
Sb(03)	23(1)	21(1)	31(1)	4(1)	2(1)	-2(1)
Sb(04)	31(2)	27(2)	32(2)	0	0	-2(2)
Rb(05)	24(2)	30(2)	40(2)	0	0	4(2)
Rb(06)	32(2)	19(1)	46(2)	-3(1)	2(2)	1(2)
Rb(07)	52(2)	40(2)	37(2)	8(2)	2(2)	1(2)

Rb(08)	59(2)	38(2)	52(2)	10(2)	-2(2)	4(2)
Rb(09)	54(4)	93(5)	52(4)	0	0	-6(3)
Rb(0A)	64(4)	52(3)	50(3)	0	0	-1(2)
Rb(0B)	52(2)	64(2)	64(2)	-13(2)	0(2)	4(2)
Rb(0C)	54(5)	38(3)	54(4)	0	0	0
Cl(0D)	27(5)	32(5)	57(7)	2(4)	0	0
Cl(0E)	40(6)	37(5)	42(6)	6(5)	0	0
Cl(0F)	54(6)	53(5)	43(5)	-2(4)	10(4)	6(4)
Cl(0G)	42(5)	53(5)	60(6)	-13(4)	6(5)	4(4)
Cl(0H)	30(4)	46(4)	53(5)	14(3)	-16(4)	3(4)
Cl(0I)	47(5)	44(4)	43(4)	7(4)	-8(4)	8(4)
Cl(0J)	32(5)	19(4)	55(6)	13(4)	0	0
Cl(0K)	36(6)	33(5)	62(8)	0	0	-16(5)
Cl(0L)	29(4)	29(3)	61(5)	2(3)	-3(4)	4(3)
Cl(0M)	62(6)	30(4)	52(5)	-3(4)	4(5)	-11(3)
Cl(0N)	73(7)	21(3)	59(6)	-3(4)	-2(5)	-15(3)
Cl(0O)	50(6)	59(5)	51(5)	-20(4)	-9(4)	-4(4)
Cl(0P)	90(11)	16(4)	44(7)	0	0	-6(4)
Cl(0Q)	143(18)	33(7)	61(10)	0	0	17(6)
Cl(0R)	94(10)	108(10)	69(8)	-41(8)	-31(8)	-19(8)
Cl(0S)	180(20)	26(6)	68(10)	0	0	22(6)
Cl(0T)	66(9)	143(13)	82(9)	-48(9)	-19(7)	-5(9)

The anisotropic displacement factor exponent takes the form: $-2\pi^2[h^2a^{*2}U_{11} + ... + 2hka^*b^*U_{12}]$.

Table 8.51. Bond lengths [Å] for $Rb_{23}Sb_9Cl_{54}$ at 293(2) K with estimated standard deviations in parentheses.

Label	Distances
Sb(01)-Cl(0D)	2.655(11)
Sb(01)-Cl(0D)#1	2.655(11)
Sb(01)-Cl(0K)#2	2.746(12)
Sb(01)-Cl(0K)	2.746(12)
Sb(01)-Cl(0P)#2	2.543(11)
Sb(01)-Cl(0P)	2.543(11)
Sb(02)-Cl(0E)	2.655(12)
Sb(02)-Cl(0J)	2.632(9)
Sb(02)-Cl(0L)#2	2.762(9)
Sb(02)-Cl(0L)	2.762(9)
Sb(02)-Cl(0O)	2.514(9)
Sb(02)-Cl(0O)#2	2.514(9)
Sb(03)-Cl(0F)	2.519(10)
Sb(03)-Cl(0G)	2.751(10)
Sb(03)-Cl(0H)	2.795(8)
Sb(03)-Cl(0I)	2.498(8)
Sb(03)-Cl(0M)	2.746(8)
Sb(03)-Cl(0N)	2.528(8)
Sb(04)-Cl(0Q)	2.353(14)

Sb(04)-Cl(0R)	2.333(12)
Sb(04)-Cl(0R)#5	2.333(11)
Sb(04)-Cl(0S)	2.303(13)
Sb(04)-Cl(0T)#5	2.354(12)
Sb(04)-Cl(0T)	2.354(12)

Symmetry transformations used to generate equivalent atoms:
(1) -x+1,y,-z+1/2 (2) x,y,-z+1/2 (3) x-1/2,y-1/2,-z+1/2 (4) -x+1,y-1,-z+1/2 (5) -x+2,y,z (6) -x+3/2,y-1/2,-z+1/2 (7) x,y-1,z (8) -x+1,y,z (9) x,y-1,-z+1/2 (10) x-1/2,y-3/2,-z+1/2 (11) -x+3/2,y+1/2,z (12) x+1/2,y+1/2,z (13) -x+3/2,y+1/2,-z+1/2 (14) -x+1,y+1,-z+1/2 (15) x+1/2,y+1/2,-z+1/2 (16) -x+3/2,y-1/2,z (17) -x+3/2,-y+1/2,z-1/2 (18) -x+3/2,y-3/2,-z+1/2 (19) x-1/2,-y+1/2,z-1/2 (20) x,-y,-z (21) -x+1/2,y+1/2,z (22) x,y+1,-z+1/2 (23) x,y+1,z (24) -x+1/2,y-1/2,z (25) x-1/2,y-1/2,z (26) -x+3/2,-y+1/2,z+1/2 (27) x+1/2,y+3/2,-z+1/2

Table 8.52. Crystal data and structure refinement for $RbSbCl_6$ at 293(2) K

Empirical formula	$RbSbCl_6$
Formula weight	419.92
Temperature	293(2) K
Wavelength	0.71073 Å
Crystal system	Monoclinic
Space group	*C*2/*c*
Unit cell dimensions	a = 12.0736(4) Å, α = 90° b = 6.3321(2) Å, β = 101.905(3)° c = 12.1366(3) Å, γ = 90°
Volume	907.90(5) $Å^3$
Z	4
Density (calculated)	3.072 g/cm^3
Absorption coefficient	10.040 mm^{-1}
F(000)	760
Crystal size	0.291 x 0.212 x 0.103 mm^3
θ range for data collection	3.431 to 42.143°
Index ranges	-18<=h<=22, -11<=k<=6, -22<=l<=22
Reflections collected	7367
Independent reflections	3080 [R_{int} = 0.0282]
Completeness to θ = 25.242°	100%
Refinement method	Full-matrix least-squares on F^2
Data / restraints / parameters	3080 / 0 / 40
Goodness-of-fit	1.068
Final R indices [I > 2σ(I)]	R_{obs} = 0.0491, wR_{obs} = 0.1311
R indices [all data]	R_{all} = 0.0726, wR_{all} = 0.1464
Extinction coefficient	0.0003(4)
Largest diff. peak and hole	4.031 and -1.890 e·$Å^{-3}$

$R = \Sigma||F_o|-|F_c|| / \Sigma|F_o|$, $wR = \{\Sigma[w(|F_o|^2 - |F_c|^2)^2] / \Sigma[w(|F_o|^4)]\}^{1/2}$ and $w=1/[\sigma^2(Fo^2)+(0.0841P)^2]$ where $P=(Fo^2+2Fc^2)/3$

Table 8.53. Atomic coordinates (x10^4) and equivalent isotropic displacement parameters (Å^{2}x10^3) for $RbSbCl_6$ at 293(2) K with estimated standard deviations in parentheses.

Label	x	y	z	Occupancy	U_{eq}^*
Sb(01)	7500	2500	5000	1	23(1)
Rb(02)	5000	1097(1)	7500	1	49(1)
Cl(03)	7117(1)	4155(2)	6632(1)	1	38(1)
Cl(04)	5787(1)	3858(2)	3910(1)	1	39(1)
Cl(05)	8492(1)	5547(2)	4624(1)	1	36(1)

$^*U_{eq}$ is defined as one third of the trace of the orthogonalized U_{ij} tensor.

Table 8.54. Anisotropic displacement parameters (Å^{2}x10^3) for $RbSbCl_6$at 293(2) K with estimated standard deviations in parentheses.

Label	U_{11}	U_{22}	U_{33}	U_{12}	U_{13}	U_{23}
Sb(01)	24(1)	25(1)	22(1)	1(1)	5(1)	1(1)
Rb(02)	49(1)	51(1)	48(1)	0	13(1)	0
Cl(03)	47(1)	39(1)	30(1)	1(1)	15(1)	-7(1)
Cl(04)	30(1)	42(1)	42(1)	6(1)	-1(1)	7(1)
Cl(05)	39(1)	31(1)	41(1)	-6(1)	12(1)	4(1)

The anisotropic displacement factor exponent takes the form: $-2\pi^2[h^2a^{*2}U_{11} + ... + 2hka^*b^*U_{12}]$.

Table 8.55. Select bond lengths [Å] for $RbSbCl_6$ at 293(2) K with estimated standard deviations in parentheses.

Label	Distances
Sb(01)-Cl(03)#1	2.3689(8)
Sb(01)-Cl(03)	2.3689(8)
Sb(01)-Cl(04)#1	2.3743(8)
Sb(01)-Cl(04)	2.3742(8)
Sb(01)-Cl(05)	2.3644(9)
Sb(01)-Cl(05)#1	2.3645(9)

Symmetry transformations used to generate equivalent atoms:
(1) -x+3/2,-y+1/2,-z+1 (2) -x+1,y,-z+3/2 (3) x-1/2,y-1/2,z (4) -x+3/2,y-1/2,-z+3/2 (5) x,-y+1,z+1/2 (6) -x+1,-y+1,-z+1 (7) -x+1,-y,-z+1 (8) x,-y,z+1/2 (9) x-1/2,-y+1/2,z+1/2 (10) x+1/2,y+1/2,z

Table 8.56. Crystal data and structure refinement for $Rb_{23}Bi_{2.50}Sb_{6.50}Cl_{54}$ at 293(2) K.

Empirical formula	$Rb_{23}Bi_{2.50}Sb_{6.50}Cl_{54}$
Formula weight	5194.28
Temperature	293(2) K
Wavelength	0.71073 Å
Crystal system	Trigonal
Space group	*R*32
Unit cell dimensions	a = 12.95670(10) Å, α = 90° b = 12.95670(10) Å, β = 90° c = 111.7130(14) Å, γ = 120°
Volume	16241.4(3) $Å^3$
Z	6
Density (calculated)	3.186 g/cm^3
Absorption coefficient	17.273 mm^{-1}
F(000)	13849
Crystal size	0.351 x 0.103 x 0.03 mm^3
θ range for data collection	1.641 to 32.495°
Index ranges	-19<=h<=19, -19<=k<=19, -168<=l<=168
Reflections collected	290427
Independent reflections	13099 [R_{int} = 0.1359]
Completeness to θ = 25.242°	99.9%
Refinement method	Full-matrix least-squares on F^2
Data / restraints / parameters	13099 / 0 / 345
Goodness-of-fit	1.088
Final R indices [I > 2σ(I)]	R_{obs} = 0.0580, wR_{obs} = 0.1029
R indices [all data]	R_{all} = 0.0802, wR_{all} = 0.1101
Largest diff. peak and hole	1.971 and -3.643 e·$Å^{-3}$

$R = \Sigma||F_o|-|F_c|| / \Sigma|F_o|$, $wR = \{\Sigma[w(|F_o|^2 - |F_c|^2)^2] / \Sigma[w(|F_o|^4)]\}^{1/2}$ and $w=1/[\sigma^2(Fo^2)+(0.0194P)^2+477.7357P]$ where $P=(Fo^2+2Fc^2)/3$

Table 8.57. Atomic coordinates (x10^4) and equivalent isotropic displacement parameters ($Å^2$x10^3) for $Rb_{23}Bi_{2.50}Sb_{6.50}Cl_{54}$ at 293(2) K with estimated standard deviations in parentheses.

Label	x	y	z	Occupancy	U_{eq}^*
Sb(5)	3333.33	6666.67	6068(1)	1	28(1)
Rb(1)	6664(5)	3781(4)	4783(1)	0.3333	47(2)
Rb(2)	6667(7)	6667(7)	5000	0.3333	68(2)
Rb(3)	6663(2)	6668(2)	5198(1)	0.6667	54(1)
Rb(4)	6661(5)	3775(4)	5219(1)	0.3333	48(2)
Rb(5)	9554(4)	9555(4)	5218(1)	0.3333	48(2)
Rb(6)	9984(3)	6666(3)	5443(1)	1	103(2)
Rb(7)	6666.67	3333.33	5706(1)	1	72(1)
Rb(8)	10000	10000	5705(1)	1	75(1)
Rb(9)	3333.33	6666.67	5669(1)	1	76(2)
Rb(10)	6834(2)	6661(2)	5975(1)	1	64(1)

Rb(11)	9718(2)	6664(2)	6224(1)	1	44(1)
Rb(12)	6219(1)	6667(1)	6449(1)	1	21(1)
Rb(13)	6666.67	3333.33	6469(1)	1	34(1)
Rb(14)	13333.33	6666.67	6666.67	1	35(1)
Rb(15)	6666.67	3333.33	6864(1)	1	35(1)
Cl(1)	5730(13)	4428(11)	4999(1)	0.3333	53(3)
Cl(2)	7623(13)	5363(12)	4999(1)	0.3333	53(3)
Cl(0A)	7955(12)	8907(12)	5000(1)	0.3333	53(3)
Cl(4)	4663(15)	3322(18)	5169(2)	0.3333	76(5)
Cl(5)	4780(12)	4791(12)	5182(2)	0.3333	58(3)
Cl(6)	8534(11)	6666(11)	5182(2)	0.3333	55(3)
Cl(7)	5335(14)	8670(14)	5169(2)	0.3333	68(4)
Cl(8)	6663(12)	8549(12)	5184(2)	0.3333	60(3)
Cl(9)	7998(14)	10003(16)	5170(2)	0.3333	72(4)
Cl(10)	6687(9)	4982(7)	5438(1)	1	130(3)
Cl(11)	4977(8)	6658(10)	5436(1)	1	144(4)
Cl(12)	8363(8)	8347(7)	5438(1)	1	129(3)
Cl(13)	5112(6)	5088(6)	5702(1)	1	74(2)
Cl(14)	8268(5)	6670(5)	5699(1)	1	70(2)
Cl(15)	6684(5)	8237(6)	5704(1)	1	74(2)
Cl(16)	6753(4)	1764(4)	5968(1)	1	45(1)
Cl(17)	6387(3)	4956(3)	6243(1)	1	35(1)
Cl(18)	9902(4)	8339(4)	5968(1)	1	45(1)
Cl(19)	8094(3)	8385(3)	6242(1)	1	35(1)
Cl(20)	1871(6)	6662(8)	5946(1)	1	98(2)
Cl(21)	4810(5)	6663(7)	6186(1)	1	95(2)
Cl(22)	8662(3)	6665(4)	6494(1)	1	42(1)
Cl(23)	8914(3)	4263(2)	6667(1)	1	26(1)
Cl(24)	11438(3)	6666(3)	6852(1)	1	26(1)
Bi(1)	3333(1)	3333(1)	5000	0.605(10)	29(1)
Bi(2)	6684(1)	6666(1)	5574(1)	0.077(7)	35(1)
Bi(3)	6666.67	3333.33	6102(1)	0.281(10)	22(1)
Bi(5)	10009(1)	6666.67	6666.67	0.551(9)	19(1)
Sb(4)	10000	10000	6102(1)	0.744(10)	22(1)
Bi(4)	10000	10000	6102(1)	0.256(10)	22(1)
Sb(1)	3333(1)	3333(1)	5000	0.395(10)	29(1)
Sb(0A)	6684(1)	6666(1)	5574(1)	0.923(7)	35(1)
Sb(1A)	6666.67	3333.33	6102(1)	0.719(10)	22(1)
Sb(6)	10009(1)	6666.67	6666.67	0.449(9)	19(1)

*U_{eq} is defined as one third of the trace of the orthogonalized U_{ij} tensor.

Table 8.58. Anisotropic displacement parameters ($Å^2x10^3$) for $Rb_{23}Bi_{2.50}Sb_{6.50}Cl_{54}$ at 293(2) K with estimated standard deviations in parentheses.

Label	U_{11}	U_{22}	U_{33}	U_{12}	U_{13}	U_{23}
Sb(5)	33(1)	33(1)	18(1)	16(1)	0	0
Rb(1)	47(2)	47(3)	50(2)	25(3)	2(2)	-5(2)

Rb(2)	72(4)	72(4)	62(5)	38(5)	-2(2)	2(2)
Rb(3)	59(2)	60(2)	44(2)	31(2)	2(1)	0(1)
Rb(4)	48(2)	49(3)	50(2)	26(3)	1(2)	4(2)
Rb(5)	43(3)	49(3)	48(2)	21(2)	-5(2)	-9(2)
Rb(6)	115(2)	140(3)	63(2)	71(2)	-2(2)	-2(2)
Rb(7)	85(2)	85(2)	45(2)	42(1)	0	0
Rb(8)	86(2)	86(2)	53(2)	43(1)	0	0
Rb(9)	99(2)	99(2)	31(2)	49(1)	0	0
Rb(10)	48(1)	67(2)	85(2)	35(1)	4(1)	-1(1)
Rb(11)	55(1)	28(1)	39(1)	12(1)	-2(1)	1(1)
Rb(12)	19(1)	21(1)	25(1)	10(1)	2(1)	0(1)
Rb(13)	38(1)	38(1)	25(1)	19(1)	0	0
Rb(14)	33(1)	33(1)	39(2)	16(1)	0	0
Rb(15)	40(1)	40(1)	26(1)	20(1)	0	0
Cl(1)	48(7)	53(7)	49(5)	19(6)	-1(5)	2(5)
Cl(2)	50(7)	57(7)	58(6)	30(6)	-1(6)	-1(5)
Cl(0A)	59(7)	52(7)	53(6)	33(7)	-6(5)	-3(5)
Cl(4)	60(9)	108(14)	84(11)	60(10)	4(8)	10(9)
Cl(5)	45(7)	54(8)	82(9)	30(7)	-4(6)	-10(6)
Cl(6)	44(7)	41(6)	75(8)	16(5)	11(6)	-3(6)
Cl(7)	55(8)	61(9)	70(9)	17(7)	12(7)	14(7)
Cl(8)	47(7)	50(7)	79(9)	22(6)	2(6)	6(6)
Cl(9)	53(8)	96(12)	76(10)	44(9)	0(7)	-2(9)
Cl(10)	174(9)	88(5)	154(7)	85(6)	9(6)	18(5)
Cl(11)	111(6)	207(11)	150(8)	106(7)	47(6)	7(7)
Cl(12)	95(6)	90(5)	146(7)	5(4)	-20(5)	-22(5)
Cl(13)	62(3)	65(3)	73(3)	15(3)	27(3)	24(3)
Cl(14)	58(3)	103(4)	60(2)	49(3)	-21(2)	2(2)
Cl(15)	98(4)	63(3)	72(3)	49(3)	2(3)	-23(3)
Cl(16)	60(2)	48(2)	38(2)	35(2)	2(2)	-9(2)
Cl(17)	53(2)	33(2)	28(2)	28(2)	-1(2)	-14(2)
Cl(18)	58(2)	40(2)	36(2)	23(2)	-1(2)	-12(2)
Cl(19)	31(2)	35(2)	29(2)	8(2)	12(2)	14(2)
Cl(20)	85(4)	188(7)	55(3)	92(5)	-22(3)	-4(4)
Cl(21)	87(4)	189(7)	42(2)	93(4)	-29(2)	4(3)
Cl(22)	36(2)	75(3)	30(2)	39(2)	-6(2)	0(2)
Cl(23)	26(2)	18(2)	31(2)	8(2)	0(2)	0(1)
Cl(24)	25(2)	25(2)	28(2)	12(2)	-7(2)	1(1)
Bi(1)	31(1)	31(1)	24(1)	15(1)	0(1)	0(1)
Bi(2)	27(1)	29(1)	49(1)	14(1)	1(1)	0(1)
Bi(3)	24(1)	24(1)	17(1)	12(1)	0	0
Bi(5)	16(1)	18(1)	24(1)	9(1)	0(1)	0(1)
Sb(4)	24(1)	24(1)	19(1)	12(1)	0	0
Bi(4)	24(1)	24(1)	19(1)	12(1)	0	0
Sb(1)	31(1)	31(1)	24(1)	15(1)	0(1)	0(1)
Sb(0A)	27(1)	29(1)	49(1)	14(1)	1(1)	0(1)
Sb(1A)	24(1)	24(1)	17(1)	12(1)	0	0

Sb(6)	16(1)	18(1)	24(1)	9(1)	0(1)	0(1)

The anisotropic displacement factor exponent takes the form: $-2\pi^2[h^2a^{*2}U_{11} + ... + 2hka^*b^*U_{12}]$.

Table 8.59. Crystal data and structure refinement for $Rb_{23}Bi_{6.97}Sb_{2.03}Cl_{54}$ at 298 K.

Empirical formula	$Rb_{23}Bi_{6.97}Sb_{2.03}Cl_{54}$
Formula weight	5584.05
Temperature	298 K
Wavelength	0.71073 Å
Crystal system	Trigonal
Space group	*R*32
Unit cell dimensions	a = 12.9731(6) Å, α = 90° b = 12.9731(6) Å, β = 90° c = 112.491(8) Å, γ = 120°
Volume	16395.9(19) $Å^3$
Z	6
Density (calculated)	3.393 g/cm^3
Absorption coefficient	23.190 mm^{-1}
F(000)	14707
Crystal size	0.27 x 0.24 x 0.05 mm^3
θ range for data collection	1.629 to 31.537°
Index ranges	-18<=h<=18, -18<=k<=18, -155<=l<=158
Reflections collected	61881
Independent reflections	11364 [R_{int} = 0.0829]
Completeness to θ = 25.242°	99.9%
Refinement method	Full-matrix least-squares on F^2
Data / restraints / parameters	11364 / 0 / 314
Goodness-of-fit	1.122
Final R indices [I > 2σ(I)]	R_{obs} = 0.1117, wR_{obs} = 0.2906
R indices [all data]	R_{all} = 0.1381, wR_{all} = 0.3129
Largest diff. peak and hole	10.126 and -2.470 e·$Å^{-3}$

$R = \Sigma||F_o|-|F_c|| / \Sigma|F_o|$, $wR = \{\Sigma[w(|F_o|^2 - |F_c|^2)^2] / \Sigma[w(|F_o|^4)]\}^{1/2}$ and $w=1/[\sigma^2(Fo^2)+(0.1728P)^2+321.6441P]$ where $P=(Fo^2+2Fc^2)/3$

Table 8.60. Atomic coordinates (x10^4) and equivalent isotropic displacement parameters (Å^{2}x10^3) for $Rb_{23}Bi_{6.97}Sb_{2.03}Cl_{54}$ at 298 K with estimated standard deviations in parentheses.

Label	x	y	z	Occupancy	U_{eq}^*
Bi(01)	-1(1)	3333.33	3333.33	1	39(1)
Bi(02)	3333.33	6666.67	3898(1)	1	43(1)
Bi(03)	0	0	3899(1)	1	45(1)
Bi(04)	13332(2)	10000	5000	1	62(1)
Bi(05)	10008(2)	6675(2)	4432(1)	0.66(2)	63(1)
Sb(06)	6666.67	3333.33	3932(1)	1	51(1)
Rb(07)	3780(2)	3335(2)	3552(1)	1	43(1)
Rb(08)	3333.33	6666.67	3527(1)	1	53(1)
Rb(09)	3333.33	6666.67	3139(1)	1	53(1)
Rb(0A)	266(4)	3338(3)	3778(1)	1	71(1)
Rb(0B)	-3333.33	3333.33	3333.33	1	52(2)
Rb(0C)	3147(4)	3337(4)	4033(1)	1	94(2)
Rb(0D)	6666.67	3333.33	4329(1)	1	99(2)
Rb(0E)	0	0	4294(1)	1	106(3)
Rb(0F)	3333.33	6666.67	4292(1)	1	103(2)
Cl(0G)	-1450(5)	3333(5)	3516(1)	1	41(2)
Rb(0H)	9980(5)	6650(5)	4804(1)	0.6667	83(2)
Rb(0I)	13314(6)	9969(6)	4557(1)	1	124(3)
Cl(0J)	1070(6)	5739(5)	3334(1)	1	49(2)
Rb(0K)	10000	6672(14)	5000	0.3333	86(6)
Cl(0L)	3600(7)	5050(7)	3756(1)	1	60(2)
Cl(0M)	1889(6)	1615(7)	3757(1)	1	60(2)
Cl(0N)	1333(7)	3329(9)	3508(1)	1	68(2)
Cl(0O)	4994(8)	6729(9)	4033(1)	1	68(2)
Cl(0P)	58(9)	1657(8)	4032(1)	1	69(2)
Rb(0Q)	12925(11)	6695(14)	4784(1)	0.3333	67(3)
Rb(0R)	10031(13)	9598(11)	4785(1)	0.3333	67(3)
Rb(0S)	7098(10)	3761(10)	4784(1)	0.3333	68(3)
Cl(0T)	5179(11)	3318(15)	3812(1)	1	111(5)
Cl(0U)	11662(12)	8320(12)	4301(1)	1	90(3)
Cl(0V)	9994(12)	5019(13)	4298(1)	1	96(3)
Cl(0W)	8371(13)	6694(12)	4298(1)	1	96(3)
Cl(0X)	6647(17)	4771(11)	4050(2)	1	114(5)
Cl(5)	9110(30)	7980(30)	5001(2)	0.3333	73(7)
Cl(6)	11310(30)	5780(30)	5000(2)	0.3333	67(6)
Cl(7)	12210(30)	7570(30)	5002(2)	0.3333	70(6)
Cl(0A)	8284(17)	4968(18)	4574(2)	1	153(8)
Cl(9)	11719(19)	6670(20)	4576(2)	1	159(8)
Cl(1A)	10020(20)	8399(19)	4573(2)	1	154(8)
Cl(8)	11880(30)	9970(30)	4821(2)	0.6667	144(11)
Cl(10)	13380(30)	8620(30)	5178(2)	0.6667	146(11)
Cl(11)	13320(30)	8520(30)	4819(2)	0.6667	151(11)
Sb(1A)	10008(2)	6675(2)	4432(1)	0.34(2)	63(1)

*U_{eq} is defined as one third of the trace of the orthogonalized U_{ij} tensor.

Table 8.61. Anisotropic displacement parameters ($Å^2x10^3$) for $Rb_{23}Bi_{6.97}Sb_{2.03}Cl_{54}$ at 298 K with estimated standard deviations in parentheses.

Label	U_{11}	U_{22}	U_{33}	U_{12}	U_{13}	U_{23}
Bi(01)	26(1)	27(1)	65(1)	14(1)	0(1)	0(1)
Bi(02)	40(1)	40(1)	48(1)	20(1)	0	0
Bi(03)	41(1)	41(1)	53(1)	20(1)	0	0
Bi(04)	75(1)	75(2)	36(1)	37(1)	0(1)	1(1)
Bi(05)	61(1)	61(1)	66(2)	30(1)	0(1)	-1(1)
Sb(06)	57(2)	57(2)	40(2)	28(1)	0	0
Rb(07)	35(1)	38(2)	57(2)	19(1)	2(1)	0(1)
Rb(08)	50(2)	50(2)	58(2)	25(1)	0	0
Rb(09)	51(2)	51(2)	58(2)	25(1)	0	0
Rb(0A)	72(2)	44(2)	84(2)	20(2)	-2(2)	0(2)
Rb(0B)	41(2)	41(2)	73(4)	21(1)	0	0
Rb(0C)	74(2)	101(3)	119(4)	54(2)	11(2)	-1(2)
Rb(0D)	119(4)	119(4)	60(3)	59(2)	0	0
Rb(0E)	112(4)	112(4)	94(5)	56(2)	0	0
Rb(0F)	116(4)	116(4)	76(4)	58(2)	0	0
Cl(0G)	36(3)	37(2)	52(3)	19(2)	6(2)	0(2)
Rb(0H)	101(5)	94(4)	47(3)	43(3)	0(2)	-1(2)
Rb(0I)	145(5)	147(5)	64(3)	60(4)	-3(3)	-3(3)
Cl(0J)	43(3)	34(3)	67(3)	15(2)	1(3)	0(2)
Rb(0K)	103(13)	98(10)	59(9)	52(7)	8(8)	4(4)
Cl(0L)	66(4)	56(4)	70(4)	40(4)	0(3)	-14(3)
Cl(0M)	43(3)	52(4)	70(4)	13(3)	9(3)	13(3)
Cl(0N)	50(4)	101(6)	68(4)	49(4)	-13(3)	0(4)
Cl(0O)	50(4)	80(5)	78(5)	35(4)	-11(4)	4(4)
Cl(0P)	90(6)	52(4)	68(5)	39(4)	-2(4)	-14(4)
Rb(0Q)	71(9)	68(6)	62(4)	34(7)	7(4)	2(5)
Rb(0R)	67(5)	74(9)	62(4)	37(7)	7(5)	11(4)
Rb(0S)	75(8)	74(8)	62(4)	42(5)	0(4)	3(4)
Cl(0T)	94(7)	198(14)	70(6)	96(9)	-27(5)	1(7)
Cl(0U)	86(7)	88(7)	78(5)	31(6)	19(6)	20(6)
Cl(0V)	123(10)	97(8)	73(5)	60(8)	1(6)	-14(6)
Cl(0W)	92(8)	116(9)	83(6)	53(8)	-24(6)	-3(6)
Cl(0X)	201(14)	76(7)	91(7)	88(9)	6(8)	-17(6)
Cl(5)	68(15)	100(20)	47(9)	38(14)	16(10)	11(11)
Cl(6)	81(16)	85(17)	40(8)	45(15)	4(9)	5(10)
Cl(7)	84(17)	82(17)	44(9)	41(14)	-9(11)	-8(11)
Cl(0A)	128(14)	135(14)	115(11)	4(10)	-43(10)	-25(10)
Cl(9)	130(15)	250(20)	144(14)	132(17)	9(11)	-11(14)
Cl(1A)	250(20)	139(15)	116(11)	125(17)	3(13)	7(10)
Cl(8)	220(30)	170(20)	54(9)	100(20)	21(12)	-7(11)
Cl(10)	160(20)	200(30)	64(10)	80(20)	-17(12)	-22(13)
Cl(11)	190(30)	180(30)	87(13)	90(20)	-14(15)	18(15)

Sb(1A)	61(1)	61(1)	66(2)	30(1)	0(1)	-1(1)

The anisotropic displacement factor exponent takes the form: $-2\pi^2[h^2a^{*2}U_{11} + ... + 2hka^*b^*U_{12}]$.

Table 8.62. Table 4. Bond lengths [Å] for $Rb_{23}Bi_{6.97}Sb_{2.03}Cl_{54}$ at 298 K with estimated standard deviations in parentheses.

Label	Distances
Bi(01)-Cl(0G)	2.785(6)
Bi(01)-Cl(0G)#1	2.785(6)
Bi(01)-Cl(0J)#1	2.709(6)
Bi(01)-Cl(0J)	2.709(6)
Bi(01)-Cl(0N)	2.624(7)
Bi(01)-Cl(0N)#1	2.624(7)
Bi(02)-Cl(0L)	2.794(7)
Bi(02)-Cl(0L)#2	2.794(7)
Bi(02)-Cl(0L)#3	2.794(7)
Bi(02)-Cl(0O)#3	2.601(9)
Bi(02)-Cl(0O)	2.601(8)
Bi(02)-Cl(0O)#2	2.601(8)
Bi(03)-Cl(0M)#6	2.791(7)
Bi(03)-Cl(0M)	2.791(7)
Bi(03)-Cl(0M)#5	2.791(7)
Bi(03)-Cl(0P)	2.593(8)
Bi(03)-Cl(0P)#5	2.593(8)
Bi(03)-Cl(0P)#6	2.593(8)
Bi(04)-Cl(5)#7	2.75(3)
Bi(04)-Cl(5)#8	2.75(3)
Bi(04)-Cl(6)#9	2.76(3)
Bi(04)-Cl(6)#10	2.76(3)
Bi(04)-Cl(7)	2.73(3)
Bi(04)-Cl(7)#11	2.73(3)
Bi(04)-Cl(8)	2.74(3)
Bi(04)-Cl(8)#11	2.74(3)
Bi(04)-Cl(10)	2.70(3)
Bi(04)-Cl(10)#11	2.70(3)
Bi(04)-Cl(11)#11	2.80(3)
Bi(04)-Cl(11)	2.80(3)
Bi(05)-Cl(0U)	2.596(12)
Bi(05)-Cl(0V)	2.614(13)
Bi(05)-Cl(0W)	2.610(13)
Bi(05)-Cl(0A)	2.74(2)
Bi(05)-Cl(9)	2.75(2)
Bi(05)-Cl(1A)	2.74(2)
Sb(06)-Cl(0T)#12	2.346(9)
Sb(06)-Cl(0T)#14	2.346(9)
Sb(06)-Cl(0T)	2.346(9)
Sb(06)-Cl(0X)#12	2.296(10)

Sb(06)-Cl(0X)	2.296(10)
Sb(06)-Cl(0X)#14	2.296(10)
Cl(0U)-Sb(1A)	2.596(12)
Cl(0V)-Sb(1A)	2.614(13)
Cl(0W)-Sb(1A)	2.610(13)
Cl(0A)-Sb(1A)	2.74(2)
Cl(9)-Sb(1A)	2.75(2)
Cl(1A)-Sb(1A)	2.74(2)

Symmetry transformations used to generate equivalent atoms:
(1) x-y+1/3,-y+2/3,-z+2/3 (2) -y+1,x-y+1,z (3) -x+y,-x+1,z (4) y+1/3,x+2/3,-z+2/3 (5) -x+y,-x,z (6) -y,x-y,z (7) -x+2,-x+y+1,-z+1 (8) -y+2,x-y+1,z (9) -x+y+2,-x+2,z (10) y+1,x,-z+1 (11) x-y+1,-y+2,-z+1 (12) -x+y+1,-x+1,z (13) -y+2,x-y,z (14) -y+1,x-y,z (15) x+1,y,z (16) -x+1/3,-x+y+2/3,-z+2/3 (17) -x+1/3,-x+y+2/3,-z+2/3 (18) y+1/3,x+2/3,-z+2/3 (19) y+1/3,x+2/3,-z+2/3 (20) -x+y-1,-x,z (21) -y,x-y+1,z (22) -x+1/3,-x+y+2/3,-z+2/3 (23) x-1,y-1,z (24) x-1,y,z (25) -x+y+1,-x+2,z (26) y,x-1,-z+1 (27) y,x,-z+1 (28) x-y,-y+1,-z+1 (29) x+1,y+1,z (30) x-y+1,-y+1,-z+1 (31) x-y+1/3,-y+2/3,-z+2/3

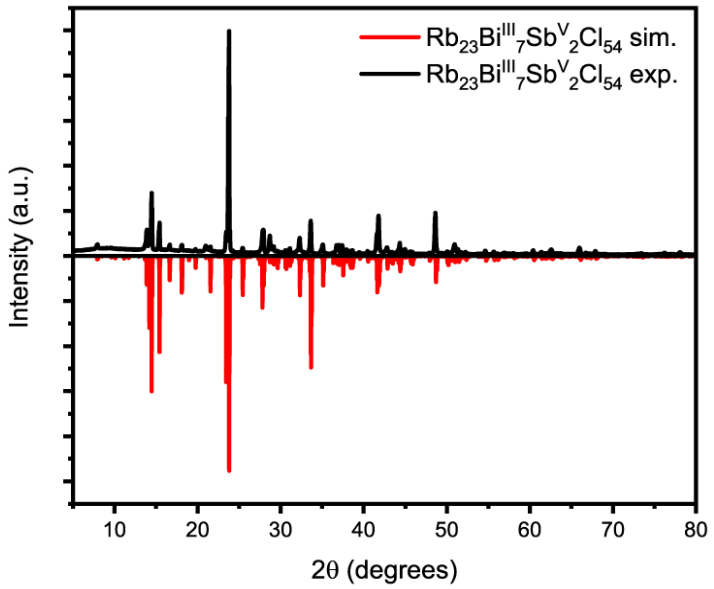

Figure 8.57. PXRD of $Rb_{23}Bi_{6.97}Sb_{2.03}Cl_{54}$.

Table 8.63. Crystal data and structure refinement for Rb_2SbCl_5O at 300 K.

Empirical formula	Rb_2SbCl_5O
Formula weight	485.94
Temperature	300 K
Wavelength	0.71073 Å
Crystal system	Orthrhombic
Space group	*Pnma*
Unit cell dimensions	a = 14.0332(6) Å, α = 90° b = 10.1091(4) Å, β = 90° c = 7.2292(3) Å, γ = 90°
Volume	1025.56(7) $Å^3$
Z	4
Density (calculated)	3.147 g/cm^3
Absorption coefficient	13.356 mm^{-1}
F(000)	872
Crystal size	0.22 x 0.18 x 0.03 mm^3
θ range for data collection	2.903 to 31.520°
Index ranges	-20<=h<=20, -14<=k<=14, -10<=l<=10
Reflections collected	11208
Independent reflections	1694 [R_{int} = 0.0415]
Completeness to θ = 25.242°	100%
Refinement method	Full-matrix least-squares on F^2
Data / restraints / parameters	1694 / 0 / 49
Goodness-of-fit	1.171
Final R indices [I > 2σ(I)]	R_{obs} = 0.0389, wR_{obs} = 0.0896
R indices [all data]	R_{all} = 0.0443, wR_{all} = 0.0930
Largest diff. peak and hole	1.503 and -0.908 e·$Å^{-3}$

$R = \Sigma||F_o|-|F_c|| / \Sigma|F_o|$, $wR = \{\Sigma[w(|F_o|^2 - |F_c|^2)^2] / \Sigma[w(|F_o|^4)]\}^{1/2}$ and $w=1/[\sigma^2(Fo^2)+(0.0408P)^2+3.5645P]$ where $P=(Fo^2+2Fc^2)/3$

Table 8.64. Atomic coordinates ($x10^4$) and equivalent isotropic displacement parameters ($Å^2x10^3$) for Rb_2SbCl_5O at 300 K with estimated standard deviations in parentheses.

Label	x	y	z	Occupancy	U_{eq}^*
Sb(01)	6146(1)	7500	6911(1)	1	23(1)
Rb(02)	6444(1)	5008(1)	1557(1)	1	37(1)
Cl(03)	7525(2)	7500	9041(2)	1	28(1)
Cl(04)	7227(2)	7500	4226(2)	1	36(1)
Cl(05)	6037(1)	5037(1)	6795(2)	1	34(1)
Cl(06)	5026(2)	7500	9570(2)	1	34(1)
O(07)	4905(4)	7500	4928(8)	1	40(2)

$^*U_{eq}$ is defined as one third of the trace of the orthogonalized U_{ij} tensor.

Table 8.65. Anisotropic displacement parameters ($Å^2x10^3$) for Rb_2SbCl_5O at 300 K with estimated standard deviations in parentheses.

Label	U_{11}	U_{22}	U_{33}	U_{12}	U_{13}	U_{23}
Sb(01)	23(1)	20(1)	26(1)	0	-2(1)	0
Rb(02)	36(1)	35(1)	40(1)	-1(1)	-5(1)	4(1)
Cl(03)	26(1)	33(1)	27(1)	0	-6(1)	0
Cl(04)	40(1)	43(1)	25(1)	0	8(1)	0
Cl(05)	40(1)	18(1)	45(1)	0(1)	-9(1)	-3(1)
Cl(06)	29(1)	34(1)	38(1)	0	10(1)	0
O(07)	36(3)	28(2)	57(3)	0	-26(3)	0

The anisotropic displacement factor exponent takes the form: $-2\pi^2[h^2a^{*2}U_{11} + ... + 2hka^*b^*U_{12}]$.

Table 8.66. Bond lengths [Å] for Rb_2SbCl_5O at 300 K with estimated standard deviations in parentheses.

Label	Distances
Sb(01)-Cl(03)	2.4727(15)
Sb(01)-Cl(04)	2.4632(17)
Sb(01)-Cl(05)#5	2.4956(11)
Sb(01)-Cl(05)	2.4956(11)
Sb(01)-Cl(06)	2.4836(16)
Sb(01)-O(07)	2.255(5)

Symmetry transformations used to generate equivalent atoms:
(1) -x+3/2,-y+1,z+1/2 (2) -x+3/2,y+1/2,z+1/2 (3) x,y,z+1 (4) x,-y+3/2,z+1 (5) x,-y+3/2,z (6) -x+3/2,-y+1,z-1/2 (7) x,y,z-1 (8) -x+1,-y+1,-z+1 (9) -x+1,y+1/2,-z+1

References

1. Monardes, N., *Dos libros, el uno que trata de todas las cosas que traen de nuestras Indias Occidentales, que sirven al uso de la medicina, y el otro que trata de la piedra Bezaar y de la yerva escuerconera*. Hernando Diaz: Sevilla, 1569.
2. Partington, J. R., Lignum nephriticum. *Ann. Sci.* **1955,** *11* (1), 1-26.
3. Muyskens, M.; Ed, V., The Fluorescence of Lignum nephriticum: A Flash Back to the Past and a Simple Demonstration of Natural Substance Fluorescence. *J. Chem. Educ.* **2006,** *83* (5), 765.
4. Acuña, A. U.; Amat-Guerri, F., Early History of Solution Fluorescence: The Lignum nephriticum of Nicolás Monardes. In *Fluorescence of Supermolecules, Polymers, and Nanosystems*, Berberan-Santos, M. N., Ed. Springer: 2007; Vol. 4.
5. Valeur, B.; Berberan-Santos, M. r. N., A Brief History of Fluorescence and Phosphorescence before the Emergence of Quantum Theory. *J. Chem. Educ.* **2011,** *88* (6), 731-738.
6. Newton, I., The Second Book of Optics. Part III. In *Opticks: Or, A Treatise of the Reflections, Refractions, Inflections and Colours of Light*, 4th ed.; London, 1730.
7. Haüy, R. J., *Traité de minéralogie*. Chez Louis: 1801; Vol. 1.
8. Brewster, D., XIII.—On the Decomposition and Dispersion of Light within Solid and Fluid Bodies. *Trans. - R. Soc. Edinburgh* **1846,** *16* (2), 111-121.
9. Brewster, D., XIX. On the Colours of Natural Bodies. *Trans. - R. Soc. Edinburgh* **1833,** *12* (2), 538-545.
10. Herschel, J. F. W., V. ’Αμόρφωϒa, no. II.— On the epipolic dispersion of light, being a supplement to a paper entitled, “On a case of superficial colour presented by a homogeneous liquid internally colourless.". *Phil. Trans. R. Soc.* **1845,** *135*, 147-153.
11. Meshnick, S. R.; Dobson, M. J., The History of Antimalarial Drugs. In *Antimalarial Chemotherapy: Mechanisms of Action, Resistance, and New Directions in Drug Discovery*, Rosenthal, P. J., Ed. Humana Press: Totowa, NJ, 2001; pp 15-25.
12. W, W. C., Intra-Mercurial Planets. *Science* **1881,** *2* (36), 94-5.
13. Stokes, G. G., XXX. On the change of refrangibility of light. *Phil. Trans. R. Soc.* **1852,** *142*, 463-562.
14. Stokes, G. G., XVI. On the change of refrangibility of light.—No. II. *Phil. Trans. R. Soc.* **1853,** *143*, 385-396.
15. Becquerel, E., Des effets produits sur les corps par les rayons solaires. *Ann. Chim. Phys.* **1843,** *9*, 257-322.
16. Becquerel, E., *La lumière, ses causes et ses effets*. Firmin Didot frères: 1867; Vol. 1.
17. Wiedemann, E., Ueber Fluorescenz und Phosphorescenz I. Abhandlung. *Ann. Phys. Chem.* **1888,** *270* (7), 446-463.
18. Eckstein, H. P., Distribution of Fluorescence Excitation of Bivalent Europium in Calcium Fluoride and of Bivalent Samarium in Calcium Sulphate. *Nature* **1938,** *142*, 256-257.
19. Edgar, A., Luminescent Materials. In *Springer Handbook of Electronic and Photonic Materials*, Kasap, S.; Capper, P., Eds. Springer International Publishing: Cham,

2017; pp 1-1.
20. Nakamura, S.; Mukai, T.; Senoh, M., High-Power GaN P-N Junction Blue-Light-Emitting Diodes. *Jpn. J. Appl. Phys.* **1991,** *30* (Part 2, No. 12A), L1998-L2001.
21. Kovalenko, M. V.; Kaufmann, E.; Pachinger, D.; Roither, J.; Huber, M.; Stangl, J.; Hesser, G.; Schaffler, F.; Heiss, W., Colloidal HgTe nanocrystals with widely tunable narrow band gap energies: from telecommunications to molecular vibrations. *J. Am. Chem. Soc.* **2006,** *128* (11), 3516-7.
22. Rose, J., Blue LEDs – Filling the world with new light. Lars Bergström, P. D., Anne L'Huillier and Olle Inganäs, the Nobel Committee for Physics, Ed. The Royal Swedish Academy of Sciences: 2014.
23. Won, Y. H.; Cho, O.; Kim, T.; Chung, D. Y.; Kim, T.; Chung, H.; Jang, H.; Lee, J.; Kim, D.; Jang, E., Highly efficient and stable InP/ZnSe/ZnS quantum dot light-emitting diodes. *Nature* **2019,** *575* (7784), 634-638.
24. Snaith, H. J., Perovskites: The Emergence of a New Era for Low-Cost, High-Efficiency Solar Cells. *J. Phys. Chem. Lett.* **2013,** *4* (21), 3623-3630.
25. Lee, M. M.; Teuscher, J.; Miyasaka, T.; Murakami, T. N.; Snaith, H. J., Efficient hybrid solar cells based on meso-superstructured organometal halide perovskites. *Science* **2012,** *338* (6107), 643-7.
26. Burschka, J.; Pellet, N.; Moon, S. J.; Humphry-Baker, R.; Gao, P.; Nazeeruddin, M. K.; Gratzel, M., Sequential deposition as a route to high-performance perovskite-sensitized solar cells. *Nature* **2013,** *499* (7458), 316-9.
27. Kojima, A.; Teshima, K.; Shirai, Y.; Miyasaka, T., Organometal Halide Perovskites as Visible-Light Sensitizers for Photovoltaic Cells. *J. Am. Chem. Soc.* **2009,** *131* (17), 6050-6051.
28. Goldschmidt, V. M., Die Gesetze der Krystallochemie. *Naturwissenschaften* **1926,** *21* (5), 477-485.
29. Stoumpos, C. C.; Kanatzidis, M. G., The Renaissance of Halide Perovskites and Their Evolution as Emerging Semiconductors. *Acc. Chem. Res.* **2015,** *48* (10), 2791-802.
30. Trots, D. M.; Myagkota, S. V., High-temperature structural evolution of caesium and rubidium triiodoplumbates. *J. Phys. Chem. Solids* **2008,** *69* (10), 2520-2526.
31. Travis, W.; Glover, E. N. K.; Bronstein, H.; Scanlon, D. O.; Palgrave, R. G., On the application of the tolerance factor to inorganic and hybrid halide perovskites: a revised system. *Chem. Sci.* **2016,** *7* (7), 4548-4556.
32. Momma, K.; Izumi, F., VESTA 3for three-dimensional visualization of crystal, volumetric and morphology data. *J. Appl. Crystallogr.* **2011,** *44* (6), 1272-1276.
33. Yakunin, S.; Dirin, D. N.; Shynkarenko, Y.; Morad, V.; Cherniukh, I.; Nazarenko, O.; Kreil, D.; Nauser, T.; Kovalenko, M. V., Detection of gamma photons using solution-grown single crystals of hybrid lead halide perovskites. *Nat. Photonics* **2016,** *10* (9), 585-589.
34. Yakunin, S.; Shynkarenko, Y.; Dirin, D. N.; Cherniukh, I.; Kovalenko, M. V., Non-dissipative internal optical filtering with solution-grown perovskite single crystals for full-colour imaging. *NPG Asia Mater.* **2017,** *9* (9), e431-e431.
35. Yakunin, S.; Sytnyk, M.; Kriegner, D.; Shrestha, S.; Richter, M.; Matt, G. J.; Azimi, H.; Brabec, C. J.; Stangl, J.; Kovalenko, M. V.; Heiss, W., Detection of X-ray photons by

solution-processed organic-inorganic perovskites. *Nat. Photonics* **2015,** *9* (7), 444-449.

36. Dou, L.; Yang, Y. M.; You, J.; Hong, Z.; Chang, W. H.; Li, G.; Yang, Y., Solution-processed hybrid perovskite photodetectors with high detectivity. *Nat. Commun.* **2014,** *5*, 5404.
37. Stranks, S. D.; Snaith, H. J., Metal-halide perovskites for photovoltaic and light-emitting devices. *Nat. Nanotechnol.* **2015,** *10* (5), 391-402.
38. Tan, Z. K.; Moghaddam, R. S.; Lai, M. L.; Docampo, P.; Higler, R.; Deschler, F.; Price, M.; Sadhanala, A.; Pazos, L. M.; Credgington, D.; Hanusch, F.; Bein, T.; Snaith, H. J.; Friend, R. H., Bright light-emitting diodes based on organometal halide perovskite. *Nat. Nanotechnol.* **2014,** *9* (9), 687-92.
39. Sutherland, B. R.; Sargent, E. H., Perovskite photonic sources. *Nat. Photonics* **2016,** *10* (5), 295-302.
40. Yakunin, S.; Protesescu, L.; Krieg, F.; Bodnarchuk, M. I.; Nedelcu, G.; Humer, M.; De Luca, G.; Fiebig, M.; Heiss, W.; Kovalenko, M. V., Low-threshold amplified spontaneous emission and lasing from colloidal nanocrystals of caesium lead halide perovskites. *Nat. Commun.* **2015,** *6*, 8056.
41. Stoumpos, C. C.; Malliakas, C. D.; Peters, J. A.; Liu, Z.; Sebastian, M.; Im, J.; Chasapis, T. C.; Wibowo, A. C.; Chung, D. Y.; Freeman, A. J.; Wessels, B. W.; Kanatzidis, M. G., Crystal Growth of the Perovskite Semiconductor CsPbBr3: A New Material for High-Energy Radiation Detection. *Cryst. Growth Des.* **2013,** *13* (7), 2722-2727.
42. Rakita, Y.; Kedem, N.; Gupta, S.; Sadhanala, A.; Kalchenko, V.; Böhm, M. L.; Kulbak, M.; Friend, R. H.; Cahen, D.; Hodes, G., Low-Temperature Solution-Grown CsPbBr3Single Crystals and Their Characterization. *Cryst. Growth Des.* **2016**.
43. Dirin, D. N.; Cherniukh, I.; Yakunin, S.; Shynkarenko, Y.; Kovalenko, M. V., Solution-Grown CsPbBr3 Perovskite Single Crystals for Photon Detection. *Chem. Mater.* **2016,** *28* (23), 8470-8474.
44. Saidaminov, M. I.; Abdelhady, A. L.; Murali, B.; Alarousu, E.; Burlakov, V. M.; Peng, W.; Dursun, I.; Wang, L.; He, Y.; Maculan, G.; Goriely, A.; Wu, T.; Mohammed, O. F.; Bakr, O. M., High-quality bulk hybrid perovskite single crystals within minutes by inverse temperature crystallization. *Nat. Commun.* **2015,** *6*, 7586.
45. Zhumekenov, A. A.; Saidaminov, M. I.; Haque, M. A.; Alarousu, E.; Sarmah, S. P.; Murali, B.; Dursun, I.; Miao, X.-H.; Abdelhady, A. L.; Wu, T.; Mohammed, O. F.; Bakr, O. M., Formamidinium Lead Halide Perovskite Crystals with Unprecedented Long Carrier Dynamics and Diffusion Length. *ACS Energy Lett.* **2016,** *1* (1), 32-37.
46. Protesescu, L.; Yakunin, S.; Nazarenko, O.; Dirin, D. N.; Kovalenko, M. V., Low-Cost Synthesis of Highly Luminescent Colloidal Lead Halide Perovskite Nanocrystals by Wet Ball Milling. *ACS Appl. Nano. Mater.* **2018,** *1* (3), 1300-1308.
47. Dirin, D. N.; Protesescu, L.; Trummer, D.; Kochetygov, I. V.; Yakunin, S.; Krumeich, F.; Stadie, N. P.; Kovalenko, M. V., Harnessing Defect-Tolerance at the Nanoscale: Highly Luminescent Lead Halide Perovskite Nanocrystals in Mesoporous Silica Matrixes. *Nano Lett.* **2016,** *16* (9), 5866-74.
48. Quan, L. N.; Quintero-Bermudez, R.; Voznyy, O.; Walters, G.; Jain, A.; Fan, J. Z.; Zheng, X.; Yang, Z.; Sargent, E. H., Highly Emissive Green Perovskite Nanocrystals in a Solid State Crystalline Matrix. *Adv. Mater.* **2017,** *29* (21).

49. Dirin, D. N.; Benin, B. M.; Yakunin, S.; Krumeich, F.; Raino, G.; Frison, R.; Kovalenko, M. V., Microcarrier-Assisted Inorganic Shelling of Lead Halide Perovskite Nanocrystals. *ACS Nano* **2019,** *13* (10), 11642-11652.
50. Nedelcu, G.; Protesescu, L.; Yakunin, S.; Bodnarchuk, M. I.; Grotevent, M. J.; Kovalenko, M. V., Fast Anion-Exchange in Highly Luminescent Nanocrystals of Cesium Lead Halide Perovskites (CsPbX3, X = Cl, Br, I). *Nano Lett.* **2015,** *15* (8), 5635-40.
51. Stranks, S. D.; Eperon, G. E.; Grancini, G.; Menelaou, C.; Alcocer, M. J.; Leijtens, T.; Herz, L. M.; Petrozza, A.; Snaith, H. J., Electron-hole diffusion lengths exceeding 1 micrometer in an organometal trihalide perovskite absorber. *Science* **2013,** *342* (6156), 341-4.
52. Protesescu, L.; Yakunin, S.; Bodnarchuk, M. I.; Krieg, F.; Caputo, R.; Hendon, C. H.; Yang, R. X.; Walsh, A.; Kovalenko, M. V., Nanocrystals of Cesium Lead Halide Perovskites (CsPbX(3), X = Cl, Br, and I): Novel Optoelectronic Materials Showing Bright Emission with Wide Color Gamut. *Nano Lett.* **2015,** *15* (6), 3692-6.
53. Akkerman, Q. A.; Raino, G.; Kovalenko, M. V.; Manna, L., Genesis, challenges and opportunities for colloidal lead halide perovskite nanocrystals. *Nat. Mater.* **2018,** *17* (5), 394-405.
54. Brandt, R. E.; Poindexter, J. R.; Gorai, P.; Kurchin, R. C.; Hoye, R. L. Z.; Nienhaus, L.; Wilson, M. W. B.; Polizzotti, J. A.; Sereika, R.; Žaltauskas, R.; Lee, L. C.; MacManus-Driscoll, J. L.; Bawendi, M.; Stevanović, V.; Buonassisi, T., Searching for "Defect-Tolerant" Photovoltaic Materials: Combined Theoretical and Experimental Screening. *Chem. Mater.* **2017,** *29* (11), 4667-4674.
55. ten Brinck, S.; Infante, I., Surface Termination, Morphology, and Bright Photoluminescence of Cesium Lead Halide Perovskite Nanocrystals. *ACS Energy Lett.* **2016,** *1* (6), 1266-1272.
56. Huang, H.; Bodnarchuk, M. I.; Kershaw, S. V.; Kovalenko, M. V.; Rogach, A. L., Lead Halide Perovskite Nanocrystals in the Research Spotlight: Stability and Defect Tolerance. *ACS Energy Lett.* **2017,** *2* (9), 2071-2083.
57. Kang, J.; Wang, L. W., High Defect Tolerance in Lead Halide Perovskite CsPbBr3. *J. Phys. Chem. Lett.* **2017,** *8* (2), 489-493.
58. DIRECTIVE OF THE EUROPEAN PARLIAMENT AND OF THE COUNCIL on the restriction of the use of certain hazardous substances in electrical and electronic equipment. 2011; pp 1-45.
59. Brandt, R. E.; Stevanović, V.; Ginley, D. S.; Buonassisi, T., Identifying defect-tolerant semiconductors with high minority-carrier lifetimes: beyond hybrid lead halide perovskites. *MRS Commun.* **2015,** *5* (2), 265-275.
60. Tomaszewski, P. E., Structural phase transitions in crystals. I. Database. *Phase Transitions* **1992,** *38* (3), 127-220.
61. Thiele, G.; Rotter, H. W.; Schmidt, K. D., Die Kristallstrukturen und Phasentransformationen von RbGeBr3. *Z. Anorg. Allg. Chem.* **1988,** (559), 7-16.
62. Stoumpos, C. C.; Malliakas, C. D.; Kanatzidis, M. G., Semiconducting tin and lead iodide perovskites with organic cations: phase transitions, high mobilities, and near-infrared photoluminescent properties. *Inorg. Chem.* **2013,** *52* (15), 9019-38.
63. McClure, E. T.; Ball, M. R.; Windl, W.; Woodward, P. M., Cs2AgBiX6 (X = Br,

Cl): New Visible Light Absorbing, Lead-Free Halide Perovskite Semiconductors. *Chem. Mater.* **2016,** *28* (5), 1348-1354.

64. Slavney, A. H.; Hu, T.; Lindenberg, A. M.; Karunadasa, H. I., A Bismuth-Halide Double Perovskite with Long Carrier Recombination Lifetime for Photovoltaic Applications. *J. Am. Chem. Soc.* **2016,** *138* (7), 2138-41.
65. Slavney, A. H.; Connor, B. A.; Leppert, L.; Karunadasa, H. I., A pencil-and-paper method for elucidating halide double perovskite band structures. *Chem. Sci.* **2019,** *10* (48), 11041-11053.
66. Slavney, A. H.; Leppert, L.; Bartesaghi, D.; Gold-Parker, A.; Toney, M. F.; Savenije, T. J.; Neaton, J. B.; Karunadasa, H. I., Defect-Induced Band-Edge Reconstruction of a Bismuth-Halide Double Perovskite for Visible-Light Absorption. *J. Am. Chem. Soc.* **2017,** *139* (14), 5015-5018.
67. Slavney, A. H.; Leppert, L.; Saldivar Valdes, A.; Bartesaghi, D.; Savenije, T. J.; Neaton, J. B.; Karunadasa, H. I., Small-Band-Gap Halide Double Perovskites. *Angew. Chem., Int. Ed.* **2018,** *57* (39), 12765-12770.
68. Volonakis, G.; Haghighirad, A. A.; Milot, R. L.; Sio, W. H.; Filip, M. R.; Wenger, B.; Johnston, M. B.; Herz, L. M.; Snaith, H. J.; Giustino, F., Cs2InAgCl6: A New Lead-Free Halide Double Perovskite with Direct Band Gap. *J. Phys. Chem. Lett.* **2017,** *8* (4), 772-778.
69. Zelewski, S. J.; Urban, J. M.; Surrente, A.; Maude, D. K.; Kuc, A.; Schade, L.; Johnson, R. D.; Dollmann, M.; Nayak, P. K.; Snaith, H. J.; Radaelli, P.; Kudrawiec, R.; Nicholas, R. J.; Plochocka, P.; Baranowski, M., Revealing the nature of photoluminescence emission in the metal-halide double perovskite Cs2AgBiBr6. *J. Mater. Chem. C* **2019,** *7* (27), 8350-8356.
70. K, N. N.; Nag, A., Synthesis and luminescence of Mn-doped Cs2AgInCl6 double perovskites. *Chem. Commun.* **2018,** *54* (41), 5205-5208.
71. Wu, W.; Cong, W. Y.; Guan, C.; Sun, H.; Yin, R.; Yu, G.; Lu, Y. B., Investigation of the Mn dopant-enhanced photoluminescence performance of lead-free Cs2AgInCl6 double perovskite crystals. *Phys. Chem. Chem. Phys.* **2020,** *22* (4), 1815-1819.
72. Zhao, F.; Song, Z.; Zhao, J.; Liu, Q., Double perovskite Cs2AgInCl6:Cr3+: broadband and near-infrared luminescent materials. *Inorg. Chem. Front.* **2019,** *6* (12), 3621-3628.
73. Lindquist, K. P.; Mack, S. A.; Slavney, A. H.; Leppert, L.; Gold-Parker, A.; Stebbins, J. F.; Salleo, A.; Toney, M. F.; Neaton, J. B.; Karunadasa, H. I., Tuning the bandgap of Cs2AgBiBr6 through dilute tin alloying. *Chem. Sci.* **2019,** *10* (45), 10620-10628.
74. Luo, J.; Wang, X.; Li, S.; Liu, J.; Guo, Y.; Niu, G.; Yao, L.; Fu, Y.; Gao, L.; Dong, Q.; Zhao, C.; Leng, M.; Ma, F.; Liang, W.; Wang, L.; Jin, S.; Han, J.; Zhang, L.; Etheridge, J.; Wang, J.; Yan, Y.; Sargent, E. H.; Tang, J., Efficient and stable emission of warm-white light from lead-free halide double perovskites. *Nature* **2018,** *563* (7732), 541-545.
75. Liu, Y.; Jing, Y.; Zhao, J.; Liu, Q.; Xia, Z., Design Optimization of Lead-Free Perovskite Cs2AgInCl6:Bi Nanocrystals with 11.4% Photoluminescence Quantum Yield. *Chem. Mater.* **2019,** *31* (9), 3333-3339.
76. Noculak, A.; Morad, V.; McCall, K. M.; Yakunin, S.; Shynkarenko, Y.; Wörle, M.; Kovalenko, M. V., Bright Blue and Green Luminescence of Sb(III) in Double Perovskite Cs2MInCl6 (M = Na, K) Matrices. *Chem. Mater.* **2020**.

77. McCall, K. M.; Friedrich, D.; Chica, D. G.; Cai, W.; Stoumpos, C. C.; Alexander, G. C. B.; Deemyad, S.; Wessels, B. W.; Kanatzidis, M. G., Perovskites with a Twist: Strong In1+ Off-Centering in the Mixed-Valent CsInX3 (X = Cl, Br). *Chem. Mater.* **2019,** *31* (22), 9554-9566.
78. González-Carrero, S.; Galian, R. E.; Pérez-Prieto, J., Organometal Halide Perovskites: Bulk Low-Dimension Materials and Nanoparticles. *Part. Part. Syst. Charact.* **2015,** *32* (7), 709-720.
79. Papavassiliou, G. C., Three- and Low-Dimensional Inorganic Semiconductors. *Prog. Solid State Chem.* **1997,** *25*, 125-270.
80. Mitzi, D. B.; Feild, C. A.; Harrison, W. T. A.; Guloy, A. M., Conducting tin halides with a layered organic-based perovskite structure. *Nature* **1994,** *369* (6480), 467-469.
81. Mitzi, D. B., Solution-processed inorganic semiconductors. *J. Mater. Chem.* **2004,** *14* (15), 2355.
82. Saparov, B.; Mitzi, D. B., Organic-Inorganic Perovskites: Structural Versatility for Functional Materials Design. *Chem. Rev.* **2016,** *116* (7), 4558-96.
83. Pelant, I.; Valenta, J., *Luminescence Spectroscopy of Semiconductors*. OUP Oxford: 2012.
84. Kokubun, Y.; Watanabe, H.; Wada, M., Photoluminescence of CdSe Single Crystals. *Jpn. J. Appl. Phys.* **1974,** *13* (9), 1393-1398.
85. Temkin, H.; Bonner, W. A., Photoluminescence study of melt grown InP. *J. Appl. Phys.* **1981,** *52* (1), 397-401.
86. Manasreh, M. O., *InP and Related Compounds*. Taylor & Francis: 2000; Vol. 9.
87. Chia, C. H.; Yuan, C. T.; Ku, J. T.; Yang, S. L.; Chou, W. C.; Juang, J. Y.; Hsieh, S. Y.; Chiu, K. C.; Hsu, J. S.; Jeng, S. Y., Temperature dependence of excitonic emission in cubic CdSe thin film. *J. Lumin.* **2008,** *128* (1), 123-128.
88. Tamargo, M. C., *II-VI Semiconductor Materials and their Applications*. Taylor & Francis: 2002; Vol. 12.
89. Ueta, M.; Kanzaki, H.; Kobayashi, K.; Toyozawa, Y.; Hanamura, E., *Excitonic Processes in Solids*. Springer-Verlag: 1986; Vol. 60.
90. Ropp, R. C., *Luminescence and the Solid State*. 2nd ed.; Elsevier: 2004; Vol. 21.
91. Liang, W. Y., Excitons. *Phys. Educ.* **1970,** *5*, 226.
92. Yu, P. Y.; Cardona, M., *Fundamentals of Semiconductors: Physics and Materials Properties*. Third ed.; Springer: 2005.
93. Song, K. S.; Williams, R. T., *Self-Trapped Excitons*. Springer-Verlag: 1993; Vol. 105.
94. Klick, C. C., Point Defects in Insulators. *Science* **1965,** *150* (3695), 451-456.
95. Hersh, H. N., Proposed Excitonic Mechanism of Color-Center Formation in Alkali Halides. *Phys. Rev.* **1966,** *148* (2), 928-932.
96. Smith, M. D.; Connor, B. A.; Karunadasa, H. I., Tuning the Luminescence of Layered Halide Perovskites. *Chem. Rev.* **2019,** *119* (5), 3104-3139.
97. Smith, M. D.; Crace, E. J.; Jaffe, A.; Karunadasa, H. I., The Diversity of Layered Halide Perovskites. *Annu. Rev. Mater. Res.* **2018,** *48* (1), 111-136.
98. Dolzhenko, Y. I.; Inabe, T.; Maruyama, Y., In Situ X-Ray Observation on the Intercalation of Weak Interaction Molecules into Perovskite-Type Layered Crystals

(C9H19NH3)2PbI4and (C10H21NH3)2CdCl4. *Bull. Chem. Soc. Jpn.* **1986,** *59* (2), 563-567.
99. Li, X.; Hoffman, J.; Ke, W.; Chen, M.; Tsai, H.; Nie, W.; Mohite, A. D.; Kepenekian, M.; Katan, C.; Even, J.; Wasielewski, M. R.; Stoumpos, C. C.; Kanatzidis, M. G., Two-Dimensional Halide Perovskites Incorporating Straight Chain Symmetric Diammonium Ions, (NH3C mH2 mNH3)(CH3NH3) n-1Pb nI3 n+1 (m = 4-9; n = 1-4). *J. Am. Chem. Soc.* **2018,** *140* (38), 12226-12238.
100. Connor, B. A.; Leppert, L.; Smith, M. D.; Neaton, J. B.; Karunadasa, H. I., Layered Halide Double Perovskites: Dimensional Reduction of Cs2AgBiBr6. *J. Am. Chem. Soc.* **2018,** *140* (15), 5235-5240.
101. Smith, M. D.; Karunadasa, H. I., White-Light Emission from Layered Halide Perovskites. *Acc. Chem. Res.* **2018,** *51* (3), 619-627.
102. Dohner, E. R.; Jaffe, A.; Bradshaw, L. R.; Karunadasa, H. I., Intrinsic white-light emission from layered hybrid perovskites. *J. Am. Chem. Soc.* **2014,** *136* (38), 13154-7.
103. Yang, S.; Lin, Z.; Wang, J.; Chen, Y.; Liu, Z.; Yang, E.; Zhang, J.; Ling, Q., High Color Rendering Index White-Light Emission from UV-Driven LEDs Based on Single Luminescent Materials: Two-Dimensional Perovskites (C6H5C2H4NH3)2PbBr xCl4- x. *ACS Appl. Mater. Interfaces* **2018,** *10* (18), 15980-15987.
104. Ishihara, T.; Takahashi, J.; Goto, T., Exciton state in two-dimensional perovskite semiconductor (C10H21NH3)2PbI4. *Solid State Commun.* **1989,** *69* (9), 933-936.
105. Pedesseau, L.; Sapori, D.; Traore, B.; Robles, R.; Fang, H. H.; Loi, M. A.; Tsai, H.; Nie, W.; Blancon, J. C.; Neukirch, A.; Tretiak, S.; Mohite, A. D.; Katan, C.; Even, J.; Kepenekian, M., Advances and Promises of Layered Halide Hybrid Perovskite Semiconductors. *ACS Nano* **2016,** *10* (11), 9776-9786.
106. Koutselas, I.; Bampoulis, P.; Maratou, E.; Evagelinou, T.; Pagona, G.; Papavassiliou, G. C., Some Unconventional Organic−Inorganic Hybrid Low-Dimensional Semiconductors and Related Light-Emitting Devices. *J. Phys. Chem. C* **2011,** *115* (17), 8475-8483.
107. Ahmad, S.; Kanaujia, P. K.; Niu, W.; Baumberg, J. J.; Vijaya Prakash, G., In situ intercalation dynamics in inorganic-organic layered perovskite thin films. *ACS Appl. Mater. Interfaces* **2014,** *6* (13), 10238-47.
108. Hu, T.; Smith, M. D.; Dohner, E. R.; Sher, M. J.; Wu, X.; Trinh, M. T.; Fisher, A.; Corbett, J.; Zhu, X. Y.; Karunadasa, H. I.; Lindenberg, A. M., Mechanism for Broadband White-Light Emission from Two-Dimensional (110) Hybrid Perovskites. *J. Phys. Chem. Lett.* **2016,** *7* (12), 2258-63.
109. Nazarenko, O.; Kotyrba, M. R.; Worle, M.; Cuervo-Reyes, E.; Yakunin, S.; Kovalenko, M. V., Luminescent and Photoconductive Layered Lead Halide Perovskite Compounds Comprising Mixtures of Cesium and Guanidinium Cations. *Inorg. Chem.* **2017,** *56* (19), 11552-11564.
110. Tsai, H.; Nie, W.; Blancon, J. C.; Stoumpos, C. C.; Asadpour, R.; Harutyunyan, B.; Neukirch, A. J.; Verduzco, R.; Crochet, J. J.; Tretiak, S.; Pedesseau, L.; Even, J.; Alam, M. A.; Gupta, G.; Lou, J.; Ajayan, P. M.; Bedzyk, M. J.; Kanatzidis, M. G., High-efficiency two-dimensional Ruddlesden-Popper perovskite solar cells. *Nature* **2016,** *536* (7616), 312-6.
111. Nazarenko, O.; Kotyrba, M. R.; Yakunin, S.; Aebli, M.; Raino, G.; Benin, B. M.;

Worle, M.; Kovalenko, M. V., Guanidinium-Formamidinium Lead Iodide: A Layered Perovskite-Related Compound with Red Luminescence at Room Temperature. *J. Am. Chem. Soc.* **2018,** *140* (11), 3850-3853.

112. Cao, D. H.; Stoumpos, C. C.; Yokoyama, T.; Logsdon, J. L.; Song, T.-B.; Farha, O. K.; Wasielewski, M. R.; Hupp, J. T.; Kanatzidis, M. G., Thin Films and Solar Cells Based on Semiconducting Two-Dimensional Ruddlesden–Popper (CH3(CH2)3NH3)2(CH3NH3)n−1SnnI3n+1 Perovskites. *ACS Energy Lett.* **2017,** *2* (5), 982-990.
113. Zhang, X.; Wang, C.; Zhang, Y.; Zhang, X.; Wang, S.; Lu, M.; Cui, H.; Kershaw, S. V.; Yu, W. W.; Rogach, A. L., Bright Orange Electroluminescence from Lead-Free Two-Dimensional Perovskites. *ACS Energy Lett.* **2018,** *4* (1), 242-248.
114. Wang, A.; Guo, Y.; Zhou, Z.; Niu, X.; Wang, Y.; Muhammad, F.; Li, H.; Zhang, T.; Wang, J.; Nie, S.; Deng, Z., Aqueous acid-based synthesis of lead-free tin halide perovskites with near-unity photoluminescence quantum efficiency. *Chem. Sci.* **2019,** *10* (17), 4573-4579.
115. Peresh, E. Y.; Sidei, V. I.; Zubaka, O. V.; Stercho, I. P., K2(Rb2,Cs2,Tl2)TeBr6(I6) and Rb3(Cs3)Sb2(Bi2)Br9(I9) perovskite compounds. *Inorg. Mater.* **2011,** *47* (2), 208-212.
116. Giustino, F.; Snaith, H. J., Toward Lead-Free Perovskite Solar Cells. *ACS Energy Lett.* **2016,** *1* (6), 1233-1240.
117. Aleksandrov, K. S.; Beznosikov, V. V., Hierarchies of perovskite-like crystals (Review). *Phys. Solid State* **1997,** *39* (5), 695-715.
118. McCall, K. M.; Stoumpos, C. C.; Kostina, S. S.; Kanatzidis, M. G.; Wessels, B. W., Strong Electron–Phonon Coupling and Self-Trapped Excitons in the Defect Halide Perovskites A3M2I9 (A = Cs, Rb; M = Bi, Sb). *Chem. Mater.* **2017,** *29* (9), 4129-4145.
119. Timmermans, C. W. M.; Cholakh, S. O.; Blasse, G., The Luminescence of Cs3Bi2Cl9 and Cs3Sb2Cl9. *J. Solid State Chem.* **1983,** *46*, 222-233.
120. Papavassiliou, G. C.; Mousdis, G. A.; Koutselas, I. B., Some New Organic–Inorganic Hybrid Semiconductors Based on Metal Halide Units: Structural, Optical and Related Properties. *Adv. Mater. Opt. Electron.* **1999,** *9*, 265-271.
121. Wang, G. E.; Sun, C.; Wang, M. S.; Guo, G. C., Semiconducting crystalline inorganic-organic hybrid metal halide nanochains. *Nanoscale* **2020,** *12* (8), 4771-4789.
122. Duong, T.-M. H.; Nobusue, S.; Tada, H., Preparation of perovskite-derived one dimensional single crystals based on edge-shared octahedrons with pyridine derivatives. *J. Cryst. Growth* **2020,** *537*, 125577.
123. Lin, H.; Zhou, C.; Neu, J.; Zhou, Y.; Han, D.; Chen, S.; Worku, M.; Chaaban, M.; Lee, S.; Berkwits, E.; Siegrist, T.; Du, M. H.; Ma, B., Bulk Assembly of Corrugated 1D Metal Halides with Broadband Yellow Emission. *Adv. Opt. Mater.* **2019,** *7* (6), 1801474.
124. Lin, H.; Zhou, C.; Chaaban, M.; Xu, L.-J.; Zhou, Y.; Neu, J.; Worku, M.; Berkwits, E.; He, Q.; Lee, S.; Lin, X.; Siegrist, T.; Du, M.-H.; Ma, B., Bulk Assembly of Zero-Dimensional Organic Lead Bromide Hybrid with Efficient Blue Emission. *ACS Mater. Lett.* **2019,** *1* (6), 594-598.
125. Yuan, Z.; Zhou, C.; Tian, Y.; Shu, Y.; Messier, J.; Wang, J. C.; van de Burgt, L. J.; Kountouriotis, K.; Xin, Y.; Holt, E.; Schanze, K.; Clark, R.; Siegrist, T.; Ma, B., One-dimensional organic lead halide perovskites with efficient bluish white-light emission. *Nat.*

Commun. **2017,** *8*, 14051.

126. Li, D.; Wu, W.; Wang, S.; Zhang, X.; Li, L.; Yao, Y.; Peng, Y.; Luo, J., A one-dimensional dual emissive hybrid perovskite with flexibly tunable white-light emission. *J. Mater. Chem. C* **2020**.

127. Jung, M.-H., Broadband white light emission from one-dimensional zigzag edge-sharing perovskite. *New J. Chem.* **2020,** *44* (1), 171-180.

128. Yue, C.-Y.; Sun, H.-X.; Liu, Q.-X.; Wang, X.-M.; Yuan, Z.-S.; Wang, J.; Wu, J.-H.; Hu, B.; Lei, X.-W., Organic cation directed hybrid lead halides of zero-dimensional to two-dimensional structures with tunable photoluminescence properties. *Inorg. Chem. Front.* **2019,** *6* (10), 2709-2717.

129. Biswas, A.; Bakthavatsalam, R.; Shaikh, S. R.; Shinde, A.; Lohar, A.; Jena, S.; Gonnade, R. G.; Kundu, J., Efficient Broad-Band Emission from Contorted Purely Corner-Shared One Dimensional (1D) Organic Lead Halide Perovskite. *Chem. Mater.* **2019,** *31* (7), 2253-2257.

130. Peng, Y.; Yao, Y.; Li, L.; Wu, Z.; Wang, S.; Luo, J., White-light emission in a chiral one-dimensional organic–inorganic hybrid perovskite. *J. Mater. Chem. C* **2018,** *6* (22), 6033-6037.

131. Mao, L.; Guo, P.; Kepenekian, M.; Hadar, I.; Katan, C.; Even, J.; Schaller, R. D.; Stoumpos, C. C.; Kanatzidis, M. G., Structural Diversity in White-Light-Emitting Hybrid Lead Bromide Perovskites. *J. Am. Chem. Soc.* **2018,** *140* (40), 13078-13088.

132. Cai, M.; Wang, G.-E.; Yao, M.; Wu, G.; Li, Y.; Xu, G., Semiconductive 1D nanobelt iodoplumbate hybrid with high humidity response. *Inorg. Chem. Comm.* **2018,** *93*, 42-46.

133. Barkaoui, H.; Abid, H.; Yangui, A.; Triki, S.; Boukheddaden, K.; Abid, Y., Yellowish White-Light Emission Involving Resonant Energy Transfer in a New One-Dimensional Hybrid Material: (C9H10N2)PbCl4. *J. Phys. Chem. C* **2018,** *122* (42), 24253-24261.

134. Fujisawa, J.-i.; Ishihara, T., Charge-transfer transitions between wires and spacers in an inorganic-organic quasi-one-dimensional crystal methylviologen lead iodide. *Phys. Rev. B* **2004,** *70* (11).

135. Akimoto, I.; Sakai, M.; Kan'no, K., Luminescent decay kinetics in a quasi-one-dimensional crystal, C5H10NH2PbI3. *J. Lumin.* **2004,** *108* (1-4), 31-35.

136. Papavassilioua, G. C.; Mousdisa, G. A.; Raptopouloub, C. P.; Terzis, A., Preparation and Characterization of [C6H5CH2NH3]2PbI4, [C6H5CH2CH2SC(NH2)2]3PbI5 and [C10H7CH2NH3]PbI3 Organic-Inorganic Hybrid Compounds. *Z. Naturforsch.* **1999,** *54*, 1405-1409.

137. Zhou, C.; Tian, Y.; Wang, M.; Rose, A.; Besara, T.; Doyle, N. K.; Yuan, Z.; Wang, J. C.; Clark, R.; Hu, Y.; Siegrist, T.; Lin, S.; Ma, B., Low-Dimensional Organic Tin Bromide Perovskites and Their Photoinduced Structural Transformation. *Angew. Chem., Int. Ed.* **2017,** *56* (31), 9018-9022.

138. Nazarenko, O.; Kotyrba, M. R.; Yakunin, S.; Worle, M.; Benin, B. M.; Raino, G.; Krumeich, F.; Kepenekian, M.; Even, J.; Katan, C.; Kovalenko, M. V., Guanidinium and Mixed Cesium-Guanidinium Tin(II) Bromides: Effects of Quantum Confinement and Out-of-Plane Octahedral Tilting. *Chem. Mater.* **2019,** *31* (6), 2121-2129.

139. Kaltzoglou, A.; Manolis, G. K.; Elsenety, M. M.; Koutselas, I.; Psycharis, V.;

Kontos, A. G.; Falaras, P., Synthesis and Characterization of Lead-Free (CH3)3SSnI3 1-D Perovskite. *J. Electron. Mater.* **2019,** *48* (11), 7533-7538.
140. Ben Rhaiem, T.; Elleuch, S.; Boughzala, H.; Abid, Y., Synthesis, crystal structure, vibrational and optical properties of chlorometalate hybrids incorporating (DABCOH2)2+ cations. *Inorg. Chem. Comm.* **2019,** *105*, 230-239.
141. Shi, Y.; Ma, Z.; Zhao, D.; Chen, Y.; Cao, Y.; Wang, K.; Xiao, G.; Zou, B., Pressure-Induced Emission (PIE) of One-Dimensional Organic Tin Bromide Perovskites. *J. Am. Chem. Soc.* **2019,** *141* (16), 6504-6508.
142. Wells, H. L., Uber die Casium- und Kalium-Blei halogenide. *Z. Anorg. Allg. Chem.* **1893,** *3* (1), 195-210.
143. Wells, H. L., ART. XVI. - On tle Caesium- and the Potassium-Lead Halides. *Am. Chem. J.* **1892**, 121-134.
144. M0LLER, C. K., Crystal Structure and Photoconductivity of Caesium Plumbohalides. *Nature* **1958,** *152*, 1436.
145. MØLLER, C. K., Electrochemical Investigation of the transition from tetragonal to cubic ceasium plumbo chloride. *Mat. Fys. Medd. Dan. Vid. Selsk* **1960,** *32* (15).
146. Møller, C. K., The Structure Of Perovskite-Like Cæsium Plumbo Trihalides. *Mat. Fys. Medd. Dan. Vid. Selsk* **1959,** *32* (2).
147. Møller, C. K., On The Structure Of Cæsiumhexahalogeno-Plumbates (Ii). *Mat. Fys. Medd. Dan. Vid. Selsk* **1960,** *32* (3).
148. Donaldson, J. D.; Grimsey; Clark, S. J., MÖssbauer Evidence for the Direct Population of Solid-State Bands by the Non-Bonding Electron Pairs in High Symmetry Tin (Ii) Antimony (Iii) and Tellurium (Iv) Compounds. *J. Phys. Colloq.* **1979,** *40* (C2), C2-389-C2-391.
149. Andrews, R. H.; Clark, S. J.; Donaldson, J. D.; Dewan, J. C.; Silver, J., Solid-state Properties of Materials of the Type Cs4MXs (where M = Sn or Pb and X = CI or Br). *J. Chem. Soc. Dalton Trans.* **1983,** (4), 767-770.
150. Wernicke, R.; Kupka, H.; Ensslin, W.; Schmidtke, H.-H., Low Temperature Luminescence Spectra Of The d10s2 Complexes C2mx6 (M=Se,Te Andx=Cl,Br). The Jahn-Teller Effect In The I'z(3t1u) Excited State. *Chem. Phys.* **1980,** *47*, 235-244.
151. Blasse, G.; Dirksen, G. J.; Abriel, W., The Influence Of Distortion Of The Te(IV) Coordination Octahedron On Its Luminescence. *Chem. Phys. Lett.* **1987,** *136* (5), 460-464.
152. Meidenbauer, K.; Gliemann, G., Effects of Temperature and Magnetic Fields on the Luminescence of Single Crystal (NH4)2TeCl6. *Z. Naturforsch.* **1988,** *43a*, 555-560.
153. Schmidtke, H.; Krause, B.; Schonherr, T., Optical Spectra of Hexahabgeno-Antimony(II1) Complex Compounds. *Ber. Bunsen-Ges.* **1990,** *94*, 700-703.
154. Blasse, G.; Grabmaier, B. C., *Luminescent Materials*. Springer-Verlag: Germany, 1994.
155. Vovna, V. I.; Dotsenko, A. A.; Korochentsev, V. V.; Shcheka, O. L.; Os'mushko, I. S.; Mirochnik, A. G.; Sedakova, T. V.; Sergienko, V. I., Electronic structure and luminescence of antimony (III) halide complexes with N,N′-diphenylguanidine. *J. Mol. Struct.* **2015,** *1091*, 138-146.
156. Wang, Z. P.; Wang, J. Y.; Li, J. R.; Feng, M. L.; Zou, G. D.; Huang, X. Y., [Bmim]2SbCl5: a main group metal-containing ionic liquid exhibiting tunable

photoluminescence and white-light emission. *Chem. Commun.* **2015,** *51* (15), 3094-7.
157. McCall, K. M.; Morad, V.; Benin, B. M.; Kovalenko, M., Efficient Lone Pair-Driven Luminescence: Structure-Property Relationships in Emissive 5s2 Metal Halides. *ACS Mater. Lett.* **2020,** *Accepted*.
158. Li, J.; Stoumpos, C. C.; Trimarchi, G. G.; Chung, I.; Mao, L.; Chen, M.; Wasielewski, M. R.; Wang, L.; Kanatzidis, M. G., Air-Stable Direct Bandgap Perovskite Semiconductors: All-Inorganic Tin-Based Heteroleptic Halides AxSnClyIz (A = Cs, Rb). *Chem. Mater.* **2018,** *30* (14), 4847-4856.
159. Ng, S. W.; Zuckerman, J. J., Where Are the Lone-Pair Electrons in Subvalent Fourth-Group Compounds? **1985,** *29*, 297-325.
160. Donaldson, J. D.; Grimes, S. M., Lone Pair Effects in Tin(II) Chemistry. In *Reviews on Silicon, Germanium, Tin and Lead, Compounds*, Gielen, M., Ed. Freund Publishing House Ltd.: Israel, 1984; Vol. 8, pp 1-132.
161. Zhou, C.; Lin, H.; Tian, Y.; Yuan, Z.; Clark, R.; Chen, B.; van de Burgt, L. J.; Wang, J. C.; Zhou, Y.; Hanson, K.; Meisner, Q. J.; Neu, J.; Besara, T.; Siegrist, T.; Lambers, E.; Djurovich, P.; Ma, B., Luminescent zero-dimensional organic metal halide hybrids with near-unity quantum efficiency. *Chem. Sci.* **2018,** *9* (3), 586-593.
162. Yunakova, O. N.; Miloslavskii, V. K.; Kovalenko, E. N., Exciton absorption spectrum of thin CsPbI3 and Cs4PbI6 films. *Opt. Spectrosc.* **2012,** *112* (1), 91-96.
163. Nikl, M.; Mhokova, E.; Nitsch, K., Photoluminescence & Decay Kinetics Of Cs_4PbCl_6 Single Crystals. *Solid State Commun.* **1992,** *84* (12), 1089-1092.
164. Nikl, M.; Mihokova, E.; Nitsch, K.; Somma, F.; Giampaolo, C.; Pazzi, G. P.; Fabeni, P.; Zazubovich, S., Photoluminescence of Cs PbBr crystals and thin films. *Chem. Phys. Lett.* **1999,** *306*, 280-284.
165. Kondo, S.; Amaya, K.; Higuchi, S.; Saito, T.; Asada, H.; Ishikane, M., Fundamental optical absorption of Cs4PbCl6. *Solid State Commun.* **2001,** *120*, 141-144.
166. Kondo, S.; Masaki, A.; Saito, T.; Asada, H., Fundamental optical absorption of CsPbI3 and Cs4PbI6. *Solid State Commun.* **2002,** *124*, 211-214.
167. Yunakova, O. N.; Miloslavsky, V. K.; Kovalenko, E. N.; Kovalenko, V. V., Exciton absorption spectrum of Cs4PbCl6 thin films. *Funct. Mater.* **2015,** *22* (2), 175-180.
168. Saidaminov, M. I.; Mohammed, O. F.; Bakr, O. M., Low-Dimensional-Networked Metal Halide Perovskites: The Next Big Thing. *ACS Energy Lett.* **2017,** *2* (4), 889-896.
169. Akkerman, Q. A.; Park, S.; Radicchi, E.; Nunzi, F.; Mosconi, E.; De Angelis, F.; Brescia, R.; Rastogi, P.; Prato, M.; Manna, L., Nearly Monodisperse Insulator Cs4PbX6 (X = Cl, Br, I) Nanocrystals, Their Mixed Halide Compositions, and Their Transformation into CsPbX3 Nanocrystals. *Nano Lett.* **2017,** *17* (3), 1924-1930.
170. Akkerman, Q. A.; Abdelhady, A. L.; Manna, L., Zero-Dimensional Cesium Lead Halides: History, Properties, and Challenges. *J. Phys. Chem. Lett.* **2018,** *9* (9), 2326-2337.
171. Riesen, N.; Lockrey, M.; Badek, K.; Riesen, H., On the origins of the green luminescence in the "zero-dimensional perovskite" Cs4PbBr6: conclusive results from cathodoluminescence imaging. *Nanoscale* **2019,** *11* (9), 3925-3932.
172. Morad, V.; Shynkarenko, Y.; Yakunin, S.; Brumberg, A.; Schaller, R. D.; Kovalenko, M. V., Disphenoidal Zero-Dimensional Lead, Tin, and Germanium Halides: Highly Emissive Singlet and Triplet Self-Trapped Excitons and X-ray Scintillation. *J. Am.*

Chem. Soc. **2019,** *141* (25), 9764-9768.
173. Palazon, F.; Almeida, G.; Akkerman, Q. A.; De Trizio, L.; Dang, Z.; Prato, M.; Manna, L., Changing the Dimensionality of Cesium Lead Bromide Nanocrystals by Reversible Postsynthesis Transformations with Amines. *Chem. Mater.* **2017,** *29* (10), 4167-4171.
174. Xie, J. L.; Huang, Z. Q.; Wang, B.; Chen, W. J.; Lu, W. X.; Liu, X.; Song, J. L., New lead-free perovskite Rb7Bi3Cl16 nanocrystals with blue luminescence and excellent moisture-stability. *Nanoscale* **2019,** *11* (14), 6719-6726.
175. Yang, H.; Cai, T.; Liu, E.; Hills-Kimball, K.; Gao, J.; Chen, O., Synthesis and transformation of zero-dimensional Cs3BiX6 (X = Cl, Br) perovskite-analogue nanocrystals. *Nano Res.* **2019,** *13* (1), 282-291.
176. Lee, D.; Kim, M.; Woo, H.-Y.; Chae, J.; Lee, D.; Jeon, S.; Oh, S. J.; Paik, T., Heating-up synthesis of cesium bismuth bromide perovskite nanocrystals with tailored composition, morphology, and optical properties. *RSC Adv.* **2020,** *10* (12), 7126-7133.
177. Creutz, S. E.; Liu, H.; Kaiser, M. E.; Li, X.; Gamelin, D. R., Structural Diversity in Cesium Bismuth Halide Nanocrystals. *Chem. Mater.* **2019,** *31* (13), 4685-4697.
178. Tan, L.; Wang, W.; Li, Q.; Luo, Z.; Zou, C.; Tang, M.; Zhang, L.; He, J.; Quan, Z., Colloidal syntheses of zero-dimensional Cs4SnX6 (X = Br, I) nanocrystals with high emission efficiencies. *Chem. Commun.* **2020,** *56* (3), 387-390.
179. Chiara, R.; Ciftci, Y. O.; Queloz, V. I. E.; Nazeeruddin, M. K.; Grancini, G.; Malavasi, L., Green-Emitting Lead-Free Cs4SnBr6 Zero-Dimensional Perovskite Nanocrystals with Improved Air Stability. *J. Phys. Chem. Lett.* **2020,** *11* (3), 618-623.
180. McCall, K. M.; Stoumpos, C. C.; Kontsevoi, O. Y.; Alexander, G. C. B.; Wessels, B. W.; Kanatzidis, M. G., From 0D Cs3Bi2I9 to 2D Cs3Bi2I6Cl3: Dimensional Expansion Induces a Direct Band Gap but Enhances Electron–Phonon Coupling. *Chem. Mater.* **2019,** *31* (7), 2644-2650.
181. Saparov, B.; Hong, F.; Sun, J.-P.; Duan, H.-S.; Meng, W.; Cameron, S.; Hill, I. G.; Yan, Y.; Mitzi, D. B., Thin-Film Preparation and Characterization of Cs3Sb2I9: A Lead-Free Layered Perovskite Semiconductor. *Chem. Mater.* **2015,** *27* (16), 5622-5632.
182. Adonin, S. A.; Sokolov, M. N.; Fedin, V. P., Polynuclear halide complexes of Bi(III): From structural diversity to the new properties. *Coord. Chem. Rev.* **2016,** *312*, 1-21.
183. Zhou, C.; Lin, H.; Worku, M.; Neu, J.; Zhou, Y.; Tian, Y.; Lee, S.; Djurovich, P.; Siegrist, T.; Ma, B., Blue Emitting Single Crystalline Assembly of Metal Halide Clusters. *J. Am. Chem. Soc.* **2018,** *140* (41), 13181-13184.
184. Garcia-Fernandez, A.; Marcos-Cives, I.; Platas-Iglesias, C.; Castro-Garcia, S.; Vazquez-Garcia, D.; Fernandez, A.; Sanchez-Andujar, M., Diimidazolium Halobismuthates [Dim]2[Bi2X10] (X = Cl(-), Br(-), or I(-)): A New Class of Thermochromic and Photoluminescent Materials. *Inorg. Chem.* **2018,** *57* (13), 7655-7664.
185. Zhou, J.; Li, M.; Ning, L.; Zhang, R.; Molokeev, M. S.; Zhao, J.; Yang, S.; Han, K.; Xia, Z., Broad-Band Emission in a Zero-Dimensional Hybrid Organic [PbBr6] Trimer with Intrinsic Vacancies. *J. Phys. Chem. Lett.* **2019,** *10* (6), 1337-1341.
186. Lee, S.; Zhou, C.; Neu, J.; Beery, D.; Arcidiacono, A.; Chaaban, M.; Lin, H.; Gaiser, A.; Chen, B.; Albrecht-Schmitt, T. E.; Siegrist, T.; Ma, B., Bulk Assemblies of Lead Bromide Trimer Clusters with Geometry-Dependent Photophysical Properties. *Chem.*

Mater. **2019,** *32* (1), 374-380.
187. Chen, M.; Ju, M.-G.; Carl, A. D.; Zong, Y.; Grimm, R. L.; Gu, J.; Zeng, X. C.; Zhou, Y.; Padture, N. P., Cesium Titanium(IV) Bromide Thin Films Based Stable Lead-free Perovskite Solar Cells. *Joule* **2018,** *2* (3), 558-570.
188. Lee, B.; Stoumpos, C. C.; Zhou, N.; Hao, F.; Malliakas, C.; Yeh, C. Y.; Marks, T. J.; Kanatzidis, M. G.; Chang, R. P., Air-stable molecular semiconducting iodosalts for solar cell applications: Cs2SnI6 as a hole conductor. *J. Am. Chem. Soc.* **2014,** *136* (43), 15379-85.
189. Saparov, B.; Sun, J.-P.; Meng, W.; Xiao, Z.; Duan, H.-S.; Gunawan, O.; Shin, D.; Hill, I. G.; Yan, Y.; Mitzi, D. B., Thin-Film Deposition and Characterization of a Sn-Deficient Perovskite Derivative Cs2SnI6. *Chem. Mater.* **2016,** *28* (7), 2315-2322.
190. Kaltzoglou, A.; Antoniadou, M.; Kontos, A. G.; Stoumpos, C. C.; Perganti, D.; Siranidi, E.; Raptis, V.; Trohidou, K.; Psycharis, V.; Kanatzidis, M. G.; Falaras, P., Optical-Vibrational Properties of the Cs2SnX6 (X = Cl, Br, I) Defect Perovskites and Hole-Transport Efficiency in Dye-Sensitized Solar Cells. *J. Phys. Chem. C* **2016,** *120* (22), 11777-11785.
191. Park, B. W.; Philippe, B.; Zhang, X.; Rensmo, H.; Boschloo, G.; Johansson, E. M., Bismuth Based Hybrid Perovskites A3Bi2 I9 (A: Methylammonium or Cesium) for Solar Cell Application. *Adv. Mater.* **2015,** *27* (43), 6806-13.
192. Lyu, M.; Yun, J.-H.; Cai, M.; Jiao, Y.; Bernhardt, P. V.; Zhang, M.; Wang, Q.; Du, A.; Wang, H.; Liu, G.; Wang, L., Organic–inorganic bismuth (III)-based material: A lead-free, air-stable and solution-processable light-absorber beyond organolead perovskites. *Nano Res.* **2016,** *9* (3), 692-702.
193. Harikesh, P. C.; Mulmudi, H. K.; Ghosh, B.; Goh, T. W.; Teng, Y. T.; Thirumal, K.; Lockrey, M.; Weber, K.; Koh, T. M.; Li, S.; Mhaisalkar, S.; Mathews, N., Rb as an Alternative Cation for Templating Inorganic Lead-Free Perovskites for Solution Processed Photovoltaics. *Chem. Mater.* **2016,** *28* (20), 7496-7504.
194. Hebig, J.-C.; Kühn, I.; Flohre, J.; Kirchartz, T., Optoelectronic Properties of (CH3NH3)3Sb2I9 Thin Films for Photovoltaic Applications. *ACS Energy Lett.* **2016,** *1* (1), 309-314.
195. Singh, T.; Kulkarni, A.; Ikegami, M.; Miyasaka, T., Effect of Electron Transporting Layer on Bismuth-Based Lead-Free Perovskite (CH3NH3)3 Bi2I9 for Photovoltaic Applications. *ACS Appl. Mater. Interfaces* **2016,** *8* (23), 14542-7.
196. Sakai, N.; Haghighirad, A. A.; Filip, M. R.; Nayak, P. K.; Nayak, S.; Ramadan, A.; Wang, Z.; Giustino, F.; Snaith, H. J., Solution-Processed Cesium Hexabromopalladate(IV), Cs2PdBr6, for Optoelectronic Applications. *J. Am. Chem. Soc.* **2017,** *139* (17), 6030-6033.
197. Zhou, C.; Tian, Y.; Yuan, Z.; Lin, H.; Chen, B.; Clark, R.; Dilbeck, T.; Zhou, Y.; Hurley, J.; Neu, J.; Besara, T.; Siegrist, T.; Djurovich, P.; Ma, B., Highly Efficient Broadband Yellow Phosphor Based on Zero-Dimensional Tin Mixed-Halide Perovskite. *ACS Appl. Mater. Interfaces* **2017,** *9* (51), 44579-44583.
198. Fu, P.; Huang, M.; Shang, Y.; Yu, N.; Zhou, H. L.; Zhang, Y. B.; Chen, S.; Gong, J.; Ning, Z., Organic-Inorganic Layered and Hollow Tin Bromide Perovskite with Tunable Broadband Emission. *ACS Appl. Mater. Interfaces* **2018,** *10* (40), 34363-34369.
199. Jing, Y.; Liu, Y.; Jiang, X.; Molokeev, M. S.; Lin, Z.; Xia, Z., Sb3+ Dopant and Halogen Substitution Triggered Highly Efficient and Tunable Emission in Lead-Free Metal

Halide Single Crystals. *Chem. Mater.* **2020**.
200. Lin, Y. C.; Karlsson, M.; Bettinelli, M., Inorganic Phosphor Materials for Lighting. *Top. Curr. Chem.* **2016,** *374* (2), 21.
201. George, N. C.; Denault, K. A.; Seshadri, R., Phosphors for Solid-State White Lighting. *Annu. Rev. Mater. Res.* **2013,** *43* (1), 481-501.
202. Muthu, S.; Schuurmans, F. J.; Pashley, M. D., Red, green, and blue LED based white light generation: issues and control. **2002,** *1*, 327-333.
203. Cho, J.; Park, J. H.; Kim, J. K.; Schubert, E. F., White light-emitting diodes: History, progress, and future. *Laser Photonics Rev.* **2017,** *11* (2), 1600147.
204. Pust, P.; Weiler, V.; Hecht, C.; Tucks, A.; Wochnik, A. S.; Henss, A. K.; Wiechert, D.; Scheu, C.; Schmidt, P. J.; Schnick, W., Narrow-band red-emitting Sr[LiAl(3)N(4)]:Eu(2)(+) as a next-generation LED-phosphor material. *Nat. Mater.* **2014,** *13* (9), 891-6.
205. Lustig, W. P.; Shen, Z.; Teat, S. J.; Javed, N.; Velasco, E.; O'Carroll, D. M.; Li, J., Rational design of a high-efficiency, multivariate metal–organic framework phosphor for white LED bulbs. *Chem. Sci.* **2020,** *11* (7), 1814-1824.
206. Tähkämö, L.; Dillon, H., Life Cycle of Lighting Technologies. **2014**, 1-18.
207. Yang, T. H.; Huang, H. Y.; Sun, C. C.; Glorieux, B.; Lee, X. H.; Yu, Y. W.; Chung, T. Y., Noncontact and instant detection of phosphor temperature in phosphor-converted white LEDs. *Sci. Rep.* **2018,** *8* (1), 296.
208. Volker Bachmann; Ronda, C.; Meijerink, A., Temperature Quenching of Yellow Ce3+ Luminescence in YAG:Ce. *Chem. Mater.* **2009,** *21* (10), 2077-2084.
209. Mitzi, D. B.; Liang, K.; Wang, S., Synthesis and Characterization of $[NH_2C(I)=NH_2]_2ASnI_5$ with A = Iodoformamidinium or Formamidinium: The Chemistry of Cyanamide and Tin(II) Iodide in Concentrated Aqueous Hydriodic Acid Solutions. *Inorg. Chem.* **1998,** *37*, 321-327.
210. Kunkely, H.; Vogler, A., Optical properties of silver(I) hexafluoroantimonate(V): luminescence from a metal-to-metal charge transfer state involving a transition and a main group metal. *Inorg. Chem. Comm.* **2004,** *7* (3), 400-401.
211. Mao, L.; Tsai, H.; Nie, W.; Ma, L.; Im, J.; Stoumpos, C. C.; Malliakas, C. D.; Hao, F.; Wasielewski, M. R.; Mohite, A. D.; Kanatzidis, M. G., Role of Organic Counterion in Lead- and Tin-Based Two-Dimensional Semiconducting Iodide Perovskites and Application in Planar Solar Cells. *Chem. Mater.* **2016,** *28* (21), 7781-7792.
212. Stoumpos, C. C.; Cao, D. H.; Clark, D. J.; Young, J.; Rondinelli, J. M.; Jang, J. I.; Hupp, J. T.; Kanatzidis, M. G., Ruddlesden–Popper Hybrid Lead Iodide Perovskite 2D Homologous Semiconductors. *Chem. Mater.* **2016,** *28* (8), 2852-2867.
213. Mao, L.; Wu, Y.; Stoumpos, C. C.; Traore, B.; Katan, C.; Even, J.; Wasielewski, M. R.; Kanatzidis, M. G., Tunable White-Light Emission in Single-Cation-Templated Three-Layered 2D Perovskites (CH3CH2NH3)4Pb3Br10-xClx. *J. Am. Chem. Soc.* **2017,** *139* (34), 11956-11963.
214. Mao, L.; Wu, Y.; Stoumpos, C. C.; Wasielewski, M. R.; Kanatzidis, M. G., White-Light Emission and Structural Distortion in New Corrugated Two-Dimensional Lead Bromide Perovskites. *J. Am. Chem. Soc.* **2017,** *139* (14), 5210-5215.
215. Soe, C. M. M.; Stoumpos, C. C.; Kepenekian, M.; Traore, B.; Tsai, H.; Nie, W.;

Wang, B.; Katan, C.; Seshadri, R.; Mohite, A. D.; Even, J.; Marks, T. J.; Kanatzidis, M. G., New Type of 2D Perovskites with Alternating Cations in the Interlayer Space, $(C(NH_2)_3)(CH_3NH_3)_nPb_nI_{3n+1}$: Structure, Properties, and Photovoltaic Performance. *J. Am. Chem. Soc.* **2017,** *139* (45), 16297-16309.

216. Stoumpos, C. C.; Mao, L.; Malliakas, C. D.; Kanatzidis, M. G., Structure-Band Gap Relationships in Hexagonal Polytypes and Low-Dimensional Structures of Hybrid Tin Iodide Perovskites. *Inorg. Chem.* **2017,** *56* (1), 56-73.
217. Lin, H.; Zhou, C.; Tian, Y.; Siegrist, T.; Ma, B., Low-Dimensional Organometal Halide Perovskites. *ACS Energy Lett.* **2017,** *3* (1), 54-62.
218. Green, M. A.; Ho-Baillie, A.; Snaith, H. J., The emergence of perovskite solar cells. *Nat. Photonics* **2014,** *8* (7), 506-514.
219. Manser, J. S.; Christians, J. A.; Kamat, P. V., Intriguing Optoelectronic Properties of Metal Halide Perovskites. *Chem. Rev.* **2016,** *116* (21), 12956-13008.
220. Hu, X.; Zhang, X.; Liang, L.; Bao, J.; Li, S.; Yang, W.; Xie, Y., High-Performance Flexible Broadband Photodetector Based on Organolead Halide Perovskite. *Adv. Funct. Mater.* **2014,** *24* (46), 7373-7380.
221. Yakunin, S.; Sytnyk, M.; Kriegner, D.; Shrestha, S.; Richter, M.; Matt, G. J.; Azimi, H.; Brabec, C. J.; Stangl, J.; Kovalenko, M. V.; Heiss, W., Detection of X-ray photons by solution-processed lead halide perovskites. *Nat. Photonics* **2015,** *9* (7), 444-449.
222. Yaffe, O.; Guo, Y.; Tan, L. Z.; Egger, D. A.; Hull, T.; Stoumpos, C. C.; Zheng, F.; Heinz, T. F.; Kronik, L.; Kanatzidis, M. G.; Owen, J. S.; Rappe, A. M.; Pimenta, M. A.; Brus, L. E., Local Polar Fluctuations in Lead Halide Perovskite Crystals. *Phys. Rev. Lett.* **2017,** *118* (13), 136001.
223. Miyata, K.; Atallah, T. L.; Zhu, X.-Y., Lead halide perovskites: Crystal-liquid duality, phonon glass electron crystals, and large polaron formation. *Sci. Adv.* **2017,** *3*, e1701469.
224. Schmidt, L. C.; Pertegas, A.; Gonzalez-Carrero, S.; Malinkiewicz, O.; Agouram, S.; Minguez Espallargas, G.; Bolink, H. J.; Galian, R. E.; Perez-Prieto, J., Nontemplate synthesis of CH3NH3PbBr3 perovskite nanoparticles. *J. Am. Chem. Soc.* **2014,** *136* (3), 850-3.
225. Akkerman, Q. A.; Motti, S. G.; Srimath Kandada, A. R.; Mosconi, E.; D'Innocenzo, V.; Bertoni, G.; Marras, S.; Kamino, B. A.; Miranda, L.; De Angelis, F.; Petrozza, A.; Prato, M.; Manna, L., Solution Synthesis Approach to Colloidal Cesium Lead Halide Perovskite Nanoplatelets with Monolayer-Level Thickness Control. *J. Am. Chem. Soc.* **2016,** *138* (3), 1010-6.
226. Huang, H.; Xue, Q.; Chen, B.; Xiong, Y.; Schneider, J.; Zhi, C.; Zhong, H.; Rogach, A. L., Top-Down Fabrication of Stable Methylammonium Lead Halide Perovskite Nanocrystals by Employing a Mixture of Ligands as Coordinating Solvents. *Angew. Chem., Int. Ed.* **2017,** *56* (32), 9571-9576.
227. Kang, B.; Biswas, K., Carrier Self-trapping and Luminescence in Intrinsically Activated Scintillator: Cesium Hafnium Chloride (Cs2HfCl6). *J. Phys. Chem. C* **2016,** *120* (22), 12187-12195.
228. Král, R.; Babin, V.; Mihóková, E.; Buryi, M.; Laguta, V. V.; Nitsch, K.; Nikl, M., Luminescence and Charge Trapping in Cs2HfCl6Single Crystals: Optical and Magnetic

Resonance Spectroscopy Study. *J. Phys. Chem. C* **2017,** *121* (22), 12375-12382.
229. Saeki, K.; Fujimoto, Y.; Koshimizu, M.; Nakauchi, D.; Tanaka, H.; Yanagida, T.; Asai, K., Luminescence and scintillation properties of Cs2HfBr6 and Cs2ZrBr6 crystals. *Jpn. J. Appl. Phys.* **2018,** *57* (3), 030310.
230. Nikl, M.; Mihokova, E.; Nitsch, K.; Somma, F.; Giampaolo, C.; Pazzi, G. P.; Fabeni, P.; Zazubovich, S., Photoluminescence of Cs4PbBr6 crystals and thin films. *Chem. Phys. Lett.* **1999,** *306*, 280–284.
231. Sedakova, T. V.; Mirochnik, A. G.; Karasev, V. E., Structure and luminescence properties of tellurium(IV) complex compounds. *Opt. Spectrosc.* **2011,** *110* (5), 755-761.
232. Bukvetskii, B. V.; Sedakova, T. V.; Mirochnik, A. G., Crystal structure and luminescence and thermochromic properties of bis-1,10-phenanthrolinium hexachlorotellurate(IV). *Russ. J. Coord. Chem.* **2012,** *38* (2), 106-110.
233. Sedakova, T. V.; Mirochnik, A. G.; Karasev, V. E., Structure and luminescence properties of antimony(III) complex compounds. *Opt. Spectrosc.* **2008,** *105* (4), 517-523.
234. Zhou, C.; Worku, M.; Neu, J.; Lin, H.; Tian, Y.; Lee, S.; Zhou, Y.; Han, D.; Chen, S.; Hao, A.; Djurovich, P. I.; Siegrist, T.; Du, M.-H.; Ma, B., Facile Preparation of Light Emitting Organic Metal Halide Crystals with Near-Unity Quantum Efficiency. *Chem. Mater.* **2018,** *30* (7), 2374-2378.
235. Elfaleh, N.; Kamoun, S., Structural characterization, vibrational studies and optical properties of a new luminescent organic-inorganic material [C 6 H 20 N 3]BiI 6 ·H 2 O. *J. Organomet. Chem.* **2016,** *819*, 95-102.
236. Myagkota, S. V.; Savchin, P. V.; Voloshinovskiĭ, A. S.; Demkiv, T. M.; Boĭko, Y. V.; Vus, R. S.; Demkiv, L. S., Luminescence properties of the CsSnBr3 phase in metastable Cs4SnBr6. *Phys. Solid State* **2008,** *50* (8), 1473-1476.
237. Hu, M.; Ge, C.; Yu, J.; Feng, J., Mechanical and Optical Properties of Cs4BX6 (B = Pb, Sn; X = Cl, Br, I) Zero-Dimension Perovskites. *J. Phys. Chem. C* **2017,** *121* (48), 27053-27058.
238. Jellicoe, T. C.; Richter, J. M.; Glass, H. F.; Tabachnyk, M.; Brady, R.; Dutton, S. E.; Rao, A.; Friend, R. H.; Credgington, D.; Greenham, N. C.; Bohm, M. L., Synthesis and Optical Properties of Lead-Free Cesium Tin Halide Perovskite Nanocrystals. *J. Am. Chem. Soc.* **2016,** *138* (9), 2941-4.
239. Wang, A.; Guo, Y.; Muhammad, F.; Deng, Z., Controlled Synthesis of Lead-Free Cesium Tin Halide Perovskite Cubic Nanocages with High Stability. *Chem. Mater.* **2017,** *29* (15), 6493-6501.
240. Thirumal, K.; Chong, W. K.; Xie, W.; Ganguly, R.; Muduli, S. K.; Sherburne, M.; Asta, M.; Mhaisalkar, S.; Sum, T. C.; Soo, H. S.; Mathews, N., Morphology-Independent Stable White-Light Emission from Self-Assembled Two-Dimensional Perovskites Driven by Strong Exciton–Phonon Coupling to the Organic Framework. *Chem. Mater.* **2017,** *29* (9), 3947-3953.
241. Smith, M. D.; Watson, B. L.; Dauskardt, R. H.; Karunadasa, H. I., Broadband Emission with a Massive Stokes Shift from Sulfonium Pb–Br Hybrids. *Chem. Mater.* **2017,** *29* (17), 7083-7087.
242. Zhou, C.; Lin, H.; Shi, H.; Tian, Y.; Pak, C.; Shatruk, M.; Zhou, Y.; Djurovich, P.; Du, M. H.; Ma, B., A Zero-Dimensional Organic Seesaw-Shaped Tin Bromide with Highly

Efficient Strongly Stokes-Shifted Deep-Red Emission. *Angew. Chem., Int. Ed.* **2018,** *57* (4), 1021-1024.
243. Kang, B.; Biswas, K., Exploring Polaronic, Excitonic Structures and Luminescence in Cs4PbBr6/CsPbBr3. *J. Phys. Chem. Lett.* **2018,** *9* (4), 830-836.
244. Lahiri, B. B.; Bagavathiappan, S.; Jayakumar, T.; Philip, J., Medical applications of infrared thermography: A review. *Infrared Phys. Technol.* **2012,** *55* (4), 221-235.
245. Jones, H. G.; Serraj, R.; Loveys, B. R.; Xiong, L. Z.; Wheaton, A.; Price, A. H., Thermal infrared imaging of crop canopies for the remote diagnosis and quantification of plant responses to water stress in the field. *Funct. Plant Biol.* **2009,** *36* (10-11), 978-989.
246. Bagavathiappan, S.; Lahiri, B. B.; Saravanan, T.; Philip, J.; Jayakumar, T., Infrared thermography for condition monitoring – A review. *Infrared Phys. Technol.* **2013,** *60*, 35-55.
247. Tang, X.; Ackerman, M. M.; Guyot-Sionnest, P., Thermal Imaging with Plasmon Resonance Enhanced HgTe Colloidal Quantum Dot Photovoltaic Devices. *ACS Nano* **2018,** *12* (7), 7362-7370.
248. Lhuillier, E.; Keuleyan, S.; Rekemeyer, P.; Guyot-Sionnest, P., Thermal properties of mid-infrared colloidal quantum dot detectors. *J. Appl. Phys.* **2011,** *110* (3), 033110.
249. Rogalski, A., Progress in focal plane array technologies. *Prog. Quantum Electron.* **2012,** *36* (2-3), 342-473.
250. Peterson, B. J., Infrared imaging video bolometer. *Rev. Sci. Instrum.* **2000,** *71* (10), 3696.
251. Mykhaylyk, V. B.; Wagner, A.; Kraus, H., Non-contact luminescence lifetime cryothermometry for macromolecular crystallography. *J. Synchrotron Radiat.* **2017,** *24* (Pt 3), 636-645.
252. Allison, S. W.; Gillies, G. T., Remote thermometry with thermographic phosphors: Instrumentation and applications. *Rev. Sci. Instrum.* **1997,** *68* (7), 2615-2650.
253. Marciniak, L.; Prorok, K.; Frances-Soriano, L.; Perez-Prieto, J.; Bednarkiewicz, A., A broadening temperature sensitivity range with a core-shell YbEr@YbNd double ratiometric optical nanothermometer. *Nanoscale* **2016,** *8* (9), 5037-42.
254. Salem, M.; Staude, S.; Bergmann, U.; Atakan, B., Heat flux measurements in stagnation point methane/air flames with thermographic phosphors. *Exp. Fluids* **2010,** *49* (4), 797-807.
255. Alaruri, S. D.; Brewington, A. J.; Thomas, M. A.; Miller, J. A., High-temperature remote thermometry using laser-induced fluorescence decay lifetime measurements of Y_2O_3:Eu and YAG:Tb thermographic phosphors. *IEEE T. Instrum. Meas.* **1993,** *42* (3), 735-739.
256. Brübach, J.; Pflitsch, C.; Dreizler, A.; Atakan, B., On surface temperature measurements with thermographic phosphors: A review. *Prog. Energy Combust. Sci.* **2013,** *39* (1), 37-60.
257. Wang, X. D.; Wolfbeis, O. S.; Meier, R. J., Luminescent probes and sensors for temperature. *Chem. Soc. Rev.* **2013,** *42* (19), 7834-69.
258. Brübach, J.; Kissel, T.; Frotscher, M.; Euler, M.; Albert, B.; Dreizler, A., A survey of phosphors novel for thermography. *J. Lumin.* **2011,** *131* (4), 559-564.
259. Sun, T.; Zhang, Z. Y.; Grattan, K. T. V.; Palmer, A. W.; Collins, S. F., Temperature

dependence of the fluorescence lifetime in Pr3+:ZBLAN glass for fiber optic thermometry. *Rev. Sci. Instrum.* **1997,** *68* (9), 3447-3451.

260. Okabe, K.; Inada, N.; Gota, C.; Harada, Y.; Funatsu, T.; Uchiyama, S., Intracellular temperature mapping with a fluorescent polymeric thermometer and fluorescence lifetime imaging microscopy. *Nat. Commun.* **2012,** *3*, 705.
261. Abram, C.; Fond, B.; Beyrau, F., Temperature measurement techniques for gas and liquid flows using thermographic phosphor tracer particles. *Prog. Energy Combust. Sci.* **2018,** *64*, 93-156.
262. Bhandari, A.; Barsi, C.; Raskar, R., Blind and reference-free fluorescence lifetime estimation via consumer time-of-flight sensors. *Optica* **2015,** *2* (11), 965.
263. Li, D. D.; Ameer-Beg, S.; Arlt, J.; Tyndall, D.; Walker, R.; Matthews, D. R.; Visitkul, V.; Richardson, J.; Henderson, R. K., Time-domain fluorescence lifetime imaging techniques suitable for solid-state imaging sensor arrays. *Sensors* **2012,** *12* (5), 5650-69.
264. Quintero-Bermudez, R.; Gold-Parker, A.; Proppe, A. H.; Munir, R.; Yang, Z.; Kelley, S. O.; Amassian, A.; Toney, M. F.; Sargent, E. H., Compositional and orientational control in metal halide perovskites of reduced dimensionality. *Nat. Mater.* **2018,** *17* (10), 900-907.
265. Kim, H. S.; Lee, C. R.; Im, J. H.; Lee, K. B.; Moehl, T.; Marchioro, A.; Moon, S. J.; Humphry-Baker, R.; Yum, J. H.; Moser, J. E.; Gratzel, M.; Park, N. G., Lead iodide perovskite sensitized all-solid-state submicron thin film mesoscopic solar cell with efficiency exceeding 9%. *Sci. Rep.* **2012,** *2*, 591.
266. Hao, F.; Stoumpos, C. C.; Cao, D. H.; Chang, R. P. H.; Kanatzidis, M. G., Lead-free solid-state organic–inorganic halide perovskite solar cells. *Nat. Photonics* **2014,** *8* (6), 489-494.
267. Tan, H.; Jain, A.; Voznyy, O.; Lan, X.; García de Arquer, F. P.; Fan, J. Z.; Quintero-Bermudez, R.; Yuan, M.; Zhang, B.; Zhao, Y.; Fan, F.; Li, P.; Quan, L. N.; Zhao, Y.; Lu, Z.-H.; Yang, Z.; Hoogland, S.; Sargent, E. H., Efficient and stable solution-processed planar perovskite solar cells via contact passivation. *Science* **2017,** *355* (6326), 722-726.
268. He, Y.; Matei, L.; Jung, H. J.; McCall, K. M.; Chen, M.; Stoumpos, C. C.; Liu, Z.; Peters, J. A.; Chung, D. Y.; Wessels, B. W.; Wasielewski, M. R.; Dravid, V. P.; Burger, A.; Kanatzidis, M. G., High spectral resolution of gamma-rays at room temperature by perovskite CsPbBr3 single crystals. *Nat. Commun.* **2018,** *9* (1), 1609.
269. Cho, H.; Jeong, S.-H.; Park, M.-H.; Kim, Y.-H.; Wolf, C.; Lee, C.-L.; Heo, J. H.; Sadhanala, A.; Myoung, N.; Yoo, S.; Im, S. H.; Friend, R. H.; Lee, T.-W., Overcoming the electroluminescence efficiency limitations of perovskite light-emitting diodes. *Science* **2015,** *350* (6265), 1222-1225.
270. Quan, L. N.; García de Arquer, F. P.; Sabatini, R. P.; Sargent, E. H., Perovskites for Light Emission. *Adv. Mater.* **2018,** *0* (0), 1801996.
271. Kovalenko, M. V.; Protesescu, L.; Bodnarchuk, M. I., Properties and potential optoelectronic applications of lead halide perovskite nanocrystals. *Science* **2017,** *358* (6364), 745-750.
272. Smith, M. D.; Jaffe, A.; Dohner, E. R.; Lindenberg, A. M.; Karunadasa, H. I., Structural origins of broadband emission from layered Pb-Br hybrid perovskites. *Chem. Sci.* **2017,** *8* (6), 4497-4504.

273. Benin, B. M.; Dirin, D. N.; Morad, V.; Worle, M.; Yakunin, S.; Raino, G.; Nazarenko, O.; Fischer, M.; Infante, I.; Kovalenko, M. V., Highly Emissive Self-Trapped Excitons in Fully Inorganic Zero-Dimensional Tin Halides. *Angew. Chem., Int. Ed.* **2018,** *57* (35), 11329-11333.
274. Hansel, R.; Allison, S.; Walker, G., Temperature dependent fluorescence of nanocrystalline ce-doped garnets for use as thermographic phosphors. In *Mater. Res. Soc. Symp. Proc.*, 2011/02/01 ed.; Cambridge University Press: 2008; Vol. 1076, pp 181-187.
275. Allison, S. W.; Buczyna, J. R.; Hansel, R. A.; Walker, D. G.; Gillies, G. T., Temperature-dependent fluorescence decay lifetimes of the phosphor Y3(Al0.5Ga0.5)5O12:Ce 1%. *J. Appl. Phys.* **2009,** *105* (3), 036105.
276. Voloshinovskii, A. S. M., V. B.; Myagkota, S. V.; Ostrovskii, I. P.; Pidzyrailo, N. S., Electronic states and luminescence properties of $CsSnBr_3$ crystal. *Opt. Spectrosc.* **1992,** *72* (4), 486-488.
277. Ahmed, N.; Kraus, H.; Kim, H. J.; Mokina, V.; Tsiumra, V.; Wagner, A.; Zhydachevskyy, Y.; Mykhaylyk, V. B., Characterisation of tungstate and molybdate crystals ABO_4 (A = Ca, Sr, Zn, Cd; B = W, Mo) for luminescence lifetime cryothermometry. *Materialia* **2018,** *4*, 287-296.
278. Savchuk, O. A.; Haro-Gonzalez, P.; Carvajal, J. J.; Jaque, D.; Massons, J.; Aguilo, M.; Diaz, F., Er:Yb:NaY2F5O up-converting nanoparticles for sub-tissue fluorescence lifetime thermal sensing. *Nanoscale* **2014,** *6* (16), 9727-33.
279. Man, M. T.; Lee, H. S., Discrete states and carrier-phonon scattering in quantum dot population dynamics. *Sci. Rep.* **2015,** *5*, 8267.
280. Rowley, M. I.; Coolen, A. C.; Vojnovic, B.; Barber, P. R., Robust Bayesian Fluorescence Lifetime Estimation, Decay Model Selection and Instrument Response Determination for Low-Intensity FLIM Imaging. *PLoS One* **2016,** *11* (6), e0158404.
281. Boens, N.; Qin, W.; Basarić, N.; Hofkens, J.; Ameloot, M.; Pouget, J.; Lefèvre, J.-P.; Valeur, B.; Gratton, E.; vandeVen, M.; Silva, N. D.; Engelborghs, Y.; Willaert, K.; Sillen, A.; Rumbles, G.; Phillips, D.; Visser, A. J. W. G.; van Hoek, A.; Lakowicz, J. R.; Malak, H.; Gryczynski, I.; Szabo, A. G.; Krajcarski, D. T.; Tamai, N.; Miura, A., Fluorescence Lifetime Standards for Time and Frequency Domain Fluorescence Spectroscopy. *Anal. Chem.* **2007,** *79* (5), 2137-2149.
282. He, Y.; Liang, B.; Zou, Y.; He, J.; Yang, J., Depth Errors Analysis and Correction for Time-of-Flight (ToF) Cameras. *Sensors* **2017,** *17* (1).
283. Bonjour, y.-E.; Singh, A.; Baechler, T.; Kayal, M., Novel Imaging Method and Optimized Demodulation Pixels for Wide-Field Fluorescence Lifetime Imaging Microscopy. *IEEE Sens. J.* **2011**.
284. Yakunin, S.; Benin, B. M.; Shynkarenko, Y.; Nazarenko, O.; Bodnarchuk, M. I.; Dirin, D. N.; Hofer, C.; Cattaneo, S.; Kovalenko, M. V., High-resolution remote thermometry and thermography using luminescent low-dimensional tin-halide perovskites. *Nat. Mater.* **2019,** *18* (8), 846-852.
285. Worku, M.; Tian, Y.; Zhou, C.; Lee, S.; Meisner, Q.; Zhou, Y.; Ma, B., Sunlike White-Light-Emitting Diodes Based on Zero-Dimensional Organic Metal Halide Hybrids. *ACS Appl. Mater. Interfaces* **2018,** *10* (36), 30051-30057.
286. Li, M.; Zhou, J.; Zhou, G.; Molokeev, M. S.; Zhao, J.; Morad, V.; Kovalenko, M.

V.; Xia, Z., Hybrid Metal Halides with Multiple Photoluminescence Centers. *Angew. Chem., Int. Ed.* **2019,** *58* (51), 18670-18675.
287. Vogler, A.; Nikol, H., The Structures of s2Metal Complexes in the Ground and sp Excited States. *Comments Inorg. Chem.* **1993,** *14* (4), 245-261.
288. Kentsch, R.; Scholz, M.; Horn, J.; Schlettwein, D.; Oum, K.; Lenzer, T., Exciton Dynamics and Electron–Phonon Coupling Affect the Photovoltaic Performance of the Cs2AgBiBr6 Double Perovskite. *J. Phys. Chem. C* **2018,** *122* (45), 25940-25947.
289. Oomen, E. W. J. L.; Dirksen, G. J., Crystal growth and luminescence of Sb3+-Doped Cs2NaMCl6 (M = Sc, Y, La). *Mater. Res. Bull.* **1985,** *20* (4), 453-457.
290. Blasse, G., Vibrational structure in the luminescence spectra of ions in solids. In *Electronic and Vibronic Spectra of Transition Metal Complexes I*, Yersin, H., Ed. Springer Berlin Heidelberg: Berlin, Heidelberg, 1994; pp 1-25.
291. Xiao, Z.; Meng, W.; Wang, J.; Mitzi, D. B.; Yan, Y., Searching for promising new perovskite-based photovoltaic absorbers: the importance of electronic dimensionality. *Mater. Horiz.* **2017,** *4* (2), 206-216.
292. Wells, H. L.; Foote, H. W., On certain double halogen salts of caesium and rubidium. *Am. J. Sci.* **1897,** *s4-3* (18), 461-465.
293. Wells, H. L., Generalizations on Double Halogen Salts. *J. Am. Chem. Soc.* **1901,** *26* (5), 389-408.
294. Aussieker, T.; Keller, H. L.; Oldag, T.; Prots, Y.; Ruck, M.; Wosylus, A., Syntheses and Crystal Structures of the Thallium(I) Iodobismuthates(III) Tl7Bi3I16 and Tl3BiI6. *Z. Anorg. Allg. Chem.* **2007,** *633* (4), 603-609.
295. Morad, V.; Cherniukh, I.; Pöttschacher, L.; Shynkarenko, Y.; Yakunin, S.; Kovalenko, M. V., Manganese(II) in Tetrahedral Halide Environment: Factors Governing Bright Green Luminescence. *Chem. Mater.* **2019,** *31* (24), 10161-10169.
296. Ninomiya, S.; Adachi, S., Optical properties of cubic and hexagonal CdSe. *J. Appl. Phys.* **1995,** *78* (7), 4681-4689.
297. Jasieniak, J.; Smith, L.; van Embden, J.; Mulvaney, P.; Califano, M., Re-examination of the Size-Dependent Absorption Properties of CdSe Quantum Dots. *J. Phys. Chem. C* **2009,** *113* (45), 19468-19474.
298. Turner, W. J.; Reese, W. E.; Pettit, G. D., Exciton Absorption and Emission in InP. *Phys. Rev.* **1964,** *136* (5A), A1467-A1470.
299. Hens, Z.; Moreels, I., Light absorption by colloidal semiconductor quantum dots. *J. Mater. Chem.* **2012,** *22* (21), 10406.
300. Moreels, I.; Lambert, K.; Smeets, D.; De Muynck, D.; Nollet, T.; Martins, J. C.; Vanhaecke, F.; Vantomme, A.; Delerue, C.; Allan, G.; Hens, Z., Size-dependent optical properties of colloidal PbS quantum dots. *ACS Nano* **2009,** *3* (10), 3023-30.
301. De Roo, J.; Ibanez, M.; Geiregat, P.; Nedelcu, G.; Walravens, W.; Maes, J.; Martins, J. C.; Van Driessche, I.; Kovalenko, M. V.; Hens, Z., Highly Dynamic Ligand Binding and Light Absorption Coefficient of Cesium Lead Bromide Perovskite Nanocrystals. *ACS Nano* **2016,** *10* (2), 2071-81.
302. Maes, J.; Balcaen, L.; Drijvers, E.; Zhao, Q.; De Roo, J.; Vantomme, A.; Vanhaecke, F.; Geiregat, P.; Hens, Z., Light Absorption Coefficient of CsPbBr3 Perovskite Nanocrystals. *J. Phys. Chem. Lett.* **2018,** *9* (11), 3093-3097.

303. Takagahara, T., Effects of dielectric confinement and electron-hole exchange interaction on excitonic states in semiconductor quantum dots. *Phys. Rev. B: Condens. Matter Mater. Phys.* **1993,** *47* (8), 4569-4584.
304. Ricard, D.; Ghanassi, M.; Schanne-Klein, M. C., Dielectric confinement and the linear and nonlinear optical properties of semiconductor-doped glasses. *Opt. Commun.* **1994,** *108* (4-6), 311-318.
305. Yu, W. W.; Qu, L.; Guo, W.; Peng, X., Experimental Determination of the Extinction Coefficient of CdTe, CdSe, and CdS Nanocrystals. *Chem. Mater.* **2003,** *15* (14), 2854-2860.
306. Fabini, D. H.; Laurita, G.; Bechtel, J. S.; Stoumpos, C. C.; Evans, H. A.; Kontos, A. G.; Raptis, Y. S.; Falaras, P.; Van der Ven, A.; Kanatzidis, M. G.; Seshadri, R., Dynamic Stereochemical Activity of the Sn(2+) Lone Pair in Perovskite CsSnBr3. *J. Am. Chem. Soc.* **2016,** *138* (36), 11820-32.
307. Huang, L.-y.; Lambrecht, W. R. L., Electronic band structure, phonons, and exciton binding energies of halide perovskites CsSnCl3, CsSnBr3, and CsSnI3. *Phys. Rev. B* **2013,** *88* (16).
308. McCall, K. M.; Liu, Z.; Trimarchi, G.; Stoumpos, C. C.; Lin, W.; He, Y.; Hadar, I.; Kanatzidis, M. G.; Wessels, B. W., α-Particle Detection and Charge Transport Characteristics in the A3M2I9Defect Perovskites (A = Cs, Rb; M = Bi, Sb). *ACS Photonics* **2018,** *5* (9), 3748-3762.
309. Motti, S. G.; Crothers, T.; Yang, R.; Cao, Y.; Li, R.; Johnston, M. B.; Wang, J.; Herz, L. M., Heterogeneous Photon Recycling and Charge Diffusion Enhance Charge Transport in Quasi-2D Lead-Halide Perovskite Films. *Nano Lett.* **2019,** *19* (6), 3953-3960.
310. Mykhaylyk, V. B.; Kraus, H.; Kapustianyk, V.; Kim, H. J.; Mercere, P.; Rudko, M.; Da Silva, P.; Antonyak, O.; Dendebera, M., Bright and fast scintillations of an inorganic halide perovskite CsPbBr3 crystal at cryogenic temperatures. *Sci. Rep.* **2020,** *10* (1), 8601.
311. Cai, Y.; Xie, W.; Ding, H.; Chen, Y.; Thirumal, K.; Wong, L. H.; Mathews, N.; Mhaisalkar, S. G.; Sherburne, M.; Asta, M., Computational Study of Halide Perovskite-Derived A2BX6Inorganic Compounds: Chemical Trends in Electronic Structure and Structural Stability. *Chem. Mater.* **2017,** *29* (18), 7740-7749.
312. Maughan, A. E.; Ganose, A. M.; Scanlon, D. O.; Neilson, J. R., Perspectives and Design Principles of Vacancy-Ordered Double Perovskite Halide Semiconductors. *Chem. Mater.* **2019,** *31* (4), 1184-1195.
313. Engel, G., Die Kristallstrukturen einiger Hexachlorokomplexsalze. *Z. Kristallogr. Cryst. Mater.* **1935,** *90* (1-6).
314. Ning, W.; Gao, F., Structural and Functional Diversity in Lead-Free Halide Perovskite Materials. *Adv. Mater.* **2019,** *31* (22), e1900326.
315. Sedakova, T. V.; Mirochnik, A. G., Luminescent and thermochromic properties of tellurium(IV) halide complexes with cesium. *Opt. Spectrosc.* **2016,** *120* (2), 268-273.
316. Setterberg, C., *Oefversigt K. Vetensk, Akad. Forhandl.* **1882,** *6* (27).
317. Jensen, K. A., Die Kristallstruktur der Verbindungen (NH,),SbBr,, Rb,SbBr, und Rb,SbCI,. *Z. Anorg. Allg. Chem.* **1937,** (232), 193-201.
318. Wells, H. L.; Metzger, F. J., On a Salt of Quadrivalent Antimony. *Am. Chem. J.* **1901,** *26*, 268-271.

319. Weinland, R. E.; Schlegelmilch, F., Über Doppelsalze des Antimonpentachlorids. *Ber. Dtsch. Chem. Ges.* **1901,** *2* (17), 905-964.
320. Tovborg Jensen, A.; Rasmussen, S. E., A Note on the Alleged Tetravalency of Antimony. *Acta Chem. Scand.* **1955,** *9*, 7.
321. Day, P., Spectra and Constitution of Antimony(III), Antimony(V) Hexahalide Salts and Related Compounds. *Inorg. Chem.* **1963,** *2* (452), 452-456.
322. Robin, M. B.; Day, P., Mixed Valence Chemistry-A Survey and Classification. In *Advances in Inorganic Chemistry and Radiochemistry*, Emeléus, H. J.; Sharpe, A. G., Eds. Academic Press: 1968; Vol. 10, pp 247-422.
323. Hackert, M. L.; Lawton, S. L.; Jacobson, R. A., Properties of lntervalence Antimony Bromides. *Proc. Iowa Acad. Sci.* **1968,** *75* (1).
324. Hubbard, C. R.; Jacobson, R. A., The Crystal Structure of Rb4SbIIISbvBr12. *Proc. Iowa Acad. Sci.* **1968,** *75* (1), 85-96.
325. Prassides, K.; Day, P.; Cheetham, A. K., Crystal structures of mixed-valency and mixed-metal salts $A_2M^{III}_{0.5}Sb^{V}_{0.5}X_6$ (A = Rb, Cs; M = Sb, Bi, In, Tl, Fe, Rh; X = Cl, Br). A powder neutron diffraction study. *Inorg. Chem.* **1985,** *24* (4), 545-552.
326. Atkinson, L.; Day, P., Charge transfer in mixed-valence solids. Part IV. Electronic spectra of hexachloroantimonates(III,V) *J. Chem. Soc. A* **1969,** (0), 2423-2431.
327. Prassides, K.; Day, P.; Cheetham, A. K., Anion ordering in mixed valence dicesium hexachloroantimonate (Cs_2SbCl_6) and related salts. *J. Am. Chem. Soc.* **1983,** *105* (10), 3366-3368.
328. Atkinson, L.; Day, P., Charge transfer in mixed-valence solids. Part V. Semiconductivity of hexachloroantimonates(III,V) *J. Chem. Soc. A* **1969,** (0), 2432-2436.
329. Day, P.; Diggle, P. J.; Griffiths, G. A., Charge-transfer Spectra of Post-transition-metal Halide Complexes. *J. Chem. Soc. Dalton Trans.* **1974,** (13), 1446-1452
330. Prassides, K.; Day, P.; Cheetham, A. K., Crystal Structures of Mixed-Valency and Mixed-Metal Salts A2MIII0.5SbV0.5X6 (A = Rb, Cs; M = Sb, Bi, in, TI, Fe, Rh; X =Cl, Br). A Powder Neutron Diffraction Study. *Inorg. Chem.* **1985,** *24* (4), 545-552.
331. Clark, R. J. H.; Trumble, W. R., Resonance Raman Spectra of Some Mixed-valence Halogeno-compounds of Antimony and Lead. *J. Chem. Soc. Dalton Trans.* **1976,** (12), 1145-1149.
332. Combs, V. E.; Oswald, I. W. H.; Neilson, J. R., Hydrothermal Crystal Growth of Mixed Valence Cs2SbBr6. *Cryst. Growth Des.* **2019,** *19* (7), 4090-4094.
333. Lawton, S. L.; Jacobson, R. A., The Crystal Structure of Ammonium Hexabromoantimonate, (NH4)4SbIIISbVBr12. *Inorg. Chem.* **1966,** *5* (5), 743-749.
334. Benin, B. M.; McCall, K. M.; Wörle, M.; Morad, V.; Aebli, M.; Yakunin, S.; Shynkarenko, Y.; Kovalenko, M. V., The Rb7Bi3-3xSb3xCl16 family: A Fully Inorganic Solid Solution with Room-Temperature Luminescent Members. *Angew. Chem., Int. Ed.* **2020,** *59*.
335. Robin, M. B.; Day, P., Mixed Valence Chemistry-A Survey and Classification. **1968,** *10*, 247-422.
336. Launay, J.-P., Long-distance intervalence electron transfer. *Chem. Soc. Rev.* **2001,** *30* (6), 386-397.
337. Gray, H. B.; Winkler, J. R., Electron Flow through Proteins. *Chem. Phys. Lett.* **2009,**

483 (1-3), 1-9.
338. Launay, J.-P., Mixed-Valent Compounds and their Properties - Recent Developments. *Eur. J. Inorg. Chem.* **2020,** *2020* (4), 329-341.
339. Beck, H. P.; Milius, W., Study on A4BX6 compounds. I. Structure Refinement of Ternary Cd Halides A4CdX6 (A = NH4, K, Rb, In, Tl; X = Cl, I). *Z. Anorg. Allg. Chem.* **1986,** *539* (8), 7-17.
340. Stoumpos, C. C.; Frazer, L.; Clark, D. J.; Kim, Y. S.; Rhim, S. H.; Freeman, A. J.; Ketterson, J. B.; Jang, J. I.; Kanatzidis, M. G., Hybrid germanium iodide perovskite semiconductors: active lone pairs, structural distortions, direct and indirect energy gaps, and strong nonlinear optical properties. *J. Am. Chem. Soc.* **2015,** *137* (21), 6804-19.
341. Li, Y.; Rao, Y.; Mak, K. F.; You, Y.; Wang, S.; Dean, C. R.; Heinz, T. F., Probing symmetry properties of few-layer MoS2 and h-BN by optical second-harmonic generation. *Nano Lett.* **2013,** *13* (7), 3329-33.
342. Zhuang, R.; Wang, X.; Ma, W.; Wu, Y.; Chen, X.; Tang, L.; Zhu, H.; Liu, J.; Wu, L.; Zhou, W.; Liu, X.; Yang, Y., Highly sensitive X-ray detector made of layered perovskite-like (NH4)3Bi2I9 single crystal with anisotropic response. *Nat. Photonics* **2019,** *13* (9), 602-608.
343. Zhang, Y.; Liu, Y.; Xu, Z.; Ye, H.; Yang, Z.; You, J.; Liu, M.; He, Y.; Kanatzidis, M. G.; Liu, S. F., Nucleation-controlled growth of superior lead-free perovskite Cs3Bi2I9 single-crystals for high-performance X-ray detection. *Nat. Commun.* **2020,** *11* (1), 2304.
344. Tanino, H.; Kobayashi, K., Relaxation of Electron-Phonon system in optically excited Quasi-1-D Mixed Valence Crystal Wolffram's Red Salt. *J. Phys. Soc. Jpn.* **1983,** *52* (4), 1446-1456.
345. Jursenas, S.; Gruodis, A.; Kodis, G.; Chachisvilis, M.; Gulbinas, V.; Silinsh, E. A.; Valkunas, L., Free and Self-Trapped Charge-Transfer Excitons in Crystals of Dipolar Molecules of N,N-Dimethylaminobenzylidene 1,3-Indandione. *J. Phys. Chem. B* **1998,** *102*, 1086-1094.
346. Jursenas, S.; Gulbinas, V.; Gruodis, A.; Kodis, G.; Kovalevskij, V.; Valkunas, L., Spectroscopy of self-trapped charge-transfer excitons in polar Đlms and crystals of N,N-dimethylaminobenzylidene 1,3-indandione (DMABI). *Phys. Chem. Chem. Phys.* **1999,** *1*, 1715-1718.
347. Weber, W. H.; Lambe, J., Luminescent greenhouse collector for solar radiation. *Appl. Opt.* **1976,** *15* (10), 2299-2300.
348. Goetzberger, A.; Greubel, W., Solar Energy Conversion with Fluorescent Collectors. *Appl. Phys.* **1977,** *14*, 123-139.
349. Levitt, J. A.; Weber, W. H., Materials for luminescent greenhouse solar collectors. *Appl. Opt.* **1977,** *16* (10), 2684-2689.
350. Markvart, T., Detailed balance method for ideal single-stage fluorescent collectors. *J. Appl. Phys.* **2006,** *99* (2), 026101.
351. Vishwanathan, B.; Reinders, A. H. M. E.; de Boer, D. K. G.; Desmet, L.; Ras, A. J. M.; Zahn, F. H.; Debije, M. G., A comparison of performance of flat and bent photovoltaic luminescent solar concentrators. *Sol. Energy* **2015,** *112*, 120-127.
352. Correia, S. F. H.; de Zea Bermudez, V.; Ribeiro, S. J. L.; André, P. S.; Ferreira, R. A. S.; Carlos, L. D., Luminescent solar concentrators: challenges for lanthanide-based

organic–inorganic hybrid materials. *J. Mater. Chem. A* **2014,** *2* (16), 5580-5596.
353. Rafiee, M.; Chandra, S.; Ahmed, H.; McCormack, S. J., An overview of various configurations of Luminescent Solar Concentrators for photovoltaic applications. *Opt. Mater.* **2019,** *91*, 212-227.
354. Debije, M. G.; Verbunt, P. P. C., Thirty Years of Luminescent Solar Concentrator Research: Solar Energy for the Built Environment. *Adv. Energy Mater.* **2012,** *2* (1), 12-35.
355. Coropceanu, I.; Bawendi, M. G., Core/shell quantum dot based luminescent solar concentrators with reduced reabsorption and enhanced efficiency. *Nano Lett.* **2014,** *14* (7), 4097-101.
356. Meinardi, F.; Colombo, A.; Velizhanin, K. A.; Simonutti, R.; Lorenzon, M.; Beverina, L.; Viswanatha, R.; Klimov, V. I.; Brovelli, S., Large-area luminescent solar concentrators based on 'Stokes-shift-engineered' nanocrystals in a mass-polymerized PMMA matrix. *Nat. Photonics* **2014,** *8* (5), 392-399.
357. Bradshaw, L. R.; Knowles, K. E.; McDowall, S.; Gamelin, D. R., Nanocrystals for luminescent solar concentrators. *Nano Lett.* **2015,** *15* (2), 1315-23.
358. Meinardi, F.; Akkerman, Q. A.; Bruni, F.; Park, S.; Mauri, M.; Dang, Z.; Manna, L.; Brovelli, S., Doped Halide Perovskite Nanocrystals for Reabsorption-Free Luminescent Solar Concentrators. *ACS Energy Lett.* **2017,** *2* (10), 2368-2377.
359. Anand, A.; Zaffalon, M. L.; Gariano, G.; Camellini, A.; Gandini, M.; Brescia, R.; Capitani, C.; Bruni, F.; Pinchetti, V.; Zavelani-Rossi, M.; Meinardi, F.; Crooker, S. A.; Brovelli, S., Evidence for the Band-Edge Exciton of CuInS
2
Nanocrystals Enables Record Efficient Large-Area Luminescent Solar Concentrators. *Adv. Funct. Mater.* **2019,** *30* (4), 1906629.
360. Wu, J.; Tong, J.; Gao, Y.; Wang, A.; Zhang, T.; Tan, H.; Nie, S.; Deng, Z., Efficient and Stable Thin-Film Luminescent Solar Concentrators Enabled by Near-Infrared Emission Perovskite Nanocrystals. *Angew. Chem., Int. Ed.* **2020,** *59* (20), 7738-7742.
361. Li, Z.; Johnston, A.; Wei, M.; Saidaminov, M. I.; Martins de Pina, J.; Zheng, X.; Liu, J.; Liu, Y.; Bakr, O. M.; Sargent, E. H., Solvent-Solute Coordination Engineering for Efficient Perovskite Luminescent Solar Concentrators. *Joule* **2020,** *4* (3), 631-643.
362. Kalytchuk, S.; Wang, Y.; Polakova, K.; Zboril, R., Carbon Dot Fluorescence-Lifetime-Encoded Anti-Counterfeiting. *ACS Appl. Mater. Interfaces* **2018,** *10* (35), 29902-29908.
363. Westphal, V.; Lauterbach, M. A.; Di Nicola, A.; Hell, S. W., Dynamic far-field fluorescence nanoscopy. *New J. Phys.* **2007,** *9* (12), 435-435.
364. Vicidomini, G.; Bianchini, P.; Diaspro, A., STED super-resolved microscopy. *Nat. Methods* **2018,** *15* (3), 173-182.
365. Blom, H.; Widengren, J., Stimulated Emission Depletion Microscopy. *Chem. Rev.* **2017,** *117* (11), 7377-7427.
366. Klar, T. A.; Jakobs, S.; Dyba, M.; Egner, A.; Hell, S. W., Fluorescence microscopy with diffraction resolution barrier broken by stimulated emission. *PNAS* **2000,** *97* (15), 8206–8210.
367. Sheldrick, G. M., A short history of SHELX. *Acta Crystallogr. Sect. A* **2008,** *64* (Pt 1), 112-22.

368. Dolomanov, O. V.; Bourhis, L. J.; Gildea, R. J.; Howard, J. A. K.; Puschmann, H., OLEX2: a complete structure solution, refinement and analysis program. *J. Appl. Crystallogr.* **2009,** *42* (2), 339-341.
369. Toby, B. H.; Von Dreele, R. B., GSAS-II: the genesis of a modern open-source all purpose crystallography software package. *J. Appl. Crystallogr.* **2013,** *46* (2), 544-549.
370. Toby, B. H., EXPGUI, a graphical user interface for GSAS. *J. Appl. Cryst.* **2001,** *34*, 210-213.

Curriculum Vitae

Personal information

E-mail	bbenin93@gmail.com
Mobile	+41 78 686 0589
Address	Brunngasse 4, 8400 Winterthur, Switzerland
Date of birth	5th April 1993
Nationality	USA (naturalized)
Permit	B
Languages	English – Native
	Russian – Fluent
	German – B1

Education

Ph.D. Inorganic Chemistry | ETH Zürich | 2016 – 2020

M.S. Inorganic Chemistry | Kent State University | 2015 – 2016

GPA: 4.00/4.00

Thesis: Synthesis and Characterization of Novel Gold-Based Nanoparticulate Chemotherapeutic Agents

B.S. Chemistry | Kent State University | 2011 – 2015

Summa Cum Laude, GPA: 3.99/4.00.

Spring semester of 2014 spent abroad at the University of Leicester (UK).

Work experience

R&D Intern | GOJO Industries Inc. | 2014 – 2015

As part of the skin science and microbiology teams, I created a knowledge-database using literature from microbiology, skin science, biochemistry, and microbiome science to generate new product ideas.

Undergraduate Research Assistant | Kent State University | 2013

In the group of Prof. Songping D. Huang, I worked on the synthesis of gallium-based nanoparticles, the hydrothermal syntheses of gallium-based metal-organic frameworks, and the investigation of metal-organic compounds for therapeutic applications.

QC/Analytical Lab Intern | Rhein Chemie Corp. | 2012

I checked and ensured that batches produced in the manufacturing facility met all necessary specifications using FT-IR, TGA, elemental analysis (CNS), and rheometery (ODR/MDR).

Teaching Experience

Teaching Assistant | ETH Zürich | 2017 – 2020

- Taught and supervised two sections of Anorganische Chemie I praktikum.
- Assisted with the preparation the new Solid-state chemistry praktikum.

Teaching Assistant | Kent State University | 2015 – 2016

Taught and supervised two sections of Organic Chemistry I and II Lab (*ca*. 60 students each).

Publications

1. McCall, K.M.; Morad, V.; **Benin, B.M.**; Kovalenko, M.V. Efficient Lone Pair-Driven Luminescence: Structure-Property Relationships in Emissive 5s2 Metal Halides. *ACS Mater. Lett.* 2020, Accepted.
2. Piveteau, L.; Marcel, A.; Yazdani, N.; Millen, M.; Korosec, L.; Krieg, F.; **Benin, B.M.**; Morad, V.; Piveteau, C.; Shiroka, T.; Comas-Vives, A.; Copéret, C.; Lindenberg, A.; Wood, V.; Verel, R.; Kovalenko, M.V. Bulk and nanocrystalline cesium lead halide perovskites as seen by halide magnetic resonance. *ACS Cent. Sci.* 2020, Accepted.
3. **Benin, B.M.**; McCall, K.M.; Wörle, M.; Morad, V.; Aebli, M.; Yakunin, S.; Shynkarenko, S.; Kovalenko, M.V. The $Rb_7Bi_{3-3x}Sb_{3x}Cl_{16}$ family: A Fully Inorganic Solid Solution with Room-Temperature Luminescent Members. *Angew. Chem. Int. Ed.* 2020, Accepted.
4. Aebli, M.; **Benin, B.M.**; McCall, K.M.; Morad, V.; Thöny, D.; Grützmacher, H.; Kovalenko, M.V. White $CsPbBr_3$: Characterizing the One-Dimensional Cesium Lead Bromide Polymorph. *Helv. Chim. Acta* 2020, Accepted.
5. Aebli, M.; Piveteau, L.; Nazarenko, O.; **Benin, B.M.**; Krieg, F.; Verel, R.; Kovalenko, M.V. Lead-Halide Scalar Couplings in ^{207}Pb NMR of $APbX_3$ Perovskites (A = Cs, Methylammonium, Formamidinium; X = Cl, Br, I). *Sci. Rep.* 2020, 10, 8229
6. Dirin, D.N.; **Benin, B.M.**; Yakunin, S.; Krumeich, F.; Frison, R.; Rainò, G.; Kovalenko, M.V. Microcarrier-Assisted Inorganic Shelling of Lead Halide Perovskite Nanocrystals. *ACS Nano* 2019, 13, 11642-11652.
7. Yakunin, S.[1]; **Benin, B.M.[1]**; Shynkarenko, S.; Nazarenko, O.; Bodnarchuk, M.I.; Dirin, D.N.; Hofer, C.; Cattaneo, S.; Kovalenko, M.V. High-resolution remote thermography using luminescent low-dimensional tin-halide perovskites. *Nat. Mater.* 2019. 18, 846–852.
8. Nazarenko, O.; Kotyrba, M.R.; Yakunin, S.; Wörle, M.; **Benin, B.M.**; Rainò, G.; Krumeich, F.; Kepenekian, M.; Even, J.; Katan, C.; Kovalenko, M.V. *Chem. Mater.* 2019, 31, 2121-2129.
9. **Benin, B.M.**; Dirin, D.N.; Morad, V.; Wörle, M.; Yakunin, S.; Rainò, G.; Nazarenko, O.; Fischer, M.; Infante, I.; Kovalenko, M.V., Highly Emissive Self-Trapped Excitons in

[1] Co-first author

Fully Inorganic Zero-Dimensional Tin Halides. *Angew. Chem. Int. Ed. Engl.* 2018, *57* (35), 11329-11333.

10. Nazarenko, O.; Kotyrba, M.R.; Yakunin, S.; Aebli, M.; Rainò, G.; **Benin, B.M**.; Wörle, M.; Kovalenko, M.V., Guanidinium-Formamidinium Lead Iodide: A Layered Perovskite-Related Compound with Red Luminescence at Room Temperature. *J. Am. Chem. Soc.* 2018, 140 (11), 3850-3853.

Public Spotlight on my Research

- "Glowing crystals help to measure temperatures from afar." *Nature Research Highlights*, 8 July 2019.
- Lee, Chris. "Painted-on salt provides glowing thermometer for tiny things." *Ars Technica*, 17 July 2019.

Patents

- Kovalenko, M.; Lüchinger, N. A.; **Benin, B**.; Dirin, D. Luminescent Composite Materials. **2018.** US10329484B2

Presentations

1. "Oxidatively stable zero-dimensional materials: the $Rb_7Bi_{3-3x}Sb_{3x}Cl_{16}$ family" at nanoGe Online Meetup conference: Beyond Lead Halide Perovskites. April 23, 2020 (ePoster).
2. "Low-dimensional tin-halides: properties and novel applications" at nanoGe, Berlin, Germany. November 12, 2019 (oral).
3. "Low-dimensional tin-halides: properties and novel applications" at SCS Fall Meeting 2019, Zurich, Switzerland. September 6, 2019 (poster).
4. "Highly Emissive Self-Trapped Excitons in Fully Inorganic Zero-Dimensional Tin-Halides" at Fall meeting of nanoGe, Torremolinos, Spain. October 25, 2018 (Oral). S4.5-O2.
5. "Studies towards Novel Gold Base Nanoparticle Chemotherapy Agents" at 251st national meeting of the American Chemical Society, San Diego, CA. March 15, 2016 (Poster). INOR 934.
6. "Studies towards the Formation of Novel Gold Copper Alloyed Anti-neoplastic Agents" at Ohio Inorganic Weekend, Bowling Green State University, OH. November 13, 2015 (Poster)
7. Three Minute Thesis (3MT) Finalist, Kent State University, October 30, 2015

Awards and Honors

- 2019 «Chemistry Travel Award» from the «Platform Chemistry» of the Swiss Academy of Sciences (SCNAT), together with the Swiss Chemical Society (SCS).
- Marie Skłodowska-Curie student (funded by SNF) as part of a European Training Network (ETN). H2020-MCSA-ITN-642656.
- ACS Division of Organic Chemistry Undergraduate Award in Organic Chemistry. Awarded by the Kent State University, Department of Chemistry and Biochemistry.
- Undergraduate Student Excellence Award. Awarded by the Kent State University, Department of Chemistry and Biochemistry.
- ACS Division of Inorganic Chemistry Undergraduate Award in Inorganic Chemistry. Awarded by the Akron chapter of the American Chemical Society.
- Dr. Raymond L. Burich Chemistry Scholarship. Awarded by the Kent State University, Department of Chemistry and Biochemistry.
- Outstanding Chemistry Junior. Awarded by the Kent State University, Department of Chemistry and Biochemistry.
- Clarence L. Cook Memorial Award. Awarded by the Kent State University, Department of Chemistry and Biochemistry.
- Inducted into Phi Beta Kappa – the oldest academic honor society within the USA (founded 1776).

Hobbies

I am an advanced open-water scuba diver (Diver no. 1908EO6895) and a violist.